Comparison of CO_2-EOR Performance between Offshore and Onshore Classes of Reservoirs

Saeed Ghanbari

Submitted for the Degree of Doctor of Philosophy

Institute of Petroleum Engineering
School of Energy, Geoscience, Infrastructure and Society
Heriot-Watt University
Edinburgh, UK

July 2017

Abstract

CO_2 has been extensively used in onshore fields, primarily for EOR. However, it has been used less offshore due to limited transportation infrastructure and the lack of secure CO_2 supply. Recently, CO_2 flooding has been reconsidered in offshore fields for both EOR and storage. The performance of CO_2 flooding in the offshore classes of reservoirs, which are characterised by fundamentally dissimilar properties and development characteristics than onshore reservoirs, might be different from the past experience of CO_2 flooding observed onshore. Offshore developments are characterised by higher rates of depletion, fewer wells, larger well spacing and higher well rates compared to onshore reservoirs which are characterised by pattern development and shorter well spacings; moreover, the motivation behind CO_2 flooding might be different offshore. The aim of this study is to review these differences between CO_2 flooding in offshore and onshore classes of reservoirs, exclusively within the context of reservoir engineering. In the first part of this study, different aspects of CO_2 flooding are compared between two major provinces i.e. the onshore Permian Basin province located in the United States and the offshore North Sea province. It will be shown that CO_2-EOR has many similar characteristics in these two provinces despite the fact that ambient reservoir conditions are fundamentally different between them. Next, flow patterns are compared between these two classes of reservoirs. Flow patterns in each of reservoirs are investigated by deriving the key dimensionless numbers which may characterise CO_2 flooding in each of them. It will be shown that CO_2 flooding is slightly more gravity dominated in the North Sea class of reservoirs. Additionally, in the absence of gravity effects, flow patterns upon CO_2 flooding are expected to be more stable in the North Sea class of reservoirs due to better mobility ratios that characterise the displacement in this province. The fact that the motivation for CO_2 flooding is potentially different between these two classes of reservoir may also promote alternate CO_2 flooding process designs offshore, which should satisfy both the EOR and storage requirements of CO_2 flooding in the offshore class of reservoirs.

The second part of this thesis investigates the grid size requirements for modelling miscible processes such as CO_2-EOR. A new approach based on measuring heterogeneity induced dispersivities in longitudinal and transverse orientations is introduced and developed. Matching these dispersivities with equivalent numerical dispersion may determine the correct size of grid blocks in a miscible displacement simulation.

To my family

For their patience and support

Acknowledgements

I would like to express my sincere appreciation to my supervisors, Professor Eric J. Mackay and Dr. Gillian E. Pickup for their supervision, guidance and support. Without their support and guidance it was not possible to complete this work.

I also wish to thank the examiners of this work, Dr. Michael King from Texas A&M University and Professor Ken Sorbie from the Institute of Petroleum Engineering of Heriot-Watt University, for examining this thesis.

Foundation CMG is also thanked for supporting the PhD studentship which has enable this work to be conducted. CMG Ltd is thanked for providing simulation software for this project in addition to training and technical support. Marco, Susan and Hossein are particularly appreciated in this regard. Susan is also gratefully thanked for her reviews of this work and her valuable feedback.

Special thanks to the small but lovely Persian community in Edinburgh for being always supportive, helpful and kind. Shahab, Amir, Hadi, Mohammad Reza, Ehsan, Edris and their lovely families, Fazel also from Dundee with whom we had lots of valuable techno-economic discussions. Yousef and Mohsen from the Persian Rug Village and many other people who made Edinburgh like my second home as I never felt away, particularly in the terrible days of my son's Guillain-Barre. I could not be even luckier than finding these lovely people. Surely I will miss all of them.

NIOC is also thanked for allowing me to pursue my PhD. Special thanks to Heather, the FAST administrative officer, for her excellent admin support.

ACADEMIC REGISTRY
Research Thesis Submission

Name*:*	**SAEED GHANBARI**		
School:	**EGIS, INSTITUTE OF PETROLEUM ENGINEERING**		
Version: *(i.e. First, Resubmission, Final)*	**FINAL**	Degree Sought:	**PhD, Petroleum Engineering**

Declaration

In accordance with the appropriate regulations I hereby submit my thesis and I declare that:

1) the thesis embodies the results of my own work and has been composed by myself
2) where appropriate, I have made acknowledgement of the work of others and have made reference to work carried out in collaboration with other persons
3) the thesis is the correct version of the thesis for submission and is the same version as any electronic versions submitted*.
4) my thesis for the award referred to, deposited in the Heriot-Watt University Library, should be made available for loan or photocopying and be available via the Institutional Repository, subject to such conditions as the Librarian may require
5) I understand that as a student of the University I am required to abide by the Regulations of the University and to conform to its discipline.
6) I confirm that the thesis has been verified against plagiarism via an approved plagiarism detection application e.g. Turnitin.

* *Please note that it is the responsibility of the candidate to ensure that the correct version of the thesis is submitted.*

Signature of Candidate*:*		Date:	

Submission

Submitted By *(name in capitals):*	**SAEED GHANBARI**
Signature of Individual Submitting:	
Date Submitted:	

For Completion in the Student Service Centre (SSC)

Received in the SSC by *(name in capitals):*			
1.1 Method of Submission *(Handed in to SSC; posted through internal/external mail):*			
1.2** E-thesis Submitted (**mandatory for final theses)			
Signature:		Date:	

Please note this form should be bound into the submitted thesis.

Publications

Ghanbari, S., Mackay, E. J., & Pickup, G. E. (2016). Comparison of CO_2-EOR Performance between Offshore and Onshore Environments. Offshore Technology Conference. doi:10.4043/26590-MS.

Ghanbari, S., Mackay, E. J., & Pickup, G. E. (2017). What are the differences between CO_2-EOR Onshore and Offshore? EAGE 2017, 19th European Symposium on Improved Oil Recovery, Stavanger, Norway.

Table of Contents

List of Figures

List of Tables

Nomenclature

The majority of the units used in this thesis are in the English system of units, except for in the dimensionless number calculations, where the SI system of units has been used.

k	permeability (*mD*)
k_z	vertical permeability (*mD*)
k_x	horizontal permeability (*mD*)
A	Area (ft^2)
ρ	density (lb/ft^3)
μ	viscosity (*cP*)
B_o	oil formation volume factor (*rb/stb*)
k_{rj}	endpoint relative permeability of phase *j*
S_{jr}	endpoint saturation of phase *j*
γ_j	relative permeability exponent in the Corey correlation
v_f	*in-situ* fluid velocity (*ft/day*)
u_t	*in-situ* fluid velocity (*ft/day*)
c	proportionality contact in *in-situ* velocity estimation correlation (day^{-1})
r	rate of depletion (fraction)
L	Length of the system, or well spacing (*ft*)
H	height of the system (*ft*)
λ_x	horizontal permeability correlation length (*ft*)
λ_z	vertical permeability correlation length (*ft*)
$\Delta\rho$	density difference (lb/ft^3)
P	pressure (*psi*)
g	gravitation constant ($9.8 m/s^2$)
α_L	longitudinal dispersivity (*ft*)
α_T	transverse dispersivity (*ft*)
w_1, w_2	weight fraction for EOR and storage in the developed objective function
N_p^*	recovered oil after CO_2 flooding
N_{OIP}	oil remaining at the beginning of the tertiary CO_2 injection
U_{CO2}	net CO_2 utilisation efficiency
V_R	total reservoir pore volume available for CO_2 storage
u_c	critical gravity stable velocity (*ft/day*)
σ_{lnk}	sample standard deviation of ln *k* (*k*: permeability)
D_l	dispersion coefficient
φ	porosity (fraction)
c	concentration (fraction)

t	time
u_x	horizontal velocity
u_z	vertical velocity
K_L	longitudinal dispersion coefficient
K_T	transverse dispersion coefficient
Δx	size of grid block in the horizontal direction
Δz	size of grid block in the vertical direction
N_x	number of grid block in the horizontal direction
N_z	number of grid block in the vertical direction
τ	Dimensionless time
ξ	Dimensionless length
α_{phy}	physical dispersion
α_{num}	numerical dispersion
S_{wc}	connate water saturation
S_{gc}	irreducible gas saturation
S_{orw}	oil saturation left after waterflooding
V_{HC}	hydrocarbon pore volume (bbl)
γ_o	oil specific gravity
γ_g	gas specific gravity
R_s	gas oil ratio (scf/stb)
cv	coefficient of variation

Fluid Model Parameters

z_i	global mole fraction of component i
M_w	molecular weight of component i
P_c	critical pressure
T_c	critical temperature
V_c	critical volume
ω	acentric factor
γ	binary interaction coefficient

Dimensionless Numbers

N_g	Gravity Number
N_{gt}	Time defined gravity number
N_{RL}	Effective aspect ratio
M	Mobility ratio
Pe_L	Longitudinal Peclet number
Pe_T	Transverse Peclet number
λ_{xD}	Dimensionless horizontal correlation length

λ_{zD}	Dimensionless vertical correlation length
V_{DP}	Dykstra-Parson coefficient of heterogeneity

Abbreviations

BBP	Bubble Point Pressure
CCS	CO_2 Capture and Storage
DLGR	Dynamic local grid refinement
DUWAG	Denver Unit Water Alternating Gas
EOR	Enhanced Oil Recovery
FCM	First Contact Miscibility
GOM	Gulf of Mexico
GOR	Gas Oil Ratio
HCPV	Hydrocarbon Pore Volume
HWAG	Hybrid Water Alternating Gas
MCM	Multiple Contact Miscibility
MER	Maximum Efficient Rate or Maximum Economic Recovery
MMP	Minimum Miscibility Pressure
MMscfd	Million standard cubic feet per day
NPD	National Petroleum Directorate (of Norway)
PV	Pore Volume
RB	Reservoir barrels (at reservoir conditions)
RF	Recovery Factor
STB	Standard barrels
STOOIP	Stock Tank Oil Originally In Place
SWAG	Simultaneous Water Alternating Gas
TWAG	Tapered Water Alternating Gas
UKCS	United Kingdom Continental Shelf
WAG	Water Alternating Gas

Mathematical Operators

Erfc(x)	Complementary error function
$Erfc^{-1}(x)$	Inverse of the complementary error function

1.3 Introduction

Many of the world's important producing provinces are located offshore and these account for a significant share of global crude oil supply. Example cases are the North Sea, the Norwegian Sea, the Gulf of Mexico, the Campos and Santos basins, offshore West Africa, the Persian Gulf, etc. Figure 1.1 shows that crude oil production from offshore provinces accounted for 29% of the entire world crude production in 2015, at a level greater than 27MMSTB per day (USEIA 2016).

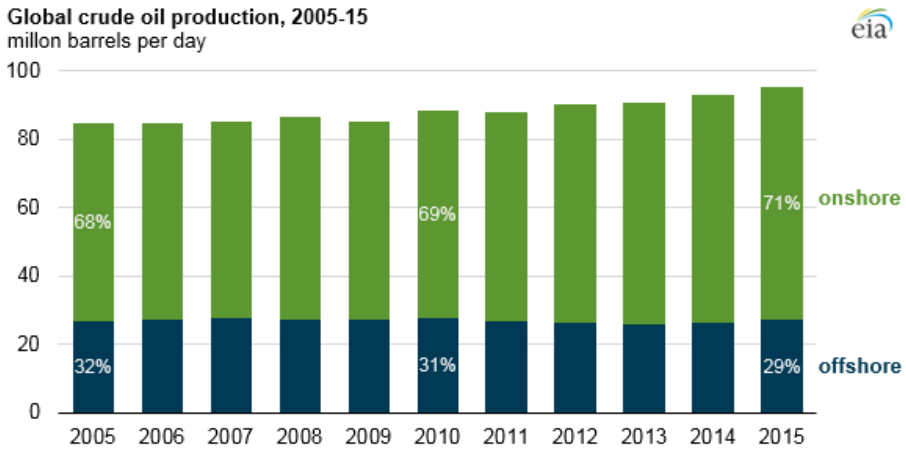

Figure 1.1: Global crude oil production in 2015 (USEIA 2016)

Similar to many onshore oil provinces, offshore provinces in many regions of the world are increasingly becoming mature and thus oil production from them is now declining. While to some extent this decline can be compensated by measures such as developing smaller pools or exploring new assets, particularly in harsher areas, the application of EOR methods, as a method of Maximising Economic Recovery (MER), should not be overlooked.

CO_2-EOR is an established EOR technique in the United States and has offered outstanding performance in this onshore province. This has caused CO_2 flooding to be seriously considered as a potential EOR technique for other mature provinces, particularly offshore ones. Reports show that in 2014, 136 fields were under CO_2 flooding in the United States, producing around 300,000bbl/day (Wallace *et al*. 2015).

The benefit of CO_2 flooding in offshore reservoirs is not limited to increasing crude oil production and security of crude supply; besides that, applying CO_2-EOR offshore can increase host governments' revenues; additionally, a more secure and safe market for CO_2 storage can be created offshore, which can be an important enabler for future CO_2 storage programmes.

Despite outstanding CO_2-EOR performance in the United States, its application in other mature provinces, particularly offshore ones, is at an elementary stage. This is principally because no secure and abundant sources of CO_2, such as those available in the United States, have yet been recognized in other provinces.

Given the large number of successful CO_2 flooding projects in the United States, this province is sometimes regarded as a benchmark for conducting CO_2-EOR activities in other regions of the world. Thus many encouraging results have been extrapolated by correlating the CO_2-EOR performances observed in the United States to other candidate provinces in the world. This is particularly relevant in the North Sea, where enormous and inspiring results for potential CO_2 flooding has been reported in the literature over the past 30 years, yet there has not been even a single complete end-to-end CO_2 flooding project in this region.

While the fundamentals of CO_2 flooding such as miscibility development, oil swelling and viscosity reduction are important considerations in evaluating and correlating the possible CO_2-EOR performance in a likely new candidate province, there are other important considerations that could affect the CO_2 flooding characteristics in a new province compared to the past history of CO_2 flooding, experienced in the United States;

- ***First***: the fluid and ambient reservoir properties of a new province might be fundamentally different than those experienced in the past CO_2-EOR projects in the United States. The Permian Basin reservoirs are characterised by both low reservoir temperatures and pressures, while in the North Sea for example, both of these parameters are high. On the other hand, in the Presalt basin located offshore Brazil, reservoir temperatures are low but pressures are high.
- ***Second***: the dominant flow patterns upon CO_2 flooding could be different in a new province (e.g. the North Sea) compared to those flow patterns observed in the United States CO_2 flooded reservoirs (e.g. Permian Basin) which are characterised by relatively shorter well spacing, lower rates of depletion and lower

formation permeabilities. The difference in flow pattern consequently may affect the macroscopic sweep efficiency of CO_2 flooding.

- ***Third***: the motivation for CO_2 flooding could also be different to the historical purely EOR driven CO_2 flooding projects common in the United States. Offshore, a combination of EOR and CO_2 storage could be the likely driving force behind any CO_2 flood.
- ***Fourth***: the profile of CO_2 availability in a new province could also be different from that observed in the United States. Both quantity and flexibility of CO_2 supply could be different offshore as anthropogenic sources of CO_2 supply would be the likely source of CO_2, with fundamentally different characteristics than those of natural CO_2 sources available in the US.

The above combinations may affect the CO_2 flooding characteristics offshore in comparison with those which have been experienced onshore. This in turn may result in different CO_2-EOR performance characteristics offshore in terms of CO_2 requirements, performance characteristics and process design than those observed onshore. It is, therefore, the target of this study to review these issues and address the likely differences between CO_2 flooding in onshore and offshore classes of reservoirs.

A variety of offshore provinces could be the target for the comparison presented in this study; however, where applicable, we explicitly concentrate the discussion on the characteristics of CO_2 flooding in the North Sea province, as North Sea has been a potential candidate for CO_2 flooding for a few decades and could remain a potential candidate in future should a CCS industry develop in this province.

In the discussion that follows in this chapter, we initially outline the current status of CO_2 flooding in the United States (Section 1.3) and a few other offshore provinces (Section 1.4). Later, some examples will be presented to show the significance of the driving force in the successful achievement of different projects in the North Sea (Section 1.5). The Next section illustrates and highlights the impact of CO_2 storage on the likely characteristics of CO_2-EOR (Section 1.6). Finally, the last section highlights the organization of the remaining chapters of this thesis (Section 1.8).

1.4 The CO_2-EOR Process

The CO_2-EOR process involves injecting supercritical CO_2 into the reservoir formation to recover additional oil; additional to the recovery obtained by previous methods e.g.

secondary waterflooding (Olden *et al.* 2015). This can be achieved by a series of favourable mechanisms, such as oil swelling, oil viscosity reduction, interfacial tension reduction and compositional exchange between CO_2 and the remaining oil in the reservoir.

In terms of applicability, CO_2-EOR perhaps has one of the most flexible screening criteria suggested in the literature (Taber *et al*. 1997), which makes it a practical EOR candidate in more than 80% of the oil reservoirs worldwide (Zhou *et al*. 2012). Figure 1.2 illustrates the suitable oil gravity range for different EOR methods. The relative size of the EOR contribution (barrel/day) is shown by the size of font. It can be seen that the combination of all gas injection EOR techniques represent the largest share of EOR undertaken worldwide.

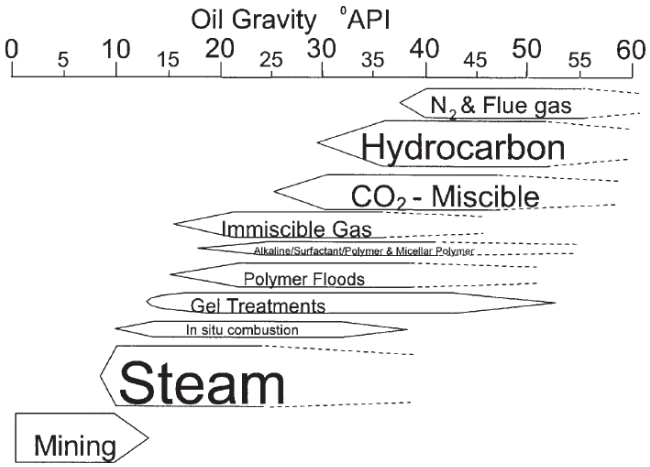

Figure 1.2: The range of suitable oil gravities for CO_2-EOR application (Taber et al. 1997)

For CO_2 flooding to be a competitive process, various conditions must be met (Stalkup 1983). First, an adequate volume of CO_2 must be available at an economic and favourable rate and cost. Second, the combination of reservoir pressure and temperature and fluid composition should allow for optimum miscibility or near miscibility development. Third, the displacement characteristics of injected CO_2 and reservoir fluid must be favourable, in that extremely heterogeneous formations with high permeability streaks are detrimental to CO_2 flooding. Finally, the project economics must withstand the added cost of the EOR operation (Stalkup 1983).

In pure EOR terms, incremental oil recovery must be both sufficiently large and also timely to achieve EOR objectives. While the first three elements may remain identical for CO_2 flooding between onshore and offshore provinces, the economics of CO_2 flooding could be different offshore, as the motivation of CO_2 flooding might be different offshore.

Chapter 2 reviews the fundamentals aspects of CO_2 flooding via modelling studies, hence the remaining technical materials are postponed for this chapter.

1.5 Onshore Evolution of CO_2-EOR in the United States

The first patent for CO_2-EOR application in the United States was granted in 1952 and the first three projects were initiated in Osage County, Oklahoma between 1958 and 1962 (Meyer 2006). However, extensive application of CO_2-EOR (along with a number of other EOR techniques) was not initiated until the 1970's, in response to the world oil crisis. Since then, the use of CO_2-EOR has grown significantly in the United States. The first CO_2-EOR commercial scale development was initiated in 1972 in the SACROC field. The Denver Unit of the Wasson Field located in West Texas is the world largest CO_2-EOR project (Tanner *et al*. 1992). Although CO_2-EOR has been practiced in other regions of the world (e.g. Canada or in the Bati Raman field in Turkey); the United States is the definite leader in this industry.

Securing a CO_2 supply has had a significant impact on the performance efficiency of CO_2-EOR; numerous examples are available in this regard. In the Ford-Geraldine field, the initial source of CO_2 was from a gas plant with erratic CO_2 supply for 5 years. Once a more stable CO_2 supply was secured in 1985, production increased from 381bpd to almost 1160bpd (3 fold increase) (Brock & Bryan 1989). Another example is the North Coles Levee (pilot) in which the source of CO_2 was from a refinery that had occasional upsets, therefore, limiting the supply to pilot area and causing the pilot to terminate early in mid-1984 (Brock & Bryan 1989). In the SACROC field, initially 220MMscfd of CO_2 were supplied from the Val Verde gas plant and then shipped via the Canyon Reef Carrier pipeline (CRC) for injection. Current supply is from Bravo Dome in Colorado and McElmo dome in the New Mexico.

CO_2 flooding entered the commercial stage in 1985 with the completion of three major CO_2 pipelines to the West Texas area (Mathews 1989). These pipelines connect the CO_2 sources at Sheep Mountain (Colorado), Bravo Dome (NM) and McElmo Dome (Colorado) to the large market of west Texas (Mathews 1989). The Oil & Gas Journal has reported that CO_2 flooding in the United States produces more oil than steam injection does (308,564 b/d vs. 300,762 b/d) and accounts for 41% of the production from all types of EOR (OGJ world EOR survey, 2012).

In the early days of CO_2 flooding in the United States, CO_2 supply was provided from industrial sources such as gas power plants and fertilizers. Example cases are SACROC (Crameik & Plassey 1972), North Cross (Pontious & Tham 1978) and Twofred (Thrash 1979) fields, all of which were initially supplied in this way.

Currently both natural and industrial (including anthropogenic) sources of CO_2 are being used in the United States and naturally supplied CO_2 in the US accounts for the 83% of the total supply (Dooley *et al*. 2010). Of the total 3.5Bcf/day CO_2 injection in the United States in 2014, 2.8Bcf/day has been provided from natural sources (5 sources) and the remaining 0.7Bcf/day has been supplied by industrial sources (12 sources) (Wallace *et al*. 2015). This suggests that supply capacity from industrial sources is far less than natural sources, which could be relevant in other provinces, thus CO_2 supply is expected to be an important challenge for other provinces, particularly offshore ones, where access to natural CO_2 resources is not feasible.

The most important natural sources of CO_2 in the United States are Sheep Mountain (1TCf at 97% CO_2 purity), Bravo Dome (6TCF), MacElmo Dome and DOE Canyon fields (>10TCF), Jackson Dome (3-5TCF of CO_2) and LaBarge-Big Piney area (20TCF of CO_2 with 70% purity from Madison and 90% from Big Horn) (Mathews 1989).

A single report published in 2006 estimates that by injecting 600MT of CO_2 in the US fields, 245,000bbl/day oil has been recovered (Meyer 2006). In terms of process technology value, almost $24 million per day or $8.8 billion per year have been produced by CO_2-EOR in the United States. Three major provinces in the United States have been the main targets for CO_2 flooding. The Permian Basin (61%), Rocky Mountains (12%) and Mississippi and Louisiana (14%) provinces comprise 87% of the total CO_2 flooding projects in the US (Jikich & Ammer 2012). Figure 1.3 (next page) shows the current map of CO_2 activities in the US, along with the major operating pipelines in this country.

There is an established CO_2 transportation network in the United States, comprising 50 individual pipelines in the United States; which spreads over one dozen States and into neighbouring Canada. The first CO_2 pipelines were constructed in the United States in the 1970s (Canyon Reef Carrier pipeline). Now the combined length of CO_2 transportation pipelines is over 4,500miles. More than 80% of the CO_2 transported in the US comes from natural sources which is expected to decline to 50%, if planned capture plants become operational as envisaged by 2020 (Wallace *et al*. 2015).

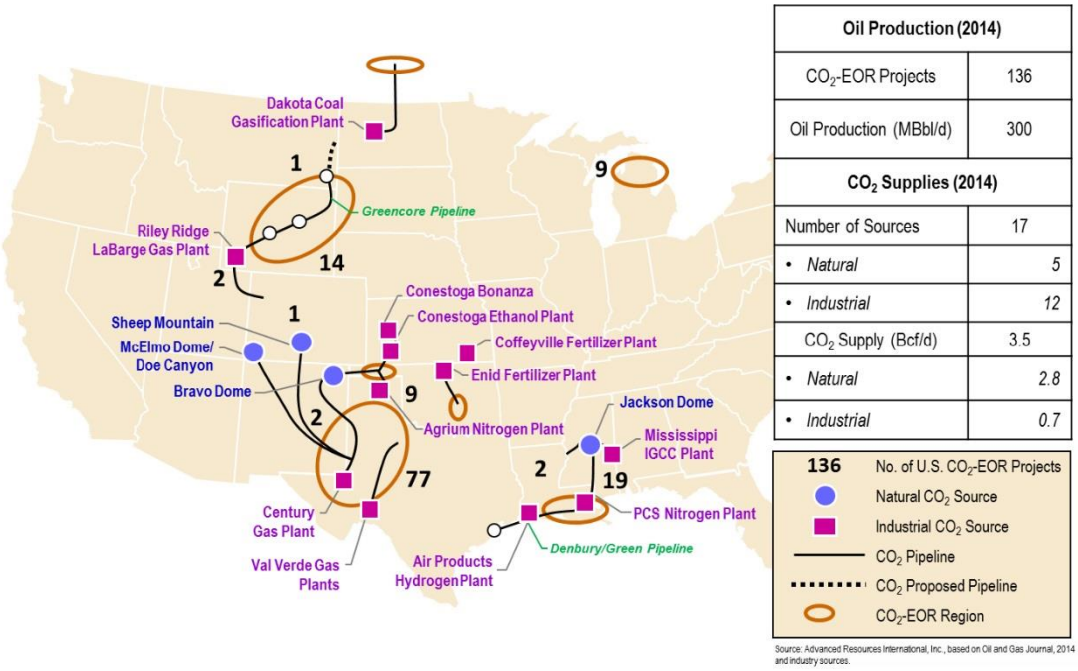

Figure 1.3: Current CO_2-EOR operations and infrastructures in the United States (Wallace et al. 2015)

In the Permian Basin, many smaller fields have benefited from the infrastructure created for larger fields. A review of CO_2 flooding history in the Permian basin shows that CO_2-EOR projects in larger fields have acted as anchor projects in the early stages of CO_2-EOR activities, and has had a significant impact on spreading of this EOR technique to smaller fields. An example is the Canyon Reef Carrier (CRC) pipeline which was constructed to supply the SACROC project; the proximity of smaller projects such as the North Cross field to this pipeline enabled implementation of CO_2 flooding in this field as well (Aryana *et al*. 2014).

Government incentivisation in spreading CO_2-EOR activities in the United States should not also be overlooked. While reservoir and fluid conditions are favourable for CO_2 flooding in this country, CO_2-EOR also has been favoured by the support received from the United States government, either in the form of direct financial support by introducing tax incentives for this EOR activity or by cost share agreements in few candidate fields; e.g. Mattoon field (Baroni 1995). Knowledge sharing, sponsored primarily by the Department of Energy (e.g. many published SPE/DOE papers) has also had a significant impact in enabling other operating companies to undertake CO_2 flooding activities as well.

Concern regarding global warming has caused the United States to undertake a number of CO_2 capture and storage activities, which if implemented can provide additional

anthropogenic CO_2 sources for enhanced oil recovery. There are a number of CCS projects currently underway in the United States. Cebrucean *et al* (2014) provides a list of the large scale CCS demonstration projects around the world. Of the 22 such projects, 7 are located in the United States, 6 of which are expected to use EOR as a storage option for CO_2 and only 1 will use saline aquifer as an storage option. The Kemper County and Petra-Nova plants are good examples of such projects in this regard, where they couple CO_2 capture with storage and consequent enhanced oil recovery from the target fields. In the Kemper power plant, 65% of the produced CO_2 will be used for CO_2-EOR which could recover 2 million barrels of oil per year (Parisi *et al.* 2015).

The Petra-Nova project is a nice example of using anthropogenic CO_2 for EOR in the United States. This project is a 50/50 joint venture project between the NRG and JX Nippon which operates on a commercial scale post combustion carbon capture facility at NRG southwest of Houston Texas (NRG 2017). This facility captures more than 90% of CO_2 from a 240 MW slipstream of the flue gas for use and ultimate sequestration of 1.6 million tons of this greenhouse gas annually. This project is the world largest post combustion CO_2 capture project installed at a power station (NRG 2017).

Figure 1.4: The location of the Petra-Nova and West Ranch oil field (NRG 2017)

The technology used in the Petra-Nova project has the potential to enhance the long-term viability and sustainability of coal-fueled power plants across the United States and around the world. The project was selected by the United States Department of Energy (DOE) to receive up to $190 million as part of the Clean Coal Power Initiative Program (CCPI), a cost-shared collaboration between the federal government and private industry (NRG 2017). This project utilizes a proven carbon capture process, which was jointly

developed by Mitsubishi Heavy Industries, Ltd. (MHI) and the Kansai Electric Power Co., that uses a high-performance solvent for CO_2 absorption and desorption (NRG 2017).

The Captured CO_2 will be used for Enhanced Oil Recovery to enhance production at the West Ranch oil field, which is operated by Hilcorp Energy Company (NRG 2017). It is expected that oil production will be boosted from around 300 barrels per day today to up to 15,000 barrels per day while sequestering CO_2 underground. This field is currently estimated to hold approximately 60 million barrels of oil recoverable by EOR operations (NRG 2017).

This capture plant is actually a retro-fit to an already existing power plant (Global CCS Institute). The CO_2 will be stored at the Frio formation (sandstone) at 5000-6300ft beneath the surface where oil has been produced since 1938. The CO_2 is transported by pipeline using an onshore to onshore transport facility. Petra Nova is the world's largest post-combustion CO_2 capture system in operation. The purity of CO_2 sent to the pipeline is greater than 99%. The captured CO_2 is transported via a new 132 km long, 12-inch diameter underground pipeline to the West Ranch oil field, located near the city of Vanderbilt in Jackson County, Texas. Nine injection wells and 16 production wells are being used initially for EOR operations. As many as 130 injection wells and 130 production wells could be used over the 20-year span of the project. In addition to satisfying the monitoring requirements of the Clean Coal Power Initiative (under which the project received federal funding) the CO_2 monitoring program is designed to satisfy the monitoring, sampling and testing requirements of the Railroad Commission of Texas (RRC) certification program for tax exemptions related to use of CO_2 for EOR and use of CO_2 from anthropogenic sources. The project officially became operational in January 2017 (Global CCS Institute).

1.6 Status of Offshore Regarding CO_2-EOR Application

Given the successful history of CO_2 flooding in the US, CO_2-EOR has been considered for a number of offshore provinces such as the North Sea, Gulf of Mexico (GOM), Vietnam, Malaysia, Brazil and UAE offshore waters. The only successful and operational offshore CO_2-EOR project is, however, the Lula field, located offshore Brazil.

1.6.1 Presalt Basin; Offshore Brazil

The Presalt basin located offshore Brazil contains a number of fields with a relatively high CO_2 concentration in their produced fluids. Lula is a super-giant deep water oil field located in the Santos basin offshore Brasil, some 250km off the coasts of Brazil. Discovered in 2006, this field contain oil of 28°API with a GOR of 240m^3/m^3 (1348scf/stb) (Pizarro & Branco 2012).

This is the first project where CO_2 is injected in ultra-deep waters, and represents a successful example of CO_2 flooding offshore. CO_2 for this project is supplied by the separated CO_2 from associated gas, which is reinjected in the field both for EOR and storage purposes. The CO_2 composition in the produced fluid varies between 8-15%. (Pizarro & Branco 2012). The reservoir is located below a 2000m thick salt layer with a relatively low reservoir temperature of (60°C-70°C). Safe storage of CO_2 is achieved due to the presence of a very thick salt layer. Gas injection (a mixture of CO_2 and hydrocarbon) in this field was started in 2011 by injecting around 1 million cubic meters of gas per day. Later, by initiating gas export to onshore, only pure CO_2 has been injected, thus reducing the injection rate to almost 350,000 m^3/day (Pizarro & Branco 2012).

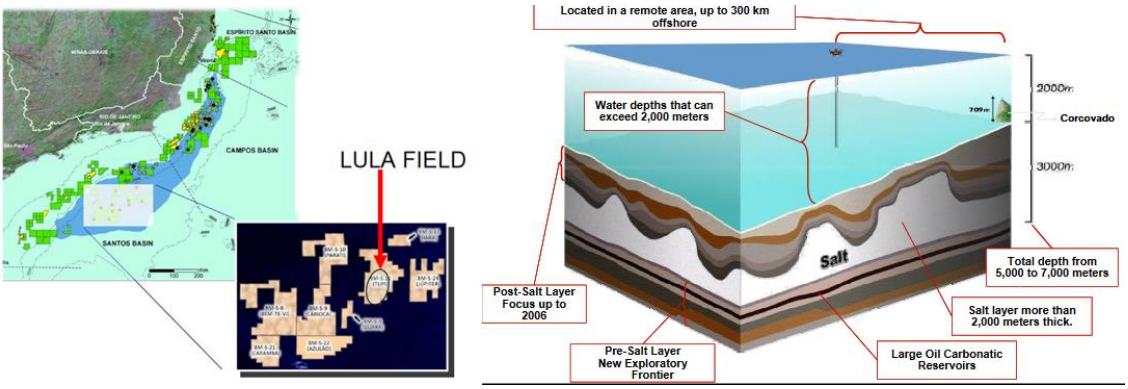

Figure 1.5: Lula field and Presalt cluster areas, Santos province Presalt model (Pizarro & Branco 2012)

The strategic decision not to vent the CO_2 to the atmosphere was the primary driving force for undertaking CO_2 flooding in this field with consequent EOR benefits. The key success of the project was phased development initiated by pilot CO_2 application to reduce the risk and increase learnings. Moreover, early planning of the CO_2-EOR in this field helped eliminate facilities installation downtimes and also provided space for EOR facilities (Pizarro & Branco 2012).

Given the successful CO_2 flooding result observed in this field, CO_2 flooding has also been considered for the nearby Jupiter field, offshore Brazil, in proximity to the Lula field and with almost the same reservoir and fluid properties (high CO_2 content in the produced fluid) (2b1stconsulting 2014).

1.6.2 Gulf of Mexico

The Gulf of Mexico (GOM) is an important offshore province for the United States, accounting for nearly 20% of the total US crude production. Since its peak in 2003, production from this province has been declining (Malone *et al*. 2014). Although a number of approaches have been suggested to enhance the production from this province, such as exploring deeper waters or developing smaller fields, one effective measure is implementing CO_2-EOR, which has a successful record in the nearby onshore Permian Basin (Malone *et al*. 2014).

No CO_2 flooding activity has yet been undertaken in this offshore province; however, a NETL[1] report describes a comprehensive review of the potential CO_2-EOR benefits in this offshore province (Malone *et al*. 2014). Increasing oil production, providing a CO_2 market for future capture plants and also providing a secure location for CO_2 storage, away from human communities, are important recognised benefits for conducting CO_2 activities in this offshore province.

The report identifies two important highlights; first, the need to take earlier action in the GOM, because many shallow water fields are approaching abandonment (once they are abandoned, cost of installing CO_2-EOR facilities will be more significant than at present), second, the deep water oil fields may benefit from early CO_2-EOR planning as has been shown in the Lula field (Malone *et al*. 2014).

The promise of additional oil recovery and secure CO_2 storage are potential significant prizes for conducting CO_2-EOR in this province. Royalty in the GOM is about 18.5% and this report estimates that the prize of implementing CO_2-EOR in the GOM region could be around 15billion barrel of oil, if 3.9GT of CO_2 is injected (Malone *et al*. 2014).

CO_2-EOR in the offshore GOM region is not, however, a new concept; in fact, five CO_2-EOR pilots have been undertaken in this region during the 1980s. The ***Quarantine Bay***

[1] National Energy Technology Laboratory

CO_2 injection started in 1981 and was completed in 1983. CO_2 was delivered by barge and injected at an average rate of 1.7MMscfd. The project was considered successful as it recovered 16.9% of OOIP with a net CO_2 utilisation of 2.6Mscf/bbl (Malone *et al*. 2014).

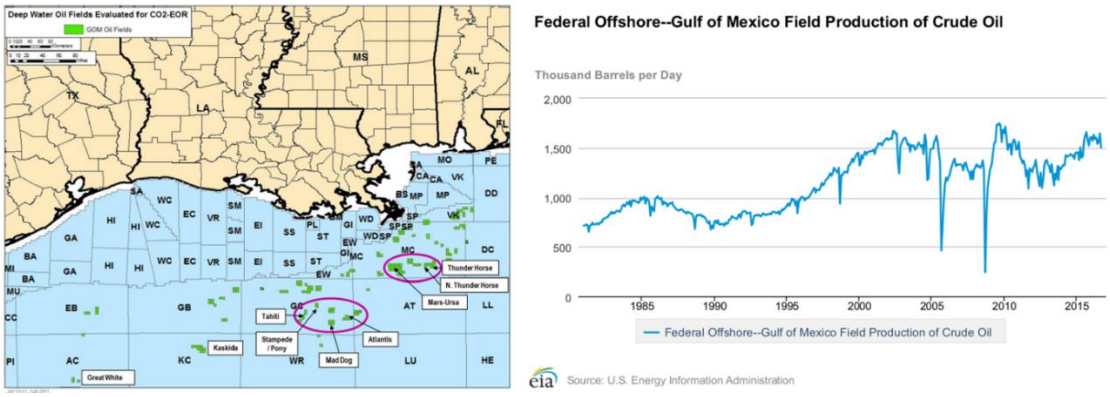

Figure 1.6: Left: GOM offshore deep water continental shelf; circles locate the position of potential future CO_2 flooding anchor fields (Malone et al. 2014). Right: Gulf of Mexico crude oil production (USEIA 2016)

In the ***Timbalier Bay*** gravity stable miscible CO_2 flood, CO_2 was injected for 15 months (30%HCPV) followed by field gas injection. The ***Bay St, Elaine field***, a gravity stable miscible CO_2 flood was also initiated in 1981. The injected gas was a mixture of CO_2, CH_4 and butane. The CO_2 injection was followed by N_2 injection in this field to reduce net CO_2 consumption. In the ***Weeks Island*** field, gravity stable CO_2 flood, Shell recovered 260,000bbl oil by injecting 24%HCPV CO_2 mixed with 6% hydrocarbon gas. The net and gross CO_2 utilizations were respectively 3.3 and 7.9Mscf/bbl. In the ***Paradis field*** gravity stable CO_2 flood initiated in 1982, CO_2 mixed with 10% N_2 was injected into this field (Malone *et al*. 2014). The fact that the majority of the above CO_2 floods have been gravity stable flooding designs (four out of five), is due to the existence of suitable dipping reservoirs in the Louisiana gulf coast area (Cardenas *et al*. 1984).

Although all of the above offshore pilot projects were deemed technically successful, none of them led to commercial scale CO_2 flooding in this offshore province, similar to the nearby Permian Basin province. The main barriers for this are limited CO_2 supply offshore GOM and high well drilling costs (Malone *et al*. 2014).

1.6.3 The North Sea

The North Sea province (Figure 1.7, left) opened for exploration and production in 1964 (Glennie 1998) and reached its peak oil production in 1999. After this, the production has been constantly declining. Currently, the North Sea is considered as a mature province.

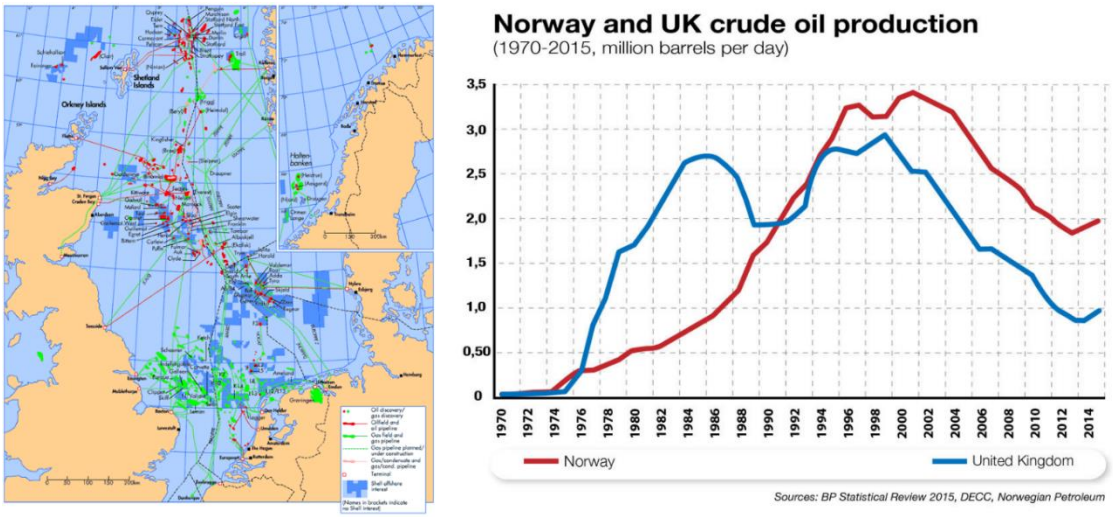

Figure 1.7: Left: North Sea Province (OGAuthority 2016), Right: UK and Norway oil production (Cryostolenergy 2016)

Figure 1.7 (right) shows the profile of oil production by UK and Norway; the two significant neighbouring North Sea countries. It can be seen that production from both countries has considerably declined compared to their peak productions. The North Sea is now considered as a mature province with the oil fields in the Central, Northern and Southern producing significantly below their initial plateau production rates (Jayasekera & Goodyear 2002).

Miscible gas and WAG-EOR have been the top EOR techniques practiced in the North Sea area (18 projects) (Awan *et al*. 2008) since high reservoir temperature and high water salinities have limited the application of other EOR methods e.g. polymer flooding (Bath 1987).

The EOR potential of the North Sea is estimated to be around 8.5-9% HCPV (Holt *et al*. 2009). The challenge, however, for any EOR method in the North Sea (including CO_2-EOR) is that waterflooding is very efficient, convenient and also cheap in this province. In fact, in some fields, the recovery factor due to waterflooding alone can reach 70%, though the average recovery for the UKCS is around 45%, which is still significant compared to other provinces. However, given the larger size of reservoirs in the North

Sea, a large EOR target can nevertheless be identified (Jayasekera & Goodyear 2002). High waterflood recovery in this province may also demand earlier application of EOR methods. The above discussion suggests that successful EOR implementation is most likely in the largest fields (Bath 1987). Table 1.1 shows a list of the EOR projects initiated in the North Sea[2].

Table 1.1: A number of EOR projects initiated in the North Sea (Awan et al 2008, Brodie et al. 2012). MG: Miscible Gas injection, MWAG: Miscible WAG injection, IMWAG, Immiscible WAG injection, FAWAG: Foam Assisted WAG injection.

#	Field Name	Operator	Prod/Start-up	Location	EOR Method
1	Ekofisk (Ekofisk fm.)	ConocoPhillips	1971	Norway	MG
2	Ekofisk (Tor fm.)	ConocoPhillips	1971	Norway	IMWAG
3	Beryl	ExxonMobil	1976	UK	MG
4	Statfjord (Statfjord fm.)	Statoil	1979	Norway	MG
5	Statfjord (Brent fm.)	Statoil	1979	Norway	IMWAG
6	Brent	Shell	1976	UK	MG
7	Alwyn North	Total	1987	UK	MG
8	Smorbukk South	Statoil	1999	Norway	MG
9	Snorre (SnA)	Statoil	1992	Norway	MWAG
10	SnA (CFB)	Statoil	1992	Norway	FAWAG
11	SnA (WFB)	Statoil	1992	Norway	FAWAG
12	South Brae	Marathon	1983	UK	MWAG
13	Magnus	BP	1983	UK	MWAG
14	Thistle	Lundin Oil	1978	UK	IMWAG
15	Gulfaks	Statoil	1986	Norway	IMWAG
16	Brage	Norsk-Hydro	1993	Norway	IMWAG
17	Oseberg Ost	Norsk-Hydro	1999	Norway	IMWAG
18	Siri	Statoil	1999	Denmark	SWAG
19	Ula	BP	1986	Norway	MWAG
20	Harding	BP	1996	UK	MG

As with other major offshore provinces, there is no commercial scale CO_2-EOR activity in the North Sea province yet. The idea of CO_2 flooding in this province is, however, not absolutely new; CO_2-EOR has been considered in the North Sea since 1982 (Alkemade 1995). CO_2-EOR, however, has been proposed in a number of projects such as Magnus, Ekofisk and Forties, but principally due to unavailability of secure CO_2 supplies, its application has been halted.

The benefit of CO_2-EOR in the North Sea is very similar to the Gulf of Mexico in that, it can extend field life, delay field abandonment and also provide a safe storage for CO_2.

[2] There are more EOR projects in the North Sea than those depicted in Table 1.1. The data depicted in Table 1.1 have been collected from open literature.

Moreover, a large fraction of produced hydrocarbon gas which is now used for EOR can be released and then diverted to European markets, once CO_2-EOR is in place.

Until recently, there have been optimistic calculations of the CO_2-EOR economic potential in the North Sea region (Pershad *et al*. 2012) for the UK economy. A report from Element-Energy identifies 19 fields as potential anchor projects for possible CO_2-EOR activities in the North Sea. This report estimates the first few CO_2-EOR projects would require substantial fiscal incentive, but later projects could be sustained with a modest fiscal incentive (Pershad *et al*. 2012). CO_2-EOR was also recognised to provide benefits such as creating a driving force for CCS deployment in the carbon constrained power generation environment envisaged for the 2020s. It has been, however, foreseen that the first CO_2-EOR project in the UK would become operational by 2020 and the cluster development by 2030 (Durusut & Pershad 2014). This is an optimistic perspective, which is unlikely to be realised, as will be illustrated later.

A DECC[3] pilot taskforce also suggested that CO_2-EOR is the best EOR technique in the UKCS (Garlick 2012). Another report estimates that the governments of UK, Norway and Denmark could receive up to £22billion in taxes, if CO_2-EOR is deployed in the North Sea (Durusut & Pershad 2014).

However, there are factors that considerably question these optimistic views; recently the potential for CO_2 flooding in the North Sea has been significantly put at risk, after withdrawal of UK £1bn CCS competition budget. Halting CO_2-EOR in the Miller field, (which occurred long before this decision was announced) was due to the delay in approving this fund which was required by the operator (BP).

In this atmosphere, many companies believe that CO_2-EOR in the North Sea can only follow a full successful CCS programme; therefore, operators practice a wait and see approach which may lead to decommissioning of facilities in the North Sea before any CO_2 project can commence (Pershad *et al*. 2012). Once platforms and facilities are removed, the application of CO_2-EOR becomes even more challenging. Figure 1.8 shows the envisaged shrinkage of the field structures in the UKCS sector of the North Sea to 2020 (Jayasekera & Goodyear 2002). This figure shows that the opportunity for EOR is becoming smaller ever in the North Sea and therefore urgent action for implementing CO_2-EOR is required, if it is ever to take place.

[3] Department of Energy and Climate Change

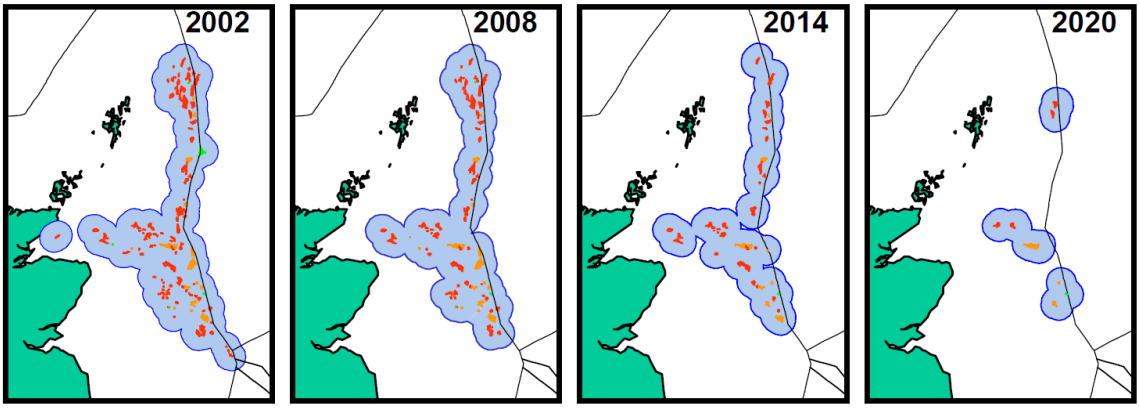

Figure 1.8: Facilities shrinkage in the UKCS sector of the North Sea (Jayasekera & Goodyear 2002)

The status of CO_2 flooding is, however, slightly different in the Norwegian sector of the North Sea. As with the UK, the same conditions prevail in the petroleum operations in the Norwegian sector of the North Sea, in that a large number of fields are increasingly become mature and a few of them are approaching abandonment (Pham & Halland 2017). Since 1982, several major Norwegian increased oil recovery programs have, however, been initiated to increase production from the Norwegian assets. In 2003 the Norwegian oil and gas taskforce identified a number of technology targets, including CO_2-EOR to increase the average oil recovery to 50% and gas to 75% from the NCS (Norwegian Continental Shelf) including the North Sea (Awan *et al.* 2008). In Norway, the CO_2 storage atlas has also been recently prepared by the Norwegian Petroleum Directorate (Pham & Halland 2017).

Recently NPD has performed several CO_2 enhanced oil recovery studies extending from regional screening to more details studies in a few oil fields in the Norwegian sector of the North Sea (Figure 1.9).

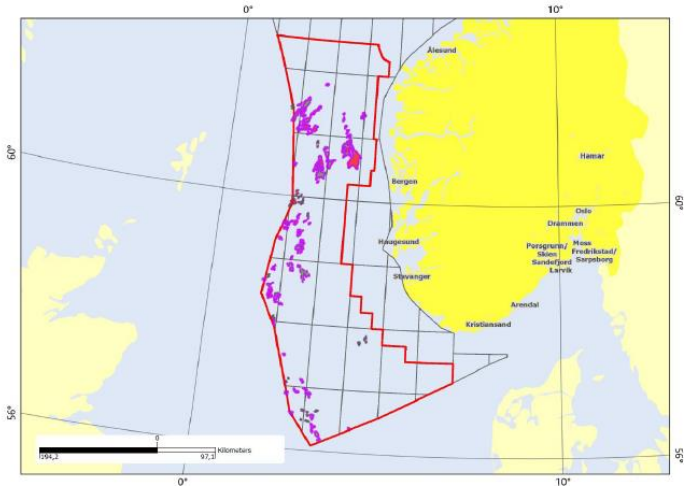

Figure 1.9: Location of the studied areal; the Norwegian North Sea (Pham & Halland 2017)

The results reconfirmed the existence of great EOR potential for CO_2 injection in the Norwegian sector of the North Sea (Pham & Halland 2017). Results of this study also revealed that an average 4% recovery factor improvement due to CO_2-EOR application with gas storage efficiency of 70-100% is potentially achievable. In comparison with dry gas (CH_4) flooding, CO_2 injection has also shown considerably better EOR results (Pham & Halland 2017).

Unlike the UK, Norway has, however, taken a different strategy toward CO_2-EOR and CO_2 storage activities in the North Sea. Norway has been the pioneer in establishing the CCS activities in the North Sea and in fact there are over 20 years of CO_2 storage experience in the Norway (Pham & Halland 2017). Since 1996, CO_2 from natural gas production on the Norwegian shelf has been captured and reinjected into sub-seabed formations. The CCS projects on the Sleipner, Gudrun and Snøhvit petroleum fields are the only industrial scale CCS projects currently in operation in Europe and the only projects in the offshore industry (NPD 2017).

A single report identifies six important steps toward establishing a full CO_2 economy in Norway, of which EOR is a significant opportunity. Important highlights are the need for meeting long term climate targets in a cost effective approach, ensuring future use of natural gas, conducting CO_2-EOR activities and finally using the current oil production infrastructure have been recognised as the crucial reasons to apply CCS in the Norwegian sector of the North Sea (Bellona 2017).

Unlike the UK, an important driving force for pursuing CO_2 storage activities in the Norwegian continental shelf, including the Norwegian North Sea is the potential positive gas production outlook in Norway, which is likely to remain important for the country's economy at least in the medium term (until 2020). In fact, Norway is the third largest gas exporter in the world (NPD 2017).

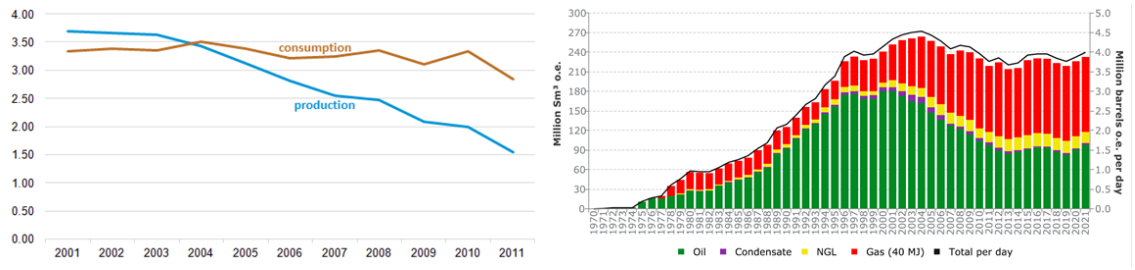

Figure 1.10: Left: UK dry natural gas consumption and production in terms of TCF (USEIA 2011), Right: Historical and expected hydrocarbon production in Norway (Norwegian Petroleum Directorate 2017).

Figure 1.10 shows that while UK gas production is declining, in Norway the trend is increasing. Additionally, the Norwegian Sea has also been proven to contain significant deposits of natural gas (NPD 2017). This is in addition to gas hydrates, the next generation natural gas resources. This reveals that unlike the UK, fossil fuels are likely to remain as a fundamental source of energy and a key element for the Norwegian economy which necessitates the application of CCS as an important option in Norway to offset and stabilise the emission targets. In the UK as was mentioned, the strategy is to shift to non-fossil fuels, thus CCS may have a considerably less opportunity.

The Norwegian Government aims to construct at least one full-scale CCS demonstration facility (NPD 2017). A techno-economic feasibility study of possible demonstration projects in Norway was completed in 2016 (NPD 2017). The Norwegian government has proposed to grant 360 million Norwegian kroner for the continued planning of a full-scale CCS demonstration facility in Norway (Norwegian Government 2016). The aim of these activities was to identify at least one technically feasible CCS chain with corresponding cost estimates. Three industrial players have completed feasibility studies of CO_2 capture. Gassco has carried out a ship transport study and Statoil has completed feasibility studies of CO_2 storage at three different sites on the Norwegian Continental Shelf (NPD 2017).

The results from the feasibility studies, which were presented in July 2016, show that it is technically feasible to establish a CCS chain in Norway. The Norwegian government has also continued the planning of a large scale CCS project in Norway. After conducting FEED studies by late 2018 and with a positive final investment decision, a large scale CCS project is likely to be operational by 2022. It is expected that by 2050, the CO_2 storage industry in Norway will be about the size of the current UK oil and gas industry (NPD 2017).

1.6.4 Other Offshore Provinces

Recently ADNOC[4] in the United Arabic Emirates has investigated the possibility of CO_2 flooding in the lower Zakum field, off the UAE coast in the Persian Gulf, to enhance the field's recovery. In this project, CO_2 will be collected from a few onshore industrial plants and will be used to replace the hydrocarbon gas which is currently used for EOR (PennEnergy 2010, Belhaj *et al*. 2012).

[4] Abu-Dhabi National Oil Company

Another pilot CO_2 flooding activity was conducted in the Rang Dong oil field offshore Vietnam. The test was a single well Huff & Puff operation with positive results in the absence of any reported injectivity problems. The injected CO_2 was initially trucked from its source onshore to the nearby port from where it is was sent to the field by barge. A total of 163MT of 99.97% purity CO_2 was transported to the field (Uchiyama *et al*. 2012, Ha *et al*. 2012).

CO_2 flooding has also been considered for EOR in the Dulang field and Baram Delta operations (BDO), offshore Malaysia (Zain *et al*. 2001, Rosman *et al*. 2011). It was identified that since MMP is higher than initial reservoir pressure, miscible CO_2 displacement would not be feasible at Dulang ambient reservoir conditions. The immiscible WAG pilot test, however, was initiated in 2002 in block E10-14 of this field and since then it has shown successful results (Abu Bakar *et al*. 2011, Nadeson *et al*. 2004, Zain *et al*. 2001).

Although these examples, plus CO_2 flooding in the Lula field, are all successful instances of CO_2 flooding offshore, none of them are considered as enabler examples for a cluster scale CO_2-EOR deployment which is considered to be the likely arrangement foreseen in the North Sea or the Gulf of Mexico, should commercial scale CO_2-EOR ever take place in these provinces.

1.7 The Challenge of CO_2 Supply Offshore

The growth in the number of CO_2 flooding projects in the United States is primarily due to the ease of access to commercial volumes of naturally occurring CO_2 and also the existence of established pipeline facilities; a prerequisite for CO_2-EOR, which is currently unavailable in many offshore provinces including the North Sea. Of the offshore provinces reviewed so far, only the Lula field has established its own secure CO_2 supply; this is only from its own produced associated gas.

Since there are no natural CO_2 reserves in the North Sea, carbon capture from anthropogenic sources is expected to be the unique solution for CO_2 supply with capacities as high as 270MT/year (Pershad & Stewart 2010). While theoretical figures for potential CO_2 supply from North Sea neighbouring countries are very encouraging, the readily available potential is very limited. The only three available CO_2 producing projects in the North Sea are perhaps Peterhead, Sleipner and Snøhvit projects with 1.0,

0.85 and 0.7Mt/year CO_2 production capacities, respectively (Global CCS Institute 2016) which at best could securely support one or two medium sized projects at the scale of EOR in the Magnus field. In Magnus, so far around 112BCF of hydrocarbon gas have been injected with rates as high as 100MMscfd (Brodie *et al*. 2012). In CO_2 equivalent terms, this could translate to a cumulative CO_2 injection of around 6MT CO_2 with injection rates as high as 2MT/year CO_2.

Similar to the Lula field, in the North Sea, CO_2 can also be supplied from produced associated gas. In fact, some fields in the North Sea have significant concentrations of CO_2 in their produced fluids. The Brae (35%), Toni and Sleipner fields are good examples, but their contribution is yet uncertain (Fayers *et al*. 1981, Jethwa *et al*. 2000). Nevertheless, this method of CO_2 supply, at best, can support a few point-to-point CO_2 flooding projects and not a full cluster scale CO_2-EOR deployment, similar to the Permian Basin.

Apart from the issues of CO_2 sources, the transportation infrastructure is not readily available for CO_2 transportation in the North Sea. Although HC-gas transportation infrastructure can be potentially converted to CO_2 transportation facilities in the North Sea (e.g. in the Goldeneye project), this can only happen once the productive life of the field has been terminated, implying that CO_2 flooding can only serve for storage and not for combined EOR and storage. If EOR is expected to be a simultaneous objective, then construction of new pipelines facilities should be essential. CO_2 pipelines, however, can utilise the same corridor laid out for hydrocarbon gas transportation (Malone *et al*. 2014).

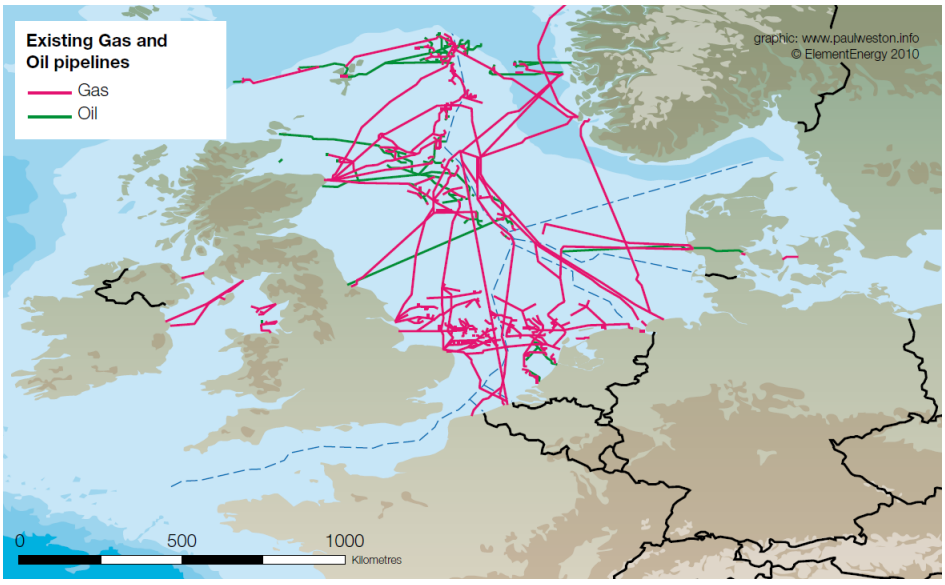

Figure 1.11: Existing oil and gas pipelines in the North Sea (Pershad & Stewart 2010)

CO_2 transportation by shipping can also be foreseen in the North Sea. Even in the early days of CO_2 activities in the Permian Basin, trucked CO_2 transportation was carried out in a number of small projects. A similar concept could be technically possible in the North Sea, similar to other offshore regions e.g. Vietnam or Malaysia; however, this method of supply may only support a small number of fields with small volumes of target EOR.

In the absence of government (policymakers) initiation of CO_2-EOR in the North Sea, supply in this region is expected to be on a point-to-point basis, in that individual projects may seek nearby opportunities to identify CO_2 resources prior to EOR initiation. The EOR story in the Magnus field, although it was HC-EOR and not CO_2-EOR, is a good example in this regard.

A review of the North Sea EOR (and recently CCS) projects initiated for the North Sea can thus provide valuable insight into the possible scenarios for CO_2 (or HC) supply in this region. This review shows that, while limited gas transportation infrastructure may look limiting for initiation of EOR, once the driving force behind conducting a project is aligned with the right recognition of the available resources, outstanding results can be achieved; with benefits sometimes beyond original expectations.

A few projects are briefly reviewed in this section; all of these are from the North Sea region. The first example is purely EOR driven (the Magnus field), the second one is purely (CO_2) storage driven (The Goldeneye field) and the last one is jointly driven by both EOR and (CO_2) storage (The Miller field).

1.7.1 HC-EOR in the Magnus Field

Magnus is the most Northerly producing oil field in the UKCS and is at a water depth of 186m. The original oil in place was 1,535MMSTB with oil of 39°API and GOR of 725scf/stb. The initial reservoir pressure was 6653psi (Haajizadeh *et al*. 2001).

Production from the field started in 1985 with a plateau production rate of 150,000stb/day, which was maintained for 10 years, until 1995. Field production decline caused Magnus to be considered for EOR. A few EOR candidate methods were considered for this field, including HC-EOR and CO_2-EOR. WAG applicability in this field has already been demonstrated by a number of authors (Haajizadeh *et al*. 2001). The S_{orw} in the Magnus field is about 25% which can be reduced to 8% by gas flooding (Moulds *et al*. 2010, Erbas

et al. 2014). This is a significant reduction and since the field is large, the relative EOR prize is considerable. Despite the above encouraging prognosis, both CO_2-EOR and HC-EOR were initially rejected due to the inability to secure appropriate supplies (Moulds *et al*. 2010, Erbas *et al*. 2014).

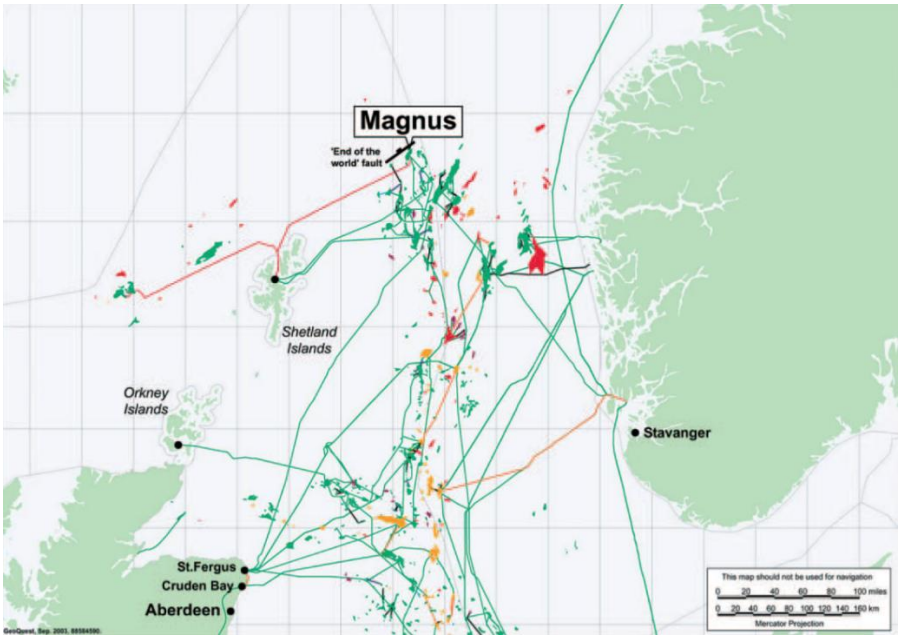

Figure 1.12: Map showing the location of the Magnus field (Macgregor et al. 2005)

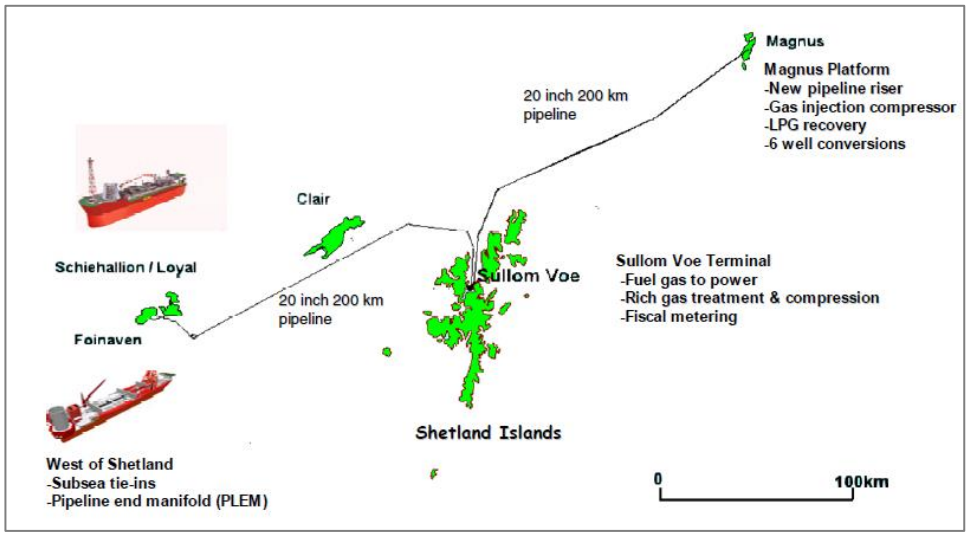

Figure 1.13: The Magnus EOR pipeline route (Moulds et al. 2010)

The source of the EOR gas was a problem until 1998, when an exceptional opportunity was identified (Erbas *et al*. 2014). A number of fields to the west of Shetland came on production and their associated gas had to be disposed of underground as there was no market opportunity. This gas was identified as the potential EOR supply gas for the

Magnus field. A 400km pipeline was subsequently constructed from the Foinaven field to the Sullom Voe Terminal (SVT) and then to Magnus (Erbas *et al*. 2014).

The gas from Foinaven was also too lean for miscibility development, thus provision was made initially in the SVT to enrich the gas with propane and butane. However, the incremental benefit of gas enrichment did not merit the purchase cost of the enriching components and the imported gas was not enriched (Moulds *et al*. 2010).

Incremental recovery not only comes from lowering the residual oil saturation to waterflooding, but also from accessing oil bypassed by the waterflood, improving voidage replacement in low permeability areas and increased drawdown through the natural gas lift in production wells. Extension of field life is another achievement of the project (Moulds *et al*. 2010).

So far 112BCF gas has been injected into this field with injection rates as high as 100MMscf/day (Erbas *et al*. 2014). Gross and net hydrocarbon utilisation efficiencies in this project are 9.8Mscf/stb and 3.5Mscf/stb respectively which is considered very good compared to other gas/CO_2 injection projects. In terms of recovery efficiency, for each 1.5rb injected gas, 1rb oil has been recovered. The imported gas had variations in supply, thus once an EOR block becomes mature, it was used for storage to buffer the fluctuation in the gas supply (Erbas *et al*. 2014).

Review of the EOR story in the Magnus field shows that the main benefits of the EOR project are not limited to EOR. In addition to enhanced oil production, a commercial gas pipeline for the West of Shetland oil fields was constructed; moreover, fuel costs in SVT were reduced with environmental benefits due to fuel replacement. The gas which was routed through SVT could also be used for fuel to replace the diesel at SVT. Deploying EOR in this field caused Magnus to be the first platform to be renewed by BP's North Sea renewal programme which is planned to extend the life of some mature BP assets in the North Sea (Moulds *et al*. 2010).

The EOR story in the Magnus field can demonstrate a valuable insight into the likely CO_2-EOR scenario in the North Sea, at least in the short term.

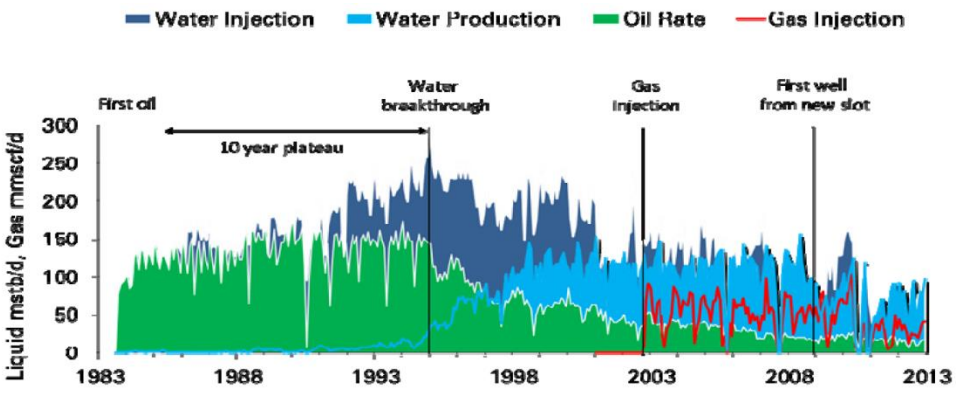

Figure 1.14: The Magnus field historical injection and producing profile (Erbas et al. 2014)

1.7.2 Goldeneye (CO_2 for CCS)

The Goldeneye gas condensate field is located some 130km offshore in the North Sea, North East of Aberdeen. The field ceased production in 2011 and it is now considered for a CCS programme by Shell. The combined project would use current Goldeneye facilities in a reverse direction to store CO_2 captured at the Peterhead Power Station (Spence *et al*. 2014). This would enable the Peterhead power station to generate 400MW of clean energy, for 15 years, cutting emission by 90% and storing 15MT of CO_2 (Shell response to the Energy and Climate Change Committee Inquiry 2016). The project was planned to be operational by 2019 (Spence *et al*. 2014).

In Goldeneye, CO_2 would be injected via 3 injectors. Around 1 million tonnes of CO_2 per year with 99% purity would be injected into this field. The injection target is the upper part of the Captain-D sub-unit. This increases both the reservoir pressure and that of aquifer, which is immediately connected to it. The Goldeneye aquifer is also connected to neighbouring fields which may provide positive pressure supporting effects for them (Goldeneye project factsheet 2015, Peterhead CCS project Report 2015).

This project was first considered as one of the three major candidates for UK-CCS competition. However, the fund was later abolished, as the UK government changed its strategy. Shell stated that it will remain committed to the completion of the project (Shell Response Report 2016). Withdrawal of the UK-CCS fund clearly will slow down or stop the project progress and also impairs the CCS outlook in the UKCS overall.

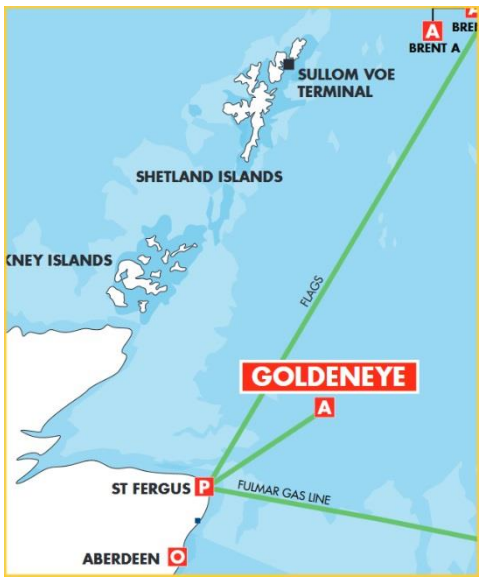

Figure 1.15: Approximate location of the Goldeneye gas condensate field (Goldeneye Project Factsheet 2015)

1.7.3 Miller Field (CO_2 for Combined EOR and CCS)

The Miller field is located in the North Sea some 240 km *NE* of Peterhead at a water depth of 100m and is one of few candidates considered for CO_2-EOR by BP. The Miller field plateau production rate was 150,000bbl/day, which was maintained between 1992 and 1997. The Miller field life came to an end in 2007, once the operator (BP) announced that it could not wait any longer for the UK government to allocate a share of the £1bn budget for conducting CO_2 flooding foreseen in this field (Miller Decommssioning Report 2011; energy-pedia, 2007). It was recognised that in the absence of government support (CCS budget), CO_2-EOR could not pay for the full platform cost. Moreover, the non-existence of a fiscal regime at the time for CO_2, too late EOR planning and a low oil price were other major CO_2 flooding disablers in this project (Duncan 2014). Collapse of the CO_2-EOR project in the Miller field meant that no operator has indicated a clear and strong plan for CO_2-EOR implementation in the North Sea. The failure of the proposed CO_2-EOR in this field shows the limitation of EOR as a sufficient driving force to initiate CO_2 injection offshore; though works are still ongoing at the Peterhead capture facilities and therefore CO_2 supply for such a project is still possible sometime in the future. These cases also show commitment at various stages by Shell and BP for initiating CO_2 related activities, in the absence of major support from the UK government.

The first phase of the Miller field abandonment has now been completed (Miller Decommissioning Status, BP website). The full abandonment is expected to cost the operator £300million. The export pipelines are, however, preserved for future plans.

1.8 CCS and EOR; Mutual Enablers with Important Implications

The EOR potential by itself has not been a sufficient driving force in securing firm CO_2 supplies for cluster scale CO_2-EOR deployment in many offshore provinces, including the North Sea. Numerous examples are available in this regard; failure to implement CO_2-EOR in the Magnus, South Brae, Gulfaks, Ekofisk and recently Miller fields show the lack of EOR potential as a sufficient driving force in this regard. In the absence of a major push from policy makers (i.e. North Sea host governments), it is expected that CCS would have to provide the necessary CO_2 supply for the likely CO_2-EOR in the North Sea.

Deploying CCS, however, is an important measure in tackling the current rise of CO_2 emissions. IEA[5] estimates that CCS could achieve 20% of the target emission reductions by 2050 (IEA CCS Technology Roadmap, 2009). The IPCC 5th assessment also estimates that without CCS, the cost of limiting global CO_2 emission to 450ppm could increase by 138% (IPCC 5th Assesment Report, 2014). Besides storage in saline aquifers or coal beds, enhanced oil recovery with CO_2 accounts for an important share of cumulative CO_2 storage. CCS is, however, a relatively expensive process and it might be difficult to obtain the necessary funding for its infrastructure deployment. Up to 2006, it was believed that EOR could be sufficient motivator to bring CO_2 storage offshore; though it has been recently recognised that the two processes are fundamentally different with different cost structures driving each of them (Dooley *et al*. 2010, Pershad & Stewart 2010).

This means that neither CCS nor EOR on their own have been sufficient driving forces for deploying CO_2 injection offshore. Instead, a combination of CO_2 storage with EOR may enable both technologies to work synergistically. CCS could provide a secure source of CO_2 supply required for EOR, similarly, EOR could allow field infrastructure, facilities and pore volume to be used for storage purposes (Gluyas 2009).

Coupling CCS with CO_2-EOR offshore has advantages compared to onshore, from the storage point of view. Offshore fields are larger, away from human communities and are more secure in terms of storage as the number of penetrations are limited. Moreover, many offshore fields are structurally located at deeper depths which makes CO_2 flooding at higher pressures safely feasible. The Lula field is an excellent example in this regard,

[5] International Energy Agency

because the field is overlain by a relatively thick salt layer which makes storage effectively safe. Many North Sea fields also have high pressures and temperatures, which makes them suitable candidates for storage as well. It has also been suggested that CO_2-EOR can store more CO_2 than a pure non-EOR CO_2 storage project would, as CO_2 can be dissolved in the immobile oil phase, thus storing it securely (Olden *et al*. 2015).

Since CCS and CO_2-EOR are basically two different processes with different objectives (Dooley *et al*. 2010), coupling them in the North Sea or anywhere else may affect the project EOR critical path compared to conventional CO_2-EOR project design, observed in other provinces, mainly the United States. The next section investigates this concept.

1.8.1 How Can the Elements of CO_2 Flooding be altered, if EOR and CCS are combined?

In the United States, around 68% of the total EOR costs are invested for purchasing CO_2 (Meyer 2006). This means that CO_2 is a valuable commodity in this province which should be paid for and project design often calls for its usage minimisation. That is why in many CO_2 flooding projects, the initial bank of CO_2 has been followed by a less expensive gas (e.g. exhaust gas or N_2) to reduce the net purchase of CO_2 (Flanders & DePauw 1993).

Unlike the way that EOR treats CO_2, CCS considers CO_2 as a substance that should be safely disposed of. This suggests that CO_2 would no longer be an expensive commodity from an EOR point of view in the North Sea; there could even be a reward for its secure storage. Moreover, full CCS deployment in the North Sea (still a very uncertain prospect) implies that supply is likely to be greater than demand.

Coupling the two processes not only makes the incremental oil recovery important (from an EOR point of view), but CCS requires optimum and secure use of the entire pore volume for CO_2 storage. Therefore in a combined EOR and CCS CO_2 flooding project both the incremental oil and the quantity of CO_2 storage are important considerations in project design. This may affect some elements of the flooding process design as well.

As an example, it is standard practice in the Permian Basin to ***waterflood*** a mature CO_2 flooded block or phase. This is practiced to recover part of the (valuable) CO_2 for future phases. However, if storage is tied to EOR, it may imply that the injected CO_2 should not be produced. In other words, either the final waterflooding phase should be avoided or it

can be replaced with extended CO_2 flooding, if abundant CO_2 is available. This way, both the EOR and storage objectives of the project can be better fulfilled.

Moreover, it is an accepted operational procedure in different provinces to operate the EOR flood, ***as close to MMP as possible*** to reduce the compression costs and reducing net CO_2 utilisation efficiency while taking advantage of full miscibility development; this is relevant in both the North Sea and Permian Basin provinces. However, coupling EOR with storage may allow for conducting the flood at even higher pressures as CO_2 storage usually increases, if the flood is conducted at elevated pressures.

Depressurization has also been practiced in a number of North Sea fields such as Brent, Alwyn North, Miller and Ekofisk once the field life approaches its end (Beecroft *et al.* 1999). In the North Sea, valuable hydrocarbon gas is injected during the tertiary phase of projects for enhancing oil recovery. This injected gas which has market opportunity and depressurization can recover part of this injected gas in addition to the *in-situ* dissolved gas. However, once CO_2 is injected for combined EOR and storage, depressurization should be avoided, or if the security of storage allows, the target formation pressure can be further increased to store more CO_2.

This discussion can be further extended to the choice of the ***type of flooding process*** i.e. horizontal flooding or gravity stable flooding (where geological conditions permit). In pure EOR terms, horizontal flooding is characterised by an earlier oil response, but lower cumulative oil recovery. Therefore, the next question is: can coupling EOR with storage in a CO_2 flood favour alternate process design e.g. gravity stable or high-pressure CO_2 flooding?

The ***timing*** of the CO_2-EOR initiation will also be potentially affected, once CO_2 flooding is practiced offshore. Offshore, because of higher EOR costs, EOR should be initiated earlier to allow part of the costs being tolerated by e.g. the previous waterflooding.

The above few examples show that the EOR design elements can be altered at individual field level, once storage and EOR are combined in a given flood.

Meanwhile, the fact that the majority of injected CO_2 in the United States is supplied from natural resources implies that the operator is more ***flexible*** in adjusting the target CO_2 injection rate based on purely technical considerations. Figure 1.16 (next page) shows the production profile of typical residential sector CO_2 in the United States between 2007 and 2012 (USEIA 2013). Although the data belong to the United States, the generally

varying nature of CO_2 production (or potentially CO_2 supply) can be clearly observed in this figure. This varying CO_2 supply concept should, however, remain relevant for other offshore provinces e.g. the North Sea.

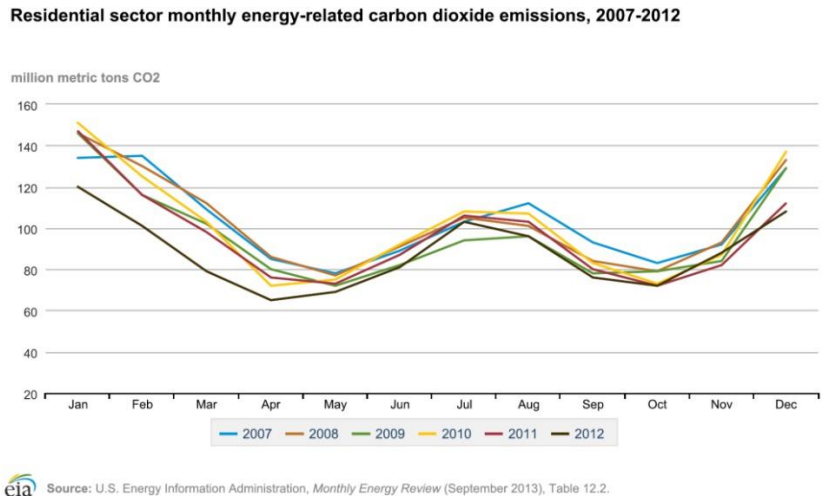

Figure 1.16: Seasonal variation of CO_2 production in residential sector in the United States (USEIA 2013)

The seasonal variations seen in this figure are imposed by periodic energy consumption, characteristic of CO_2 supply for each province; e.g. in the North Sea, there could be higher CO_2 production in the winter and less in the summer. If this CO_2 is considered for supplying a project, the operator has to consider these variations in its process design, considering the fact that emission of captured CO_2 for whatever reason may face significant penalties, if CO_2 is supplied from a capture plant. This means that ***all the allocated*** CO_2 must be received and safely injected (stored), either in the EOR site or elsewhere for pure storage. Thus the operator either has to consider these variations into its EOR process design to capture these highs and lows of CO_2 supply or design its processes based on the minimum supplied CO_2 and store any additional supplied CO_2 elsewhere. In the Magnus EOR, the injected gas had a marketing opportunity which was recognised by the operator in the design of WAG timings. The same concept should be relevant in combined EOR and storage CO_2 flooding.

Contrary to the requirement to receive all the allocated CO_2 stated above, CO_2 supply contracts in the United States are sometimes characterised by an "***up to***" clause (e.g. Pontious & Tham 1978), implying that there is a maximum limit for receiving CO_2 from a common pipeline, below which the operator is absolutely flexible. This may also reflect the situation of the CO_2 market in the United States, where demand is higher than supply.

The above consideration indicates that there might be less supply flexibility, at least for the first few combined EOR/CCS projects at the very beginning stages of CO_2 deployment in an offshore province e.g. the North Sea, before full cluster development is established (Goodyear *et al*. 2011). Hence, EOR projects supplied by CO_2 from capture plants may require swing CO_2 storage to capture the supply variations. This could be an aquifer storage or storage in a mature block. Even pure HC-EOR driven scenarios (e.g. the Magnus field) have considered swing gas storage to capture possible supply variations (Moulds *et al*. 2010).

Confinement is also another important consideration which is likely to remain equally important for both pure EOR and combined EOR and storage scenarios in onshore and offshore provinces, however, from a different perspective. In the Permian Basin which is purely EOR driven, confinement is important because CO_2 is an expensive commodity which should be retained within the flooding area e.g. Hasting Field (Davis *et al*. 2011). Similarly, in the North Sea, which will be potentially driven by combined EOR and storage, CO_2 should stay within the storage complex, because security of CO_2 storage requires this.

1.9 Closing Remarks

The future of CO_2-EOR in the North Sea, Gulf of Mexico and many other offshore provinces depends on the measures taken by policymakers in the atmosphere of constrained CO_2 emissions. In all these provinces immediate action for implementing CO_2-EOR activities must be taken; otherwise, facilities can be removed and the opportunity lost. In the United States, fossil fuels remain a considerable source of energy supply and therefore CO_2-EOR can satisfy twin purposes of increasing domestic crude oil supply and storing more CO_2. In the UK, however, a radically different policy has been undertaken in that, CO_2 emission will be constrained by *less* fossil fuel consumption and switching to alternate fuel supplies.

In this environment, the already existing regulations to constrain CO_2 emissions may have a significant impact on the future of CO_2-EOR activities. The Lula field is a good example in this regard; while the EOR benefit of CO_2 flooding in the Lula field may be an encouraging driving force for initiating CO_2 flooding in this field, the impact of emission restrictions set by the Brazilian authorities should not be overlooked. We

believe that in the absence of these restrictions, other development plans could be envisaged e.g. venting the produced CO_2 directly to the atmosphere as is currently practiced in many other provinces throughout the world.

In the absence of major support from host North Sea governments, private companies may yet support CO_2 activities in this province; nevertheless, this would be on a much smaller scale to promote the public perception of their operations. The combination of the above suggests that the most likely scenario for CO_2-EOR deployment in the North Sea could be a point-to-point supply and not a full cluster scale development, similar to the United States.

1.10 Aim and Organization of this Thesis

The introductory materials presented above set the context for the research question addresses in this thesis. They are required to provide the reader with a clear insight into the problem.

The aim of this thesis is to investigate the ***likely differences*** between CO_2-EOR in those offshore classes of reservoirs in comparison with the CO_2 flooding principally undertaken in the Permian Basin and investigate what ***new characteristics*** may emerge as a result of these differences. The introductory materials presented above may suggest that the likely CO_2 flooding differences between onshore and offshore classes of reservoirs can be briefly categorised as below;

1. The motivation of CO_2 flooding will be potentially different between onshore and offshore classes of reservoirs. This means that CO_2 flooding offshore will benefit from a different economics and cost structure compared to onshore CO_2 flooding.
2. This different motivation may favour alternate CO_2 flooding project designs, contrary to conventional practices undertaken in the Permian Basin of the United States.
3. The characteristics of CO_2 supply is yet uncertain offshore. However, since it will be supplied from anthropogenic sources, it should be relatively pure, less flexible, with much tighter emission restrictions and bounded to seasonal energy consumption.
4. The development characteristics will be different between the two classes of reservoirs. Offshore reservoirs are fundamentally bigger, with fewer wells and

relatively larger spacing between wells which are depleted at higher depletions rates, hence CO_2 flooding may have different characteristics in this group of reservoirs.

5. Whether onshore or offshore, each province is characterised by a different ambient reservoirs conditions and fluid properties, which may affect the CO_2 flooding performance compared to another province.
6. At the very bottom level, the design of wells and facilities could be also different between the two groups of reservoirs.

It is, however, not intended in this study to investigate all the above differences, particularly project design and economics. Instead, the discussions in this thesis, mostly concentrate on reservoir engineering issues, in that Sections 2, 4 and 5 will be addressed in this study.

The remainder of this study is organized as follows. **Chapter 2** will show the details of model construction along with some discussions pertaining to the fundamental concept of CO_2 flooding. **Chapter 3** compares the fundamental elements of CO_2 flooding between two different classes of reservoirs; first the North Sea group of reservoirs and second, the United States CO_2 flooded reservoirs. It will be shown in this chapter that the North Sea province is characterised by essentially different ambient reservoir conditions and fluid properties compared to the Permian Basin and other CO_2 flooded reservoirs in the United States. In the first part of **Chapter 3**, fundamental elements of CO_2 flooding e.g. miscibility development and CO_2-water interactions will be compared between the two provinces. In the second part of this chapter, the performance of CO_2 flooding will be compared between representative models of the onshore United States and offshore North Sea classes of reservoirs.

Chapter 4 investigates the likely flow patterns upon CO_2 flooding in the onshore United States and offshore North Sea classes of reservoirs, taking into account the fundamental differences that already has been addressed in Chapter 3. The type of flow pattern essentially determines the macroscopic sweep efficiency in each classes of reservoirs.

Chapter 5 investigates the impact of CO_2 flooding driving force on the CO_2 flooding project design. The materials presented in Section 1.8 will be the background materials for this Chapter.

Chapter 6 of this study investigates a fundamentally different topic. This chapter investigates grid requirement for miscible processes such as CO_2-EOR, based on

measuring the system dispersivity in different orientations. The dispersivities are then matched with appropriate grid block sizes which can be used in reservoir simulation.

Finally, **Chapter 7** outlines the conclusions of this work and in addition plans for future research activities.

Chapter 2 Basic Concepts and Fundamentals in CO_2 flooding Processes

2.1 Introduction

The aim of the study presented in this chapter is to highlight some of the technical aspects pertinent to CO_2 flooding such as miscibility development, oil swelling, formation of transition zone and its consequent impacts on the CO_2 flooding characteristics. Also, it will be shown how dispersion may affect the CO_2 flooding characteristics by enlarging the transition zone already developed between oil and CO_2. The impact of pressure on the CO_2 flooding characteristics will also be reviewed; it will be shown that in additions to affecting miscibility development and microscopic sweep efficiency, pressure may affect macroscopic sweep efficiency of the CO_2 flood by affecting the properties of CO_2 i.e. its density and viscosity. The relative benefit of WAG in microscopic and macroscopic scales will also be reviewed later in this chapter. It will be shown that a gravity dominated displacement may adversely affect the performance of CO_2-WAG. The observations presented in this chapter will also be compared with the findings of other researchers in the literature.

In the beginning part of this chapter, we first introduce the constructed numerical model parameters (Section 2.1). The developed model will be used to investigate the above mentioned CO_2 flooding characteristics in this chapter. This model will also be used later for further numerical analysis presented in Chapters 3 and 5.

2.2 Description of the Model

We use a compositional simulation model in this study to represent concepts such as oil/gas component exchange and miscibility development, oil swelling and oil viscosity reductions. Todd provides a full review of different aspects that need to be correctly represented in a CO_2 flooding simulation (Todd 1979). CMG-GEM is the compositional flow simulator used in this study (CMG-GEM 2014.10). The fluid model for this study is taken from the Jema field in the United States characterised by Khan *et al*. (Khan *et al*. 1992, Ghomian *et al*. 2008). However, the properties are slightly modified to make an oil of desired density and viscosity. Table 2.1 shows the properties of this fluid model.

Table 2.1: Detail of the fluid model properties used in this study (Khan* et al. *1992)

Comp.	Z_i	M_w	Weight Fraction	P_c (psi)	T_c (°R)	V_c (ft^3/lb-mole)	ω	Parachor	γ_{CO2-i}
CO_2	0.0192	44.0	0.0054	1069.8	547.5	1.5057	0.2250	49.0	0
C_1	0.0693	16.0	0.0071	667.1	300.0	1.5858	0.0080	71.0	0.05
C_{2-3}	0.1742	36.0	0.0401	660.3	609.8	2.8277	0.1260	135.7	0.05
C_{4-6}	0.1944	59.9	0.0876	488.6	839.0	4.9850	0.2439	231.6	0.05
C_{7-16}	0.3138	125.1	0.2950	303.8	1100.0	9.5	0.6386	439.1	0.09
C_{17-29}	0.1549	256.2	0.2982	230.3	1400.0	18.0	1.0002	788.2	0.09
C_{30+}	0.0742	478.3	0.2667	229.7	1750.0	35.0	1.2812	1112.4	0.09

Table 2.2 shows estimated oil properties using this fluid model at two different representative reservoir conditions of onshore Permian Basin and offshore North Sea provinces (Fayers *et al*. 1981, Warner 1977).

Table 2.2: Calculated oil properties at two different representative reservoir conditions

	ρ_o (lb/ft^3)	ρ_{CO2} (lb/ft^3)	μ_o (cP)	μ_{CO2} (cP)	*BBP* (psi)	*MMP* (psi)	B_o (Rb/stb)	*GOR* (scf/stb)
Offshore, North Sea (5000psi, 212°F)	44.98	43.75	0.657	0.059	778	2400	1.18	232
Onshore, Permian Basin (3000psi, 113°F)	45.86	50.34	0.796	0.069	577	1200	1.23	232

The relative permeability data used for this work are also taken from the work of Dria *et al.* (1993) for experimental CO_2 core flooding with the endpoints and exponents illustrated in Table 2.3 and Figure 2.1. The Stone-1 model was used for the representation of 3-phase oil relative permeability. Spiteri and Juanes thoroughly investigated and compared the performances of Stone 1, Stone 2 and Saturated Weighted Index (SWI) relative permeability models (Spiteri & Juanes 2006) and concluded that the Stone 1 model is the one that agrees best with experimental data.

Hysteresis was only modelled in the gas phase with a trapped gas saturation of S_{gc}=0.16. Hysteresis was not modelled in the water phase, as it has been assumed that the formations are water-wet and hysteresis in the wetting phase is very small. Care was also taken to smooth the relative permeability curves for the separation which may occur around the critical point for the sharp transition between gas and oil phases (CMG-GEM 2014.10). Certain features such as capillary pressure effects and water blocking (Muller & Lake 1991) were not considered in this study.

Table 2.3: Relative permeability model parameters (Dria et al. 1993)

Phase	k_{rj}^o	s_{jr}	γ_j
water	0.36	0.36	3.1
oil (with water)	0.57	0.37	2.9
oil (with gas)	0.57	0.16	2.9
gas	0.28	0.16	2.9

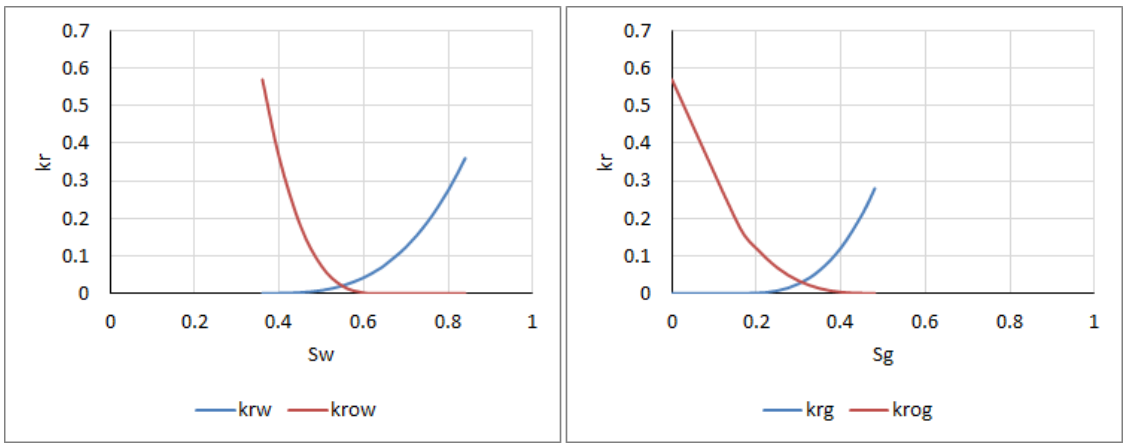

Figure 2.1: water-oil (left) and gas-oil (right) relative permeabilities adopted for this study (Dria et al. 1993)

This set of relative permeability data has been used by a number of researchers. Roper *et al.* (1992) used these data to analyse the tertiary CO_2 injectivity. Chang *et al.* (1994) also used them to investigate the actual CO_2 flow patterns under multiple contact miscibility conditions.

Figure 2.2 shows the fractional flow curves, respectively for water and gas displacing oil. The fractional flow curve for water displacing oil has been generated assuming a mobility ratio of 3.3 for water displacing oil (water and oil viscosities of 0.28cP and 0.92cP respectively). Similarly, the fractional flow curve for CO_2 displacing oil was generated based on a mobility ratio of 18.4 (gas and oil viscosities of 0.05cP and 0.92cP respectively).

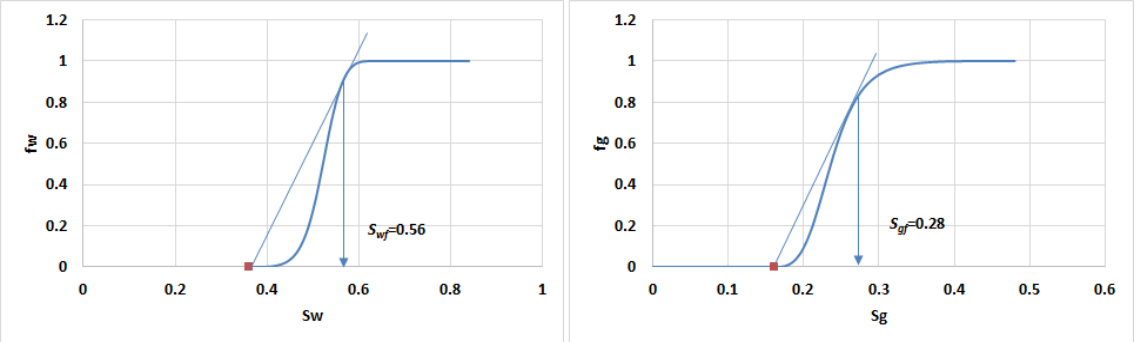

Figure 2.2: Fractional flow curves for water (left) and gas (right) displacing oil for the set of relative permeability depicted in Table 2.3

A significant amount of the findings depicted in this study relies on the set of the relative permeability that have been selected in this study. In this section an alternate set of relative permeability data has been identified and then is compared with the default set, and is depicted in Table 2.3. This will allow comparison of the characteristics of the two

relative permeability models. The alternate set of relative permeability data has been taken from the simulation work of Goodyear *et al.* (2003) with the end point's and exponents depicted in Table 2.4 and Figure 2.3 (Goodyear *et al.* 2003, SHARP[6] Reports 2001).

Table 2.4: The relative permeability parameters for the alternate set of relative permeability data (Goodyear 2003, SHARP Reports 2001)

Phase	k_{rj}^{o}	s_{jr}	γ_j
water	0.3	0.25	2
oil (with water)	0.57	0.25	4
oil (with gas)	0.57	0	4
gas	0.57	0.025	2

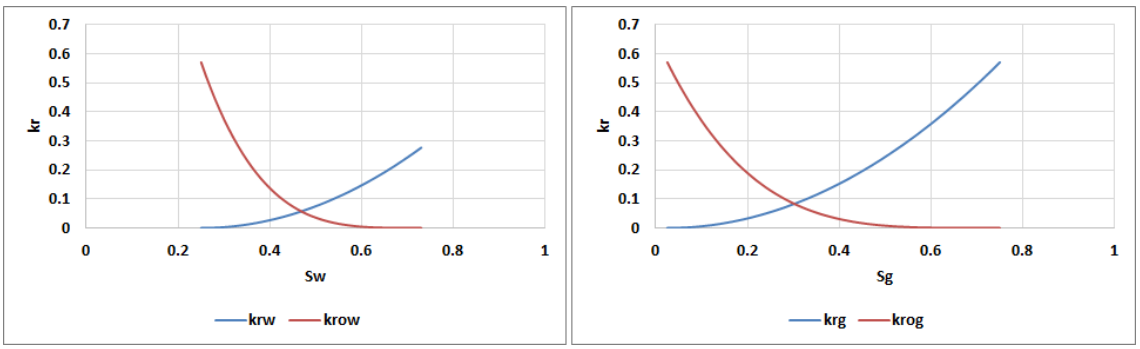

Figure 2.3: Alternate set of relative permeability model (Table 2.4); water-oil (left) and gas-oil (right).

Figure 2.4 compares the fractional flow curves between the two sets of relative permeability models depicted above and for water and gas displacing oil under the same mobility ratios of 3.3 (w/o) and 18.4 (g/o).

Figure 2.5 compares the actual water/gas saturation profiles after 0.2HCPV gas/water injection in a one dimensional model (with 500 grid blocks) and with the mobility ratios described above. The saturation of the shock front has also depicted in each figure for both water and gas displacing the oil phase; note that there is fair agreement between the magnitude of shock front saturations which can be inferred from Figure 2.4 and Figure 2.5.

A significant difference between the two sets of relative permeability is the extent of multiphase region that is created upon using each of them in a given simulation. For the base set of relative permeability (Table 2.3), the created multiphase region is apparently much smaller and thus a rather piston-like displacement may be obtained.

[6] UK-DTI Sustainable Hydrocarbon Additional Recovery Programme (SHARP).

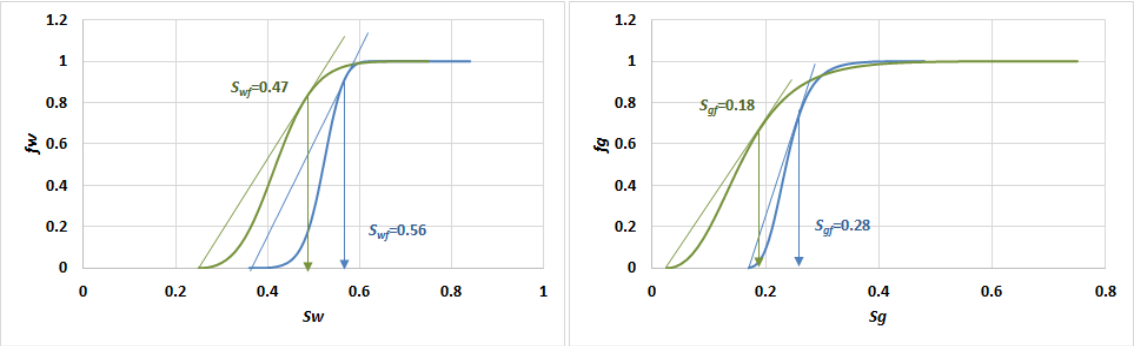

Figure 2.4: Fractional flow curves for water (left) and gas (right) displacing oil; Blue: the base set of relative permeability (Table 2.3), Green: the alternate set of relative permeability (Table 2.4)

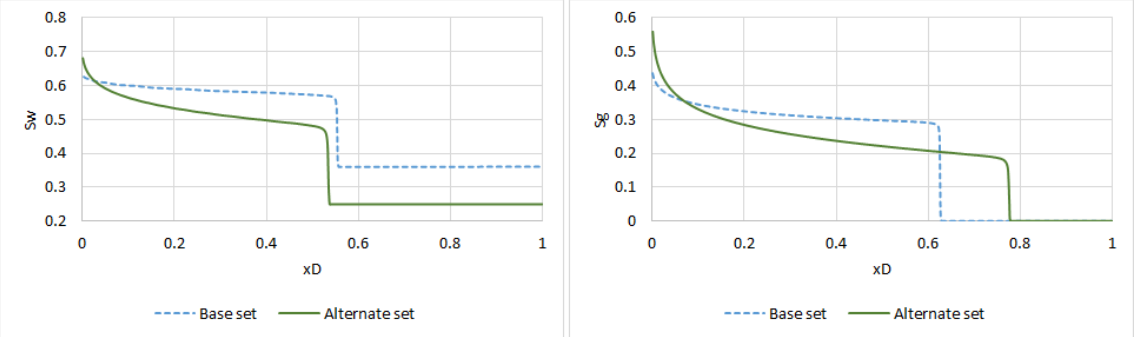

Figure 2.5: water (left) and gas (right) saturations after 0.2HCPV water/gas injection in a 1D model. The solid-green data represent the alternate set relative permeability model. The dashed-blue data represent the base set relative permeability model.

Figure 2.5 shows that the location of the water front is roughly similar between the two relative permeability models. However, for gas this is not the case as the critical gas saturation is fundamentally different between the two models. The alternate relative permeability model predicts a much wider two phase region and accordingly a gas saturation front that is ahead compared to that of the base set of relative permeability model with resultant earlier gas breakthrough. Another important difference between the two relative permeability models is the significance of gravity upon using either of them. The alternate set of relative permeability model (Table 2.4) predicts a larger multiphase region, which in turn may increase the contact between different phases with consequent larger gravity effects. Note that the two relative permeability models may generate the same gravity number (Appendix-2) as the oil relative permeability endpoint is similar in both of them. However, since the two phase regions of either of the relative permeability models are different, the effect of gravity could be different upon using each of them.

Figure 2.6 compares the three phase oil relative permeabilities obtained by Stone-1 correlation between the two relative permeability models. The white regions in each

figure shows the region that either oil does not exist or cannot flow. It can be seen that the base set of relative permeability predicts a much smaller mobile oil window. The relative distribution of each oil relative permeability ranges is roughly identical between the two models. Note, however, that the two sets of relative permeability have the same oil endpoint relative permeability.

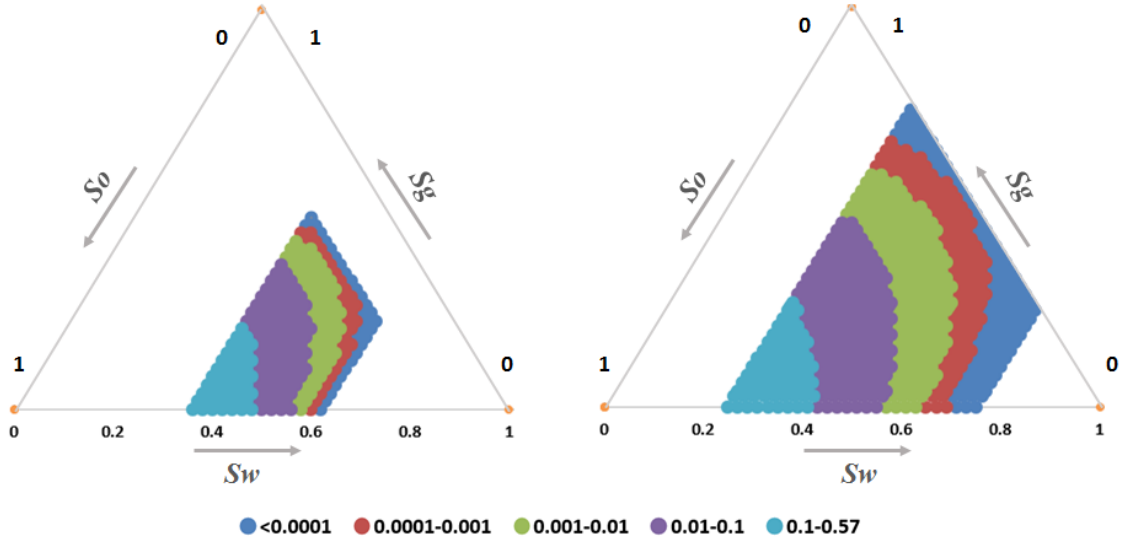

Figure 2.6: 3-phase oil relative permeability calculated with Stone-1 model; left: the base set relative permeability model (Table 2.3), right: the alternate set relative permeability model (Table 2.4)

For the majority of the discussions presented in this chapter and later studies in Chapter 3 and 5, we use the first set of relative permeability depicted in Table 2.3. However, the second set of relative permeability model will be used in Chapter 3 to compare the likely performance of cross sectional North Sea and Permian Basin representative models with an alternate sets of relative permeability model in addition to the default set of relative permeability. This will allow investigation weather the obtained results are sensitive to the chosen set of relative permeability model. It will be shown that although the results are quantitatively different, they are qualitatively very similar (Figure 3.18).

2.3 Miscibility Development and Miscibility Pressure

Miscibility development in CO_2-oil systems is of multiple contact (MCM) type in that a few contacts are required for miscibility to be developed. First contact miscible (FCM) CO_2 flooding is not operationally achievable as the required pressure would be very high. A CO_2 swelling experiment at 212°F with the above fluid description showed that pressures as high as 14000psi are required for FCM CO_2 flooding.

Figure 2.7 (left) shows the development of miscibility in a slimtube simulation at 2500psi and 212°F. The slimtube model parameters have been depicted in Table 2.5. This 1D slimtube model will be used for the majority of the 1D simulations conducted in this Chapter. The slimtube model permeability is high enough (4000mD) to minimise pressure variations across the model. CO_2 injection velocity was also adjusted in accordance with the recommendation of Yellig and Metcalfe (Yellig & Metcalfe 1980).

Note that upon miscibility development, oil and gas densities approach each other, though they never converge completely (Figure 2.7-left). This is because of dispersion. Multiple contact miscibility development is sensitive to the level of dispersion which always exists in any system. The dispersion in this slimtube simulation is only due to numerical gridding. Figure 2.7 (right) shows the corresponding evolution of k-values as they approach unity upon miscibility development; implying existence of only one phase.

Table 2.5: Slimtube model parameters

Grid	500×1×1
Grid Dimensions	0.1ft × 0.1ft × 0.1ft
Average horizontal permeability	4000mD
Porosity	0.25
Temperature	212°F
MMP	2400psi
Well locations	Injector on the left, producer on the right
Fluid model	Table 2.1
Relative permeability model	Table 2.3

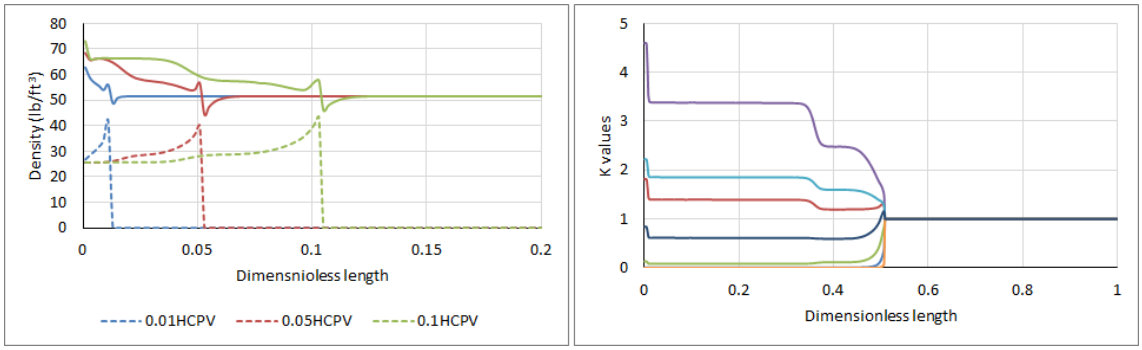

Figure 2.7: Left: oil and gas densities after 0.01, 0.05 and 0.1 HCPV at 2500psi and 212°F. Right: equilibrium K-values at 0.5PV CO_2 injection; individual colours represent each of the seven components k-values. Model properties have been depicted in Table 2.5.

Figure 2.8 (next page) shows the predicted miscibility pressure after injecting 1.2PV of CO_2 in the above slimtube models at two different temperatures of 113°F and 212°F. The

estimated minimum miscibility pressures are around 1200psi and 2400psi (the point where two tangents intersect) for the 113°F and 212°F temperatures, respectively.

While these figures show that at high flooding pressures recovery factor approaches 100% in both models, in reality the ultimate slim-tube recoveries never attain 100% (Stalkup 1983). Some factors are responsible for this, including the wall effects, dead end pores and dispersion which were not taken into account for these slimtube simulations.

A significant difference for miscibility developments between the two representative temperatures is the onset development of miscibility at each respective temperature. The rapid onset development of miscibility at 113°F compared to 212°F is due to the impact of a smaller transition zone between CO_2 and oil at lower temperatures. This behaviour has also been observed experimentally by Yellig and Metcalfe (Yellig & Metcalfe 1980) which indicates that at lower temperatures, miscibility development could be more sensitive to pressure variations. In other words, the miscibility development in a CO_2-EOR process in the Permian Basin is likely more sensitive to pressure variations than in the North Sea. Transition between miscibility and immiscibility affects the balance between microscopic and macroscopic sweep efficiencies and injectivities as will be shown later.

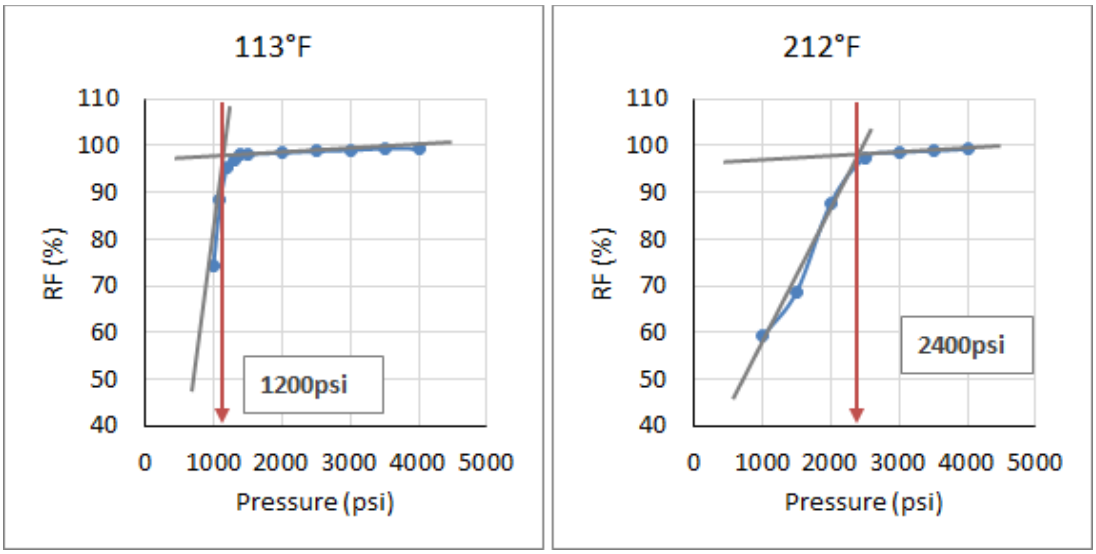

Figure 2.8: Minimum miscibility pressure estimated at 113°F and 212°F by slimtube simulations

Figure 2.9 shows oil viscosity and saturation profiles after injecting 0.4HCPV CO_2 in the above slimtube model at 2400psi and 212°F; oil viscosity ahead of the CO_2 *gas* front has been significantly reduced from slightly below 1 to 0.2. This phenomenon has also been observed by other researchers (Gardner *et al*. 1981, Mungan 1982). The stepwise change

of oil viscosity behind the CO_2 front is due to the chromatographic evaporation of oil components as further CO_2 is injected.

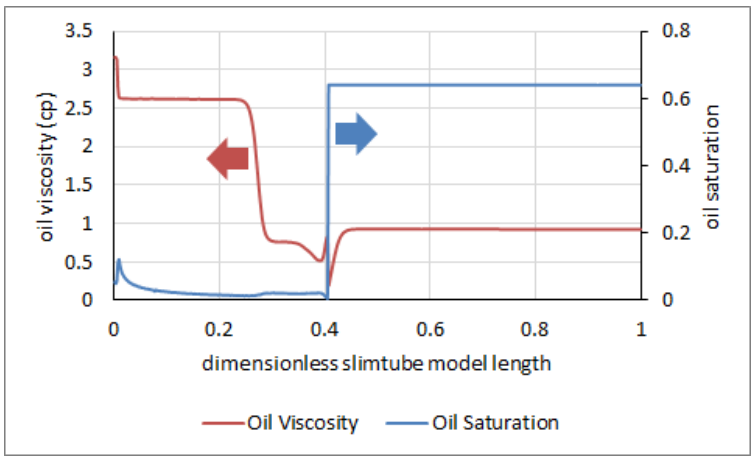

Figure 2.9: Oil viscosity and saturation after 0.4HCPV CO_2 injection (212°F) in the slimtube described above (Table 2.5).

Holm & Josendal (1974) reported that the formation of a methane bank ahead of the CO_2 front could be an indication of immiscible displacement. Figure 2.10 shows the effluent methane and CO_2 concentrations for two slimtube simulations conducted below and above minimum miscibility pressure at 212°F (MMP=2400psi); a bank of methane can be identified prior to CO_2 breakthrough at lower than miscibility pressure.

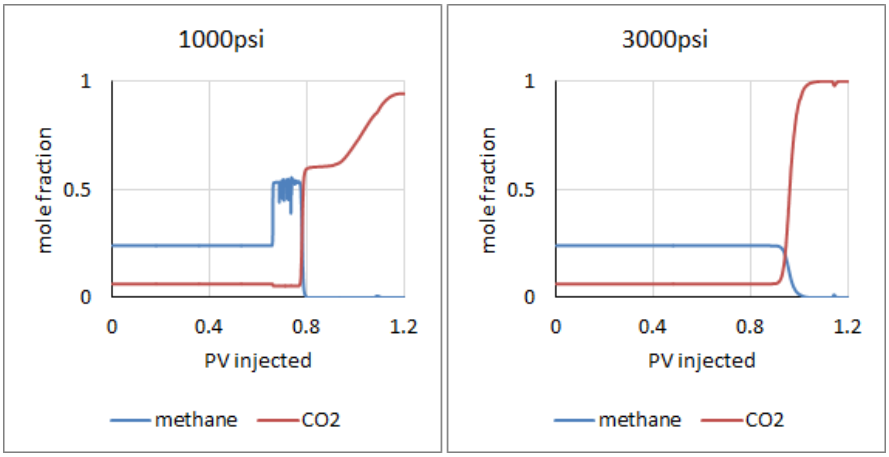

Figure 2.10: Outlet methane and CO_2 mole fractions in two slimtube simulations below (left) and above (right) minimum miscibility pressure.

The presence of impurities such as methane can significantly increase the CO_2 minimum miscibility pressure. The effect is, however, different at different temperatures. This can affect the need for CO_2 separation and recycling should the methane presence significantly increase the MMP.

In this regard, Figure 2.11 compares the results of MMP measurements with mixtures of CO_2 and methane at two different temperatures (113ºF and 212ºF), representative of the Permian Basin and North Sea provinces. The MMPs are measured by Winprop (CMG-WinProp 2014.10) with the method developed by Ahmadi *et al.* (2011). It can be seen that the difference in the MMPs become progressively smaller as the presence of methane (or impurities) in the CO_2 stream increases. This result indicates two things; first, the measured MMPs are less sensitive to temperature at high concentrations of impurities. Second, the impact of the presence of methane is less considerable at elevated temperatures; note that the difference between pure CO_2 and pure methane MMPs is around 3462psi at 113ºF, while at 212ºF it is only 2037psi.

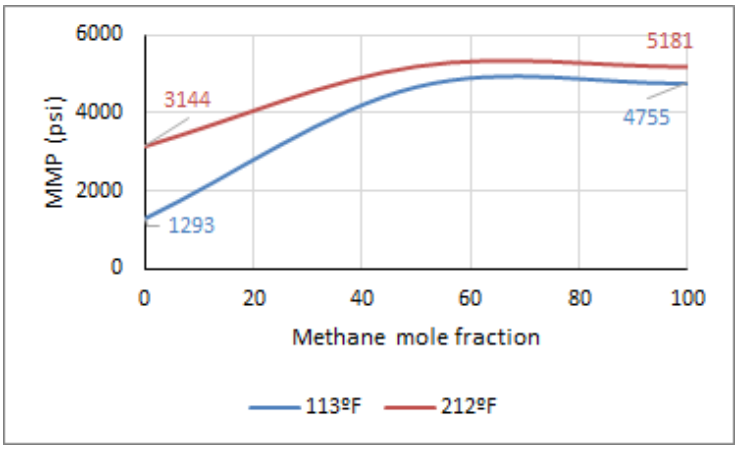

Figure 2.11: Impact of methane on the measured CO_2 MMP at different temperatures, numbers show MMPs at the corresponding conditions of temperature and methane mole fraction.

2.4 Transition Zone; Concept and Importance in CO_2 Flooding

The concept of the transition zone in MCM miscible displacements is very similar to the concept of capillary effects in immiscible displacements; in that, depending on the status of miscibility, a low mobility transition zone develops between CO_2 and oil phases which may substantially affect the sweep efficiency and injectivity responses. This, however, could be different at different temperatures.

Figure 2.12 schematically illustrates the concept of transition zone along with the profiles of mobility ahead and behind the CO_2 front. A transition zone in miscible displacements is defined as the region where the solvent concentration lies between 0.1 and 0.9 (Orr 2007). The size of the transition zone can, however, be affected by two mechanisms; *phase behaviour* and *dispersion* which will be discussed in this section.

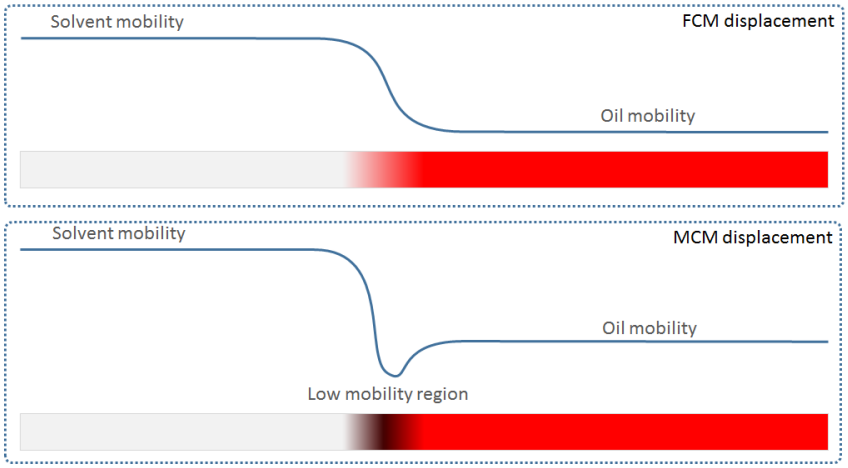

Figure 2.12: Schematic illustration of transition zone and corresponding mobilities in FCM and MCM miscible displacements.

Phase Behaviour: In MCM processes (such as CO_2-EOR), miscibility development requires a minimum number of contacts between CO_2 and oil as was described before. Thus, a minimum distance is required for the phase behaviour to act by transferring mass between oil and CO_2 and hence develop miscibility (Gardner *et al*. 1981).

The more contacts required to develop miscibility, the larger will be the size of the transition zone. This usually occurs where the conditions are less favourable for miscibility development e.g. at higher temperatures, lower pressures or in the presence of impurities.

Figure 2.13 shows CO_2 concentration (left) and total mobility (right) in a number of slimtube simulations, all at 212°F but at several different pressures below and above MMP (MMP=2400psi). The total mobilities have been calculated by the summation of the mobilities of all the three phases. The properties of the slimtube models are also as previously described in Table 2.5.

The profiles have been shown after injecting 0.4HCPV CO_2. Recalling the definition of the transition zone (where the CO_2 concentration varies from 0.1 to 0.9), it can be seen that the size of the transition zone becomes successively smaller as pressure increases. At pressures well above the MMP (3000psi), the transition zone (due to compositional effects) has almost disappeared and only the numerical dispersion effects the displacement.

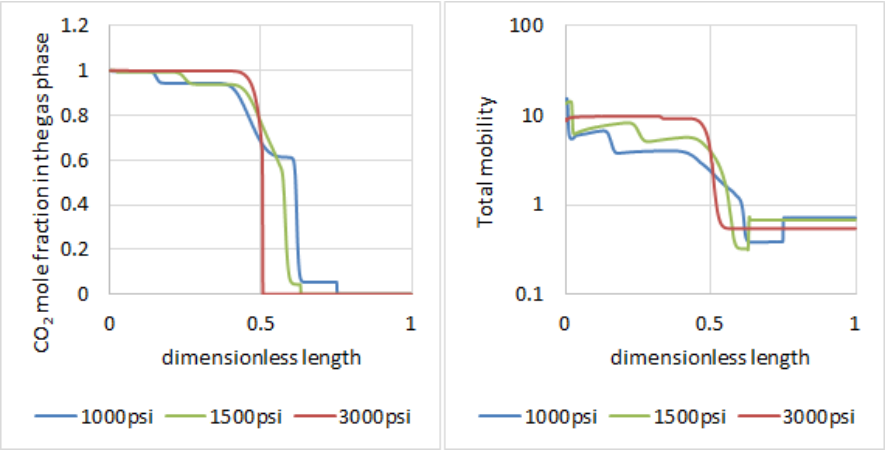

Figure 2.13:The transition zone becomes continuously smaller as pressure increases, comparison in a number of slimtube simulations after 0.4HCPV CO_2 injection at different pressures. Left: CO_2 concentration along the model length. Right: The corresponding total mobility. Model properties have been described in Table 2.5.

Figure 2.13 (right) illustrates that while at high pressure (3000psi) mobility smoothly decreases from CO_2 phase to oil phase, at lower pressures, a low mobility region between CO_2 and oil phases can be identified. This zone becomes successively smaller as pressure further increases and finally disappears at 3000psi.

This is because as pressure reduces, miscibility reduces, thus some oil will be left behind the CO_2 front which forms a multiphase region with a characteristic reduced total mobility. This may significantly affect the quality of the macroscopic sweep between fully miscible and immiscible CO_2 floods as will be shown later.

Dispersion: Dispersion is the second mechanism which affects the size of the transition zone in a CO_2 flood. A larger dispersivity acts like a stronger magnifier and further enlarges the size of the transition zone, which may have been developed already by phase behaviour; thus further exaggerating the oil precipitation behind the CO_2 front and subsequent mobility reduction.

Figure 2.14 compares the final total mobilities along the above described slimtube model at 212°F and 1500psi (less than MMP of 2400psi), for two different magnitudes of dispersion (0.05ft and 0.005ft). Figure 2.14 illustrates that the final total mobility is considerably lower in the model with higher dispersion. This is due to the expansions of transition zone by dispersion. This behaviour also affects the injectivity response of the system upon next waterflooding as will be shown later (Section 2.4.2). Note that waterflooding is usually carried out after CO_2 injection to sweep both CO_2 and the oil bank ahead of it.

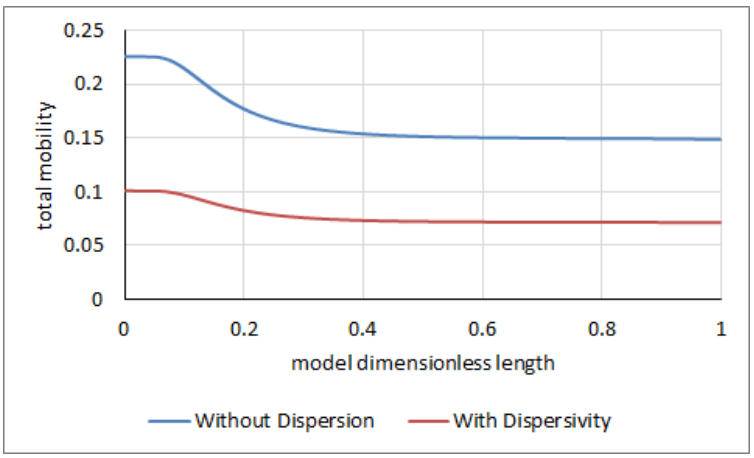

Figure 2.14: Comparison of total mobility at the end of simulations between two different MCM flooding scenarios, with and without dispersivity. Model properties have been described in Table 2.5.

Figure 2.15 compares the recovery factors for two immiscible (at 1000psi-left) and miscible (at 3000psi-right) slimtube simulations, but with different magnitudes of dispersion. The slimtube model parameters are as before depicted in Table 2.5. While in both scenarios, the cumulative recovery decreases as a result of dispersion, the impact is slightly more significant for the fully miscible displacement.

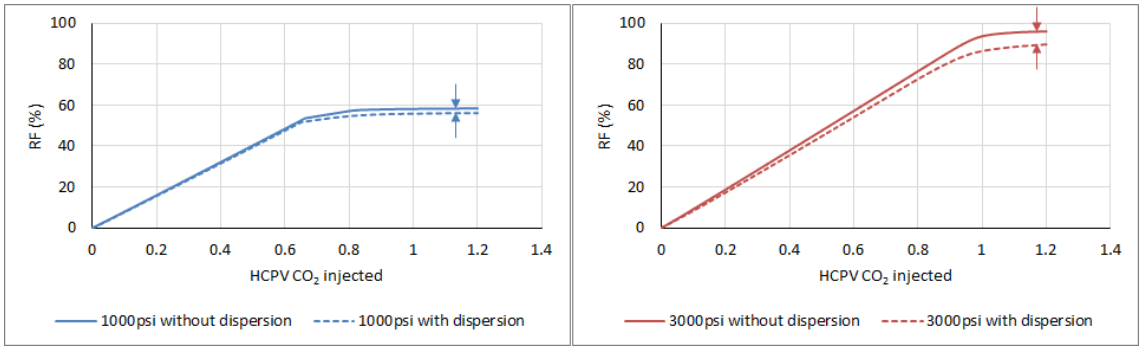

Figure 2.15: Impact of dispersion on the cumulative oil recovery below (left) and above (right) MMP

This is because, in an immiscible displacement (left figure), a transition zone already exists because of phase behaviour effects as was described earlier, which is only slightly *expanded* once dispersion is introduced in the system. In a fully miscible displacement scenario (right figure), the transition zone is already much smaller, therefore, the impact of dispersion on the size of transition zone is much more significant.

Dispersion always exists within the system at both microscopic and macroscopic scales, due to small and large scale heterogeneities (Stalkup 1983). The dispersed zone usually grows with time and its importance is significant in estimating the minimum size of CO_2 slug size required to flood the volume of the system (Mungan *et al*. 1981).

2.4.1 Impact of Dispersion on the Composition Path

Dispersion can also affect the composition path in an MCM flood and makes an already miscible displacement completely immiscible. To investigate this, a number of slimtube simulations with varying numbers of grid blocks were conducted in this section. The three different number of grid blocks (500, 50 and 5) may represent different magnitudes of dispersion (0.05ft, 0.5ft and 5ft). The same of set of simulations have been repeated at two different pressures; slightly above MMP and slightly above FCM pressure to illustrate the significance of dispersion on the composition path in both MCM and FCM flooding scenarios. For this analysis, we use a synthetic 3-component fluid model instead of the full compositional model described earlier. This is because representation of the outlet composition path on a ternary diagram is far easier for a 3-component system. The details of the model are shown in Table 2.6. All the ternary diagrams illustrated in this section have been generated with Schlumberger *PVTi* (Schlumberger PVTi 2014).

Table 2.6: Model parameters used in this section

Grid	**500×1×1**
Grid Dimensions	0.1ft × 0.1ft × 0.1ft
Average horizontal permeability	4000mD
Porosity	0.25
Phases Present	**Oil and Gas**
Components	NC_4, C_{10} and CO_2
Initial composition	NC_4 (50%), C_{10} (49%) and CO_2 (1%) by molar percentage
Model Temperature	290 ºF
Initial Model Pressure	2000psi
MCM Pressure	1882psi
FCM Pressure	2281psi

Figure 2.16 (next page) illustrates the outlet composition path predicted at 2000psi (slightly above MCM pressure) when the dispersion magnitude is negligible (500 grid blocks). Note that, for those compositions on the right of the green line in the ternary diagram, miscible displacement can be achievable.

Figure 2.16 shows that at this level of dispersion, the composition path, noted by points 1 to 4, never enters the two phase region (green dashed area). Next, the model was coarsened 10 and 100 times to represent larger dispersions. Figure 2.17 (next page) illustrates results.

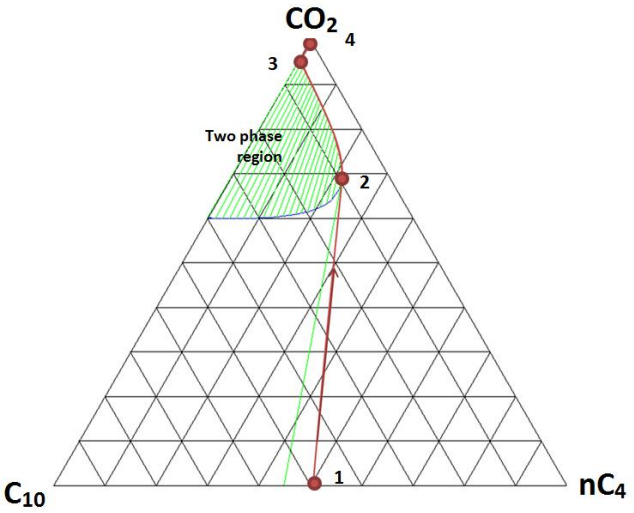

Figure 2.16: Representation of the outlet composition path on the ternary diagram, at the minimum magnitude of numerical dispersion (500 grid blocks).

Figure 2.17 shows that as the model becomes coarser, the composition path goes deeper into the two phase region. This may result in more oil left behind the CO_2 flood as was described earlier, resulting in a lower microscopic sweep efficiency, further mobility reduction and a more consequent injectivity impairment. This figure also shows that a displacement that was otherwise (near) miscible, becomes immiscible purely due to an increase in the magnitude of dispersion.

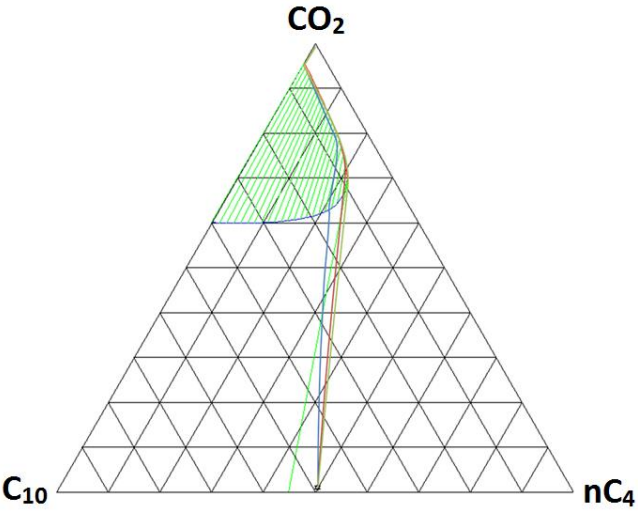

Figure 2.17: Evolution of the outlet composition paths at different magnitudes of dispersion; Green: 500 cells, Red: 50 cells and Blue: 5 cells.

The same experiments now have been repeated at 2000psi (slightly above FCM pressure). Results show that unlike MCM scenarios, for the FCM scenarios, the dispersion has absolutely no impact on the composition path. Figure 2.18 illustrates the ternary plot predicted for at this pressure along with the outlet composition path at different

dispersions. It can be seen that, all the models follow the same composition path irrespective of the magnitude of dispersion.; Note that although dispersion does not affect the composition path in an FCM flood, it may affect the time of solvent breakthrough (Gardner *et al*. 1981).

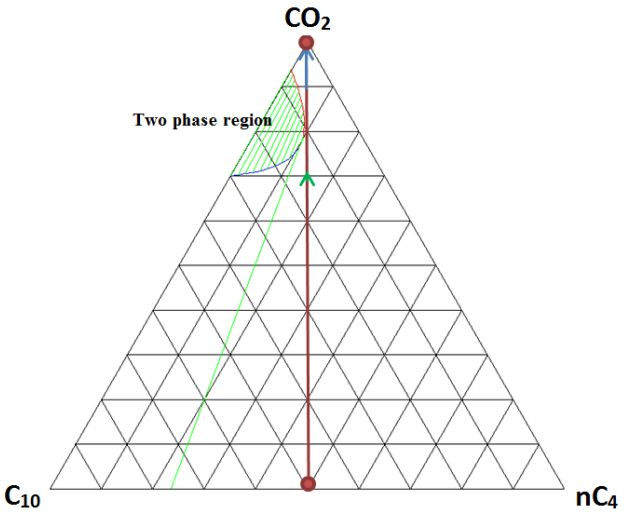

Figure 2.18: Outlet composition profile at different dispersion levels, when pressure is higher than FCM pressure

The findings can be extended to multi-component CO_2 flooding. Figure 2.19 compares miscibility development in two similar slimtube simulations at the same pressure and temperatures of 212°F and 2500psi but with different magnitudes of dispersion. The slimtube model parameters are similar to those depicted in Table 2.5. Physical dispersion in the left and right models are respectively zero and 0.5ft; though a background numerical dispersion of 0.05ft already dominates the displacement in both models. Figure 2.19 shows that miscibility development has been further affected (impaired) in the model with higher physical dispersion.

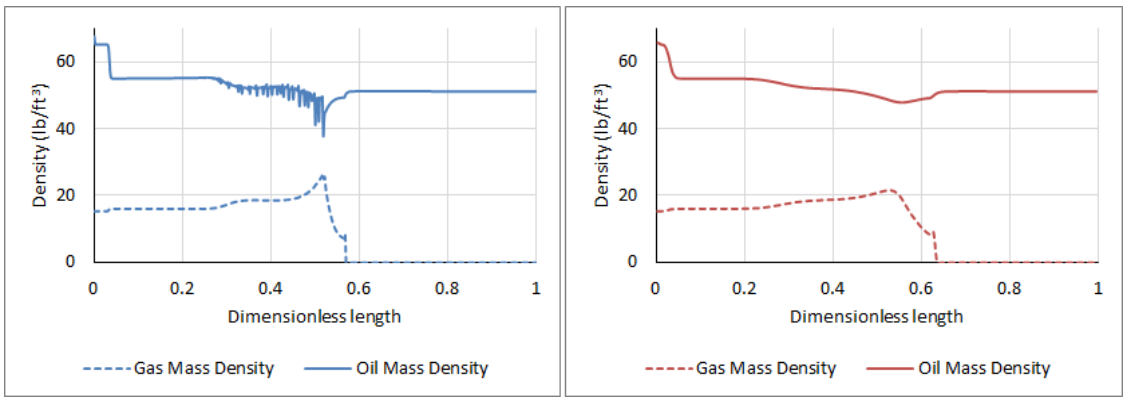

Figure 2.19: Impact of dispersion on the miscibility development in a slimtube simulation. The left model is free of physical dispersion, while the right model has dispersion (0.5ft). Model properties have been described in Table 2.5.

2.4.2 Impact of Phase Behaviour and Dispersion on System Injectivity

Injectivity in CO_2 flooding processes can be affected by various phenomena, including but not limited to three phase relative permeability effects, CO_2 and water interactions and formation of a possible fourth hydrocarbon phase. Rogers *et al.* (2001) provide a comprehensive review of the injectivity issues encountered in CO_2 flooding. The impact of "*a reduced mobility transition zone*" could, however, be significant on the injectivity response in CO_2 flooding processes.

The injectivity in this context refers to the injectivity of waterflooding *before* and *after* CO_2 flooding. Roper *et al.* (1992) showed that dispersion considerably affects injectivity in a CO_2 flooding system. Figure 2.20 compares injectivity responses for two CO_2 core flood (1D) simulations, above (at 1000psi-blue) and below (at 3000psi-red) the MMP. Table 2.7 shows the details of the core models.

Table 2.7: Core flooding model parameters

Grid	500×1×1
Grid Dimensions	0.02ft × 0.02ft × 0.02ft
Average horizontal permeability	4000mD
Porosity	0.25
Temperature	212°F
MMP	2400psi
Well locations	Injector on the left, producer on the right
Fluid model	Table 2.1
Relative permeability model	Table 2.3

In both core models, flooding initiates with injecting 1HCPV water, followed by injecting 0.4 HCPV CO_2 and finally terminates by injecting another 1HCPV water. Injectivities have been measured by dividing the throughput by the pressure difference between the two ends of the core model. All the injectivities then have been normalised by the terminal initial waterflood injectivity (i.e. injectivity at the end of initial waterflood where τ=1) and then were plotted in Figure 2.20. There is no physical dispersion in either of the models, except for the prevailing numerical dispersion which is identical for the two models. Different injectivity responses can be observed for the final water flooding depending on the miscibility status of the system.

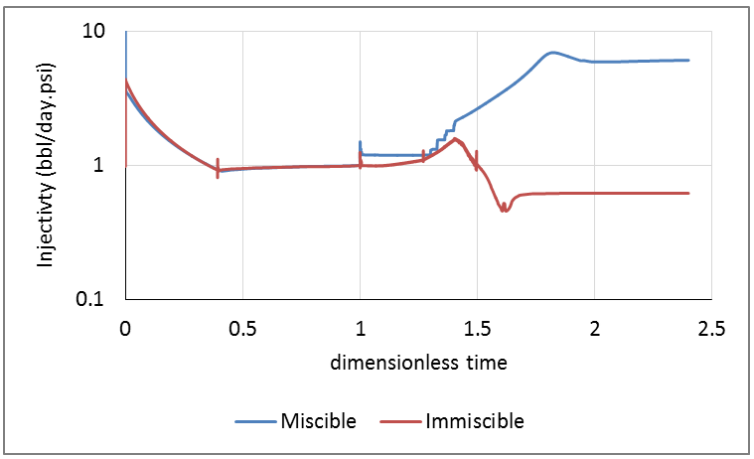

Figure 2.20: Evolution of the injectivity responses for miscible and immiscible CO_2 floodings. Note that CO_2 is injected between 1 and 1.4HCPV.

Figure 2.20 shows that during gas injection injectivity increases in both simulations as gas is less viscous than water (note that CO_2 is injected between 1.0 and 1.4 HCPV). The injectivity responses during gas injection are fairly similar between the two models. However, the final waterflood injectivity is significantly different between the two models. When the pressure is above MMP, the follow-up water injectivity is higher than the original waterflood injectivity; while when it is below MMP, the follow-up water injectivity is lower than it. This is because the remaining oil saturation in an immiscible flood in significantly higher which creates a considerably larger 3-phase region upon final waterflooding and significantly reduces the total mobility and injectivity upon final waterflood. However, when the pressure is above MMP, an only 2-phase (water-hydrocarbon) may dominates the displacement during the final waterflood with a relatively much better injectivity.

The impact of dispersion on the evolution of injectivity responses is also depicted in Figure 2.21, for both miscible and immiscible scenarios. Figure 2.21 shows the injectivity responses for the above two core flooding simulations depicted in Figure 2.20, but with different magnitudes of physical dispersions. Note that dispersion has adversely affected the injectivity responses for both models, though the relative effect is not similar. During CO_2 injection, dispersion slightly increases (gas) injectivity. However, once the final waterflooding initiates, this remaining unswept oil saturation creates a larger multiphase region and further impairs injectivity in both flooding scenarios. Figure 2.21 shows that this phenomenon can be observed at both below and above MMP, though with different significance; the effect is far less noticeable for an immiscible displacement (left figure) and is more significant for a miscible displacement (right figure).

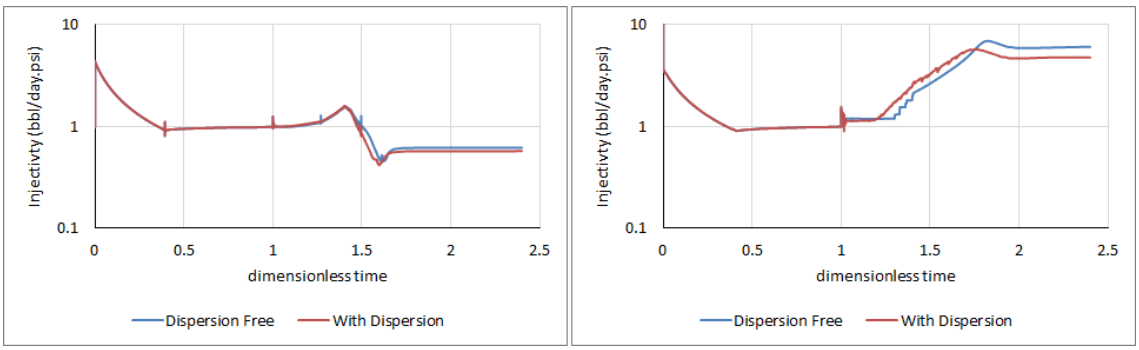

Figure 2.21: Impact of dispersion on the evolution of injectivity; immiscible (left) vs miscible (right) floodings. Note that CO_2 is injected between 1.0 and 1.4HCPV.

As before this is because, in immiscible displacement, a transition zone already exists which only becomes larger once dispersion is introduced; while for the miscible scenario, the transition zone is created as the transition zone size was already very negligible and the introduction of dispersion significantly affects the results. The effect is very similar to the results observed in Figure 2.19.

2.4.3 The Mutual Impact of Microscopic and Macroscopic Sweep Efficiencies

While formation of a transition zone in a near miscible or immiscible displacement may impair the microscopic sweep efficiency and consequently the system injectivity as was shown before, it may provide some benefit for the macroscopic sweep efficiency. In other words, a reduction of pressure in an MCM flood does not necessarily correlate with a performance impairment, proportional to the slimtube recovery impairment. Chang showed that immiscible or near miscible CO_2 flood are dominated by endpoint relative permeability effects, which makes the displacement more stable than for an equivalent FCM flood (Chang *et al*. 1994).

To investigate this, a number of CO_2 flooding simulations were conducted in an identical 2D heterogeneous (areal) permeability field at several different pressures. Up to 1HCPV CO_2 is injected in all these simulations without any water injection before or after CO_2 injection. Table 2.8 shows the 2D model parameters. Note that this 2D model will also be used for further simulations presented later in Sections 2.6 and 2.7.

Figure 2.22 shows the recovery factors at several different pressures for both slimtube (blue) and heterogeneous (red) models. It can be seen in Figure 2.22 (left) that as long as the pressure is above MMP (MMP=2400psi), the two curves are nearly parallel.

However, once pressure declines below MMP, the slimtube recovery factors significantly drop, while the overall sweep efficiencies follow almost the same profile.

Table 2.8: Model properties used in this section

Grid	256×64×1
Grid Dimensions	0.1ft × 0.1ft × 0.1ft
Dip angle	0
Average horizontal permeability	100mD
k_y/k_x	0.1
Porosity	0.2
Temperature	212°F
MMP	2400psi
λ_{xD}	0.25
λ_{zD}	0.1
V_{DP}	0.8
Well locations	Injector on the left, producer on the right
Fluid model	Table 2.1
Relative permeability model	Table 2.3

Noting that $E_{overall} = E_{mic} \times E_{mac}$, then E_{mac} can be approximated by dividing the observed recovery factor in the heterogeneous models to that of the slimtube models (E_{mic}). Figure 2.22 (right) illustrates the calculated E_{mac}s for the displacement at several different flooding pressures. Starting from very high pressures, it can be seen that E_{mac} initially decreases down to a *minimum point* and then increases for floodings at lower pressures.

The location of this minimum point correlates fairly well with the MMP magnitude. Above MMP, macroscopic sweep efficiency gradually declines as pressure decreases. This is because above MMP, a reduction of pressure only reduces CO_2 viscosity (mobility) but does not affect the compositional interactions between oil and CO_2. However, as pressure further decreases below MMP, displacement becomes immiscible and a low mobility zone between CO_2 and oil is developed, which in turn improves CO_2 mobilities and macroscopic sweep efficiency as well. This improvement, however, comes at the cost of lower total mobilities and hence reduced injectivities.

The results show that, the macroscopic sweep efficiencies (E_{mac}) should have been improved for the pressures below MMP to compensate for the microscopic sweep efficiency impairments observed at below minimum miscibility pressures.

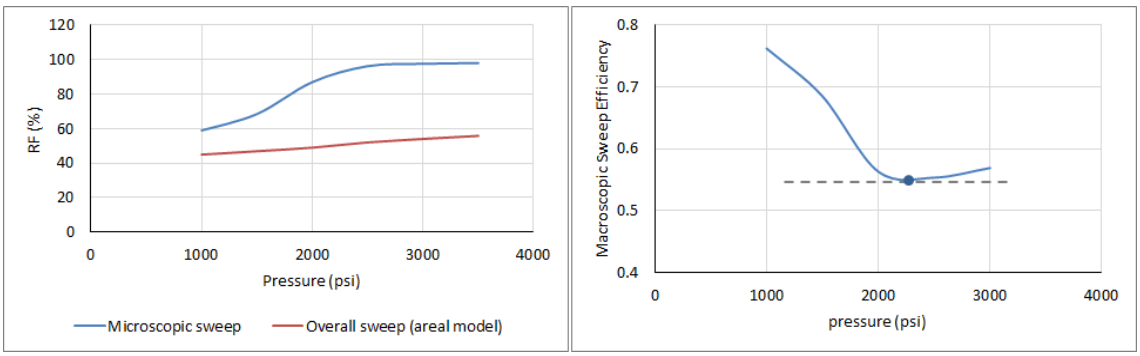

Figure 2.22: Left: comparison of heterogeneous and slimtube recovery factors at different pressures; Right: The calculated macroscopic sweep efficiency. Model properties have been described in Table 2.8.

Figure 2.23 compares the CO_2 concentration prolife after injecting 0.4HCPV CO_2 at two different pressures of 1000psi and 3000psi (below and above MMP of 2400psi). Note that at 3000psi, CO_2 has already broken through, while at 1000psi, it is still far away from the producer.

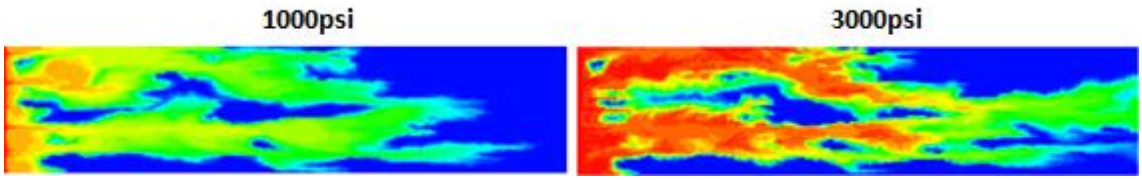

Figure 2.23: Comparison of CO_2 concentration profiles after 0.4HCPV CO_2 injection at 1000psi (left) and 3000psi (right) for a similar heterogeneous model whose properties are depicted in Table 2.8. Both profiles have been represented after similar volumes (HCPV) of CO_2 injection. Model properties have been described in Table 2.8.

Similarly, Figure 2.24 compares the onset CO_2 breakthrough in both models. It can be seen that in the high pressure model, CO_2 has broken through slightly earlier; CO_2 breakthrough occurs after 0.33HCPV and 0.41HCPV CO_2 injection in low and high pressure models.

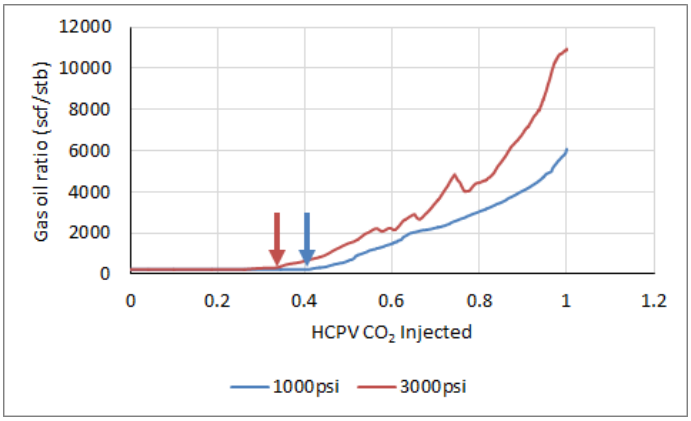

Figure 2.24: Gas oil ratio evolution comparison; comparison between flooding at 1000psi and 3000psi; arrows show the onset CO_2 breakthrough at respective pressures.

The results show that operating below MMP does not necessarily correlate to a significant loss of recovery proportional to those observed by slimtube simulations. That is why immiscible CO_2 floods, although they have lower recovery efficiencies, have been efficient at least in a number of CO_2 floods in the United States (Brock & Bryan 1989).

The behaviour observed in Figure 2.22 can, however, be slightly different, depending on the system temperature. Figure 2.25 compares the same behaviour at two different temperatures which could be representative of the North Sea (212°F) and the Permian Basin (113°F) provinces. As before, once pressure declines, the macroscopic sweep efficiency decreases for those pressures above MMP. However, the location of the minimum point can be better distinguished at lower reservoir temperature (blue data). This is because miscibility development and the balance between microscopic and macroscopic sweep efficiencies are more sensitive to pressure variation at lower temperatures as was discussed previously (Figure 2.8).

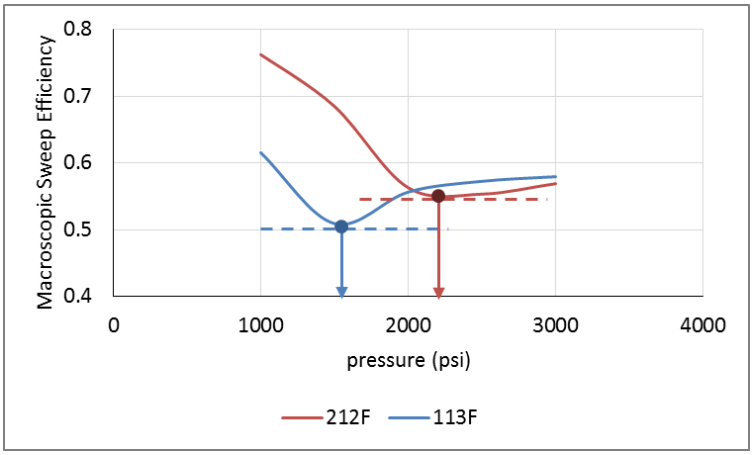

Figure 2.25: Evolution of macroscopic sweep efficiencies (E_{mac}) at two different reservoir temperatures

Figure 2.25 also shows that while for pressures above MMP, macroscopic sweep efficiencies are comparable between the two 212°F and 113°F temperature scenarios, at pressures below MMP, macroscopic sweep efficiency of the immiscible CO_2 flooding (at higher temperature of 212°F) is relatively higher. This can be explained by the fact that at lower flooding temperatures, since the flooding temperature is much closer to CO_2 critical temperature (88°F), the properties of CO_2 become extremely sensitive to pressure variations; in that CO_2 viscosity significantly drops by a relative pressure drop at lower temperatures, hence macroscopic sweep efficiency becomes significantly poorer. In fact, one great advantage for CO_2 flooding in the North Sea classes of reservoirs is the

relatively higher temperatures of these systems which are further away from the CO_2 critical point.

2.5 Impact of Pressure on the CO_2 Flooding Characteristics

From the discussions presented above, it can be concluded that in addition to microscopic sweep efficiency, pressure can also affect macroscopic sweep efficiency and thus the displacement stability by affecting the compositional interaction between oil and CO_2. In addition to compositional effects, pressure can also directly affect the macroscopic sweep efficiency by affecting the density and viscosity of CO_2.

This is because CO_2 properties are more sensitive to pressure variations than typical hydrocarbon gases. Figure 2.26 shows CO_2, methane and water densities at 212°F and at several different pressures; it can be seen that CO_2 is far more compressible than methane (William & Plisga 2011). Methane was depicted in this figure only for comparison as it is the first candidate gas for many tertiary EOR projects in the North Sea (Awan *et al.* 2008).

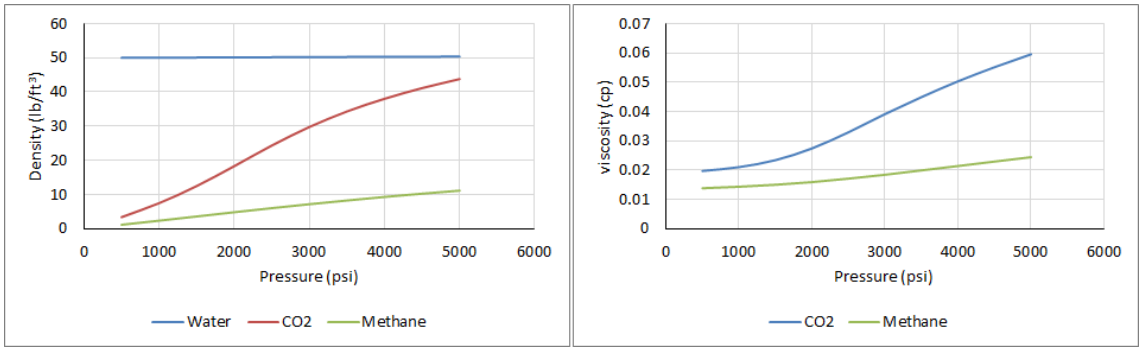

Figure 2.26: Left: CO_2, methane and water densities at 212°F. Right: Evolution of CO_2 and methane viscosities at 212°F. Data have been generated with Winprop (CMG-WinProp 2014.10).

Pressure can also affect the balance of gravity to viscous forces in a given CO_2 flood. To investigate this two CO_2 flooding simulations were conducted in an identical heterogeneous cross sectional model, but at two different pressures of 2000psi and 4500psi. Table 2.9 shows the cross sectional model parameters.

Figure 2.27 shows the CO_2 concentration profiles after injecting identical CO_2 volumes (0.4HCPV) in both models. It can be seen that at 2000psi the displacement is severely gravity dominated, while at 4500psi, gravity has been significantly supressed. Pressure

can also affect the stability of the CO_2 flood by improving the mobility of CO_2 as was discussed earlier (Figure 2.26-right).

Table 2.9: Model properties used in this section

Grid	256×1×64
Grid Dimensions	0.1ft × 0.1ft × 0.1ft
Dip angle	0
Average horizontal permeability	100mD
k_z/k_x	0.1
Porosity	0.2
Temperature	212°F
MMP	2400psi
λ_{xD}	0.02
λ_{zD}	0.1
V_{DP}	0.8
Fluid model	Table 2.1
Relative permeability model	Table 2.3

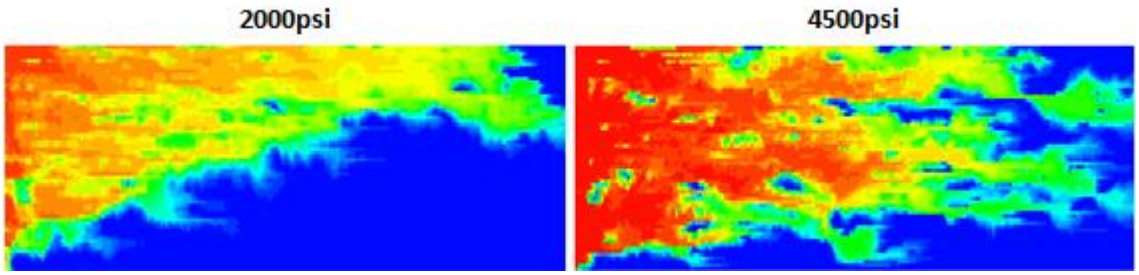

Figure 2.27: Comparison of CO_2 concentration profiles after 0.4HPCV CO_2 injection at two different flooding pressures of 2000psi (left) and 4500psi (right). The model properties have been depicted in Table 2.9.

2.6 Water Alternating Gas (WAG) Injection

CO_2 and water can be co-injected in different configurations and the choice depends on economics, injectivity and balancing oil response against cumulative oil recovery. In ***slug CO_2 injection,*** all the desired volume of CO_2 is injected as one single batch, while in ***WAG***, CO_2 and water are injected alternately. Because of the adverse mobility ratio between CO_2 and oil, the majority of CO_2 flooding projects in the Permian Basin have undertaken a variety of WAG. WAG also reduces net CO_2 utilisation which is important in the Permian Basin where CO_2 is a valuable commodity (Bellavance 1996, Brock & Bryan 1989). Exceptions of WAG applications are low permeability formations where co-injection of water and gas may reduce injectivity or in cases where macroscopic sweep without WAG is satisfactory.

WAG improves the ultimate oil recovery, at the cost of delaying the oil response. Figure 2.28 compares recovery factors in a heterogeneous areal model with and without WAG. The model parameters are similar to those depicted in Table 2.8 and the flood in both models are conducted at above MMP (3000psi). In both models, flooding initiates with injecting 1HCPV of water, followed by injecting 0.4HCPV CO_2 (single slug and WAG at 1:1 ratio) and then terminates by injecting another 1HCPV of water. It can be seen that the recovery has been improved by WAG, but the oil response has appeared later. Because of the slow oil response of WAG, different varieties of WAG such as SWAG (Simultaneous WAG), HWAG (Hybrid WAG) and TWAG (Tapered WAG) have been invented in the industry to balance the oil response versus ultimate oil recovery.

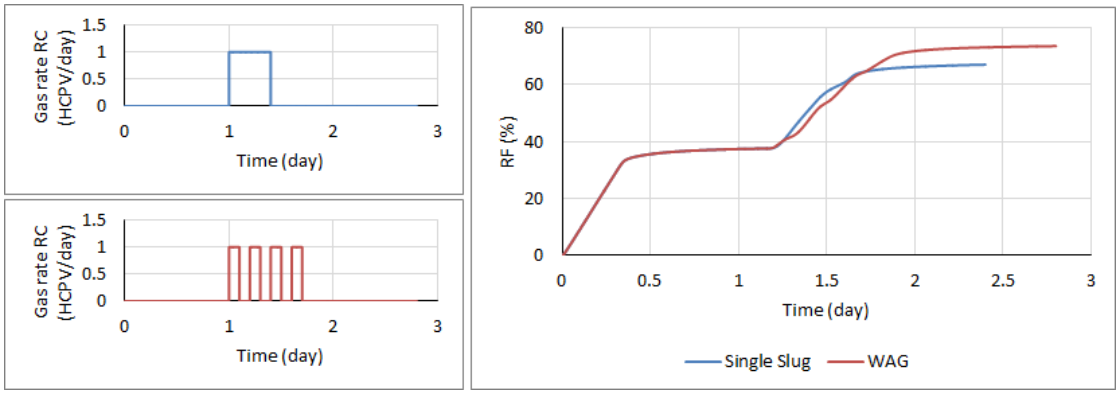

Figure 2.28: Comparison between WAG and single slug CO_2 injection in a 2D areal model; the same volume of CO_2 (0.4HCPV) has been injected in both models. The 2D model properties have been depicted in Table 2.8.

The WAG benefits are *scale dependent* in that at the ***microscopic scale***, recovery improves by increasing the cyclic nature of injected gas and water which consequently increases the three phase region (Fatemi & Sohrabi 2012, Skauge & Sorbie 2014). At the ***macroscopic scale***, recovery improves by the mobility improvement offered by co-injection of water and gas (Caudle & Dyes 1958).

2.6.1 The Benefit of WAG at Microscopic Scales

At microscopic scales, WAG is most effective, if the displacement is already immiscible and three distinct phases can be recognised. Once the displacement becomes miscible, oil and gas form a single hydrocarbon phase and the mechanism of oil recovery changes significantly (Skauge & Sorbie 2014).

To investigate this, the ultimate recovery factors for two CO_2 flooding processes i.e. CO_2-WAG and single slug CO_2 injections are compared at two different pressures in two (1D) core flood simulations. The core model parameters are similar to those depicted in Table 2.7. The two models are at 212°F. The injection strategy in either of the models are replicated at two different pressures; fully miscible (3000psi) and fully immiscible (1000psi). The flooding strategy is similar to the previous example in that 1HCPV waterflooding is conducted before and after CO_2 injection.

Figure 2.29 shows the results. It can be seen that the WAG relative improvement is very small for the miscible displacement scenario, while it is significant for the immiscible model. A miscible displacement, however, implies that the microscopic sweep efficiency is already good and can be hardly improved by WAG. The experimental result obtained by Fatemi *et al.*, however, suggests that WAG is still effective, even at around near miscible conditions (Fatemi & Sohrabi 2012).

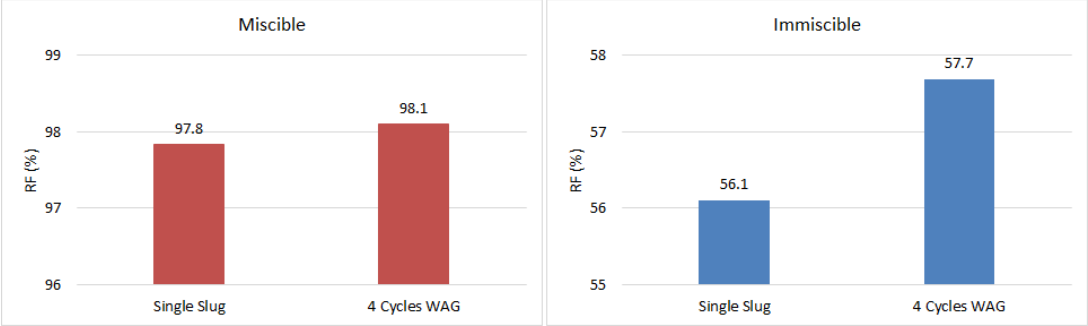

Figure 2.29: Comparison of single slug and WAG-CO_2 final recoveries in two core models at miscible and immiscible conditions. The 1D model properties have been depicted in Table 2.7.

2.6.2 Impact of WAG Ratio at Different Scales

WAG ratio mainly affects the degree of mobility corrections offered by WAG; the larger the WAG ratio, the better will be the ultimate recovery at the cost of slower oil response. Thus, the impact of WAG ratio can be best observed only at the macroscopic scale and not in the microscopic scale.

To investigate this, the impact of WAG ratio was compared in two different models-2D heterogeneous and 1D core flood-but under otherwise identical flooding strategies. The 2D heterogeneous model properties are the same as those depicted in Table 2.8. The 1D core flood model properties as similar to Table 2.7. The flooding strategy is the same in both models in that 1HCPV water is injected in both models followed by 0.4HCPV CO_2

injection (at different WAG ratios), and then terminated by another 1HCPV water injection. Figure 2.30 (left) compares the ultimate recovery factors at corresponding WAG ratios between 1D core flood and 2D heterogeneous models. It can be seen that while varying the WAG ratio affects the ultimate recovery factors in macroscopic (2D heterogeneous) models, its impact is negligible at the microscopic (core) scale.

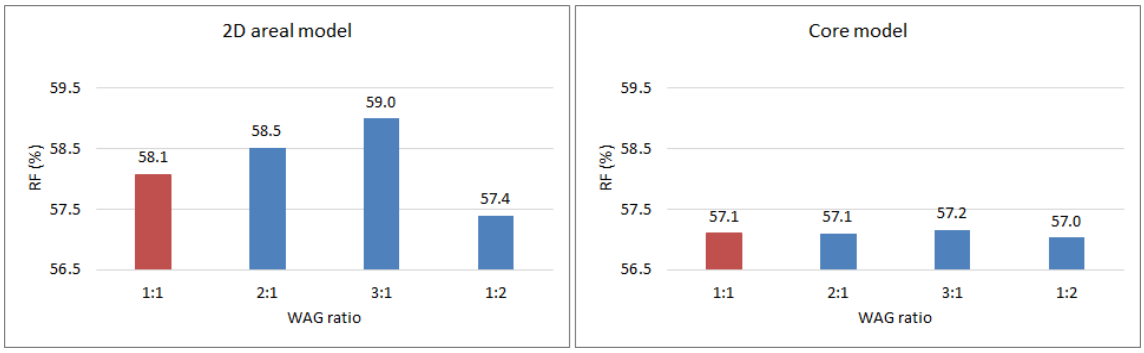

Figure 2.30: Impact of different WAG ratios; comparison at Macroscopic (2D model, left) and Microscopic (1D model right) scale impacts. The 2D and 1D model properties have been depicted in Table 2.8 and Table 2.7.

The optimum WAG ratio occurs at the gas and water saturations where the mobility of both phases becomes identical, hence the two phases can travel at the same velocity (Caudle & Dyes 1958). In practice, for the majority of CO_2 flooding projects, a WAG ratio of 1:1 has been the optimum WAG ratio (Christensen *et al*. 2001). With this set of relative permeability used in this study (Figure 2.1), the optimum WAG ratio is around 1:1.2-1:1.3. However, for the majority of WAG simulations conducted in this study a WAG ratio of 1:1 has been chosen accordingly.

2.6.3 Impact of the Number of WAG Cycles; Comparison between Miscible and Immiscible Scenarios

Increasing the number of WAG cycles (i.e. making each WAG cycle size smaller but injecting the same volume of CO_2), generally improves the ultimate recovery. However, this improvement reaches some asymptotic limit as the number of WAG cycles increases beyond a threshold limit. Nevertheless, this threshold could be different between miscible and immiscible displacement scenarios.

To investigate this, the relative benefit of increasing the number of WAG cycles were compared in an identical 2D areal heterogeneous model but between two miscible (4000psi) and immiscible (2000psi) scenarios. The heterogeneous model parameters are

similar to those depicted in Table 2.8. For each of the WAG scenarios, similar volumes of CO_2 have been injected, however, under different number of WAG cycles of 2, 10, 20 and 100. Figure 2.31 shows the results. It can be seen that in both scenarios, recovery progressively improves as the number of WAG cycles increases, though they reach asymptotic limit after a certain number of WAG cycles.

Increasing the number of cycles makes the duration and width of each gas cycle smaller accordingly. If the thickness of the gas cycle becomes smaller than the size of the transition zone, then the gas and oil ahead of it become fully mixed and the separation between gas and oil banks disappears.

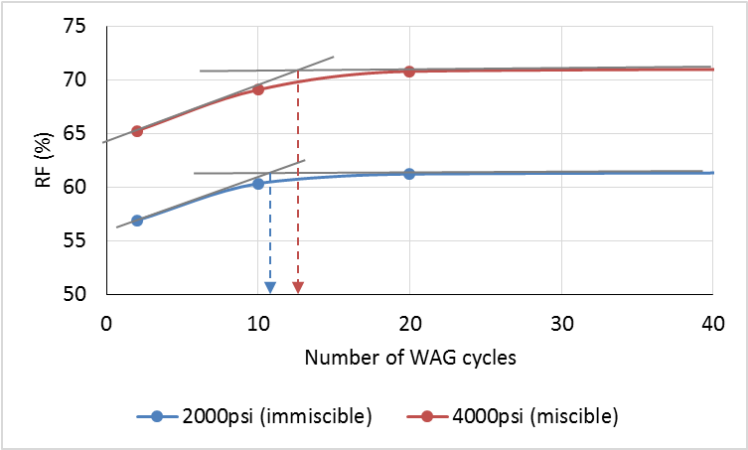

Figure 2.31: Impact of the number of WAG cycles on the cumulative final recovery; comparison between miscible and immiscible CO_2 flooding. The model properties have been depicted in Table 2.8.

The break over point (where the two tangents intersect) in Figure 2.31 may be correlated with the maximum number of WAG cycles after which decreasing the size of WAG cycle sizes does not further improve the recovery. Figure 2.31 shows that the location of the break over point is slightly shifted to the right for the miscible flooding scenario.

This indicates that smaller WAG cycle sizes (or larger number of WAG cycles) could still be effective for the miscible displacement scenario. This is because of a smaller transition zone which dominates the displacements in this flooding conditions as was discussed earlier (Section 2.4), hence smaller WAG cycle sizes can still be effective in this flooding scenario before mixing destroys the integrity of the gas bank.

2.6.4 Applying WAG to a Gravity Dominated Displacement

For WAG to offer mobility improvement and improve recovery by 3-phase effects, gas and water should travel *together* in that they should not segregate due to buoyancy. If the conditions are favourable for gravity domination (e.g. high formation permeabilities), then co-injection of gas and water may make the displacement significantly gravity dominated, in that water and gas may segregate and the benefit of WAG might become limited to only a small region around the injection well.

To investigate this, the CO_2-WAG performance was compared between two areal and cross sectional models, but with otherwise identical properties. The displacement in the cross sectional model is significantly gravity dominated, while the areal model is not affected by gravity. The 2D areal and cross sectional model properties are exactly identical to those depicted in Table 2.8 except that the orientations of the two models are different. The flooding strategy in both models initiates with injecting 1HCPV water, followed by injecting 0.4HCPV CO_2 which is alternated with gas under a 1:1 WAG ratio and finally terminates with injecting another 1HCPV water in each model.

Figure 2.32 compares the recovery factors between the two models. This figure shows that the performance of the gravity dominated (cross sectional) model is considerably poorer as water and gas segregate in this model and cannot flow together.

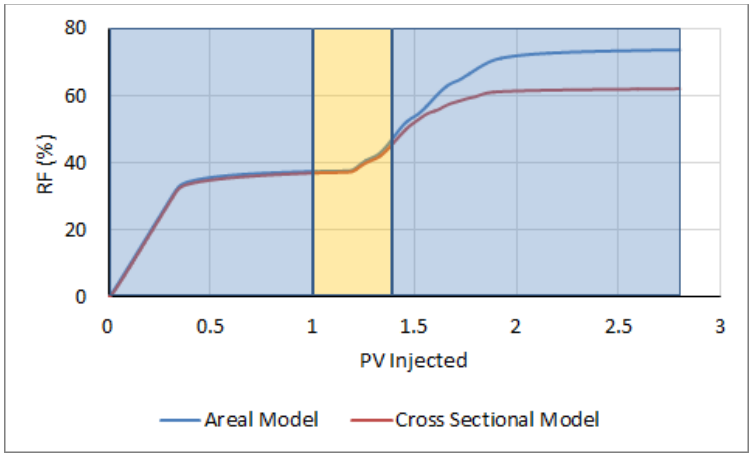

Figure 2.32: Impact of gravity on the WAG performance efficiency; comparing between areal and cross sectional models. Blue and yellow shades respectively represent water and CO_2-WAG injection periods.

An only 2-phase flooding, e.g. water-oil or CO_2-oil flooding may not be gravity dominated, however, once the third phase is introduced in the system, the flow pattern could become considerably gravity dominated because of gravity effects between any two particular phases (e.g. gas and water). For example, the initial waterflooding is not

gravity dominated in Figure 2.32 as the performances of waterflooding is identical between the two models, while the later CO_2-WAG injection is significantly gravity dominated. This is principally because of gravity effects between CO_2 and water which are now injected alternately after each other.

Another example may better illustrate this concept. In this next example, we compare the performance of two different CO_2 flooding processes to illustrate that gravity effects might become significantly limited, if CO_2 is injected in a medium previously not waterflooded. The comparison in this example is conducted in an identical 2D cross sectional *homogeneous* model. The models are homogeneous to better represent the gravity effects in the absence of other unstable flow patterns. The model properties are the same as the previous example except that the models are no longer heterogeneous. In the first flooding scenario, CO_2 is injected after an initial phase of waterflooding (i.e. tertiary CO_2 flooding), whereas, in the second scenario, there is no initial waterflooding and CO_2 is injected directly into the oil column (i.e. secondary CO_2 flooding). Figure 2.33 schematically illustrates the two flooding scenarios.

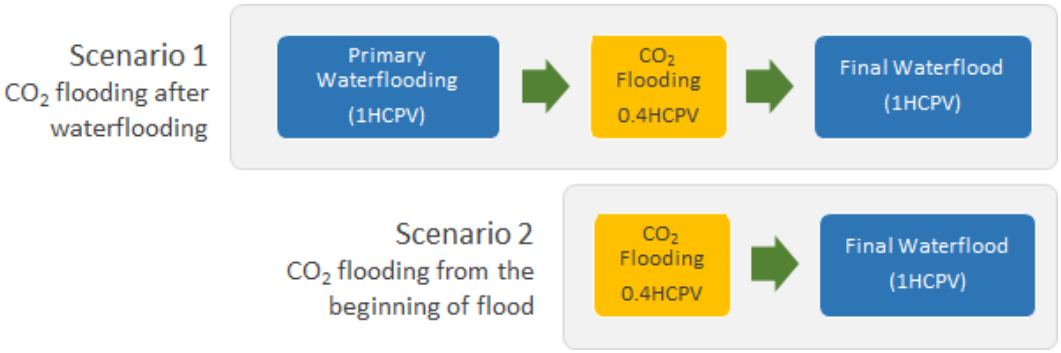

Figure 2.33: Schematic illustration of two different CO_2 flooding scenarios

Figure 2.34 shows the results. The left figure compares recovery factors between the two flooding scenarios. While more fluid (water and gas) has been injected in the first scenario (2.4HCPV), its final recovery is still lower than the second scenario, where less fluid has been injected (1.4HCPV). This indicates that CO_2 flooding in a system not previously waterflooded is significantly less gravity dominated than CO_2 flooding in an already waterflooded medium.

The right figure compares the average vertical CO_2 velocity between the two models upon CO_2 injection. Note that the onset of CO_2 injection is different between the two models. Therefore, two horizontal axis (top and bottom) have been shifted to match the onset of CO_2 injection in both models in this figure. Figure 2.34 (right) shows that the vertical

CO_2 velocity is considerably higher in Scenario 1, indicating a rapid segregation of CO_2 upon injection in the already waterflooded model. Nevertheless, once CO_2 segregates, and reaches the top of the models, it continues to flow horizontally, thus the average vertical velocities gradually decreases in both models.

This observation could be significant for CO_2 flooding in the North Sea classes of reservoirs, which are characterised by better reservoir and formation qualities than the Permian Basin reservoirs in the United States.

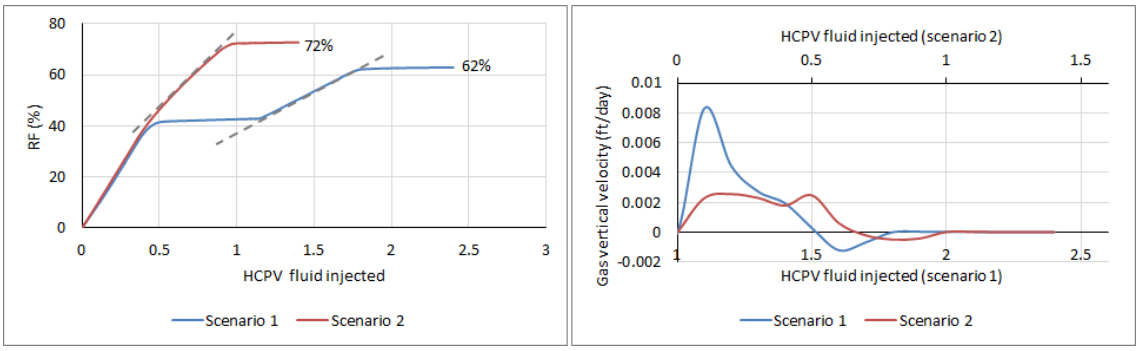

Figure 2.34: Left: Comparison of recovery factors between the above two scenarios. Right: Gas vertical velocity in both models.

2.7 Impact of CO_2 Solubility in Water on CO_2 Flooding

CO_2 is a soluble agent in water and its solubility is actually much higher than that of hydrocarbon gases. The dissolved CO_2 in water may become inaccessible for EOR and this may reduce displacement efficiency. Figure 2.35 compares equilibrium CO_2 and methane mole fraction in water at 212°F. It can be seen that even at very high pressures, equilibrium CO_2 mole fraction in water is less than 3% (mole percentage). This may indicate that changes of water properties as a result of CO_2 dissolution in water could be very negligible and can be ignored in the time scale over which EOR simulations are conducted. However, it could be important in storage driven simulations where the simulation time scale is orders of magnitudes larger than EOR (Ghanbari *et al.* 2006).

The impact of CO_2 solubility in water has rarely been taken into account in EOR oriented simulations conducted in the Permian Basin (Lin & Poole 1991, Pontious & Tham 1978, Winzinger *et al*. 1991, Mungan 1981). Warner reported that CO_2 solubility in water has a very limited impact on the properties of either water or CO_2 and also on the final CO_2 flood simulation results (Warner 1977).

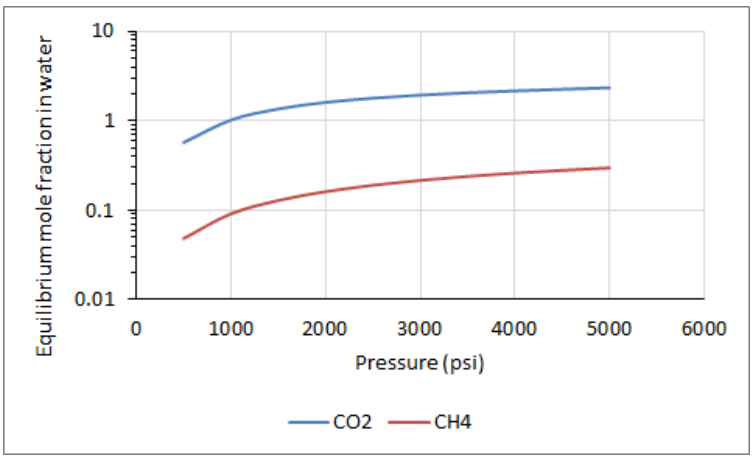

Figure 2.35: CO_2 and methane equilibrium mole fraction in water at 212°F Data are generated with WinProp (CMG-WinProp 2014.10)

Figure 2.36 compares two WAG simulation in an identical permeability model with and without considering CO_2 solubility in water. The model properties are similar to those depicted in Table 2.8. The flooding strategy is identical for the two models in that the CO_2-WAG phase is preceded and followed by two phases of 1HCPV water injection. For the CO_2-WAG phase, a total of 0.4HCPV CO_2 has been injected in any of the models in four equal cycles and under 1:1 WAG ratio.

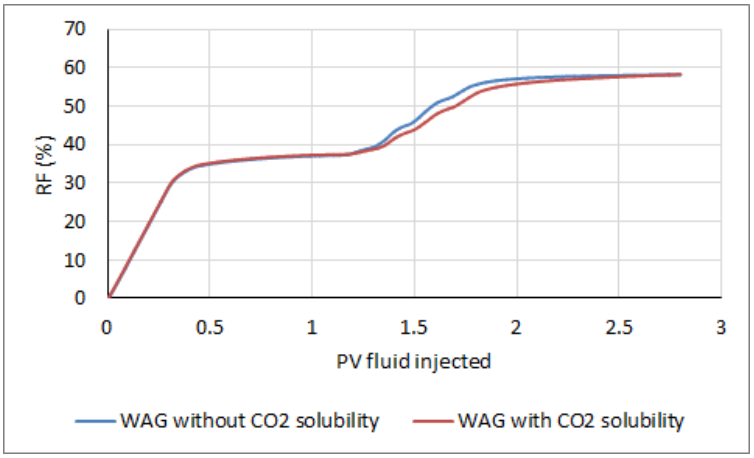

Figure 2.36: Comparison of WAG performance with and without CO_2 solubility in water. The model properties are similar have been depicted in Table 2.8.

Figure 2.36 shows that although during each WAG cycle, recovery is slightly lower for the solubility enabled model, the final recoveries are almost identical for both models. During each WAG cycle, CO_2 solubility makes a fraction of CO_2 inaccessible for EOR by dissolving it into the injected and connate waters. However, once the final waterflood is initiated, injected water dissolves the immobile (trapped) CO_2 and transports it to other regions of the model which consequently can recover some additional oil.

Figure 2.37 shows CO_2 concentration profiles at the end of simulations. This figure shows that the CO_2 that should otherwise be trapped by hysteresis, becomes dissolved particularly from around the injector and is transported deep within the model. This is not certainly favourable in terms of the security of storage.

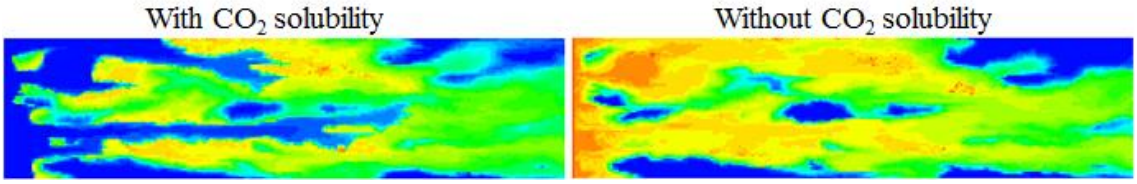

Figure 2.37: CO_2 concentration profiles at the end of the simulations with and without CO_2 solubility in water. The model properties are similar to those described in Table 2.8.

Figure 2.38 shows (CO_2) gas saturation within each model during simulation. It can be seen that the total gas saturation is always smaller in the model with CO_2 solubility in water. Additionally, gas saturation gradually decreases during final waterflood, which means that immobile trapped CO_2 dissolves into the injected water and is produced. This is an important consideration in scenarios where retention of CO_2 within a geologic complex is important; e.g. combined EOR and storage CO_2 flooding which is the likely CO_2 flooding scenario in offshore provinces. These result show that while CO_2 dissolution in water does not significantly affect the EOR prediction of the model, it significantly affects the storage response of the model.

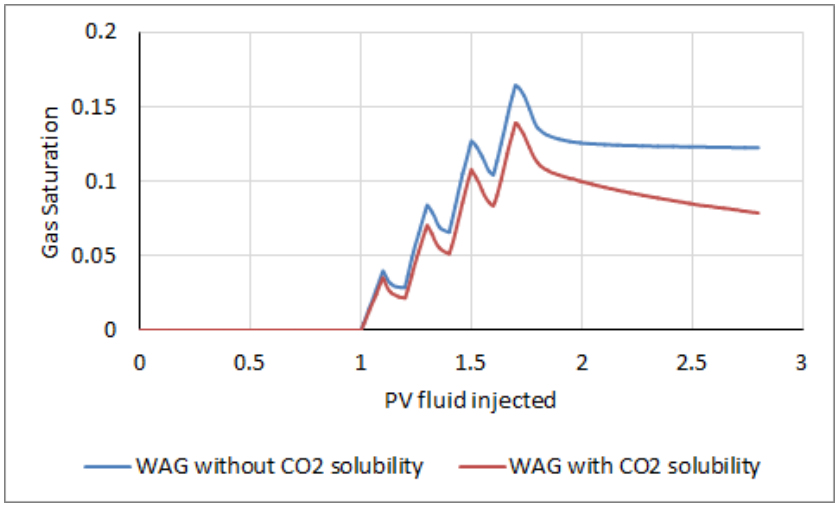

Figure 2.38: Average gas saturation during simulations, with and without CO_2 solubility in water.

2.8 Closing Remarks

In this chapter, a few CO_2 flooding characteristics were revisited with a modelling study. Some of these features will be pertinent for the comparative study that will be undertaken in the next chapters (3-5). The final highlights from this chapter are:

- Miscibility development is sensitive to pressure. However, the onset development/impairment of miscibility is more sensitive to pressure at lower temperatures than at higher temperatures. This indicates that a few hundred psi pressure drop below MMP may have different impacts on the CO_2 flooding efficiency depending on the system temperature. It will be shown in Chapter 3, that the North Sea and the Permian Basin classes of reservoirs are characterised with significantly different reservoir temperatures.
- Phase behaviour can affect the injectivity response of the system. It was shown that the injectivity response of the system could become better or poorer depending on the miscibility status of the displacement.
- In a near miscible process, dispersion can affect the composition path, injectivity response of the system and both microscopic and macroscopic sweep efficiencies. A higher level of dispersion may make an already miscible process, completely immiscible by pushing the composition path further into the two-phase region.
- Phase behaviour can also affect the balance between microscopic and macroscopic sweep efficiencies of CO_2 flood at around MMP.
- While macroscopic sweep efficiencies of *miscible* CO_2 flooding at both low and high temperatures are relatively comparable (Figure 2.25), macroscopic sweep efficiency of an *immiscible* CO_2 flooding is relatively higher at higher temperatures.
- In addition to compositional effects and microscopic sweep efficiency, pressure can also affect CO_2 properties. Thus, pressure is an important factor in adjusting the macroscopic sweep efficiency. Flooding at higher pressures better reduces the significance of gravity. It will be shown in Chapter 3 that pressure may have a considerable impact on the significance of gravity in the North Sea classes of reservoirs characterised with better formation permeabilities.
- While varying the size of WAG cycles affects both microscopic and macroscopic sweep efficiencies, the impact of WAG ratio is only limited to macroscopic scales.

- Smaller WAG cycles sizes can be more effective for a miscible process than for an immiscible one. This is due to a smaller transition zone that prevails in the displacements in miscible conditions.
- Gravity has a detrimental impact on the performance of WAG, should it trigger segregation of water and CO_2 due to buoyancy and not allow them to flow together. Due to gravitational effects, injection of CO_2-WAG into reservoirs that not previously waterflooded yields higher recoveries than into waterflooded reservoirs. It will be shown in the next chapter that due to higher formation permeabilities in the North Sea classes of reservoirs, WAG may not have the same benefit as in the low permeability onshore United States CO_2 flooded reservoirs.
- While the effect of CO_2 solubility in water may be negligible in terms of EOR, it could be significant in terms of (CO_2) storage and the ultimate fate of CO_2. Consequently, CO_2 dissolution in water will be taken into account for all the simulation studies which will be conducted in Chapters 3 and 5.

Chapter 3 Correlating Different Aspects of CO_2 Flooding between North Sea and Permian Basin Provinces

3.1 Introduction

CO_2 flooding is an established and mature EOR technology in the Permian Basin of the United States which has shown promising results in this province. On the other hand, North Sea reservoirs are rapidly maturing and the opportunity for application of EOR techniques is time limited. CO_2-EOR has been considered in a number of projects in the North Sea (Fayers *et al*. 1981, Awan *et al*. 2008); however, there have been no actual CO_2 flooding applications yet. This is primarily because no secure long term source of CO_2 is available in this province (Jensen *et al*. 2000). CO_2-EOR offers several advantages in those reservoirs located offshore compared to those onshore as offshore reservoirs are often bigger and the EOR target is more significant. These reservoirs are also better sites for CO_2 storage as they are extensive and away from human communities.

Although there is no purely EOR driven CO_2 flooding taking place in the North Sea, a number of CO_2 storage projects in this province suggest that a CO_2 supply is likely to become available as part of different storage programmes with subsequent EOR opportunities arising. In fact, CO_2 storage projects such as Sleipner, Snøhvit and Goldeneye (Gluyas & Mathias 2013) illustrate that in future CO_2 may become increasingly available in the North Sea and can be used for EOR as well. While CO_2-EOR is an established EOR technology in many onshore provinces, including the United States, it is relatively new in the North Sea and its EOR performance and process design might be different compared to other mature provinces.

CO_2-EOR in the Permian Basin benefits from favourable reservoir conditions coupled with the flexibility and ease of operation, characteristics of onshore systems. This, coupled with the availability and flexibility of CO_2 supply, makes CO_2-EOR an ideal EOR choice in this province.

In the North Sea, reservoirs are, however, of larger size, deeper, of different reservoir qualities and are at different ambient conditions compared to Permian Basin reservoirs. Moreover, the development and operation concept in this province could be different as a result of characteristics of offshore systems. The motivation for CO_2 flooding is also likely to be different in this province. In the North Sea, CO_2 is expected to be supplied

as part of a CCS program with a different driving force compared to the pure EOR CO_2 supply in the Permian Basin. The combination of the above factors suggests that the likely CO_2-EOR performance characteristics in the North Sea reservoirs might be different from those observed in other onshore provinces such as in the United States.

Previous authors have investigated possible application of CO_2 for EOR purposes in the North Sea group of reservoirs. Goodyear *et al.* (2003) provide a review of the subsurface issues for CO_2 flooding for UKCS[7] reservoirs. They reviewed possible specific CO_2 flooding characteristics in the North Sea province compared to the US, and conclude that CO_2 injection is far more complex than HC (hydrocarbon) gas injection from a subsurface point of view in the North Sea. This is mainly because CO_2 and reservoir fluid phase behaviour is more complex when compared with typical hydrocarbon systems. Bath (1987) also provides a review of the potential EOR candidates in the North Sea. He rejects the application of CO_2 in the North Sea due to its high compressibility and because the density difference with reservoir oil might be prohibitive for any gravity stable process design, which is a common practice in the North Sea. Fayers *et al.* also provide a review of the potential application of CO_2 as an EOR process in the North Sea reservoirs (Fayers *et al.* 1981). They identified some key differences between the North Sea and US land-based reservoirs; North Sea reservoirs are at higher pressure and temperature compared to onshore CO_2 flooded reservoirs; the oil viscosity is also relatively lower offshore North Sea; moreover, oils are of better quality with a considerable C_2-C_5 fractions, which allows effective miscibility development.

Having said that, this study tries to compare the likely performance of CO_2 flooding in the offshore North Sea province with that observed in the United States assuming CO_2 availability is not an issue. Therefore, in the first part of this study, important elements that affect CO_2-EOR performance between these two provinces are identified and compared. This comparison requires each province being correctly characterised. We review the status of EOR activities in these two provinces. Later the ambient reservoir conditions and fluid properties in the North Sea are assessed regarding suitability for CO_2-EOR by comparing them with proposed screening criteria available in the literature. In the second part of this study, the results of two modelling studies will be presented. The first modelling study compares the CO_2 flooding performances between two cross sectional box models having broadly average reservoir and fluid properties taken from

[7] United Kingdom Continental Shelf

the results of the initial field surveys. Additional sensitivity analysis will be conducted as well for each reservoir scenario. The second modelling study compares CO_2 flooding performance in an identical geological structure, having average North Sea and Permian Basin reservoir fluid and properties.

It is important to note that this study only investigates the subsurface CO_2-EOR issues between the two provinces from an engineering point of view; issues relating to surface facilities and economics are not within the scope of this consideration.

3.2 A Review of the EOR Status in the two Provinces

The status of CO_2-EOR in the United States has been reviewed by various authors (Brock & Bryan 1989, Grigg & Schechter 1997, Stalkup 1978, Hadlow 1992). In the United States because of rising oil prices and the decline in the US domestic oil production between 1973 and 2010, an intense interest in the application of EOR methods such as CO_2-EOR was created (Stalkup 1978). The EOR driven nature of CO_2 application coupled with the favourable reservoir conditions in the US helped significantly toward the widespread application of this technology in the US. The main areas for CO_2-EOR activity have been the Permian Basin in West Texas and New Mexico (Hadlow 1992). CO_2 flooding in the United States has been applied to different types of formation lithologies (Brock & Bryan 1989) and its application generally has resulted in gross and net CO_2 utilisation efficiencies of around 7Mscf/bbl and 3-7Mscf/bbl respectively, (Stalkup 1978); nevertheless, there have been cases with much higher utilisation efficiencies. Since CO_2 has been considered as a valuable commodity in this province, efforts were made by operators to ensure the optimum use of injected CO_2, including pattern realignment or drilling new infill wells to reduce well spacing and sometimes change the wells pattern (Hadlow 1992). In this province, CO_2-EOR has increased recovery factors by 8-14% (Hadlow 1992). Both secondary and tertiary CO_2 floods have been undertaken, though the majority of them have been tertiary floods. The majority of projects have CO_2 slug sizes between 15-30%PV. Most projects experience CO_2 breakthrough after 0.05-0.2PV of the total fluid injection and breakthrough occurs shortly after or coincident with the tertiary oil response (Stalkup 1978).

On the other hand, hydrocarbon gas injection is a mature EOR technology in many offshore provinces, including the North Sea (Awan *et al*. 2008). In the North Sea,

Hydrocarbon (HC) gas injection, either WAG or gravity stable, has been used for almost 40 years and is considered very mature (Awan *et al*. 2008). The injected gas in the North Sea is a mixture of different hydrocarbon gases sourced from either the same field (e.g. South Brae) or nearby fields (e.g. Magnus) or imported from another location (e.g. Ula). Unlike the Permian Basin, in the North Sea, HC availability is good, both in terms of sources and transportation infrastructure.

In the North Sea, because of favourable water-oil mobility ratios, efficient oil recovery by waterflooding has generally been the case; however, the target for EOR is still significant as reservoir sizes are large (Fayers *et al*. 1981). The gas injection efficiency in the North Sea varies from 1.3 to 7.6 Mscf/bbl; similarly, the incremental oil recovery also varies from 3 to 12% in this province (Awan *et al*. 2008).

As an example, in South Brae the calculated gas utilisation efficiency (gross) has been 8.7 Mscf/bbl (Jethwa *et al*. 2000). In the Magnus field, the net and gross gas utilisation efficiencies have been 3.5 and 9.7 Mscf/bbl, respectively (Zhang *et al*. 2013). In the Ula field in the North Sea, the incremental oil recovery has also been 8-10% (Erbas *et al*. 2014). These results show that the EOR performance between the two provinces, although not identical, is somewhat similar.

Although there is no actual CO_2 flooding in the North Sea, CO_2 has also been considered in some EOR studies (Halil, *et al*. 2002, Jensen *et al*. 2000, Agustsson & Grinestaff 2004, Mathiassen 2003). In the Forties field, CO_2-EOR was considered to be the best option, capable of yielding 4.7% of STOOIP. However, the lack of CO_2 sources, costly surface facilities modification and the nature of the project fiscal regime were recognised as the main barriers for CO_2 application. A separate study summarises the results of likely CO_2 flooding performances in the above fields (Mathiassen 2003). It suggests that CO_2-EOR incremental recoveries vary between 4-8% in those above mentioned fields, slightly lower than in the Permian Basin; though it is not conclusive. Another study investigated possible CO_2-EOR recovery performance in both fluvial and shallow marine reservoir types in the North Sea for a wide range of model input parameters. They conclude that incremental recovery in shallow marine type reservoirs is slightly better than in fluvial type reservoirs under both continuous and WAG CO_2 injection strategies (Akervoll & Bergmo 2010).

The designs of the EOR projects in the two provinces have also been affected by their respective motivations as well. CO_2 flooding in the United States has been purely driven

by EOR, which means that both the oil quantities and relative oil production response are equally important. In this province, horizontal flooding is very popular as it generates a favourable EOR response and hence there are very few gravity stable projects; however, formation characteristics are better suited for horizontal flooding (low vertical permeability in the majority of reservoirs). Gravity stable CO_2 flooding is not an attractive option in the Permian Basin (Brock & Bryan 1989). On the other hands offshore North Sea, a considerable portion of projects are designed as gravity stable EOR projects. The need to store the produced HC gas which sometimes has little marketing opportunity, coupled with good structural dip and good vertical permeability in many North Sea reservoirs, makes gravity stable EOR design an ideal process in the North Sea. Hence many EOR projects in the North Sea serve dual purposes; they are both EOR and storage (HC gas) projects (Awan *et al*. 2008). Likewise, a gravity stable design is also expected to be a favourable option for CO_2 flooding in the North Sea by which both EOR and storage are maximised if economics permit.

3.3 Revisiting the Screening Criteria for CO_2 Flooding

The first step before bringing CO_2 to a new field or province is to check the fluid and reservoir conditions against screening criteria developed for CO_2 application. Different screening criteria have been suggested for CO_2-EOR application in the literature (Goodrich 1980, Taber *et al*. 1997). Table 3.1 highlights the major points of Tarbet *et al*. (1997) screening criteria for CO_2 flooding in a given new reservoir.

Table 3.1: Summary of the screening criteria suggested by Tarbet et.al (1997) for CO_2-EOR application

Parameter	Applicable range
Oil API	>22 º
μ_o	< 10.0cP
S_{orw}	>20%
Formation lithology	sandstone or carbonate
Formation thickness	wide range
Formation depth	>2500ft
Reservoir temperature	not important
Formation permeability	not important
Fluid composition	high percentage of C_5-C_{12}

A review of the literature, which will be introduced later, suggests that all the above criteria effectively prevail in the North Sea province (Awan *et al*. 2008, Jensen *et al*.

2000) and there is no limitation for applying CO_2-EOR in the North Sea from a reservoir engineering point of view. Oils are of good quality with a considerable C_2-C_5 fraction, are present to allow miscibility development. Oil viscosities are also far below 10cP in the North Sea.

3.4 Impact of Development Characteristic on the in-situ Fluid Velocities

The sizes of the EOR candidates are relatively larger in the North Sea province; i.e. only those medium to large scale reservoirs are suitable candidates for EOR deployments; at least in the initial stages of CO_2 flooding in this province, similar to the experience observed in the United States. This is because developments and operations in offshore provinces are usually more expensive and the same is expected to be relevant during CO_2 injection. Figure 3.1 compares the STOIIP between various fields in both provinces.

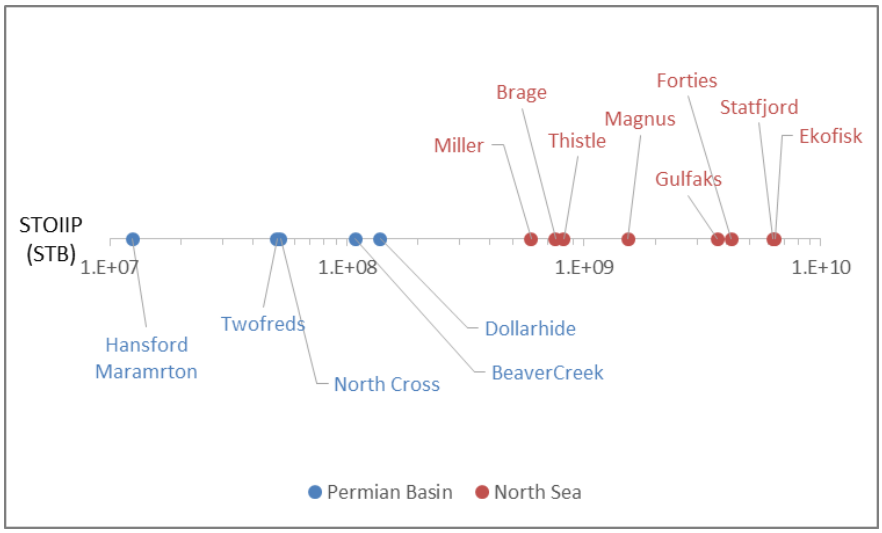

Figure 3.1: Comparison of STOOIP between various reservoirs in the North Sea and in the Permian Basin

Bigger reservoirs coupled with more expensive drilling in the North Sea makes well spacing larger in this province. Unlike the Permian Basin, a single injector or producer in the North Sea should target a larger area of the reservoir. In the North Sea, reservoirs are also deeper (Figure 3.4), which makes drilling even more expensive. While 10, 20 and 40 acres well spacing is common practice in the Permian Basin, the pattern areas in the North Sea are in the order of 200-400 acres (Bath 1987) and consequently well spacing in the order of 0.5-1.5km can be observed (Fayers *et al*. 1981). Table 3.2 shows well spacing for a number of reservoirs in the Permian Basin.

On the other hand, while in the Permian Basin wells are positioned based on regular patterns (i.e. 5-spot, 9-spor or inverted 9-spot), in the North Sea wells are mostly placed as line drive creating a peripheral flood or are placed by geological considerations (Awan *et al*. 2008).

Table 3.2: Well spacing examples in the Permian Basin

Field	**Well spacing (*acres*)**	**Reference**
Mattoon	10	(Sim *et al*. 1994)
Dollarhide	40	(Wang & Robertson 1998)
Hanford	20	(Merritt & Groce 1992)
Sharon Ridge	40	(Brinkman *et al*. 1999)
Twofreds	40	(Kirkpatrick *et al*. 1985)
Means San Andres	10, 20 and 40	(Stiles & Magruder 1992)
North Cross	22 to 40	(Aryana *et al*. 2014)

Fewer wells per acre in the North Sea means that under the same rates of depletion, *rates per well* are higher. However, apart from individual well rates; the average rates of reservoir depletion are also higher in this province compared to the Permian Basin. This is because the operational costs are significant and higher rates of depletion are required to keep the project economics viable (Stewart 1997). North Sea reservoirs are sometimes depleted even beyond their MER[8] limits and it is common in this province to produce up to 10% of the reserves per annum (Stewart 1997). The case of the Gullfaks field is an example where the operator was forced to reduce the production rate, possibly to keep it within MER limits (Petterson *et al*. 1990). Moreover, fields in the North Sea are awarded based on a licensing scheme which is valid for only a certain period of time, while in the Permian Basin mineral actual rights are transferrable; these force the operators in the North Sea to increase the depletion rates even further. Figure 3.2 compares the rate of depletion in a number of the North Sea and the Permian Basin reservoirs[9].

The combination of the higher rate of depletion and larger spacing between wells in the North Sea makes the *in-situ* fluid velocities relatively higher in this province compared to the Permian Basin.

[8] Maximum Efficient Rate; MER also used to refer to Maximum Economic Recovery.
[9] Rate of depletion have been approximated by dividing the total annual production at *plateau* rate over original oil in place (OIIP).

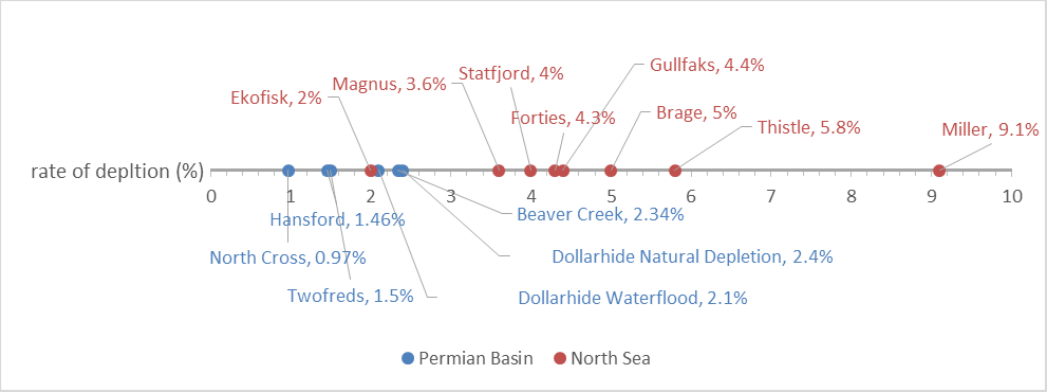

Figure 3.2: Percentage of STOIIP produced annually in various North Sea and Permian Basin reservoirs

3.4.1 The Impact of Cold Sea Water Injection on the Performance of CO_2 Flooding in the North Sea

Unlike the Permian Basin where the source of water is from local supplies (e.g. the Hansford field) or deeper horizons (e.g. the Salt creek field), in the North Sea, the natural source of water is the sea water with a relatively low temperature (43ºF to 63ºF depending on the season). A prolonged cold sea waterflooding causes a region of low temperature to be developed around the injection well which then propagates within the reservoir. The temperature front usually propagates at 1/3 the velocity of the saturation front (Stewart 2011). This means that by the time that EOR initiates, usually more than 1/3 of reservoir volume have lower than initial reservoir temperature. Although lower temperatures may have positive effects in terms of improving CO_2 miscibility development (Goodyear *et al*. 2003), it may have a few adverse unwanted consequences.

First, it increases the risk of multiphase hydrocarbon formation and alternate injectivity impairment. Formation of multiphase hydrocarbon phases upon CO_2 flooding has been observed in a few Permian Basin reservoirs (Khan *et al*. 1992). In fact several West Texas crudes separate into three hydrocarbon phases at CO_2 concentrations above 55% and pressure ranging from 900 to 1300psi. In the Permian Basin, this phenomenon mostly occurs when the reservoir temperatures are low, i.e. around 120ºF or lower. In the North Sea, original reservoir temperatures are, however, higher (165ºF to 266ºF) and at first, this phenomenon is not expected to occur in this province.

Second, the formation of a low temperature region around injectors in the North Sea may also trigger the possibility of CO_2 hydrate formation as a result of direct contact between CO_2 and cold water. Hydrate formation was also observed in the Ekofisk field during pilot hydrocarbon injection and is believed to be the cause of abrupt injectivity reduction

in this field (Jensen *et al*. 2000). This, however, requires further investigation regarding the PVT properties of the North Sea reservoir fluids within the expected range of temperatures in the North Sea; similar to those investigations carried out for the Permian Basin in the United States (Metcalfe *et al*. 1979).

Finally, creation of micro-fractures upon cold sea water injection has had a significant impact regarding better than expected water injectivities in the North Sea (Guan *et al*. 2006). Recycling hot CO_2 (effluent CO_2 from recycling compressors are expected to be hot) may close these micro fractures during CO_2 flooding, leading to possible injectivity impairment during CO_2 flooding (SHARP Reports 2001).

3.5 Prevailing Reservoir Conditions; A Comparison between the two Provinces

The ambient reservoir condition is mostly a function of the province in which a given group of reservoirs is located. Whilst the Permian Basin reservoirs are characterised by low reservoir temperatures and pressures, North Sea reservoirs are at both higher pressures and temperatures. Figure 3.3 compares the relative ambient pressure and temperatures for the two provinces.

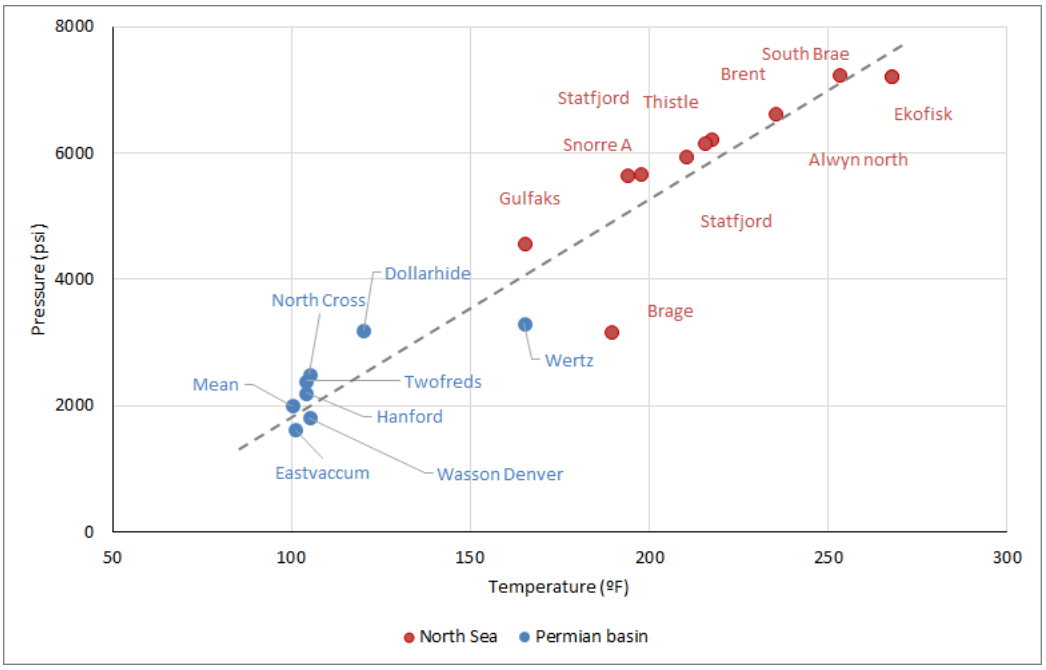

Figure 3.3: Cross plot of pressure vs. temperature in a number of offshore North Sea and onshore Permian Basin reservoirs (Brock & Bryan 1989, Awan et al. 2008).

Although there is a significant contrast between the ambient reservoir conditions in the two provinces, CO_2 properties are still similar between them as will be shown later. Figure 3.4 and Figure 3.5 compare reservoir depths and thicknesses between the two groups of reservoirs. Pays are generally thicker in the North Sea and reservoirs are also deeper in this province. It can be seen in Figure 3.4 that the two provinces are located on slightly different temperature gradients.

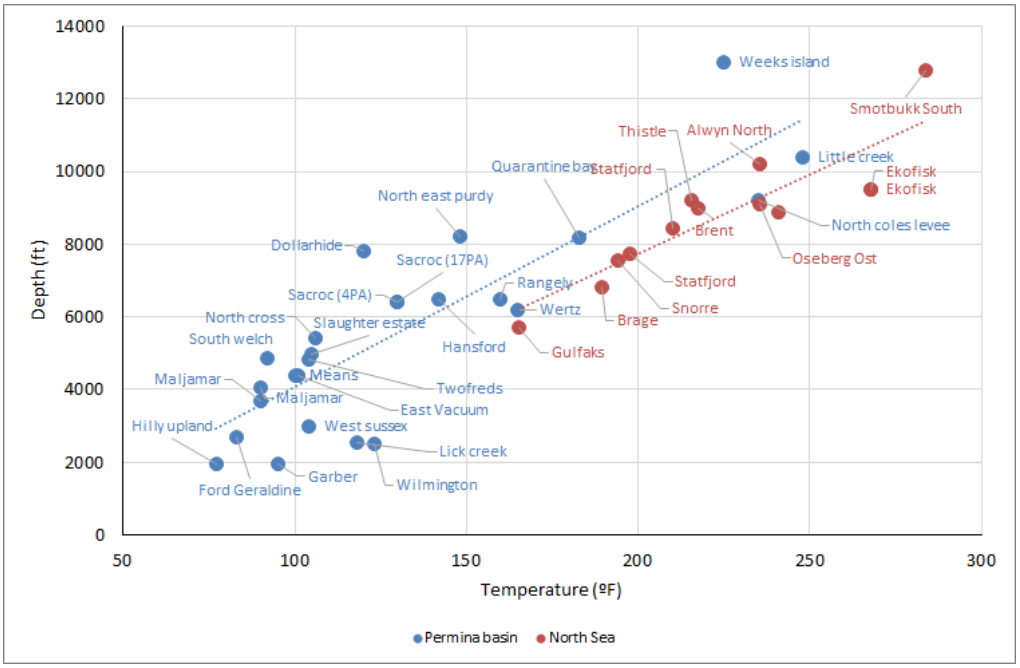

Figure 3.4: Comparison between reservoir depths in the two provinces (Brock & Bryan 1989, Awan et al. 2008).

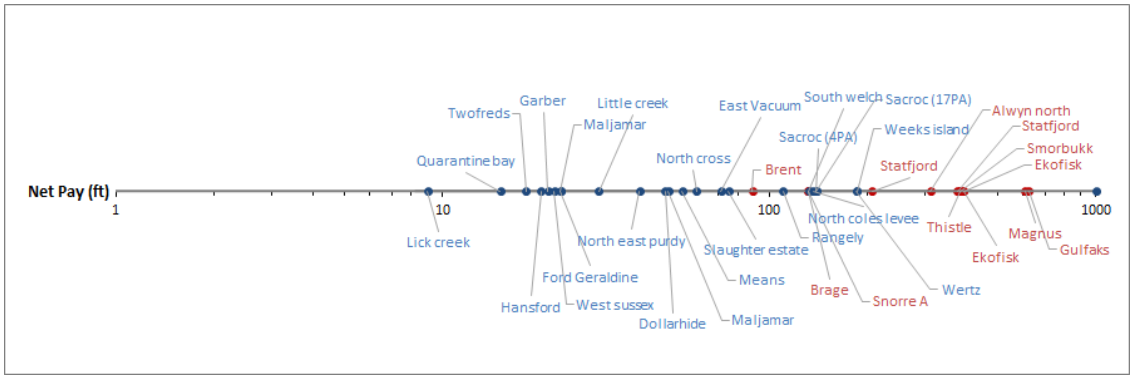

Figure 3.5: Comparison between pay thicknesses in the two provinces (Brock & Bryan 1989, Awan et al. 2008).

The depth at which the two groups of reservoirs are located is important and has consequences in terms of applicability of CO_2-EOR process. Figure 3.6 shows the window between fracturing and miscibility pressure in Permian Basin reservoirs (Taber *et al*. 1997). Although this figure has been derived with Permian Basin data, the concept is still relevant in other provinces such as the North Sea. It shows that, the deeper the

formation, the wider will be the opportunity to carry out a miscible flood. In fact, a number of reservoirs in the US (e.g. Salt Creek field) are flooded immiscibly with CO_2 because they are not located deep enough to tolerate high injection pressures and the miscibility pressure is higher than the fracturing pressure. Since North Sea reservoirs are generally deep, this is not expected to be an issue in these groups of reservoirs and the window between fracturing and miscibility pressure is expected to be wide enough for miscibility to be attained.

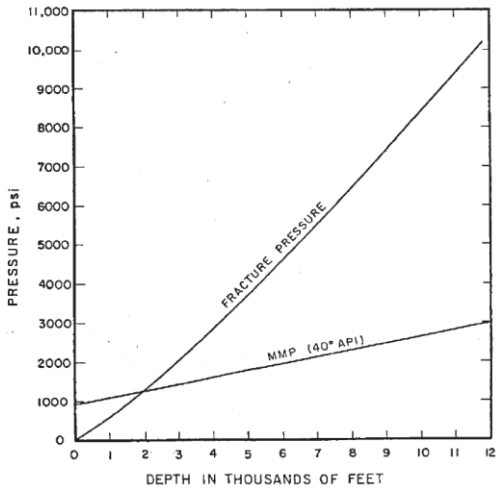

Figure 3.6: Window between CO_2 MMP and fracture pressure as a function of depth (Taber et al. 1997)

In terms of formation properties, there is a large contrast between the two groups of reservoirs. Most of the CO_2 flooded reservoirs in the US have permeabilities in the range of 10-100mD, while reservoirs qualities are much better in the North Sea by an order of magnitude. In fact permeabilities in the order of 1000mD are common in the North Sea (Brock & Bryan 1989, Awan *et al*. 2008). This may favour a gravity dominated flow during CO_2 injection in those fields.

3.6 Fluids Characteristics and Miscibility Development; Comparison between the two Provinces

3.6.1 Oil Properties

Both provinces benefit from relatively good oil qualities which are favourable for miscibility development. Figure 3.7 compares oil API's for several reservoirs in the two provinces.

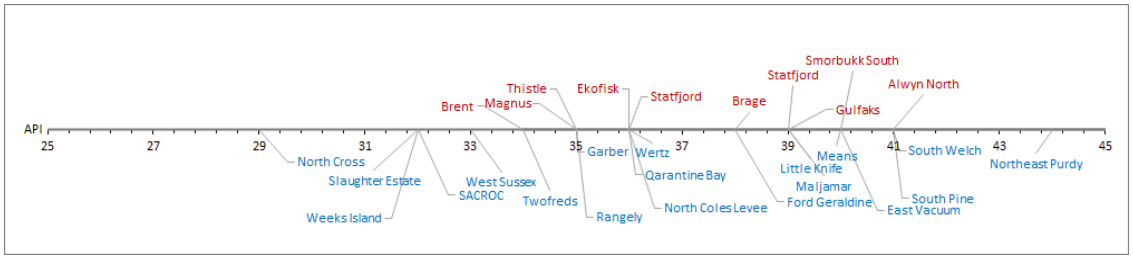

Figure 3.7: **Comparison of crude API's, offshore North Sea vs. onshore US Permian Basin**

Reported oil API's for CO_2-EOR projects in the Permian Basin range between 28 and 32 (Brock & Bryan 1989) while North Sea crudes have APIs between 34 and 42 (Awan, *et al*. 2008). These data suggest that oil qualities in the North Sea are as good as the Permian Basin for possible miscible CO_2 flooding.

While oil qualities are similar in the two provinces, there is a contrast between oil viscosities. Figure 3.8 shows a cross plot of oil viscosity versus reservoir temperature. Many North Sea reservoirs contain oil of low viscosity which ensures a more favourable mobility ratio upon both gas and water flooding. In fact, this has been one of the main reasons for efficient water flood recoveries (40-55%) observed so far in the North Sea (Bath 1987).

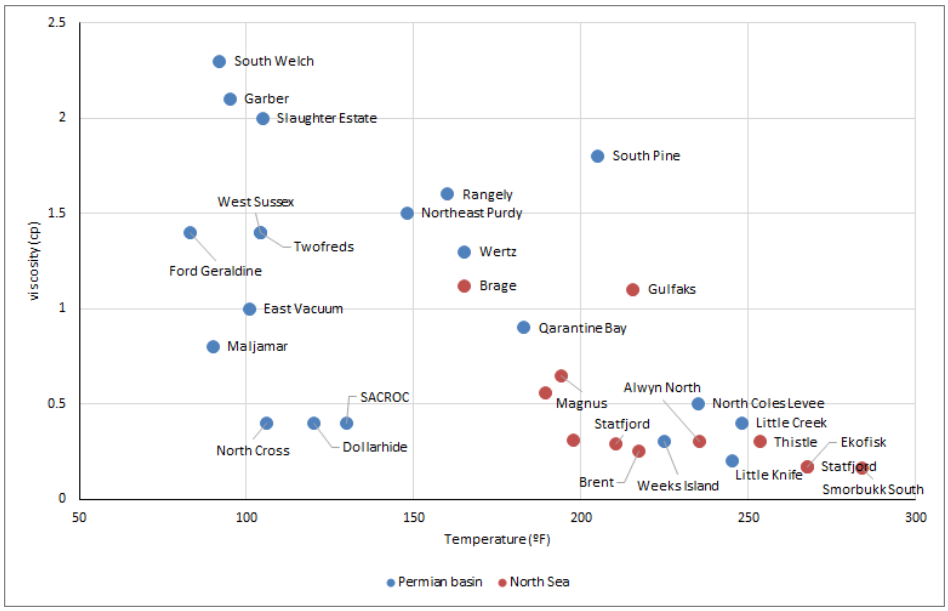

Figure 3.8: Oil viscosity vs. reservoir temperature in various offshore North Sea and onshore Permian Basin fields (data from Brock et.al, 1989 and Awan et.al, 2008)

3.6.2 *In-Situ* CO_2 Properties

In both provinces, CO_2 will be in a supercritical state at reservoir conditions. Apart from miscibility development, CO_2 properties also affect CO_2 requirement and macroscopic sweep efficiency as well. *In-situ* CO_2 density determines the project CO_2 requirements and also affects the degree of gravity segregation between CO_2 and other reservoir fluids. Likewise, CO_2 viscosity affects the macroscopic sweep (by altering mobility ratio) of the process.

Figure 3.9 compares CO_2 densities and viscosities across the *P-T* cross plot shown before. Although ambient reservoir conditions are fundamentally different between the two provinces (Figure 3.3), CO_2 properties are very similar in both of them. It can be seen in this figure that CO_2 density and viscosity are different by only around 5% between the two provinces.

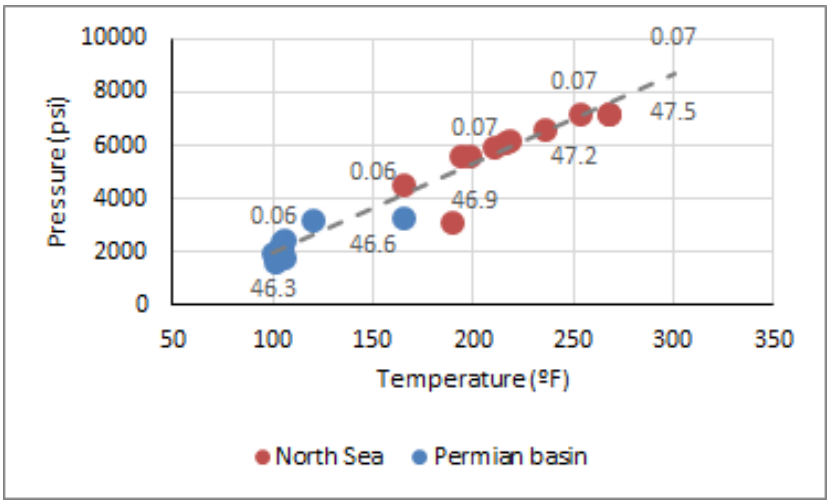

Figure 3.9: Estimated CO_2 density (lower data; lb/ft^3) and viscosity (upper data; cP) under the Permian Basin and North Sea reservoir conditions; data are generated using Winprop (CMG-WinProp 2014.10)

3.6.3 Miscibility Attainment with CO_2

Miscibility development in a CO_2-EOR process largely controls the quality of microscopic sweep efficiency. In the US, the majority of CO_2 flooding projects have been miscible floods. CO_2 flooding in the Permian Basin benefits from relatively lower reservoir temperatures as this promotes easier miscibility development.

Since North Sea reservoirs are at higher temperatures, miscibility will require higher pressures as well (Fayers *et al*. 1981). While this may appear discouraging, data from

different sources suggest that miscibility with CO_2 can be effectively attained in the North Sea. The data presented by Goodyear *et al*. show that although the minimum miscibility pressures for some North Sea crudes are relatively high, they are still within the operating limits and an effective miscible displacement is attainable (Goodyear *et al*. 2003). This is illustrated by other authors as well (Stewart 1997). The EOR study of the Forties (Halil, *et al*. 2002), Gulfaks (Agustsson & Grinestaff 2004) and Ekofisk (Jensen *et al*. 2000) fields show that miscibility with CO_2 is attainable in all the above examples.

Successful miscible hydrocarbon flooding in many North Sea reservoirs is also another positive indication of effective CO_2 miscibility attainment in this province; as CO_2 requires significantly lower miscibility pressures compared to typical hydrocarbon systems. For example, in South Brae HC-EOR, a 300psi difference between the minimum miscibility pressures of rich (24%CO_2, 73%HC and 3%N_2) and lean (5%CO_2, 91%HC and 4%N_2) gases was identified, both being lower than the reservoir pressure (Jethwa *et al*. 2000). In the Magnus field in the North Sea, the injected gas was very lean (90% CH_4) and had a minimum miscibility pressure of around 5000psi (Brodie *et al*. 2012) close to the reservoir pressure. In the Ula field the initial injection gas composition was mainly C_1 (72%); however, the flood was still miscible (Zhang *et al*. 2013).

Figure 3.10 shows the miscibility pressure (both with CO_2 and hydrocarbon) versus reservoir pressure in various EOR projects in both provinces. It can be concluded that CO_2 miscible displacement is *possible* in the North Sea.

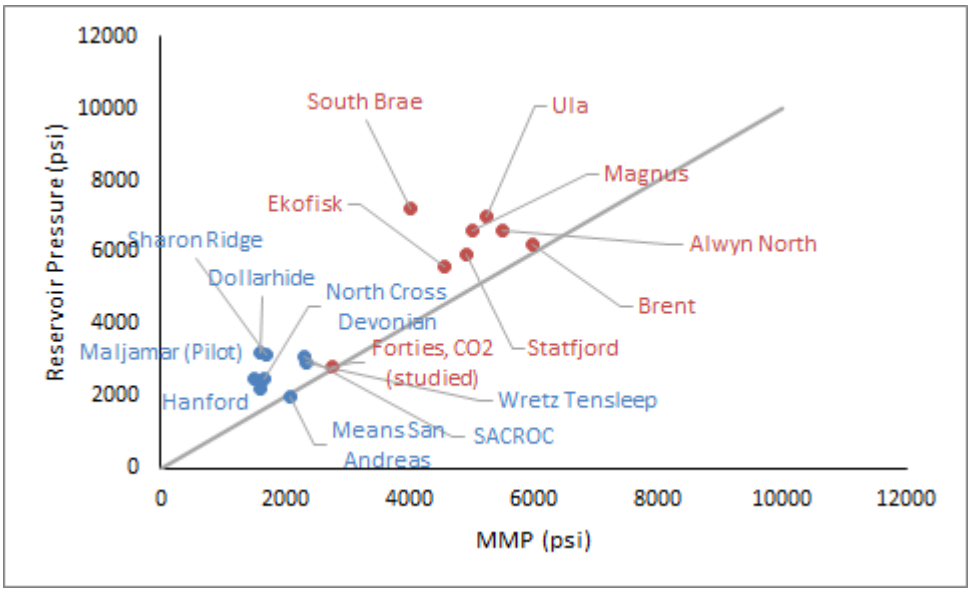

Figure 3.10: Reported miscibility pressures (with CO_2 and hydrocarbon) in various fields in both provinces.

3.6.4 CO_2-Water Interactions

CO_2 solubility in water could be important as it makes a fraction of CO_2 unavailable for EOR and may affect water properties. It may also promote further geochemical reactions leading to possible scale formation and deposition (Ribeiro *et al*. 2016). Although CO_2 dissolution in water slightly increases water density, its impact is barely significant for EOR processes which are conducted typically for a number of decades. Its impact is, however, more significant for CCS processes where the location of CO_2 storage may be monitored over a longer period.

CO_2 solubility in water historically has been ignored in the Permian Basin reservoir simulations (Warner 1977, Lin & Poole 1991), since it had minimal impact on the CO_2 flood performance and water properties. However, as a result of different ambient conditions in the North Sea, this assumption needs to be reconsidered. Figure 3.11 shows the CO_2 solubility in water as a function of temperature and pressure (Kohl & Nielsen 1997). The positions of the blue and red points in this figure show the approximate ambient conditions of Permian Basin and North Sea provinces, respectively.

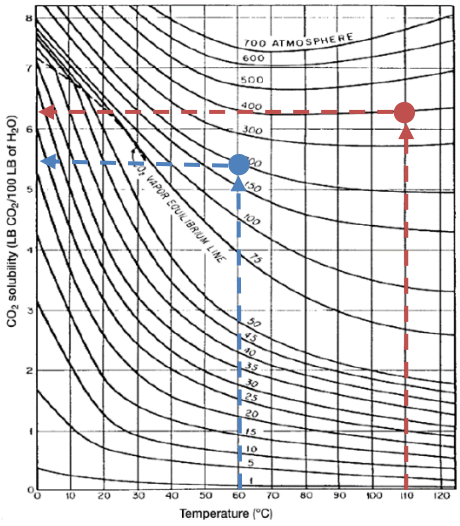

Figure 3.11: Approximate CO_2 solubility in water in both provinces (Kohl & Nielsen 1997)

It can be seen that the difference between the magnitudes of CO_2 dissolution in water for the two provinces is not significant. The relative position of these two points, however, indicate that unlike in the Permian Basin, CO_2 solubility, under North Sea ambient conditions is less sensitive to temperature variations and is mostly a function of reservoir pressure.

Figure 3.12 (left) compares the magnitude of CO_2 solubility in water across the pressure and temperature cross plot shown already in Figure 3.3. Figure 3.12 (right) compares the

equilibrium water mole fraction in the CO_2 phase along the same cross plot connecting the two provinces. The data in this figure illustrate that, while CO_2-water interactions are slightly higher in the North Sea province, they are still small in both of them.

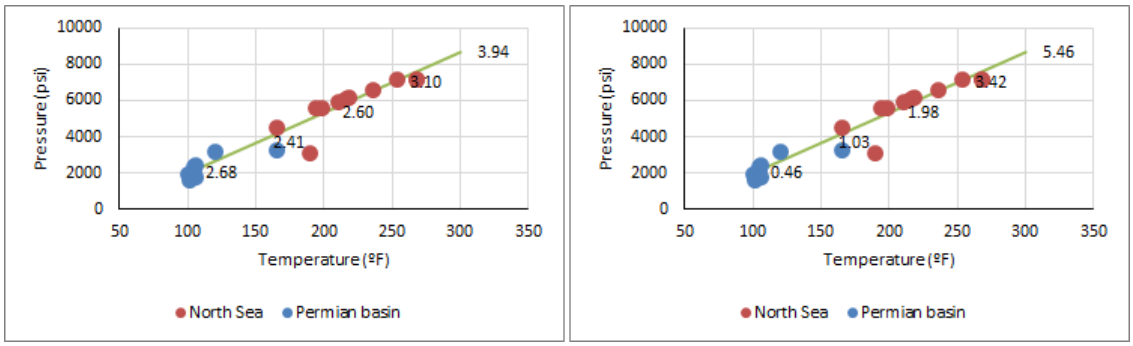

Figure 3.12: CO_2 mole fraction in the water phase and water mole fraction in the CO_2 phase across the two provinces. Data have been generated with Winprop (CMG-WinProp 2014.10)

Figure 3.13 shows that a 50/50 (volume basis) water-CO_2 sample under prevailing conditions in the Permian Basin would partition into a 52/48 water-CO_2 ratios in the North Sea. In other words, the relative volume of the water phase only slightly increases at the North Sea prevailing conditions and therefore it may not have a serious impact on CO_2 flooding process similar to the Permian Basin province (e.g. CO_2 slug size or WAG cycles).

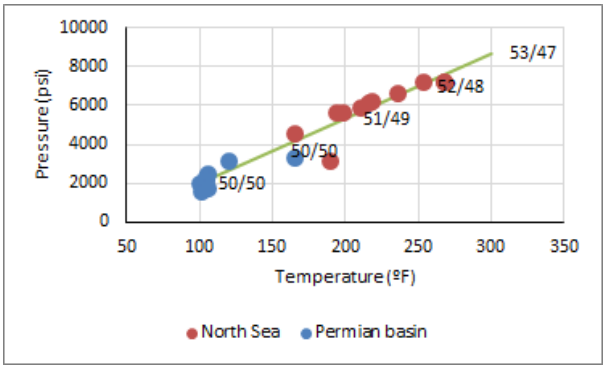

Figure 3.13: Relative volume of a 50/50 mixture at the Permian Basin at different prevailing reservoir conditions

The combination of these figures suggests that CO_2-water interactions would be slightly higher in the North Sea; although they are not fundamentally different between the two provinces. In fact, if salinity is taken into account, both provinces may have similar CO_2-water solubilities. Salinities are generally higher in the North Sea, which reduces CO_2-water solubility. Reported salinities in the North Sea are between 25,000ppm and 280,000ppm in a number of reservoirs (Fayers *et al*. 1981, Bath 1987, Warren & Smalley 1994).

Nevertheless, since CO_2 flooding in the North Sea is expected to be coupled with storage, it might be vital to correctly consider CO_2 dissolution in the water for accurate estimation of the proportions of CO_2 stored by different mechanisms (e.g. stratigraphic, residual, solubility and mineral trapping).

3.7 Simulation Studies (1)

In this section of the study, CO_2 flooding performance is compared between two representative models of the North Sea and the United States CO_2 flooded reservoirs using the average fluids and reservoir properties taken from the field surveys presented earlier in Sections 3.3 to 3.5. This allows comparison of the characteristics of CO_2 flooding under average prevailing reservoir conditions of these two respective provinces and also under different flooding objectives of pure EOR, pure storage (CCS) and a combination of EOR and storage (CCUS).

The comparison presented in this section is initially conducted in two representative base case models. Sensitivity analysis will, however, be conducted for each of the model parameters within their appropriate ranges of variations inferred from previous field surveys.

3.7.1 Base Case Model Properties

In this section, the representative onshore Permian Basin and offshore North Sea model parameters are introduced and discussed. From now on, the representative box model for the onshore United States classes of reservoirs will be identified simply as the '*onshore model*'. Similarly, the representative offshore North Sea model will be identified as the '*offshore model*'.

Model Dimensions: The CO_2 flooding performance in each class of reservoirs will be investigated by constructing two different *2D cross sectional* models. 2D models were preferred over 3D models, as they allow definition of a finer degree of heterogeneity, particularly in the vertical orientation, which is not generally affordable with three dimensional models. 2D cross sectional models are an appropriate tool for conducting sensitivity analysis prior to full field simulations (e.g. Brinkman *et al.* 1999).

The geometries of the base case models are important, in that they can affect the majority of the obtained results. The base case onshore and offshore conceptual sector model dimensions are taken from relevant literature (Warner 1977, Fayers *et al.* 1981). The two model dimensions are fundamentally different in that the offshore model is significantly larger and thicker than the onshore model. This reflects both larger spacing between wells and thicker pays of the North Sea systems. The well spacing in the onshore model may represent a well separation in a quarter 5-spot well placement pattern of 1320ft. The thickness of the onshore model is also 40ft, an average taken from the data in Figure 3.5.

Inspection of the North Sea data shows that the average well spacing in this province is around 1km (3280ft) or more (Crogh *et al.* 2002, Bath 1987). Accordingly this value has been used for the offshore model well spacing (L). An average thickness of 300ft was considered to be representative of the reservoirs located in the offshore North Sea systems. This 300ft may represent the Charlie sand of the Forties field located in the North Sea (Fayers *et al.* 1981). With this configuration, the offshore model is respectively 2.5 and 7.5 times longer and thicker than the onshore model. The two models are horizontal. There are two vertical wells in each of them, one injector on the left and one producer on the right. The injector can inject either water or CO_2.

There are 100×100 grid blocks in horizontal and vertical orientations in both models. Thus, the size of the grid blocks are *not* identical between the two models, whilst the *number* of grid blocks are similar. The grid selection for this study allows effective simulation of small dimensionless permeability correlation lengths (λ_{xD} and λ_{zD}) of 0.025 and 0.02 in horizontal and vertical orientations for the sensitivity analyses.

Heterogeneity: The formation permeabilities are significantly better in the North Sea (Awan *et al.* 2008, Brock & Bryan 1977). To appropriately reflect this, the allocated absolute permeability to each model should be different. The average horizontal permeability for the offshore and onshore models are respectively 400mD and 25mD taken from relevant literature (Awan *et al.* 2008, Brock & Bryan 1977, Fayers *et al.* 1981). Sensitivity analysis will also be conducted around these base case magnitudes in the later section of this study.

The heterogeneity in this work is described with the aid of the correlated random field[10] (El-Feghi 1992). Both models use the same identical heterogeneous permeability fields;

[10] The concept of Correlated Random Field (CRF) will be introduced and explained in the next Chapter (4).

despite the fact that their dimensions are different. This allows comparison of the performances of the two models under *comparable* permeability fields. This, accordingly, means that while the dimensionless permeability correction lengths (λ_{xD} and λ_{zD}) are comparable between the two models, the absolute correlation lengths (λ_x and λ_z) are not. The base case model dimensionless correlation lengths in two fundamental horizontal and vertical orientations are respectively 0.5 and 0.1. Sensitivity analysis will also be performed on the dimensionless correlation lengths in both models and in both orientations. All the permeability fields have been generated using Schlumberger Petrel (Schlumberger Petrel 2014) with a spherical variogram using sequential gaussian simulation. The permeabilities in both models are lognormally distributed with a V_{DP}=0.8. Note that no sensitivity analysis was performed on the degree of heterogeneity (V_{DP}) in either of the models.

Porosity is not constant is either of the two models and is coupled to permeability with the following correlation (Holtz 2002).

$$k = 7\times10^{7}\times\varphi^{9.61} \tag{3.1}$$

This correlation predicts porosities between 0.47 and 0.17 for the offshore model (average of 0.29) and between 0.35 and 0.12 for the onshore model (average of 0.22).

Finally, the ratio of vertical to horizontal permeability (k_z/k_x) was chosen as 0.1 in both systems. As with other parameters, sensitivity analysis will be conducted for a range of k_z/k_x ratios as will be illustrated later.

Initial Conditions: The initial conditions i.e. initial pressure and temperature are taken from the average of the values depicted in Figure 3.3 respectively for the North Sea and the Permian Basin systems. For the North Sea offshore representative model, the initial pressure and temperature are 5000psi and 190°F, while for the onshore United States model, they are 2500psi and 120°F respectively. The initial pressure in both models are well above the MMP. There is no aquifer connected to either of the models.

Fluid Description: We have used a modified version of the Jema field crude description which has been characterised by Khan *et al.* (1992) and in the same way that has been used by Chang *et al.* (1994), Roper *et al.* (1992) and Ghomian *et al.* (2008). The details of the fluid model is depicted in Table 2.1 in Chapter 2. The estimated MMP at onshore reservoir conditions is 1500psi (slimtube simulation, Chapter 2). For the offshore model, the estimated MMP is higher at around 2300psi. The two onshore and offshore reservoir

models use the same fluid models which consequently may generate similar oil and CO_2 properties at both models prevailing reservoir conditions. We believe this is a reasonable approach since in both provinces, fluids are of similar (good) qualities which allows effective miscibility development.

There is, however, an exception. As was shown previously (Figure 3.8), the crude viscosities are typically lower in the North Sea. To take this into account, the viscosity volume shift (V_c) for the three heaviest components in the onshore model fluid descriptions have been slightly modified to resemble a fluid of slightly higher viscosity at that respective reservoir conditions. Therefore, while the two onshore and offshore fluid descriptions predict similar results in terms of CO_2-oil compositional interaction, slightly higher oil viscosities are predicted for the onshore model. CO_2 dissolution in water has also been taken into account for all the modelling studies conducted in this section and in both models (Figure 3.11 and Figure 3.12).

Flooding Strategy: The simulation in both models follows an identical flooding strategy. There is no initial natural depletion phase in either of the models. Flooding in both models begins with an initial phase of waterflooding. As soon as watercut reaches 85%, tertiary CO_2 flooding is initiated. A fixed 35% HCPV CO_2 is injected as a single slug (i.e. not alternated with water) in both models. Once the desired volume of CO_2 has been injected, CO_2 injection is halted and final waterflooding is resumed. Final waterflooding recovers additional oil and part of the injected CO_2 and continues until watercut reaches 95% where at this point the simulation stops. Note that since the criteria for process changeover is not on the time basis in either of the models, each phase of the flooding may be completed in different times and after injecting dissimilar volumes of water (in terms of HCPV) in either model. We, however, believe that this configuration of process changeover is more realistic than injecting fixed volumes of water in both of the models.

This depletion strategy is similar to the flooding strategy undertaken by Warner (1977) which is considered the most conventionally practiced CO_2 injection strategy, at least in the United Stated, which is tailored for EOR. This flooding strategy, similarly, has been practiced in the North Sea, where tertiary solvent injection follows the secondary waterflooding (e.g. Magnus field, Brodie *et al.* 2012). Sensitivity analysis will also be conducted on the initial threshold of watercut (i.e. the watercut threshold of 0.85 where after this CO_2 flooding initiates) to investigate to what extent it may affect the results.

The offshore and onshore models are depleted respectively at 4% and 2% of their HCPV annually. The rate of depletion is different between the two models in accordance with the observation made earlier in Figure 3.2.

The injection strategy allow the average pressure to remain always at around initial reservoir pressure for each of the models. A fracture to initial reservoir pressure ratio of 1.4 determines the maximum bottom-hole injection pressure for either of the models. This is similar to the simulation study of CO_2 injection into the Bunter sandstone in the North Sea (Williams *et al.* 2013).

The injected gas is pure CO_2. Sensitivity analyses will also be conducted to evaluate the impact of the presence of impurities on the performance of each model.

Relative Permeability Models: Dria's *et al.* (1993) measured relative permeabilities based on the modified Corey relationship as was described in Chapter 2 has been used in this analysis. An alternative set of relative permeability parameters will, however, be used as a further sensitivity analysis to investigate to what extent the findings are dependent on the chosen set of relative permeability. Both sets of relative permeability have already been depicted and described in Chapter 2 (Figure 2.1 and Figure 2.3, Table 2.3 and Table 2.4). Table 3.3 shows the parameters of the two relative permeability models. The two relative permeability models are characterised by dissimilar extents of the multiphase region, in addition to different predicted 3-phase oil relative permeability under Stone 1 model (Figure 2.6).

Table 3.3: The two sets of relative permeability models used for this study (left: the base set, right: the alternate set)

	Default set of relative permeability	Alternate set of relative permeability
S_{wc}	0.36	0.25
S_{orw}	0.37	0.25
S_{org}	0.16	0
S_{gc}	0.16	0.025
k_{rw}	0.36	0.3
k_{row}	0.57	0.57
k_{rog}	0.57	0.57
k_{rg}	0.28	0.57
n_w	3.1	2
n_{ow}	2.9	4
n_{og}	2.9	4
n_g	2.9	2
References	Dria *et al. 1993*, Roper *et al. 1992*	Goodyear *et al.* 2003, SHARP reports 2001.

The measures of performance: we define three performance indicators (or indices) namely I_{EOR}, I_{CCS} and I_{CCUS} defined as below to analyse and compare the pure EOR, pure storage (CCS) and combined EOR and storage (CCUS) performances of the two models.

$$I_{EOR} = \frac{N_p}{N_t} \tag{3.2}$$

$$I_{CCS} = \frac{V_{CO2_{Stored}}}{V_{CO2_{Injected}}} \tag{3.3}$$

$$I_{CCUS} = 0.5 \times I_{EOR} + 0.5 \times I_{CCS} \tag{3.4}$$

N_p and N_t in Equation 3.1 are respectively, the cumulative tertiary oil *produced* after completion of the secondary waterflooding and the cumulative tertiary oil *available* for recovery after secondary waterflooding, thus the ratio represents the fraction of tertiary oil that has been recovered by CO_2 injection. $V_{CO2(stored)}$ and $V_{CO2(injected)}$ in Equation 3.2 are respectively the cumulative quantity of CO_2 stored and injected in the reservoir model at any time during the simulation. I_{CCUS} is the combination of the two I_{EOR} and I_{CCS} indices which depends on the weight factor being chosen for each of its constituents. Here, we have assumed that both EOR and storage are equivalently important and hence assigned a 0.5 weight factor for each of the two sub-indices.

Table 3.4 (next page) summarises the base case properties of the onshore and offshore models used in this study. The reservoir simulator used for this study is the CMG-GEM compositional reservoir simulator (CMG-GEM, 2014.10).

3.7.2 Base Case Model Results and Analysis

Table 3.5 compares the final performances of the two models. By all metrics, the performance of the onshore model is better than the offshore one. Incremental recovery factor is better in the onshore model. Gross CO_2 utilisation is also lower in the onshore model. Net CO_2 utilisation is slightly higher in the onshore model, since the prevailing flow pattern upon CO_2 flooding is different in the onshore model allowing CO_2 to come into larger contact with other reservoir fluids, leading to further dissolution of CO_2 in both the oil and water phases.

Table 3.4: Base case model parameters for offshore and onshore models

	Offshore model	**Onshore model**
Length	3280ft (1000m)	1320ft (40-acre spacing)
Thickness	300ft	40ft
Size of the Grid blocks (ft)	32.8ft×32.8ft×3ft	13.2ft×13.2ft×0.4ft
Number of blocks	100×1×100 (10000)	100×1×100 (10000)
k_z/k_x	0.1	0.1
Average k_x	400mD	25mD
Average Porosity	0.29	0.22
Initial pressure and temperature	190°F, 5000psi	120°F, 2500psi
***In-situ* oil density and viscosity**	45.7 lb/ft^3, 0.58cP	46.0 lb/ft^3, 1.24cP
***In- situ* CO_2 density and viscosity**	46.86 lb/ft^3, 0.065cP	45.00 lb/ft^3, 0.059cP
MMP	2300psi	1500psi
V_{DP}	0.8	0.8
λ_{xD}, λ_{zD}	0.5, 0.1	0.5, 0.1
Injection Strategy	Single Slug CO_2 injection	
Rate of Depletion (%HCPV annually)	4%	2%
Dip angle	0	0

Inspection of the onset of gas breakthrough in both models also shows that gas breakthrough in the onshore model occurs after 0.3HCPV CO_2 injection, while in the offshore model it occurs after only 0.14HCPV CO_2 injection. This is mainly because of different flow patterns that influence the displacement in either of the two models as will be discussed later. The ratio of gross to net CO_2 utilisation can provide an estimate of the recycling requirement for each respective model. For onshore and offshore models these ratios are respectively 1.8 and 2.8, which again indicates that the flooding is more efficient in the onshore model, in that it can achieve its final better results with even less CO_2 recycling.

Table 3.5: Comparison of final performances between the two models

	Offshore	***Onshore***
Recovery factor after initial waterflooding	36.1%	35.0%
HCPV water injected during initial waterflooding	0.39	0.38
Cumulative HCPV Fluid injected (water and CO_2)	1.32	1.21
Final Recovery Factor	54.10%	56.61%
Incremental Recovery	15.13%	18.47%
Net CO_2 utilisation (Mscf/bbl)	2.21	2.86
Gross CO_2 utilisation (Mscf/bbl)	6.25	5.26
I_{EOR}	28.2%	33.2%
I_{CCS}	35.4%	54.3%
I_{CCUS}	31.8%	43.7%

Figure 3.14 compares the recovery factors between the two models. The two processes are completed by injecting dissimilar volumes of fluids (water and CO_2) mainly due to different displacement characteristics.

The performances of the two models are nearly identical during waterflooding and just before CO_2 flooding, which indicates that waterflooding is not as sensitive as CO_2 flooding to the differences between the two model's properties. Note that, although the waterflood recovery is better in the offshore model, the ultimate performance of the offshore model is poorer than the onshore model.

At any comparable injected fluid volumes (in terms of HCPV), the onshore model performance is relatively better. Additionally, note that by the time that the simulation terminates in either of the models, more fluid (mainly water) has been injected in the offshore model. The summary of the above states that CO_2 flooding in the offshore model has relatively poorer characteristics.

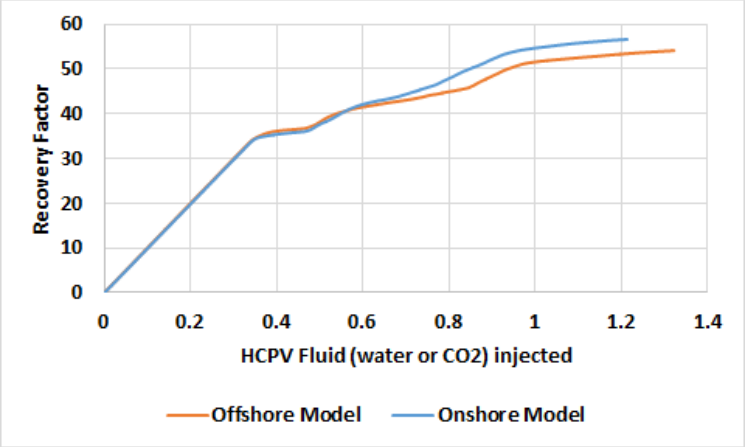

Figure 3.14: Comparison of the recovery factors between the two models.

A comparison between the performances of the areal and cross sectional versions of the two models may provide an estimate of the significance of gravity in either of them. Figure 3.15 compares the ultimate recovery factors between the areal and cross sectional versions of the onshore and offshore models. This figures shows that while both models are to some extent affected by gravity, the gravity effects are more significant in the offshore model.

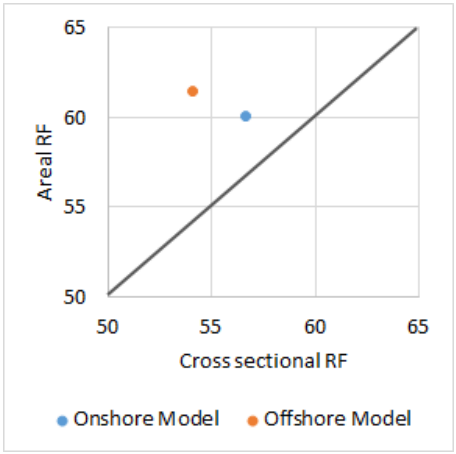

Figure 3.15: Comparison between cross sectional and areal recovery factors for offshore and onshore models

In each model, the gravity effect is controlled by a combination of model characteristics including the rate of depletion, formation permeability and finally the dimensionality of the each model (*L/H*). While formation permeabilities are significantly better in the offshore model, the rate of depletion is lower in the onshore model. However, the final balance implies that gravity is more significant in the offshore model. It is important to note that gravity is significant in the offshore model because of density difference between *injected water* and CO_2 and not because of density differences between oil and CO_2 (Chapter 2). As was shown previously, the density difference between CO_2 and oil is negligible, at least in this modelling study.

Figure 3.16 compares the evolution of the I_{EOR}, I_{CCS} and I_{CCUS} performance indices between the two models. The sharp rise of the I_{CCS} indices in both models corresponds to the onset of CO_2 injection just before CO_2 breakthrough. Note that I_{CCS} never attains 1, since CO_2 is already produced by oil production as the oil in place already has a small fraction of CO_2 (1.92% mole fraction). Similarly in both models, the I_{EOR} index gradually improves as more fluid is injected, while the I_{CCS} response declines; this corresponds to more oil recovery as a result of further fluid (either water or CO_2) injection and simultaneously more CO_2 breakthrough which impairs I_{CCS}.

The fact that the evolution of I_{EOR} and I_{CCS} indices are different suggest that the likely path of optimisation and operation for a given CO_2 flooding process could be different as a consequence; e.g. the value of shut-in versus continuing production could be different between an EOR and storage optimised process.

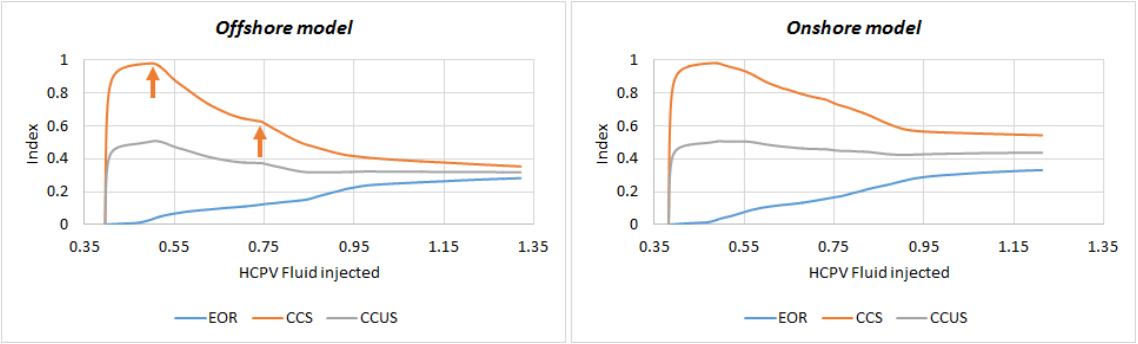

Figure 3.16: Evolution of the I_{EOR}, I_{CCS} and I_{CCUS} indices for the two models

While the evolution of the I_{EOR} indices are fairly similar between the two models, the I_{CCS} evolutions are slightly different. In the onshore model, after a sharp rise, the I_{CCS} response decreases gradually as more fluid (water or CO_2) is injected; however, in the offshore model, two shocks can be identified (noted by arrows in Figure 3.16).

The first shock corresponds well with the onset of CO_2 breakthrough, while the second shock corresponds with CO_2 production due to final water injection that follows CO_2 flooding. Since CO_2 flooding is more gravity dominated in the offshore model, injected CO_2 accumulates underneath the top of the model and rapidly breaks through; this makes the first shock.

The accumulated gas in the offshore model has a relatively higher local saturation in that CO_2 is not well distributed within the entire system. The next waterflooding rapidly pushes out this accumulated CO_2, causing creation of the second shock in the offshore model. It can be seen that the final I_{CCS} is relatively higher for the onshore model than the offshore model as was depicted previously in Table 3.5.

Figure 3.17 compares evolution of the normalised injector bottomhole pressures for both models. The injection pressures have been normalised by dividing injectors bottomhole pressure to initial reservoir pressure (p_i) in either of the models. This result shows that the evolution of the injector bottomhole pressure is much more limited in the offshore model despite its larger well spacing and higher rate of depletion.

This is due to significantly better formation permeability in the offshore model. This may suggest that voidage replacement could be less problematic in the offshore systems despite their larger intra-well spacing and higher rates of depletion.

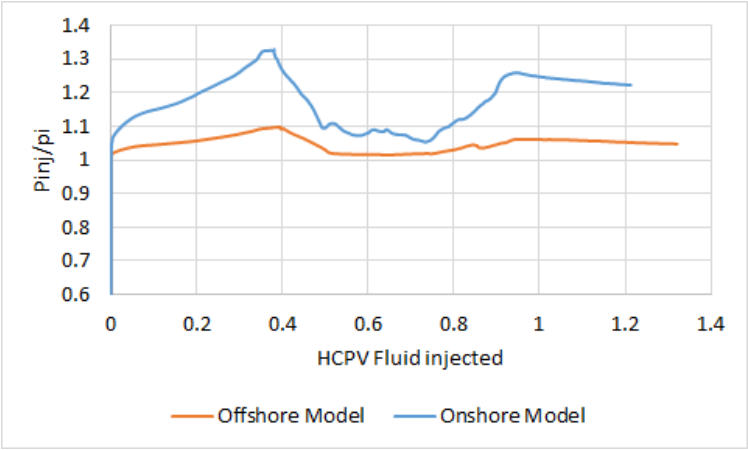

Figure 3.17: Injector bottomhole pressure evolution; comparison between the two models

As a final exercise, we repeat the above simulations in both models with the alternate set of relative permeability functions described earlier (Table 3.3) to check if the observed results are sensitive to the chosen set of relative permeability data. Figure 3.18 compares the evolution of the recovery factors between the two models based on the cumulative HCPV fluid injected. It can be seen that the same observation of Figure 3.14 is replicated in this figure, in that the initial waterflooding recovery is slightly better in the offshore model. However, as before, during CO_2 flooding onshore model recovery factor gradually improves and finally outperforms that in the offshore model. Nevertheless, the displacement is more gravity dominated in both models with the new set of relative permeability data (and particularly in the offshore model) due to a larger multiphase region, characteristic of this alternate set of relative permeabilities. Note that unlike the simulations conducted previously with the base set of relative permeability data (Figure 3.14), now with this alternate set of relative permeabilities, more fluid (water) has been injected in the onshore model.

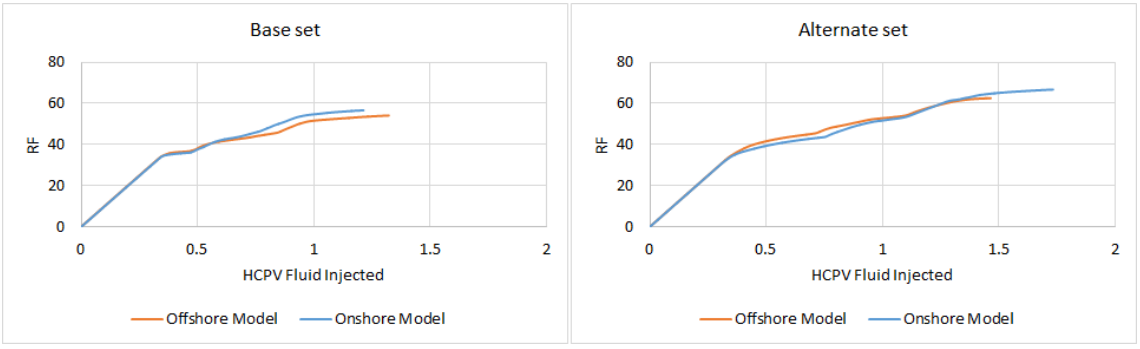

Figure 3.18: Comparison of onshore and offshore model performances with base and alternate sets of relative permeability models.

3.7.3 Sensitivity Analysis

A number of sensitivity analysis were conducted for each parameters in both onshore and offshore models around the base case values described previously in Table 3.4. For each parameter in either onshore or offshore models, the sensitivity analysis covers the observed ranges of variation in the previous field surveys, depicted in Section 3.3 to 3.5. The final ranges of the sensitivity analysis are depicted in Table 3.6.

Table 3.6: Range of the sensitivity analysis conducted for each parameter in offshore and onshore models

	Offshore Model			***Onshore Model***		
	Min	**Base**	**Max**	**Min**	**Base**	**Max**
Well spacing (*L*)	1640ft	**3280ft**	13120ft	660ft	**1320ft**	5280ft
Thickness (*H*)	150ft	**300ft**	600ft	20ft	**40ft**	80ft
k_z/k_x	0.01	**0.1**	1	0.01	**0.1**	1
k_x	40mD	**400mD**	4000mD	2.5mD	**25mD**	250mD
Initial Pressure	4000psi	**5000psi**	6000psi	2000psi	**2500psi**	3000psi
λ_{xD}	0.025	**0.5**	3.0	0.025	**0.5**	3.0
λ_{zD}	0.02	**0.1**	0.5	0.02	**0.1**	0.5
Rate of Depletion (%HCPV/year)	2%	**4%**	8%	1%	**2%**	4%
Threshold	0.45	**0.85**	-	0.45	**0.85**	-
Slug Size (HCPV)	20%	**35%**	50%	20%	**35%**	50%
Impurity	-	**100%CO_2**	50%CO_2 50% CH_4	-	**100%CO_2**	50%CO_2 50% CH_4

In addition to final recovery factors, this sensitivity analysis investigates the sensitivities of all the three performance indices introduced previously. The flooding procedure in this sensitivity analysis is the same as the base case model. The sensitivity analysis conducted in this section is of OFAT[11] type, in that only one parameter is varied for each sensitivity case, while the rest of the model parameters are kept at their base case values.

Results: Figure 3.19 shows the Tornado plot for the results of the sensitivity analysis conducted in this section. The variation of ultimate recovery factors and three main performance indices for onshore and offshore models have been all depicted in this figure. The majority of the results observed in this figure may be explained by the background discussions of the dominant flow patterns in both of the onshore and offshore models.

[11] One Factor at A Time.

From the discussion presented earlier, it was concluded that CO_2 flooding was more gravity dominated in the offshore model.

a) Model Geometries: The model geometries have been varied to investigate CO_2 flooding performance in a broader range of reservoir dimensions for each class of reservoirs than those depicted in Table 3.4. Varying the geometry of the two models has different impacts on the performances of each model. Note that by varying the model geometries, the absolute permeability correlation lengths in both of the models are not altered (λ_x and λ_z), in that the simulation will still be conducted in the same (but larger) permeability field in either of the orientations and in both models.

Results of the sensitivity analysis with regard to well spacing (L) show that CO_2 flooding in both system of reservoirs are similarly sensitive to the variation of well spacing. Note that well spacing has been varied in both models by a factor of 0.5 and 4.0 relative to the original base case model well spacing. In both models, increasing well spacing may create further opportunity for cross flow, thus improving all the key performance indices for both models. A similar decrease of well spacing has negative impact in both models. Note, however, that this conclusion has been obtained having the background assumption that sand bodies can be well correlated between individual wells, irrespective of well spacing. If connectivity is lost then increasing well spacing may have a negative effect.

Unlike well spacing, variation of reservoir thickness (H) has different impacts in both models. An increase/decrease in the formation thickness in the offshore model improves/impairs the CO_2 performance characteristics in that the significance of gravity is supressed by a reduction in the effective aspect ratio and at the same time by promoting the channelling nature of the displacement. For the onshore model where the displacement is not already gravity dominated, increasing the formation thickens has a very limited negative impact in that the displacement becomes slightly more channelling dominated leading to relatively poorer recoveries. However, a reduction of formation thickness in the onshore model has again a negative impact since the displacement now becomes gravity dominated, hence all the main three indices and recovery factors decline. The conclusion is that CO_2 flooding in thicker pays in the North Sea offshore classes of reservoirs may have the added benefit of supressing gravity and hence improving the recovery. For the onshore systems, the conclusion depends on the heterogeneity description and balance of gravity and viscous forces.

Figure 3.19: Tornado plot representing sensitivity of each of the indices to the variation of an input parameter in onshore and offshore models. Yellow and green colours show respectively increase or decrease of a certain parameter in the offshore (left) model. Blue and grey colours show respectively increase or decrease of a certain parameter for onshore (right) model.

b) k_z/k_x ratio: The magnitude of the k_z/k_x ratio controls the degree of cross flow within the system or alternately affects the severity of gravity for a gravity dominated displacement. The chosen range of k_z/k_x ratio in this sensitivity analysis is large, but identical k_z/k_x ranges are used in both models (from 0.01 to 1.0). Variation of the k_z/k_x ratio has different impacts in each of the models characterised with different flow patterns. In both models, a reduction of k_z/k_x ratio from 0.1 (base case k_z/k_x) to 0.01, impairs all the performance indices, nevertheless, to different extents. This is because at very low k_z/k_x ratios, while gravity is suppressed, the cross flow becomes simultaneously very limited, leading to channelling dominated displacement and hence poor recoveries.

Consequently, a further increase of k_z/k_x from 0.1 to 1.0, impairs all the *main* performance indices in the offshore model as the displacement now becomes significantly gravity dominated in this model. However, for the onshore model, the performance indices remain fairly unchanged or reduce only slightly as a result of k_z/k_x increase, possibly because of limited gravity effects in this model.

c) Absolute permeability: The absolute permeability in this sensitivity analysis has been varied by an order of magnitude around the base case k_x for both onshore and offshore models to cover the observed ranges of permeabilities in both classes of reservoirs (Awan *et al.* 2008, Brock & Bryan 1977). The impact of varying k_x is similar and comparable in both models, in that the significance of gravity to viscous forces might be varied and the performances become respectively worse or better by a relative increase or decrease of k_x. This effect is, however, more significant for the offshore model. Results also indicate that in the onshore model, a 10-fold decrease of horizontal permeability makes voidage replacement significantly challenging in that the injectors pressure reach the maximum allowable injection pressure.

d) Flooding pressure: A further sensitivity analysis was conducted to investigate the impact of varying pressure in each model. The pressure was varied by between $\pm$20% of the original base case value in each of the onshore/offshore models. The ranges of pressure variation in both models are still above their respective MMP of 2300psi (offshore model) and 1500psi (onshore model).The effect of varying pressure is, however, more significant for the offshore model. Varying pressure, changes the CO_2 density at the respective reservoir conditions which may lead to suppressing or promoting the gravity effects within the systems. For the onshore model, since the displacement is not strongly

gravity dominated, varying pressure does not have a significant impact on the performance characteristics.

e) Dimensionless correlation lengths: The dimensionless correlation lengths are those relatively uncertain parameters which depend mainly on the depositional environment for each reservoir system. A range of three dimensionless correlation lengths has been investigated for each model and for each orientation. The three different longitudinal dimensionless correlation length correspond to correlation length significantly larger than well spacing (λ_{xD}=3.0), comparable with well spacing (λ_{xD}=0.5, base case model) and much smaller than well spacing (λ_{xD}=0.025). The impact of varying the dimensionless horizontal correlation length (λ_{xD}) in both models is similar and in fact is relatively straightforward, in that all performance indices improve or decline as a result of increasing or decreasing the λ_{xD}. The extent of this effects is, however, comparable in both models Note that for all the comparable λ_{xD}s, all the main performance indices are better in the onshore model.

The impact of varying the vertical dimensionless correlation length (λ_{zD}) is dissimilar between the two models. In a gravity dominated displacement, characteristic of the offshore systems, as λ_{zD} increases, gravity can further dominate, thus all the performance indices become simultaneously poorer. Similarly, a λ_{zD} decrease may improve the performance since the impact of gravity may be retarded. On the other hands, for the onshore model a dissimilar behaviour can be observed, in that both increasing and decreasing λ_{zD} impairs the performance as has been depicted in Figure 3.19. An increase of the λ_{zD} in the onshore model makes the displacement more channelling and thus reduces the performance efficiency of all indices, while an increase of λ_{zD} makes the displacement more gravity dominated, both of which make the performances poorer than the base case onshore scenario.

f) Rate of depletion: The chosen rate of depletion has been varied by a factor of 2 above and below the original rate of depletion in both onshore and offshore models. The ranges have been selected by inspecting the data in Figure 3.2. As with the horizontal permeability (k_x), varying the rate of depletion (r) has a direct relationship with all the performance indices and similarly in both models. An increase in the rate of depletion makes the displacement less gravity dominated in both models, though the relative improvement is more significant for the offshore model where the displacement is already more gravity dominated. Note, however, that the chosen higher rate of depletion may not

be effectively maintained in the onshore model, due to its very low horizontal permeability.

g) Threshold for tertiary CO_2 initiation: A further set of sensitivity analysis investigates how the performance of each model is sensitive to the critical threshold chosen to control the onset CO_2 injection. The threshold watercut now has been decreased from 85% to 45%. Decreasing this threshold implies that less water will have been injected in either of the models during primary waterflood.

Results show that for the onshore model where its displacement is not gravity dominated, the recovery factor slightly decreases because less fluid now has been injected in this model, whereas in the offshore model, due to less water injection, the displacement is less gravity dominated, hence the recovery factor slightly improves.

h) CO_2 slug size: The chosen CO_2 slug size has been varied for both onshore and offshore models by $\pm$15% compared to the original base case CO_2 slug size (35%HCPV). Varying the injected CO_2 slug size has a relatively similar effect in both models in that recovery factor improves or declines as a result of more or less CO_2 injection. As the injected CO_2 volume increases, the I_{CCS} diminishes and I_{EOR} improves, implying that a larger fraction of injected CO_2 has now broken through, while more oil is produced. However, the relative improvement or impairment is less noticeable for the offshore model indicating that a large fraction of its injected CO_2 breaks through anyway, hence its performance is rather less sensitive to the size of CO_2 slug. This is again due to larger gravity effects in this model.

i) Presence of impurities: The injected gas may not be pure CO_2 in either classes of reservoirs, either because of recycling or supply characteristics. The impact will be addressed as the final set of sensitivity analysis. Results of this sensitivity analysis show that the presence of impurities significantly impairs the I_{EOR} response, due to several effects. First, MMP increases due to the presence of impurities; the presence of 50% methane in the CO_2 stream increases MMP respectively from 1500psi to 3200pis for the onshore model and from 2300psi to 4300psi for the offshore model. Note that the relative MMP variation is smaller at elevated temperatures, i.e. offshore North Sea systems may be less sensitive to the presence of impurities (Chapter 2). These figures illustrate that the displacement may now have become immiscible in the onshore model while this is not the case in the offshore model. Second, the presence of impurities may change gas properties (i.e. density and viscosity) to that extent that the flow patterns might be

affected. A 50% presence of methane in the CO_2 stream in this sensitivity analysis may reduce the gas stream density and viscosity by 47% and 40% in the offshore model and by 61% and 55% in the onshore model. Note again that the relative changes are larger for the onshore model. Inspection of results show that in the offshore model, the flow pattern now becomes slightly more gravity dominated. Nevertheless, the significant reduction of recovery factor and I_{EOR} in the offshore model are principally due to poorer compositional interactions in both models rather than a significant change of flow patterns.

Summary and Discussions: Figure 3.20 compares the ranges of the main indices obtained by conducting sensitivity analysis in both onshore and offshore models.

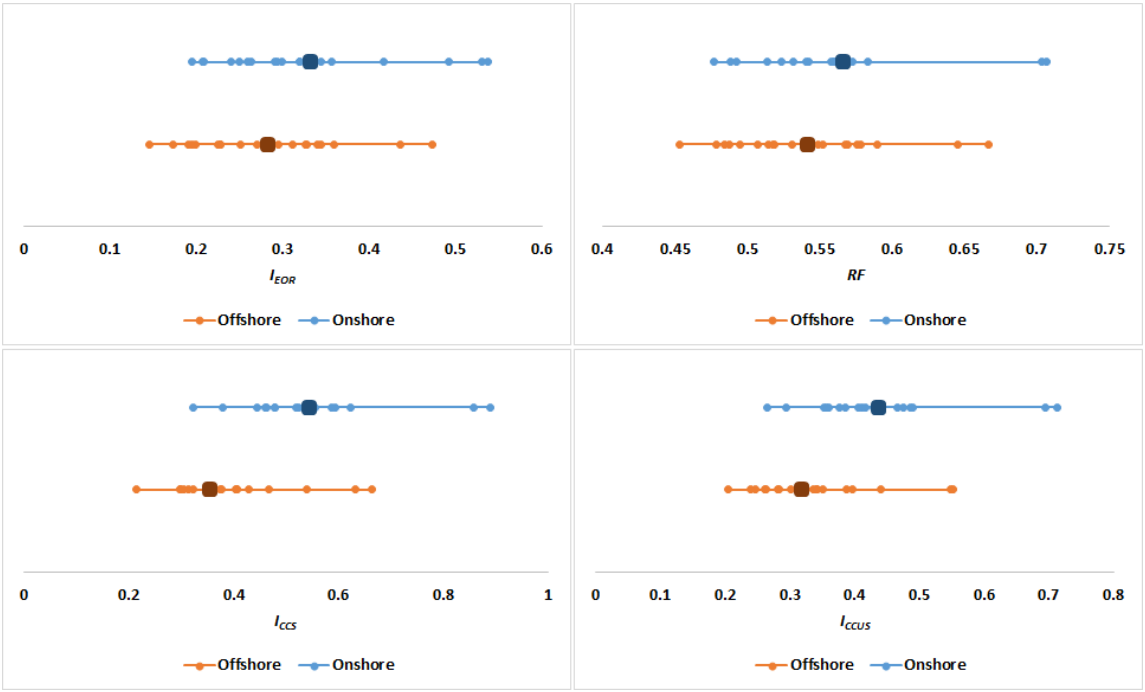

Figure 3.20: Ranges of the main indices observed after sensitivity analysis in onshore and offshore models. The large solid dots shows the base case magnitudes for each of the relevant indices.

As expected, the minimums and maximums for each individual index are relatively higher in the onshore model. However, it is interesting to note that the ranges of the variations for each individual index is always smaller in the offshore model, despite the fact that the sensitivity ranges employed are comparable. This is particularly relevant for storage efficiencies (I_{CCS}). The significant gravity effects observed in the offshore model may explain this.

A few conclusions can be drawn from the sensitivity analysis conducted in this section. First, there is generally a correlation (or synergy) between the EOR (I_{EOR}) and storage

(I_{CCS}) responses in that the two indices improve or decline simultaneously. Second, for the majority of the sensitivity scenarios investigated in this section, the waterflood recovery varies only between 0.35-0.37 and in fact is very insensitive to the variation applied to individual model parameters. Third, for some of the onshore models, the voidage replacement cannot be effectively maintained e.g. as a result of low formation permeabilities or higher rates of depletion. This is not the case for the offshore model.

Since CO_2 flooding is significantly gravity dominated in the offshore model (due to initial waterflooding), an alternate flooding strategy might be practiced in these systems where CO_2 is injected as the *secondary* means of recovery and not as the *tertiary* recovery process. This may in turn reduce the significance of gravity. Figure 3.21 compares recovery factors between two different CO_2 flooding processes in both onshore and offshore models. The dashed recovery factors in both left and right figures represent the tertiary CO_2 flooding process as was described previously, whereas the solid lines represent the secondary CO_2 flooding where CO_2 is injected right from the beginning of the flood and is not preceded with any secondary waterflooding. The model parameters are exactly similar as previously depicted in Table 4.3. As before, once the desired volume of CO_2 is injected, waterflooding resumes in both models to recover additional oil and part of the injected CO_2. The process terminates in each of the models once watercut reaches 95%.

Figure 3.21 (left) shows that recovery factor has been significantly improved in the offshore model (+14%), whilst in the onshore model, this improvement is relatively smaller (+2%).

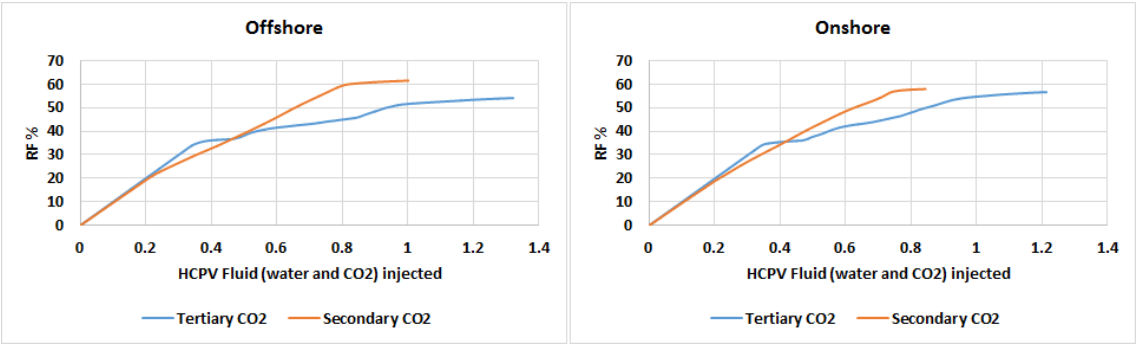

Figure 3.21: Secondary and tertiary CO_2 flooding; comparison between the two models

Although the results presented in this section may suggest that by all means the performance characteristics of the onshore model is relatively better, we do not conclude that the efficiency of the CO_2 flooding process is *generally* better in onshore classes of

reservoirs. Instead emphasis is made on the proper recognition of the differences in the observed displacement characteristics between the two models i.e. the dominant flow pattern and the evolution of pressure response during CO_2 flooding between the two models. Apparently, recovery might be better or worse than that observed in this study depending on the pattern of heterogeneity which may not be necessarily comparable between the two classes of reservoirs, relative permeability effects and detailed fluid descriptions.

3.8 Simulation Studies (2)

The next simulation study presented in this section compares the CO_2 flooding performance in an identical geological description but under two different flooding scenarios. The first scenario is representative of an average onshore Permian Basin reservoir, while the second scenario is representative of an average offshore North Sea reservoir. The aim of this simulation study is to investigate the combined impact of well spacing and reservoir properties on the CO_2 flooding performance in these two provinces.

Figure 3.22 shows initial oil saturation (left) and the permeability field (right) in the chosen geological model. There is a water leg connected to the hydrocarbon column in this model. Few faults are present in the model. The reservoir model is thick near the crest and progressively becomes thinner at the peripheries. Therefore those wells located near the crest of the model are more prolific than the periphery wells.

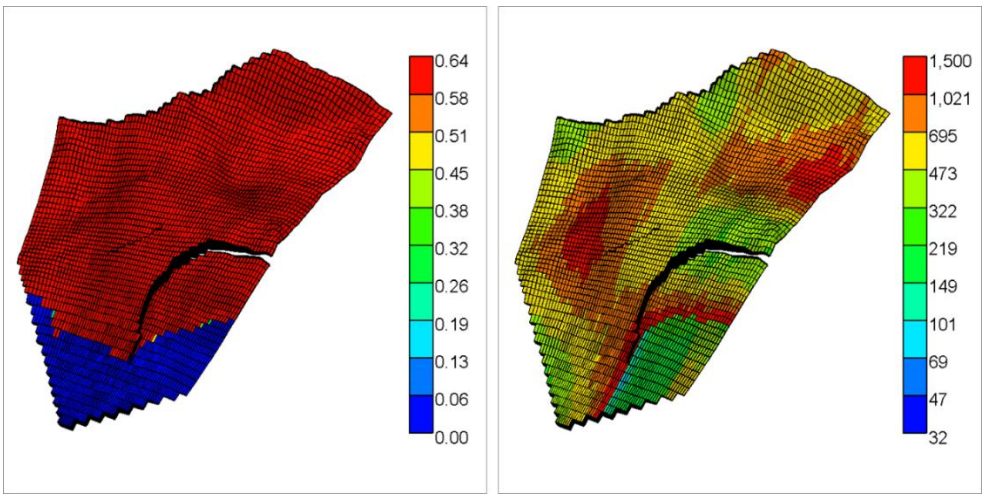

Figure 3.22: Initial oil saturation (legend is oil saturation) and permeability field (legend is mD) in both models.

Well spacing and placement is a significant dissimilarity between the two provinces; thus the North Sea representative model entails fewer wells and larger well spacing. Figure 3.23 shows well placement in each modelling scenario. There are 27 wells (14 producers and 13 injectors) which are positioned approximately on a 40 acre 5-spot pattern in the Permian Basin representative model, except for the south of the model where the pattern is slightly modified to avoid completion of producers in the water leg. Meanwhile, in the North Sea representative model, there are 10 wells (5 producers and 5 injectors) which are positioned in those regions which are believed to be more prolific. The wells in the North Sea representative models should be more prolific to accommodate the chosen production/injection rates efficiently. This is, however, a reasonable assumption as wells offshore are typically drilled with larger bores or sometimes horizontally which makes them prolific.

The depths at which the two reservoir models are located are also different with consequent impact on their fracturing pressure and also lift requirements. The Permian Basin representative model is assumed to be located at a shallower depth (4000ft) and therefore its maximum formation fracture pressure was set to 4000psi. For the North Sea representative model which is located deeper (8000ft), the maximum fracture pressure was set higher, at 7000psi. These values were also considered as the maximum injection pressures for both models. The minimum bottomhole pressure for producers is also different between the two models. The North Sea representative model bottomhole pressures were set to 4000psi to provide enough lift for produced fluids as well. For the onshore representative model, it is only 2000psi, as it is located shallower.

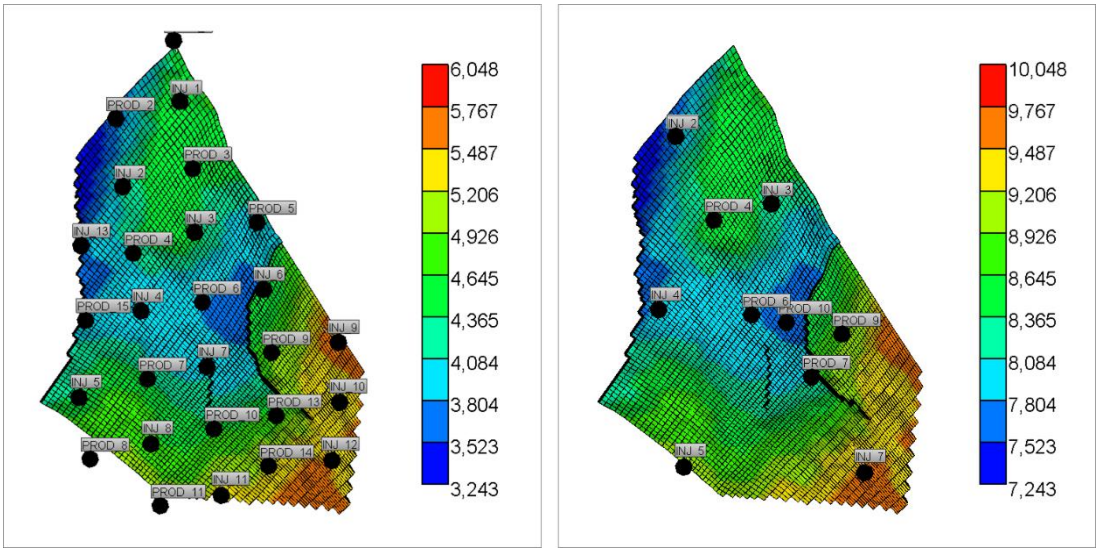

Figure 3.23: Well placement in each development scenario, legends shows the model depth (ft)

The ratio of vertical to horizontal permeability (k_z/k_x) was assumed 0.1, similar in both models. Porosity and permeability *fields* are identical in both models; however, the *absolute permeabilities* are 10 times larger (in all orientations) in the North Sea representative model, in accordance with reported data. Table 3.7 shows all the differences that have been taken into account between the two modelling scenarios. The relative permeabilities and fluid models are assumed identical for both models taken from Chapter 2 (Table 2.3 and Figure 2.1) after the work of Dria *et al*. (1993) and Khan *et al*. (1992). The MMP between CO_2 and oil for the two respective reservoir conditions are around 1200psi and 2400psi respectively (Chapter 2); therefore CO_2 is considered to be fully miscible in both reservoir conditions. Although the same fluid description has been used in both models, the calculated oil viscosity is slightly lower in the North Sea representative model; in accordance with the observations made in Section 4.5.1. Both models have the same number of grid blocks (78×65×13=65910). A cut-off pore volume of 1,000bbl significantly reduces the convergence problems during simulations. The solubility of CO_2 in water was not taken into account for this modelling study, as the time required for three phase flash calculations was prohibitive. The rate of depletion (flooding) for both water and CO_2 flooding is identical for both models, at around 4%HCPV per year.

Table 3.7: Summary of the North Sea and Permian Basin representative models

	Offshore Model	***Onshore Model***
Grid	78×65×13	78×65×13
Length	15000ft	15000ft
Width	8600ft	8600ft
Dip angle	0	0
Horizontal Permeability	710mD	71mD
Vertical Permeability	71mD	7.1mD
Porosity	20%	20%
Depth of the top structure	8000ft	4000ft
Initial Pressure	5000psi	3000psi
Initial Temperature	212F	113F
Number of injectors	5	13
Number of producers	5	14
MMP	2400psi	1200psi
BHP_{min} for producers	3000psi	2000psi
BHP_{max} for injectors	7000psi	4000psi
STOOIP	519MMSTB	529MMSTB
HCPV	591MMRB	591MMRB

In both models, simulation starts with an initial phase of waterflooding. The CO_2 flooding phase initiates, once production drops below 5,000bbl/day. A total of 40%HCPV CO_2 volume is injected in the same injectors as water was already injected. Once injecting the desired CO_2 volume, simulation continues with the final phase of waterflooding, where another 1HCPV of water is injected. The injection and production rates for each reservoir model are controlled only at the reservoir level (at around 55,000bbl/day), i.e. individual well rates are determined automatically by the simulator based on the injectivity or productivity observed for each well. CMG-GEM is the flow simulator used in this study (CMG-GEM 2014.10).

3.8.1 Results

Figure 3.24 compares the recovery factor and watercut profiles between the two models. Note that the notion of "onshore" and "offshore" models in the legends of the following figures refer respectively to the onshore Permian basin and offshore North Sea representative models, as described earlier.

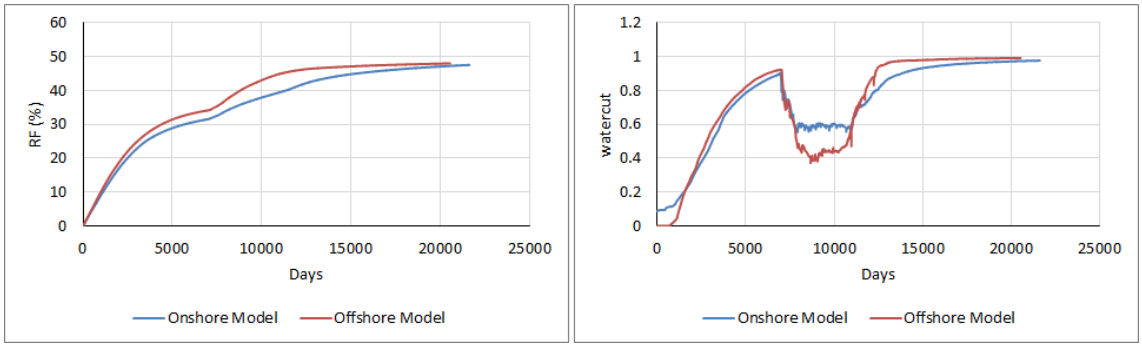

Figure 3.24: Recovery factor and watercut comparison between the two models

In terms of final recovery factor, the two models show very similar results (Figure 3.24, left). During waterflooding, the onshore model shows slightly poorer performance. This is because of proximity of a few producers to the water leg in the onshore model, which causes very early water breakthrough; although their positions had already been modified. The similarity of the initial waterflooding performance between the models shows that the combination of well spacing and placement and also reservoir properties differences have minimal impact on the performance of waterflooding. It can be seen that the watercut profile follows almost the same trend in both models, although well placement and spacing is fundamentally different between the two models.

However, during CO_2 flooding, the performance of the two models becomes markedly different. In both models, the watercut decreases which indicates that oil has been mobilised by CO_2 flooding; nevertheless, this is more significant in the offshore model.

Upon final waterflooding, watercut rapidly increases in both models, though the profiles are again slightly different. In the offshore model, watercut rapidly increases, while in the onshore model, this increase is rather more gradual. Comparison of the oil production rate between the two models is also depicted in Figure 3.25.

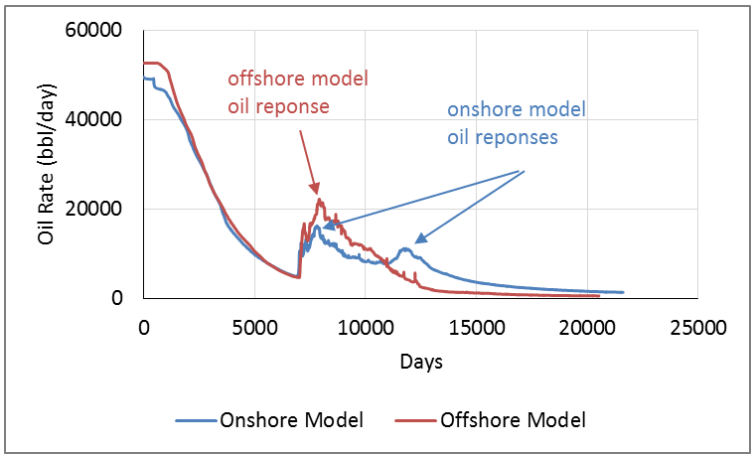

Figure 3.25: Oil production rate comparison between two models

Figure 3.25 shows that two separate oil responses can be identified in the onshore model; the first response occurs once CO_2 injection initiates and the second response occurs upon final waterflooding. For the offshore model, however, only one response can be identified; upon CO_2 injection.

The existence of two oil responses in Figure 3.25 can be attributed to the gravity effects as well; the first oil response is the oil which is recovered by direct oil displacement with CO_2; this is, however, similar in both models. The second oil response in the onshore model is due to mobilisation of a fraction of oil that has been contacted with CO_2 and is CO_2 saturated, but because of CO_2 adverse mobility has not had the chance to become mobilised and displaced to the producers; in other words, it has been bypassed by CO_2.

In the offshore model, the contact between CO_2 and oil is further limited, as gas segregates to the top of the model and thus the second oil response can be hardly recognised. This can be attributed to the higher formation permeability in the offshore representative model. Note that the severity of gravity in the offshore model, is not because of gravity effects between oil and CO_2, though these densities are very similar, however, it is because of gravity effects between CO_2 and water, as was discussed in Chapter 2.

Figure 3.26 compares CO_2 concentration at the end of simulation. It can be seen that CO_2 has been accumulated as a plume underneath the top of the model in the offshore representative model, while in the onshore model, it has been better distributed within the model.

Figure 3.27 shows the gas saturation profiles for two representative producers in onshore (left) and offshore (right) reservoir models in comparison with the profile of heterogeneity (permeability definition). For the onshore model, gas saturation profile follows almost the same pattern of heterogeneity, in that the displacement in this model is dominated by the heterogeneity definition of the system, while for the offshore model, gas is apparently accumulated underneath the top of the model and no correlation can be identified between gas saturation and heterogeneity.

These suggest that gravity is more significant in the offshore representative model. In the onshore representative model, CO_2 distribution within the model is controlled by the permeability irregularities (heterogeneities) which gives a very good contact between CO_2 and reservoir fluid.

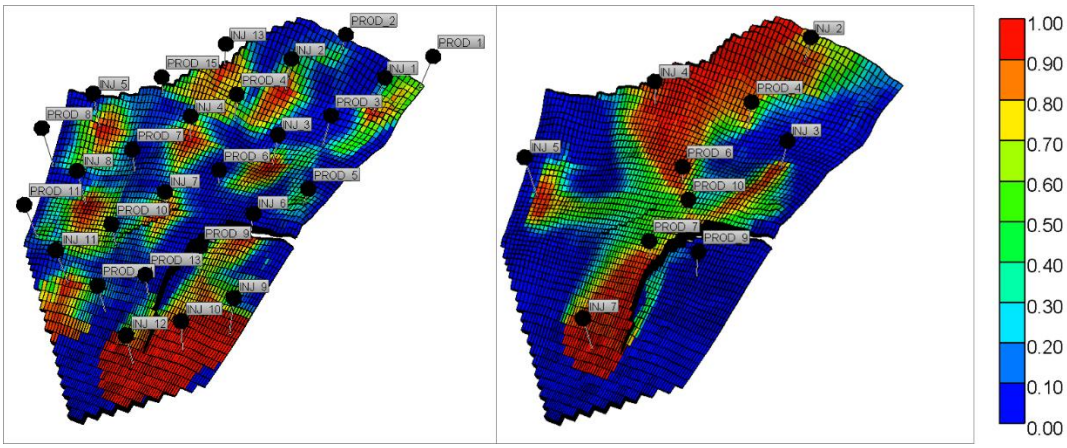

Figure 3.26: CO_2 concentration profile at the end of simulation; comparison between onshore (left) and offshore (right) models.

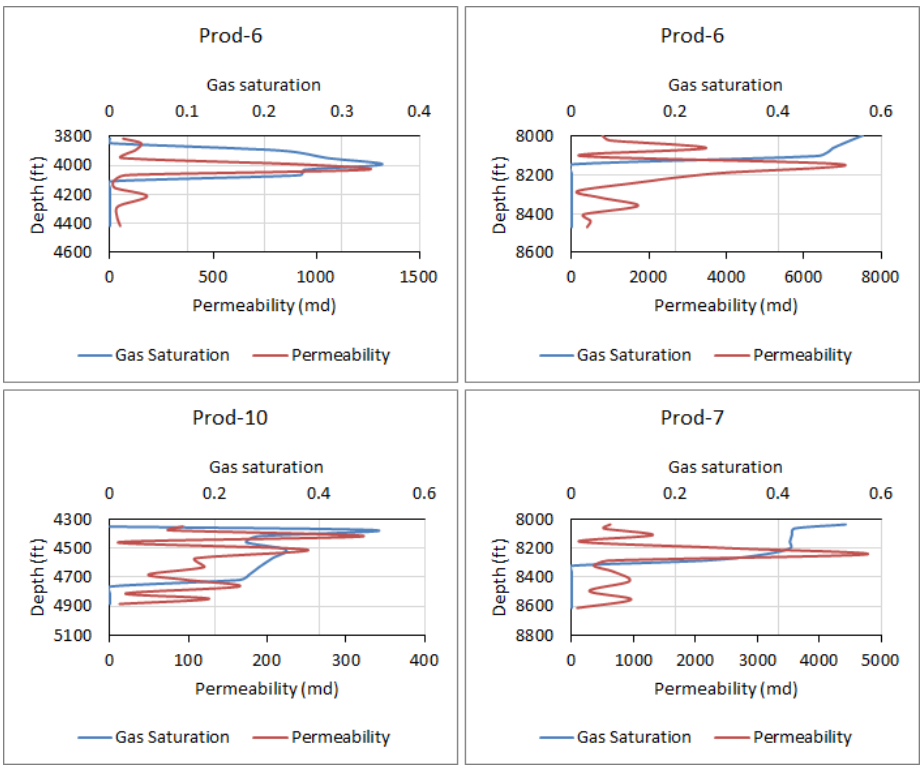

Figure 3.27: Correlation of gas saturation and permeability profiles at the end of CO_2 injection (left: two sample wells in the onshore model, right: two sample wells in the offshore model)

Figure 3.28 shows the fraction of CO_2 that is retained in the oil phase during simulation for the two simulation scenarios. The sharp drop of CO_2 mole fraction in this figure corresponds with the onset CO_2 injection as the majority of injected CO_2 remains in the gas phase. Again because of better CO_2-oil contact in the onshore model, a larger fraction of CO_2 dissolves and remains in the oil phase.

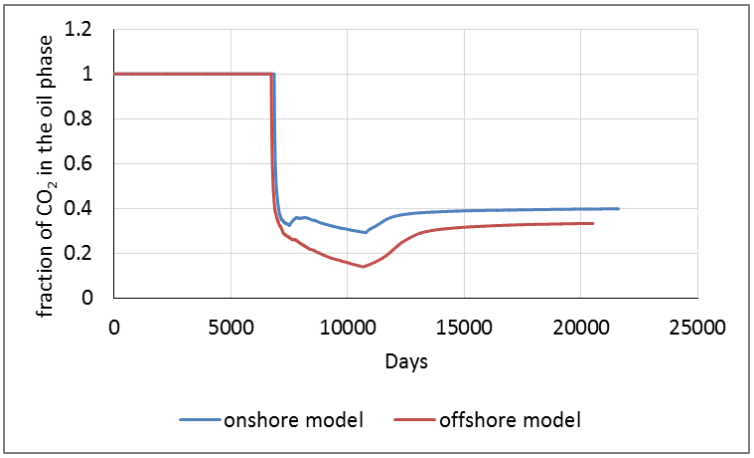

Figure 3.28: Fraction of CO_2 which is retained in the oil phase; comparison between onshore and offshore representative models.

Figure 3.29 (next page) compares the evolution of gas saturation profiles in both models. Note that, although gas saturation in the offshore model increases to higher values during CO_2 flooding period, once waterflooding resumes, it rapidly decreases and stabilises to lower than onshore model values.

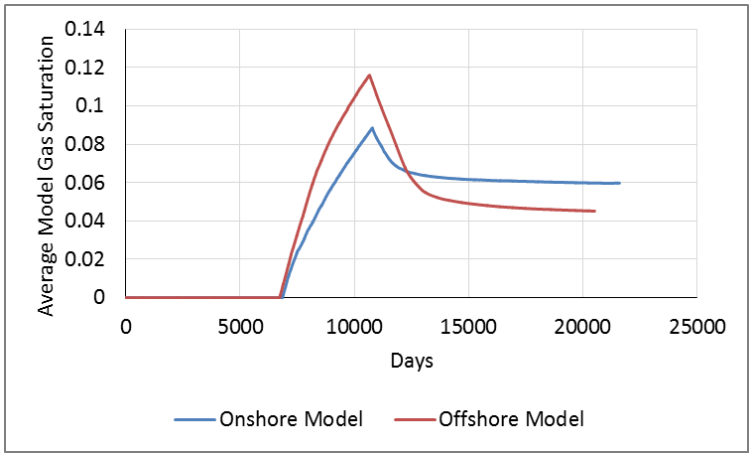

Figure 3.29: Evolution of average gas saturation in both models.

The gravity dominated nature of the displacement in the offshore model can describe this behaviour as well. In the offshore model, the injected gas accumulates underneath the top of the model as a single plume; thus average gas saturation in this region is higher than average gas saturation in the onshore model. On the other hand, in the onshore model, injected CO_2 is distributed across the entirety of the model due to heterogeneity and comes into greater contact with oil, thus a larger fraction of it dissolves in the oil phase and gas saturation increases to relatively lower values. Upon final waterflooding, a larger fraction of the mobile gas in the offshore model is reproduced and hence a smaller fraction of it is trapped, while for the onshore model the fraction of trapped CO_2 is larger, as CO_2 is already better distributed within the model and has not been concentrated in a specific region of the model.

The pressure responses of the two models are also different. Figure 3.30 shows the evolution of average pressure in the two models. The offshore model apparently operates at higher pressure because of its imposed well restrictions. However, note that the evolutions of average pressure have an opposite behaviour at the beginning of CO_2 flooding between the two models (within the yellow shaded area). Upon CO_2 injection, the average pressure in the onshore model increases, while in the offshore model, it decreases.

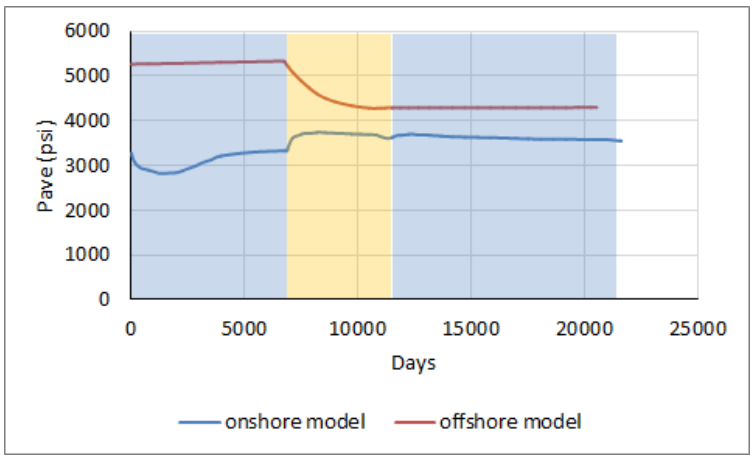

Figure 3.30: Evolution of average pressures in onshore and offshore representative models. Blue and yellow shades represent water and CO_2 injection phases respectively.

This behaviour can be explained by the difficulty in the onshore model to maintain the target voidage rate i.e. injection/withdrawal ratio during waterflooding. In fact, in the onshore model, injection/production to/from a few wells have been restricted to their imposed bottomhole limiting pressures. The already set pressure difference between injectors and producers in the onshore model (2000psi) is not able to effectively accommodate the target (voidage) rate during waterflooding, though well spacing is shorter in this model. Upon CO_2 injection, because of lower CO_2 viscosity, the voidage rate can be better maintained and thus the average pressure in the onshore model increases. In the offshore model, this is not the case as due to higher formation permeabilities, voidage replacement is efficiently maintained. In the offshore model, as CO_2 is injected, average pressure decreases, as due to lower CO_2 viscosity, injectivity significantly improves, thus the average pressure decreases. Table 3.8 compares the final CO_2 flooding performance characteristics between the two models. Note that net CO_2 utilisation is almost two times larger in the onshore model. This is generally because CO_2 has an increased contact with oil in the onshore system. This causes CO_2 to be trapped more in both oil and gas phases and is retained within the formation (Figure 3.28 and Figure 3.29). This explains why the net CO_2 utilization is higher in the onshore representative model.

Table 3.8: Final performance comparison between onshore and offshore representative models.

	Onshore model	**Offshore model**
Net CO_2 utilization efficiency (Mscf/bbl)	8.46	4.65
Final recovery factor	47.5%	47.9%
Incremental recovery	16.2%	14.1%

Figure 3.31 shows the sensitivity of ultimate recovery factor and incremental oil recovery with regard to the injected CO_2 volume, in both reservoir models.

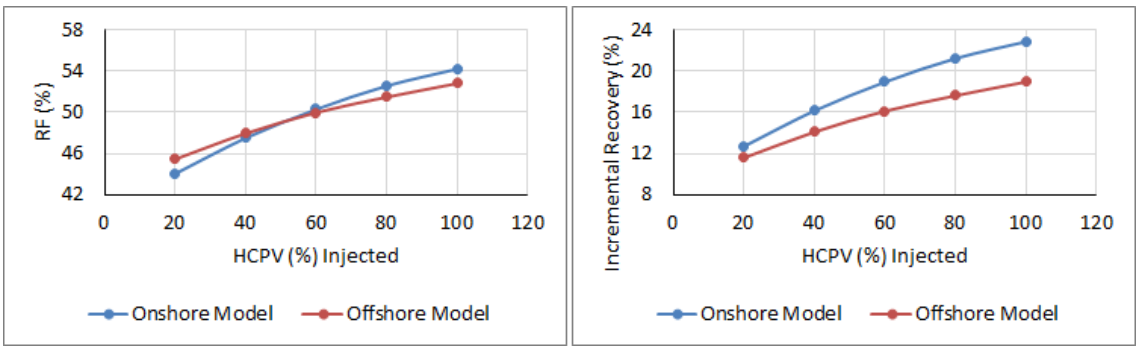

Figure 3.31: Recovery factor and incremental oil recovery for different chosen CO_2 slug volumes injected in each reservoir model.

The fact that incremental oil recovery is always smaller for the offshore model is because of its smaller EOR target (Figure 3.31, right). However, the slopes of the two profiles are slightly different in both right and left figures, which indicates that the benefit of further CO_2 injection is more significant in the onshore model.

A gravity dominated displacement may also impair the WAG performance as was shown in Chapter 2. Figure 3.32 compares the relative benefit of WAG compared to single slug CO_2 injection in each model and for several injected CO_2 volumes. In all the WAG scenarios, the WAG ratio is 1:1 with individual WAG cycle sizes of 0.04HCPV. This figure shows that WAG has generally negative impact (i.e. loss) in the offshore model. In the onshore model, WAG improves the CO_2 mobility ratio since water and CO_2 can better travel together, while in the offshore model, co-injection of water and gas makes the displacement, even more gravity dominated, which further impairs performance (Chapter 2).

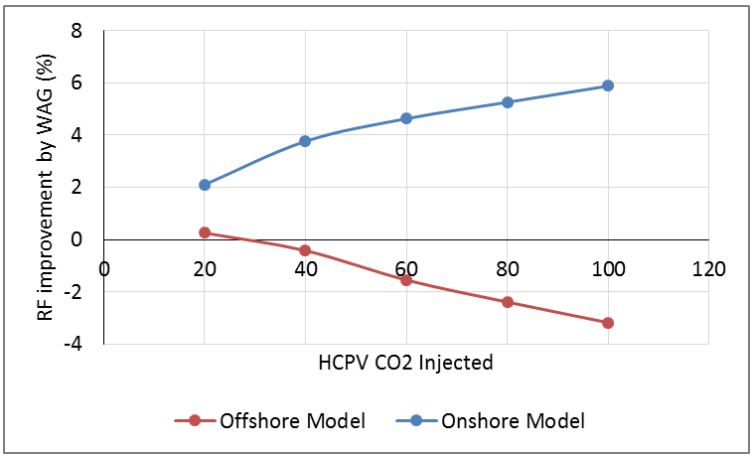

Figure 3.32: Relative WAG improvement in each modelling scenario

One effective measure to reduce the severity of gravity is to conduct the flood at higher pressures as was depicted in Chapter 2. This makes the process more expensive since compression is expensive, however, it allows better elimination of the adverse impact of gravity and improves displacement stability. Additionally more CO_2 will be stored within the system which could be advantageous in combined EOR and CCS CO_2 flooding (Chapter 5).

To illustrate this, the operating pressure of both models were increased by 2000 psi, although this is beyond maximum fracturing pressure, but only to better illustrate the potential benefit on flooding at higher pressures. Figure 3.33 compares the final recovery efficiencies.

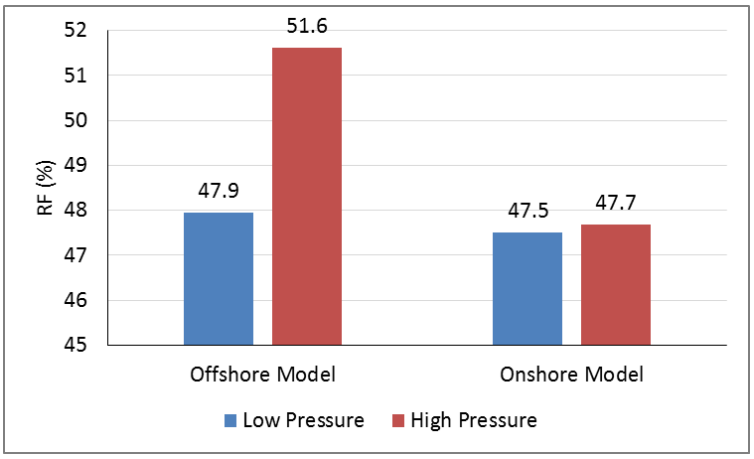

Figure 3.33: Impact of pressure on the recovery efficiency, comparison between onshore and offshore models.

In both models, recovery improves, though the relative improvement is higher in the offshore model. The residual improvement observed in the onshore model is because of improving the mobility ratio of CO_2, though the pressure is already above MMP and the displacement was not gravity dominated. However, for the offshore model, the improvement is more significant, which is due to better countering of the adverse impact of gravity.

Two important conclusions can be drawn from the simulation study conducted in this section. First, the results show that horizontal flooding is expected to be a challenging flooding strategy for those high permeability reservoirs offshore North Sea, principally because of the gravity effects between CO_2 and water. Either injection rates should be increased or gravity stable projects should be undertaken in the North Sea. However, gravity stable projects have their own challenges in the North Sea ambient reservoirs

conditions as will be discussed in the next Chapter. Second, the voidage replacement i.e. injection/withdrawal ratio is not expected to be a challenging problem offshore North Sea since formation permeabilities are generally greater.

3.9 Conclusions

The aim of this study was to correlate different aspects of CO_2 flooding between two important provinces i.e. the North Sea and the Permian Basin provinces. It was found that;

- Significant differences in terms of ambient reservoir conditions exist between the two provinces. Reservoirs in the North Sea are generally deeper, thicker, hotter and are at higher pressures compared to the reservoirs in the Permian Basin.
- Both provinces benefit from relatively good oil compositions, which ensures miscibility development at their prevailing reservoir conditions.
- Screening criteria suggest that apart from the availability of CO_2 sources in the North Sea, CO_2 flooding should be a practical EOR method in this province, similar to the Permian basin.
- Despite fundamental differences in the ambient reservoir conditions, *in-situ* CO_2 properties in terms of CO_2 density and viscosity are similar between the two provinces.
- Solubility of CO_2 in water is very similar and small relative to solubility in oil in both provinces.
- Upon CO_2 flooding, gravity is more significant in the North Sea classes of reservoirs due to considerably better formation permeabilities in this province. This is principally because of density difference between water and CO_2 not because oil and CO_2.
- A higher rate of depletion is favourable in both classes of reservoirs, though it is better for the offshore North Sea systems as it suppresses gravity effects that hinders the displacement in these systems.
- Due to better formation permeabilities in the North Sea classes of reservoirs, maintaining injection/withdrawal ratio is less problematic in this province despite their relatively larger well spacing.

- CO_2 flooding in thicker formations is better in the North Sea classes of reservoirs, while onshore the Permian Basin, this depends on the pattern of heterogeneity.
- Due to larger gravity effects, offshore North Sea systems are less sensitive to the variation of CO_2 slug sizes.
- Pressure is a significant controlling factor in determining the macroscopic sweep efficiency in the North Sea classes of reservoirs. This is due to the impact of pressure on the balance of viscous to gravity effects.
- Due to larger gravity effects, WAG is less effective in the offshore classes of reservoirs.

Chapter 4 CO_2 Flow Patterns Comparison between Offshore North Sea and Onshore United States CO_2 Flooded Reservoirs

4.1 Introduction

CO_2 flooding has been practiced in a large number of reservoirs in the United States. These reservoirs are characterised with thin pays, low reservoir permeabilities, low reservoir temperatures and finally low reservoir pressures. CO_2 flooding in the North Sea classes of reservoirs is likely to be characterised by fundamentally different flooding conditions, both in terms of the formation characteristics and the *in-situ* fluid properties, as was discussed in Chapter 3.

The aim of the study presented in this chapter is to characterise and compare the CO_2 flow patterns between the North Sea and the United States CO_2 flooded classes of reservoirs based on the concept of dimensionless numbers and scaling analysis. This study relies on the field survey findings presented earlier in Chapter 3.

It is important to mention that it is not the aim of this study to explore the different flow regimes in heterogeneous formations from a theoretical point of view as this has been addressed previously by a number of researchers, instead the emphasis is to identify the dominant flow patterns in each class of reservoirs upon CO_2 flooding. This will clarify other characteristics of CO_2 flooding e.g. expected macroscopic sweep efficiencies and the likely extent of WAG bnefit in each of them.

4.2 An Introduction to Random Correlated permeability Field (RCF)

We compare the CO_2 flow pattern between the two classes of reservoirs using synthetic models populated with stochastic permeability fields. The permeability irregularity in this study is represented with the concept of random correlated permeability field (RCF), which is the simplest model of porous medium characterisation with which both variability and permeability structure can be represented in a systematic approach (El-Feghi 1992).

For a given permeability realisation, three geostatistical parameters are enough to describe the heterogeneous nature of the stochastic permeability field; the degree of

heterogeneity variability (V_{DP}) and correlation structures in the two fundamental (λ_x and λ_z) orientations (El-Feghi 1992). For a lognormal permeability distribution, V_{DP} can be approximated with the following correlation.

$$V_{DP} = 1 - \exp(-\sigma_{lnk}) \tag{4.1}$$

Where σ_{lnk} is the sample standard deviation of natural logarithm of permeability values. V_{DP} always lies between 0 and 1. A zero V_{DP} implies that the permeability is absolutely homogeneous, while 1 indicates that formation is perfectly heterogeneous. For most reservoirs the magnitude of V_{DP} lies between 0.4 and 0.9 (Fanchi 2000). Alternate approaches for characterising the heterogeneity is also available. For example Gelhar and Axness introduced the heterogeneity index (I_H) as another measure of the degree of heterogeneity (Sorbie *et al*. 1994). This alternate definition may combine both the correlation length and degree of heterogeneity in one single number.

$$I_H = -{\sigma_{lnk}}^2 \lambda_x \tag{4.2}$$

In this study, the degree of heterogeneity in all the stochastic permeability fields is represented via the concept of V_{DP} and correlation length in fundamental orientations. For a random correlated permeability field, correlation length may determine the maximum distance over which the permeability values are still dependent. The correlated permeability field is modelled using a semivariogram, which is defined as below;

$$\gamma(\vec{h}) = \frac{1}{2n}\sum_{i=1}^{n}\left[k(\vec{x}_i) - k(\vec{x}_i + \vec{h})\right]^2 \tag{4.3}$$

Where γ is the semivariance of the permeability, $k(x_i)$ is the permeability at point (x_i) and $k(x_i+h)$ is the permeability at the spatial point on x_i+h. h is the lag distance vector in a specified direction and n is the number of data pairs used to estimate the semi (Garmeh 2010, Deutsch 2002).

This range measures, how well neighbouring permeability values are related to each other (Waggoner 1992). Qualitatively this number describes different depositional settings. High energy system may be characterised by a relatively short correlation length, while low energy systems may be characterised by a longer correlation length (Waggoner 1992). When the correlation length approaches zero, the medium becomes uncorrelated, in that there is no correlation between the adjacent permeabilities and they are randomly distributed. Similarly an infinite correlation length describes a perfect layered system.

Correlation length can be defined in both horizontal and vertical orientations. The ratio of correlation length in a given orientation to model dimensions can be regarded as the *dimensionless* correlation length in that particular orientation.

$$\lambda_{xD} = \frac{\lambda_x}{L} \tag{4.4}$$

$$\lambda_{zD} = \frac{\lambda_z}{H} \tag{4.5}$$

For a given set of V_{DP} and dimensionless correlation lengths, a number of permeability realisations having identical correlation lengths and V_{DP} may be created. The choice of the correct realisation for the reservoir under study relies significantly on the past information from the field e.g. production history (Waggoner *et al*. 1992).

Different geostatistical models are available to produce the correlated random permeability fields. Waggoner used the turning-band method (TBM) to generate the RCF (Waggoner *et al*. 1992). Sorbie *et al*. (1994) used nearest-neighbour method of Smith and Freeze to generate their random correlated permeability field. Garmeh *et al*. used FFTSim (Jennings *et al*. 2000) to construct their specific random correlated permeability field.

4.3 Scaling Analysis and Dimensionless Numbers

We use scaling analysis for our comparative flow pattern analysis in this study. Scaling analysis and dimensionless numbers are powerful approaches in comparing different flooding scenarios for systems with different dimensions and/or properties. This technique allows transposing different systems into a unique dimensionless domain where different system properties can be described and compared with only a limited set of (dimensionless) numbers. This may make comparison much easier and more straightforward.

In a fully miscible (FCM) displacement scenario, the characteristics of displacement can be described with five dimensionless numbers which may describe different system characteristics. A brief description of these five dimensionless numbers is provided in this section. The derivation method of these dimensionless numbers have not been shown here. Readers can refer to Shook *et al*. (1992) and Gharbi *et al*. (1998) for a more detailed description on the derivation of these dimensionless numbers.

Note that although these scaling numbers have been derived for a FCM process, they can be applied to near miscible processes e.g. CO_2 flooding, where due to near-miscibility effects, the relative permeability effects are negligible (Garmeh *et al*. 2010).

***Mobility ratio*:** This number illustrates the mobility ratio between the displaced and displacing fluids. Since in a FCM displacement only one single phase prevails, the dependence of mobilities on end points relative permeabilities disappears. Hence, the mobility ratio becomes a function of only viscosity ratios.

$$M = \frac{\mu_o}{\mu_s} \tag{4.6}$$

Where μ_o and μ_s respectively refer to the viscosity of oil and solvent (in this case CO_2). Mobility ratio greater than 1 implies an unfavourable displacement in that the displacement may become unstable and the injected solvent breaks through leading to poor recovery efficiencies.

***Effective Aspect Ratio (N_{RL} or Shape Factor)*:** The effective aspect ratio is the ratio of the time required for the fluid to cross the reservoir in the horizontal direction to that in the vertical direction (Garmeh 2010, Novakovic 2002).

$$N_{RL} = \frac{L}{H}\sqrt{\frac{k_z}{k_x}} \tag{4.7}$$

The magnitude of N_{RL} illustrates the degree of cross flow within the system. This number also controls the occurrence of vertical equilibrium (*VE*) in a given flood, in that for N_{RL}s>10 vertical equilibrium may prevail (Lake 1989). Vertical equilibrium may imply the existence of infinite vertical permeability in the system (Coats *et al.* 1991) where all the driving forces transverse to the direction of bulk flow sum to zero. In horizontal flow, vertical equilibrium implies that the pressure gradient in the vertical direction is zero (El-Feghi 1992). Use of vertical equilibrium can lead to the reduction of the dimensionality of the problem (Yortsos 1992). A zero N_{RL} indicates that no cross flow can occur within the system.

***Gravity number*:** This number determines the significance of gravity relative to viscous forces. Gravity number has been cited by different formulations in the literature (Tchelepi *et al*. 1994, Araktingi and Orr 1990, Shook *et al*. 1992). Tchelepi *et al*. (1994) used the Fayers and Muggeridge gravity number formulation defined as the ratio of viscous to gravity forces.

$$R_{v/g} = 2\left({}^{\bar{v}\Delta\mu}/_{\Delta\rho g k_z}\right)\left({}^{h}/_{L}\right) \tag{4.8}$$

Novakovic (2002) provides a comprehensive list of different gravity number formulations used in the petroleum engineering literature. In this study we use the gravity number formulation suggested by Shook *et al*. (1992) and Gharbi *et al*. (1994). Chang *et al.* (1994) has also used this gravity number formulation to characterise different CO_2 flow patterns.

$$N_g = \frac{H}{L}\frac{k_x \Delta\rho g}{\mu_o u_T} \tag{4.9}$$

Where H and L are respectively the thickness and length of the formation. k_x is the absolute permeability in the horizontal direction. $\Delta\rho=\rho_o-\rho_s$ is the density difference between oil and solvent (in this study CO_2), g is the gravitational constant, μ_o is the oil viscosity and u_t is the injection pore velocity (i.e. interspatial velocity). This definition of gravity number illustrates the ratio of gravity to viscous forces. This expressed form of gravity number may indicate that gravity is more significant in thicker formations (with larger H).

If, however, time is taken into account, i.e. the time that is required for gravity to act and segregate the fluid from the bottom to the top of the formation, then gravity number will have a different formulation (Novakovic 2002).

$$N_{gt} = \frac{{}^{L}/_{u_x}}{{}^{H}/_{u_z}} = \frac{t_v}{t_g} = \frac{L}{H}\frac{u_z}{u_x} = \frac{L}{H}\frac{k_z \Delta\rho g}{\mu_s u_T} = M N_{RL}{}^2 N_g \tag{4.10}$$

This number (N_{gt}) could be regarded as the combination of several other dimensionless numbers. Appendix-2 shows how this alternate definition of gravity number (N_{gt}) can be derived. This alternate formulation indicates that gravity is more significant *in longer and thinner* formations as opposed to the previous definition (Equation (4.9)) (Novakovic 2002). In this study we use both definitions of gravity numbers.

If, however, the *in-situ* velocity (u_t) is expressed in terms of the rate of depletion and well spacing (Equation (4.16)), then N_{gt} will not be dependent on well spacing (L).

***Longitudinal and transverse Peclet Numbers*:** These two last numbers illustrate the ratio of component transport by viscous mechanisms to that of diffusion/dispersion mechanisms in two fundamental orientations.

$$Pe_L = \frac{L}{\alpha_L} \tag{4.11}$$

$$Pe_T = \frac{H^2}{L\alpha_T} \tag{4.12}$$

A large Peclet number may imply that diffusion/dispersion effects are negligible compared to viscous transport phenomena. For the analysis conducted in this study, these last two scaling groups will not be taken into account. Nevertheless, there will be a fixed background dispersion as a result of discretisation of the stochastic permeability field (i.e. numerical dispersion).

4.4 A Review of Different Flow Regimes

A review of different flow patterns is presented in this section. In principal, flow patterns can be categorised in one of the main four categories. A *Gravity dominated* flow pattern, is that where the injected fluid segregates due to buoyancy effects. A *Fingering dominated* flow pattern occurs at adverse mobility ratio and at low degree of heterogeneity, and is usually found in the laboratory cores or sandpacks (Waggoner *et al*. 1992). A *Channelling dominated* flow pattern is that where the injected fluid preferentially follows the high permeability streaks. These two last flow regimes (fingering and channelling) are collectively referred to as unstable flow patterns, though the underlying mechanism for instability is different between them. If neither of these flow patterns dominates, then the displacement will be dominated by *dispersive* (stable) flow pattern.

Flow pattern characterisation has been an active area of research (Waggoner *et al*. 1992, Kempers 1990, Chang *et al*. 1994, Sorbie *et al*. 1994). Waggoner *et al*. (1992) found that good transverse communication (a minimum value of cross flow) is required to initiate fingering (Waggoner). They also showed that for M=10 (adverse mobility ratio) in permeability fields with very low correlation length, flow should be dispersive at the level of heterogeneity $0.3< V_{DP} <0.9$ assuming *VE*. At larger $V_{DP,}$ the characteristic of displacement is determined by both the heterogeneity and the spatial arrangement of permeability rather than V_{DP}.

Sorbie *et al*. (1994) studied the significance of effective aspect ratio in affecting the flow regime. They showed that the effective aspect ratio (N_{RL}) significantly affects the balance

between dispersive-fingering flow regimes in displacements characterised with adverse mobility ratios.

They showed that it is possible for the dispersive effect of the permeability field to dominate the fingering tendency of the mobility ratio in highly heterogeneous systems which depends on the magnitude of the effective aspect ratio (Sorbie *et al*. 1994). The effect of shape factor is much more important at short correlation lengths (Sorbie *et al*. 1994). They found that effective aspect ratio (N_{RL}) is less important in channelling flow regimes (Sorbie *et al*. 1994).

Chang *et al.* (1994) studied the CO_2 flow patterns by conducting compositional simulations, taking into account the effect of relative permeabilities and multiple contact miscibility effects. They found that unlike FCM simulations, for MCM simulations, due to relative permeability effects and also formation of a transition zone (Chapter 2), the fingering regime is supressed significantly and is extremely small.

They concluded that CO_2 flooding at the field scale is dominated by viscous fingering only when N_g is very small and the permeability field is characterised with small V_{DP} and short correlation length; therefore viscous fingering is not expected to be a dominant flow pattern for field scale CO_2 flooding, even without WAG.

The distinction between flow patterns is both important and challenging. Different criteria exists in the literature to assist distinguishing between different flow regimes. The dispersive (stable) and unstable flow patterns can be characterised based on the characteristic length of their mixing zone.

A mixing zone that increases linearly with time (t) characterises an unstable or bypassing (either fingering or channelling) displacement whereas a mixing zone that increases with the square root of time ($\sqrt{t}$) is dispersive (Figure 4.1) (Waggoner *et al*. 1992). A dispersive flow regime exhibits iso-concentration lines that are roughly equivalent in the vertical direction (Waggoner *et al*. 1992).

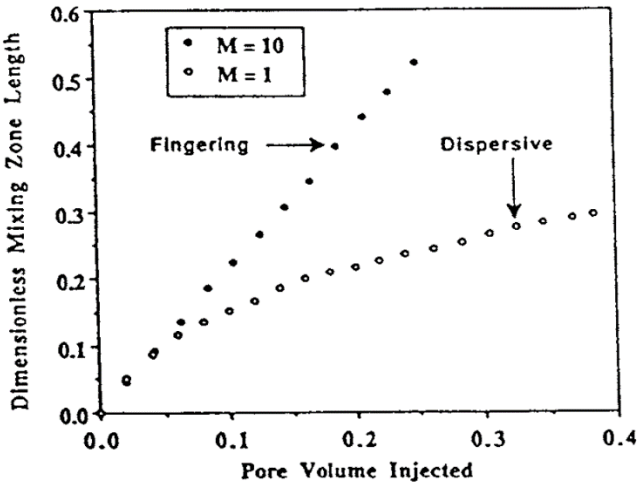

Figure 4.1: Mixing zone growth with two mobility ratios representing Fingering and Dispersive flow patterns (Sorbie et al. 1994)

Kempers used another criterion to distinguish the dispersive and fingering flow regimes using I_H and M described above. However, Sorbie *et al*. (1994) showed that this criterion, although informative, is not good enough for all the systems under investigation as the significance of effective aspect ratio has been taken into account for this criterion.

Waggoner *et al*. (1992), Sorbie *et al*. (1994) and Chang *et al*. (1994) developed maps in terms of the magnitude of different dimensionless numbers to characterise the dominant flow patterns. Figure 4.2 shows the Chang *et al.* (1994) flow regimes map.

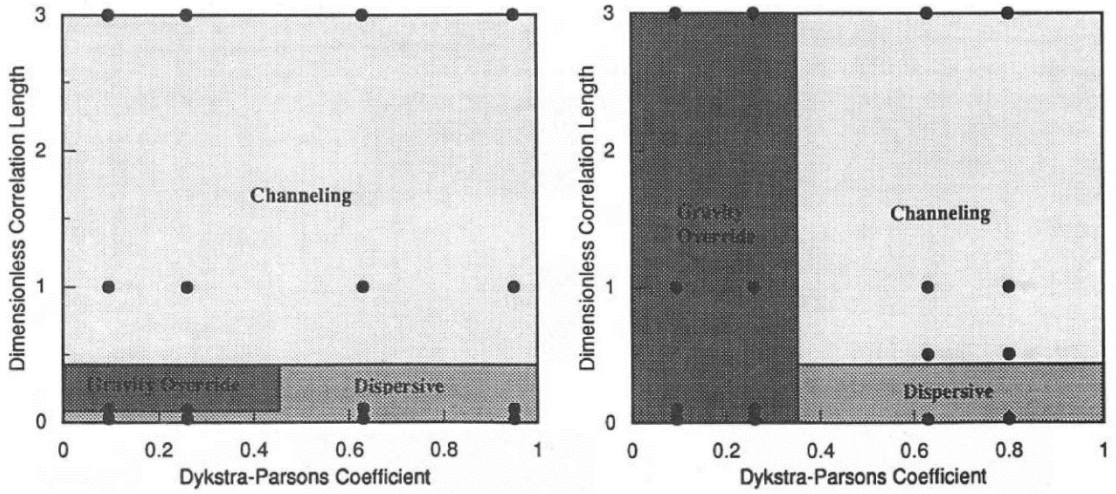

Figure 4.2: Flow regime maps for isotropic MCM CO_2 flood at Ng=0.016 (left) and Ng=0.049 (right). (Chang et al. 1994)

These maps, although useful, are of limited application for our study. This is because the underlying assumptions in generating them could be different than those in our study. For example, Waggoner *et al*. (1992) derived their flow pattern maps assuming the displacement is conducted at the condition of *VE*. Similarly Sorbie *et al.* (1994)

developed flow pattern maps that only work in the absence of gravity effects and at similar correlation lengths in both orientations. Only Chang *et al*. (1994) have developed maps that take into account all the major four flow patterns; however, they have investigated flow patterns for only two magnitudes of effective aspect ratio of 16.4 and 50.

To characterise flow patterns in this study, we use the same approach used by Chang *et al*. (1994) for flow pattern identification in that the dominant flow regimes are recognised by repeating the *same simulation in three different flooding configurations* i.e. cross sectional, areal and areal with unit mobility ratio. A gravity dominated flow pattern can be identified by comparing flow patterns between cross sectional and areal simulation models. Similarly, channelling and fingering flow patterns can be distinguished by comparing flow patterns at *unit mobility* and *actual mobility* ratios. A channelling dominated flow pattern will not be very sensitive to the mobility ratio and will show almost the same concentration profile irrespective of the mobility ratio, while a fingering dominated flow pattern may not be observed at unit mobility ratio (Waggoner *et al*. 1992, Chang *et al*. 1994).

Flow patterns can affect the design of a given CO_2 flood. If the displacement is significantly gravity dominated, then horizontal flow is not perhaps the best flooding strategy. For a gravity dominated flow pattern, WAG has no or limited benefit as it is hard for gas and water to travel together due to buoyancy. In this condition the impact of WAG will be limited to only the near wellbore region. A stable (dispersive) flow pattern implies that the recovery is only sensitive to the *quantity* of injected solvent (or CO_2) and not to the *timing* of solvent and water injection, if WAG is practiced. For an unstable displacement, recovery will be sensitive to *both* the timing and the quantity of injected solvent.

4.5 Estimating Dimensionless Numbers for the Onshore United States and Offshore North Sea Classes of Reservoirs

The first step in characterising the flow patterns in each class of reservoirs is to have an estimate of the ranges of key dimensionless numbers which may characterise the displacement in each of them. Table 4.1 and Table 4.2 show major reservoir properties for these two classes of reservoirs.

Table 4.1: Major reservoir properties for a number of reservoirs located in the North Sea (Awan et al. 2008)

Offshore	*Formation*	*P (psi)*	*T (F)*	*API*	*Oil viscosity (cP)*	*H (ft)*	*K (mD)*	*B_o (rb/bbl)*	*GOR (scf/stb)*
Ekofisk	Ekofisk	7218	268	36	0.17	394	100	1.76	1476.7
Ekofisk	Tor	7218	268	39	0.17	197	100	1.76	1476.7
Statfjord	Statfjord	5939	210	34	0.29	207	750	1.54	870.3
Statfjord	Brent	5660	198	41	0.31	377	2300	1.58	1066.9
Brent	Statfjord/Unit 1	6218	217	40	0.25	89	2000	2	2173.0
Alwyn North	Brent	6615	235	35	0.30	312	2000	1.6	954.6
Smorbukk	Gam	5954	284	35	0.16	384	600	2.2	1965.3
Snorre A	Statfjord	5630	194	39	0.70	131	2000	1.35	449.2
South Brae	Upper Brae	7232	253	38	0.30	164	130	1.7	1342.0
Magnus	MSM/LKCF	6747	241	34	0.50	607	1000	1.5	724.3
Thistle	Brent-Tarbert	6145	216	36	1.10	384	1220	1.25	292.0
Gulfaks	L-Brent	4557	165	36	1.12	623	4500	1.25	561.5
Brage	Fensfjord.	3161	190	41	0.56	131	200	1.29	522.2

Table 4.2: Major reservoir properties for a number of CO_2 flooded reservoirs in the United States (Brock & Bryan 1977)

Onshore	*Formation*	*Pressure (psi)*	*Temperature (F)*	*API*	*Oil viscosity (cP)*	*H (ft)*	*K (mD)*	*B_o (rb/bbl)*	*GOR (scf/stb)*	*Pattern Area*
Dollarhide	Devonian	3300	120	40	0.4	48	9	1.656	1270	80acre
East Vaccum	San Andres	1613	101	38	1	71	11	1.29	465	20 acre
Ford Geraldine	Delaware	1400	83	40	1.4	23	64	1.26	575	40 acre
Means	San Andres	2000	100	29	6	54	20	1.04	250	10acre
North Cross	Devonian	2500	106	44	0.4	60	5	1.986	1688	22acre
Norht East Purdy	Springer	3500	148	35	1.5	40	44	1.38	724	80acre
Rangely	Weber	2750	160	32	1.6	110	50	1.1	300	20acre
Sacroc	Canyon Reef	3122	130	41	0.4	139	3	1.472	1000	40 acre
South Welch	San Andres	2100	92	34	2.3	132	13.9	1.111	209	10acre
Twofreds	Delaware	2385	104	36	1.4	18	33.4	1.179	441	80 acre
Wertz	Tensleep	3300	165	35	1.3	185	16	1.16	205	10acre
Little Creek	Tuscaloosa	4840	248	39	0.4	30	75	1.32	555	31acre (pilot)
Maljamar	San Andres	2600	90	36	0.8	49	11.2	1.23	500	5 acre
Maljamar	Gray Burg	2600	90	36	0.8	23	13.9	1.23	500	5acre
North Coles Levee	Stevens	4000	235	36	0.5	136	9	1.507	800	5acre
Quarantine Bay	4sand	3830	183	32	0.9	15	230	1.23	435	1000ft
Slaughter Estate	San Andres	1710	105	32	2	75	8	1.228	460	20 acre
Weeks Island	S Sand R (B)	6013	225	33	0.3	186	1200	1.62	1200 (assumed)	500ft
West Sussex	Shannon	2150	104	39	1.4	22	28.5	1.143	284	9.6acre pilot
Little Knife	Mission Canyon	4409	245	41	0.2	16	30	1.769	1119	5acre
Hansford Marmaton	Marmaton sandstone	142	2080	48	38	20	1750	1.36	640	5acre
Lickcreek	Meakin	1200	118	17	160	9	1200	1.05	200 (assumed)	20 acre

We use the data depicted in these tables to calculate the key dimensionless numbers i.e. the effective aspect ratio (N_{RL}), gravity numbers (N_g and N_{gt}) and the mobility ratio (M)

upon CO_2 flooding in in each individual reservoir. Next sections illustrate how these dimensionless numbers may be inferred from the data depicted in the above tables. The majority of the data were obtained from Brock & Bryan (1977) and Awan *et al*. (2008). Additional data for each of the reservoir parameters were obtained from appropriate literature.

4.5.1 Effective Aspect Ratio (N_{RL})

To estimate the effective aspect ratios (N_{RL}), an estimate of the spacing between wells (L), the thickness of the formation (H) and the ratio of vertical to horizontal permeability (k_z/k_x) is required (Equation 4.5). The spacing between wells for the reservoirs located onshore United States (Table 4.1) were inferred from their reported developed pattern area. For example a 5-spot 40-acre pattern development, may equate to 1320ft spacing between pairs of injectors and producers.

The thickness of the formations is taken from relevant tables. The ratio of k_z/k_x, however, was assumed equal to 0.1 for the entire list of reservoirs. This is a fairly good first guess for the majority of reservoir studies.

For the reservoirs in the offshore system (Table 4.2), well spacing, although larger, is not typically constant, since offshore North Sea wells are mostly placed based on geological considerations rather than following a specific pattern. Inspection of field data shows that average spacing between wells in the offshore North Sea is in the order of 1km (3280ft) (Crogh *et al*. 2002, Bath 1987).

This was taken to be a first approximation of well spacing for all the entire reservoirs located offshore North Sea. The reservoir thickness for the offshore fields is taken from Awan *et al*. (2008). As with the onshore fields a first guess of 0.1 was taken as the best estimate of the ratio of k_z/k_x in this study. Figure 4.3 compares the ranges of calculated N_{RL}s for the reservoirs located in these two classes of reservoirs.

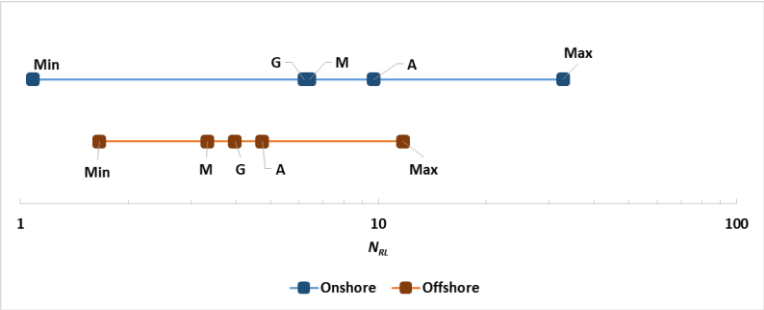

Figure 4.3: Range of effective aspect ratio (N_{RL}) estimated for onshore United States and offshore North Sea classes of reservoir. The solid dots show the magnitude of the minimums (min), maximums (max), arithmetic (A) and geometric (G) averages and finally the medians (M) of the data.

4.5.2 Gravity Number (N_g)

Calculation of gravity number upon CO_2 flooding is not straightforward, as it needs additional information about the densities of oil and CO_2 at relevant ambient reservoir conditions. Moreover, an estimate of the *in-situ* fluid velocity is required (Equations 4.7 and 4.8).

While oil densities at surface condition (in terms of the oil's API) are widely reported in the literature, the *in-situ* oil densities at ambient reservoir conditions are rarely reported and hence need to be approximated by appropriate correlations. The *in-situ* oil densities (ρ_o) were estimated using the correlation below (McCain 1991).

$$\rho_o = \frac{62.4\gamma_o + 0.0136\gamma_g R_s}{B_o} \tag{4.13}$$

γ_o and γ_g are oil and gas specific gravities respectively and R_s and B_o are gas oil ratio and oil formation volume factor. γ_o and R_s in the above correlation are generally known for the majority of reservoir fluids in both classes of reservoirs. However, an estimate of the produced gas specific gravity (γ_g) is required which typically is not well reported in the literature. Gas specific gravities (γ_g) were approximated using the following correlation proposed by McCain (1991), given the formation volume factor (B_{ob});

$$B_{ob} = 0.9759 + 12(10^{-5}){C_{Bob}}^{1.2} \tag{4.14}$$

$$C_{Bob} = R_s \left({\gamma_g}/{\gamma_o}\right)^{0.5} + 1.25T \tag{4.15}$$

The uncertainly in the estimation of γ_g may in turn affect oil densities. This is more significant in the offshore North Sea system as gas-oil ratios are generally higher and oil densities are thus more sensitive to the magnitude of γ_g.

Figure 4.4 compares the range of calculated oil densities in both classes of reservoirs. The calculated *in-situ* oil densities for the North Sea systems ranges from 32 to 46lb/ft^3 while for the United States reservoirs, this is between 35 and 57lb/ft^3.

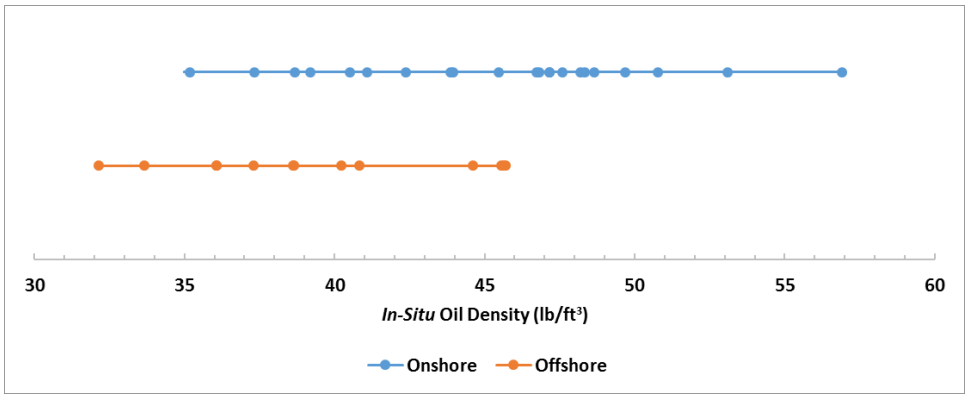

Figure 4.4: Comparison of the ranges of calculated oil densities between the two classes of reservoirs

The *in-situ* CO_2 properties i.e. density and viscosity were estimated using the CMG-WinProp software at appropriate ambient reservoir conditions. Our results show that while oil and CO_2 densities are more comparable in the United States CO_2 flooded reservoirs, CO_2 densities at ambient reservoir conditions in the North Sea are slightly higher than oil densities, which may produce *negative* gravity numbers upon CO_2 flooding.

Additionally, an estimate of the *in-situ* fluid velocities is also required for the calculation of gravity numbers (N_g and N_{gt}). To do this, we have used the proposed correlation of Parsons (1974) which estimates the *in-situ* velocities for a developed 5-spot pattern. We modified the Parsons correlation to estimate the *in-situ* fluid velocity as a function of well spacing and the rate of depletion.

$$v_f\,(\text{ft/day}) = 0.003259 \times r\,(\text{fraction}) \times L\,(\text{ft}) \qquad (4.16)$$

Appendix-1 shows how this correlation has been derived. Although this correlation has been derived for a 5-spot well spacing, we have used it for all the reservoirs in both onshore and offshore systems. The *in-situ* velocity by Equation (4.16) is in field units and should be converted to *SI* units prior to calculating gravity number. The rate of depletion in the above correlation (r) is the fraction of HCPV which is produced annually and can

be approximated based on the ratio of annual cumulative production (at reported plateau production rate) to *STOIIP* for each single reservoir.

$$\boldsymbol{r}(fraction) = \frac{q\left(^{stb}/_{day}\right) \times 365(days)}{N_{STOIIP}\,(stb)} \tag{4.17}$$

Where q is the plateau production rate and N is the *STOIIP*. Where data are missing, an average values as 2% and 4% respectively for the onshore United States and offshore North Sea reservoir systems have been assumed based on inspecting the data from other available reservoirs. Figure 4.5 compares estimated average velocities between the two groups of reservoirs. Figure 4.5 shows that velocities are roughly an order of magnitude higher in the North Sea classes of reservoirs. While the median velocity in the North Sea classes of reservoirs is around 0.47ft/day, in the onshore United States CO_2 flooded reservoirs, this is only 0.043ft/day.

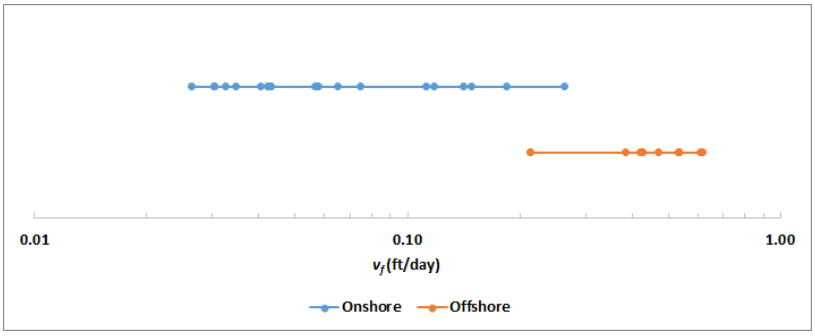

Figure 4.5: Range of the in-situ velocity (v_f) estimated for onshore and offshore reservoir systems

Having calculated the gravity number constituents, Figure 4.6 and Figure 4.7 compare the calculated ranges of gravity and time-defined gravity numbers (N_g and N_{gt}) for the two classes of reservoir. It can be seen that both N_g and N_{gt} are slightly higher for the reservoir systems located in the North Sea.

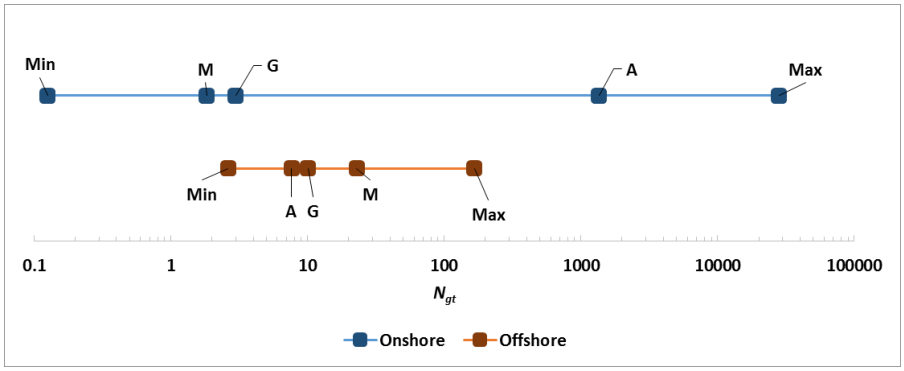

Figure 4.6: Range of time-defined gravity number (N_{gt}) estimated for onshore and offshore reservoir systems. The solid dots show the relative position of minimums (min), maximums (max), arithmetic (A) and geometric (G) averages and finally the median (M) of the data.

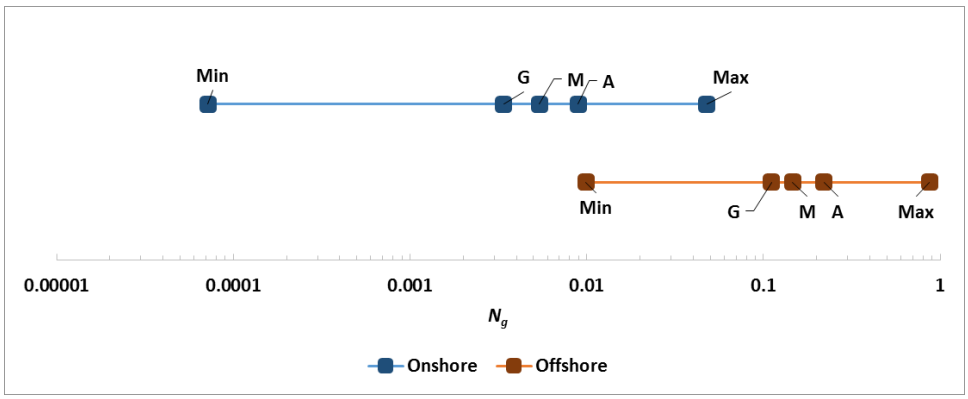

Figure 4.7: Range of gravity number (N_g) estimated for onshore and offshore reservoir systems. The solid dots show the relative position of minimums (min), maximums (max), arithmetic (A) and geometric (G) averages and finally the median (M) of the data.

4.5.3 Mobility Ratio (*M*)

The mobility ratios were estimated using the ratio of the reported oil viscosity to the CO_2 viscosity calculated at relevant ambient reservoir conditions. Figure 4.8 shows results. Note that mobility ratios are generally better in the North Sea classes of reservoirs.

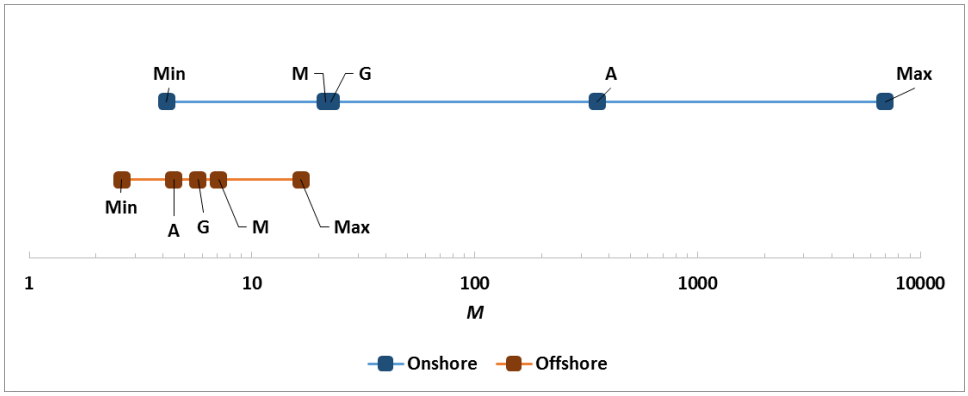

Figure 4.8: Ranges of the mobility ratio (M) estimated for onshore and offshore reservoir systems. The solid dots show the relative position of the minimums (min), maximums (max), arithmetic (A) and geometric (G) averages and finally the median (M) of the data.

4.5.4 Summary of Dimensionless Numbers

Figure 4.9 to Figure 4.11 show cross plot of effective aspect ratio (N_{RL}), mobility ratio (M) and time-defined gravity (N_{gt}), all versus gravity number (N_g) for both classes of reservoirs.

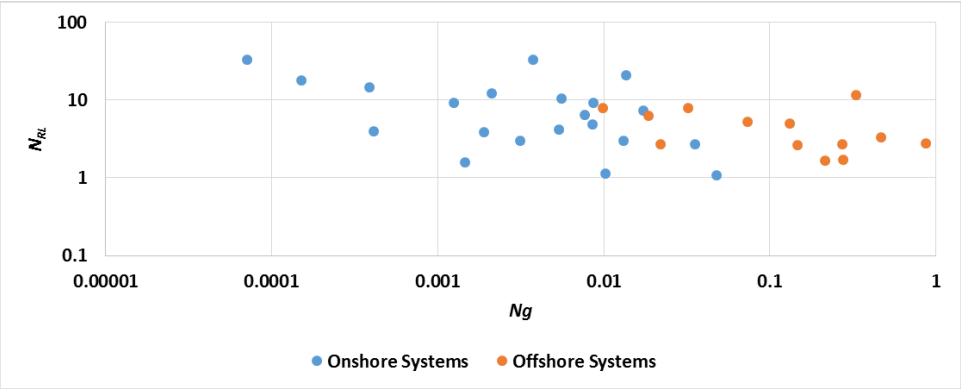

Figure 4.9: Cross plot of effective aspect ratio (N_{RL}) vs. gravity number (N_g) in the two reservoir systems

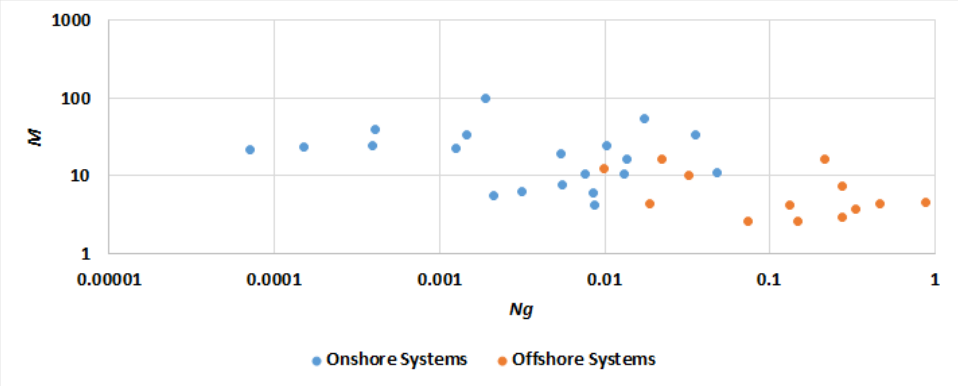

Figure 4.10: Cross plot of mobility ratio (M) vs. gravity number (N_g) in the two reservoir systems

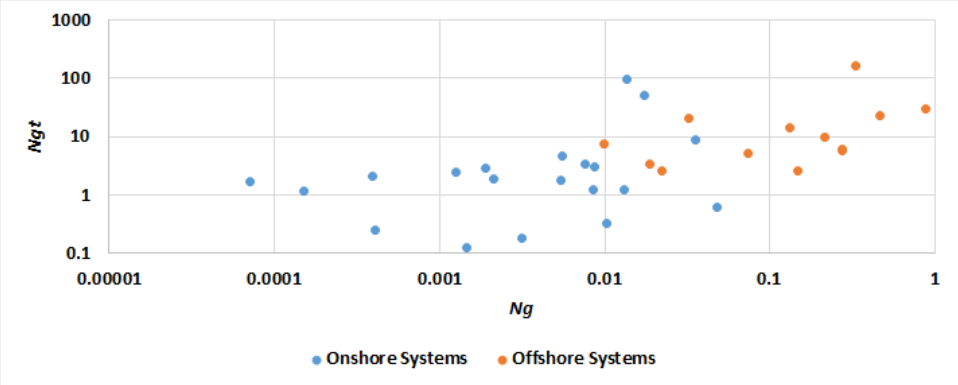

Figure 4.11: Cross plot of time defined gravity number (N_{gt}) vs. gravity number (N_g) in the two reservoir systems

As a summary, gravity numbers are an order of magnitude smaller in the onshore classes of reservoirs, effective aspect ratios are slightly higher in the onshore classes of reservoirs and mobility ratios are better in the North Sea. This may create significant differences in the dominant flow patterns upon CO_2 flooding between the two classes of reservoirs as will be shown later.

The final calculated dimensionless numbers are depicted in Table 4.3. The individual dimensionless numbers are not reported in this table, instead, main sample representatives for each class of reservoirs are reported. The reported *medians* in each class of reservoirs will be used later as the base cases magnitudes for investigating dominant flow patterns in the respective classes of reservoirs.

Table 4.3: Averages, median, minimum and maximum of the estimated dimensionless numbers for each classes of reservoirs

		N_{RL}	N_g	N_{gt}	M_o
Offshore reservoir systems	Geometric Average	3.97	0.111	10.04	5.72
	Arithmetic Average	4.74	0.220	7.63	4.47
	Median	***3.32***	***0.146***	***22.82***	***7.10***
	Min	1.66	0.010	2.61	2.60
	Max	11.71	0.871	165.87	16.59
Onshore reservoir systems	Geometric Average	6.216	0.0034	2.970	22.63
	Arithmetic Average	9.714	0.0090	1352	353.71
	Median	***6.416***	***0.0054***	***1.828***	***21.3***
	Min	1.085	0.0001	0.125	4.13
	Max	32.795	0.0478	28221	6956

4.5.5 Uncertainty in the Estimated Dimensionless Numbers

Before using the above numbers to characterise the flow patterns in each class of reservoirs, it is important to evaluate the impact of uncertainty for each dimensionless number in either class of reservoirs.

Five parameters have been chosen in this section to investigate the impact of their uncertainty on the evaluation of N_{RL} and N_g dimensionless numbers; horizontal permeability (k_x), rate of depletion (r), well spacing (L), formation thickness (H), k_z/k_x ratio and finally gas specific gravity (γ_g). Sensitivity analyses were only conducted for gravity and effective aspect ratio numbers and not for the mobility ratio, since mobility ratios have been exactly calculated from literature values with minimum uncertainty.

Except k_z/k_x ratio, sensitivity analysis was conducted by doubling and halving the above input parameters and investigating the ranges of variation of relevant dimensionless numbers. For k_z/k_x ratio, sensitivity analysis was conducted by increasing and decreasing the base case k_z/k_x by an order of magnitude around the base case value of 0.1. Figure 4.12 shows the results of the sensitivity analysis. The left and right images respectively show the ranges of estimated of gravity (N_g) and effective aspect ratio (N_{RL}) numbers.

The top and bottom images represent the variability of dimensionless numbers in onshore and offshore systems.

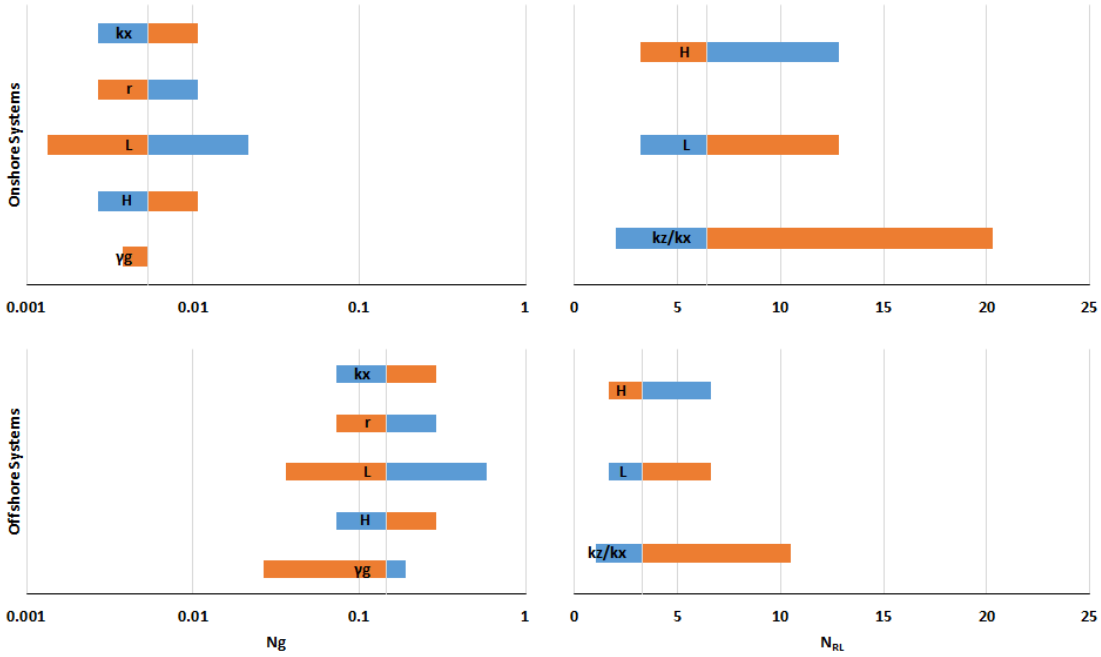

Figure 4.12: Sensitivity analysis for gravity (left) and effective aspect ratio (right) numbers for onshore (top) and offshore (bottom) systems

The results depicted in Figure 4.12 show that for gravity number, even taking into account the range of uncertainty for either of the systems, there is still far a big distinction between the magnitudes of gravity numbers (N_g) for both systems. For effective aspect ratio (N_{RL}), this is not the case and the two systems have a considerable degree of overlap.

4.6 Investigating Flow Patterns in both Classes of Reservoirs

The next step is to conduct a number of simulations using the derived ranges of dimensionless number in both classes of reservoirs to characterise the flow patterns in each of them. The simulations are performed for some representative dimensionless numbers across the entire obtained ranges for each of them. This includes minimums, maximums and the medians identified previously in Figure 4.3 and Figure 4.6 to Figure 4.8 for both onshore and offshore reservoir systems. Table 4.4 shows the detail of all the simulations conducted in this study. Each and simulation scenario has been repeated in six different correlated random permeability fields which will be described later. The terminology used in this table may help identifying different simulation scenarios. Each simulation scenario is formed of three letters; the first letter, second and third letter

respectively refer to the corresponding magnitude of effective aspect ratio (N_{RL}), gravity number (N_g) and mobility ratio (M). *H*, *L* and *M* in Table 4.4 (the scenario column) refer respectively to high, low and median values for each dimensionless number derived previously for both classes of reservoirs (Table 4.3). For example a *LHM* scenario in the onshore section of Table 4.4 (scenario #4) will refer to a simulation scenario where the flow patterns have been investigate at the minimum effective aspect ratio (N_{RL}), maximum gravity number (N_g) and the median mobility ratio (M) for the reservoir systems in the onshore classes of reservoirs (Table 4.4).

Table 4.4: Different flooding scenarios investigated in this study

	#	**Scenario**	N_{RL}	N_g	N_{gt}	M_o	**Comments**
Onshore Scenarios	1	*MMM*	6.42	0.005	4.52	20.4	Base case Study
	2	*LLM*	1.09	0.0001	0.0024	20.4	Flow pattern investigation at the extremes of N_{RL} and N_g (N_{gt})
	3	*HHM*	32.8	0.048	1045.8	20.4	
	4	*LHM*	1.09	0.048	1.15	20.4	
	5	*HLM*	32.8	0.0001	1.57	20.4	
	6	*MML*	6.42	0.005	0.92	4.13	Comparative studies
	7	*MMH*	6.42	0.005	21.8	98.2	
	8	*MLM*	6.42	0.0001	0.06	20.4	
	9	*MHM*	6.42	0.048	40.03	20.4	
	10	*LMM*	1.09	0.005	0.13	20.4	
	11	*HMM*	32.8	0.005	118.07	20.4	
	12	*MMM*	6.42	0.005	4.52	20.4	Refined *MMM* scenario
	#	**Scenario**	N_{RL}	N_g	N_{gt}	M_o	**Comments**
Offshore Scenarios	1	*MMM*	3.33	0.146	7.23	4.47	Base case Study
	2	*LLM*	1.66	0.01	0.12	4.47	Flow pattern investigation at the extremes of N_{RL} and N_g (N_{gt})
	3	*HHM*	11.7	0.872	534.49	4.47	
	4	*LHM*	1.66	0.872	10.79	4.47	
	5	*HLM*	11.7	0.01	6.08	4.47	
	6	*MML*	3.33	0.146	4.22	2.61	Comparative studies
	7	*MMH*	3.33	0.146	26.84	16.6	
	8	*MLM*	3.33	0.01	0.49	4.47	
	9	*MHM*	3.33	0.872	43.17	4.47	
	10	*LMM*	1.66	0.146	1.81	4.47	
	11	*HMM*	11.7	0.146	89.54	4.47	
	12	*MMM*	3.33	0.146	7.23	4.47	Refined *MMM* scenario

The simulation studies in this table has been divided into a number of identical groups for both onshore and offshore reservoir systems. The first simulation group (case 1)

investigates the flow patterns at the median estimated dimensionless numbers for each class of reservoirs (*MMM* scenario). The next group (cases 2-5) represents four simulation scenarios, where the flow patterns have been investigated at the *extremes* combinations of N_{RL} and N_g numbers, whilst the mobility ratio (M) is kept at its median magnitude. The third group (cases 6-11) of simulations investigate the flow patterns at the extremes of only one dimensionless number in onshore and offshore reservoirs systems whilst the other two dimensionless numbers are kept at their median values. For example cases 8 and 9 may investigate the flow patterns at the extreme ranges of gravity number (N_g) in both classes of reservoirs.

Figure 4.13 schematically illustrates the location of the scenarios depicted in Table 4.4. Note that scenarios *MML* and *MMH* have not been shown in this figure.

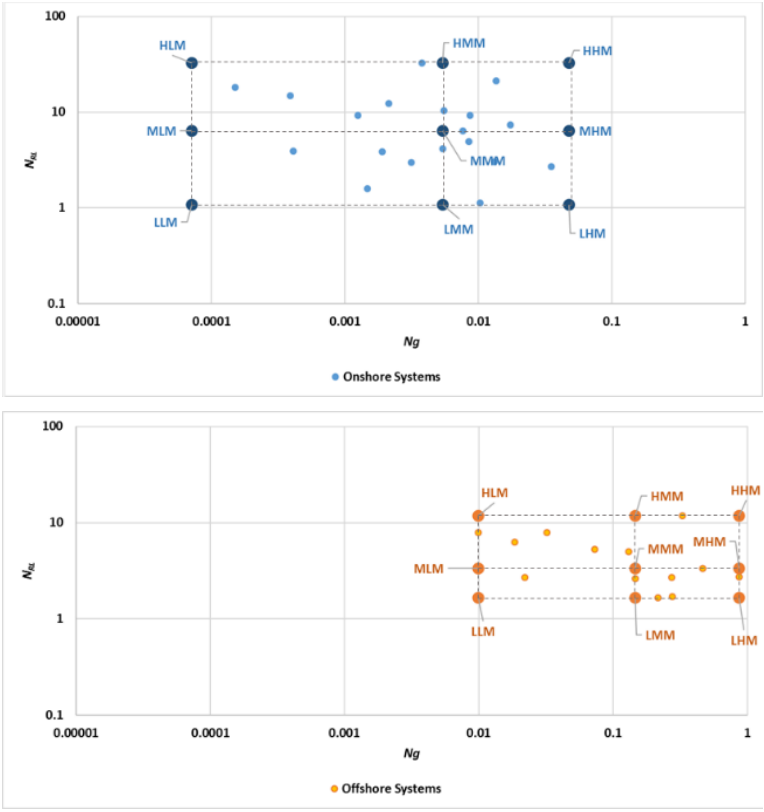

Figure 4.13: Schematic illustration of the scenarios depicted in Table 4.4. Note that cases MML and MMH have not been shown in these figures.

One last simulation in each group of reservoirs (case 12), investigates the sensitivity of the flow patterns to the degree of grid refinement. For this simulation scenario, all the dimensionless numbers are again kept at their respective medians similar to Case 1 (*MMM*) while a two times grid refinement is applied in each orientations. This in turn allows investigation to what extent mixing created by heterogeneity will be affected by numerical dispersion and thus the flow patterns may be affected by grid refinement.

Generating representative stochastic permeability fields for each class of reservoirs requires an estimate of the degree of heterogeneity (V_{DP}) and respective correlation lengths in the fundamental orientations (λ_x and λ_z), which is rather challenging. The data in the literature are, however, very limited. For the Permian Grayburg Formation in the Dune field located in West Texas, horizontal and vertical correlation lengths have been roughly estimated at 4-5ft and 12-13ft in the vertical direction and 2000ft and 1000ft for the major horizontal orientations (parallel and perpendicular to the main grainstone trend) (Lucia & Fogg 1990, Schenk 1992). In the absence of required data, we use the same methodology practiced by other researchers (Sorbie *et al.* 1994, Chang *et al*. 1994 and Waggoner *et al.* 1992) in that we investigate flow patterns in a range of correlated random field parameters rather than only one representative value.

Therefore, in this study flow patterns have been investigated under *six* different stochastic permeability fields comprising a range of three different dimensionless horizontal correlation length (λ_{xD}) of 0.025, 0.5 and 3.0 at two different degrees of permeability heterogeneity (V_{DP}) i.e. 0.5 and 0.8.

The chosen range of dimensionless correlation length covers a large range of correlated random permeability fields from nearly uncorrelated to almost layered system. For all the stochastic permeability fields, the vertical dimensionless correlation (λ_{zD}) length was kept constant at 0.1. Waggoner *et al.* (1992) investigated flow patterns in a number of stochastic permeability fields, all with λ_{zD} =0.2. Sorbie *et al.* (1994) have investigated the problem under identical correlation lengths in the two fundamental orientations. Note that we only have used one permeability realisation in this study.

All the stochastic random correlated permeability fields (RCF) have been generated with Schlumberger Petrel (Schlumberger Petrel, 2014). Permeability in all the stochastic permeability fields is log-normally distributed with a geometric average of 100mD. Porosity was held constant at 0.2 for all models. Figure 4.14 shows the actual permeability fields.

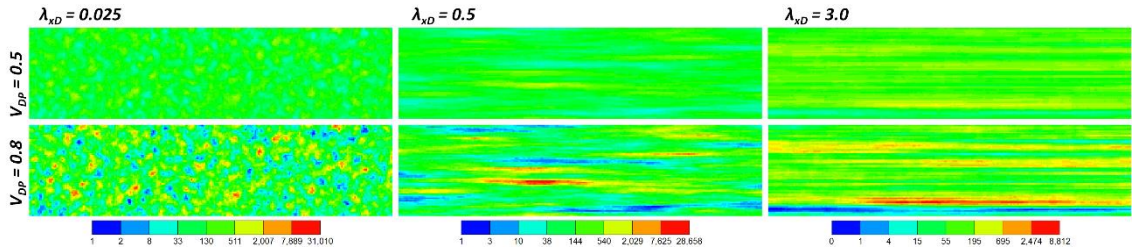

Figure 4.14: Six different stochastic permeability fields used in this study (legends are in mD).

***Computational procedure*:** The simulation model used in this study is a 2D cross sectional model. The model is 1600ft by 100ft in horizontal and vertical orientations, making an aspect ratio (*L/H*) of 16. The grid is 256 by 64 in horizontal and vertical directions, respectively. The injection pore-velocity (interstitial velocity) is held constant at 0.5ft/day. A compositional FCM model which has only two completely miscible components (oil and solvent) has been constructed in CMG-GEM (CMG-GEM, 2014.10). Appendix-3 shows the model code. For each of the simulation scenarios depicted in Table 4.4, three series of simulations were constructed and performed. These are cross sectional, areal and areal at unit mobility simulation scenarios. Comparison between these three rows of simulations will assist identifying the dominant flow patterns as was described earlier. Up to 1PV solvent is injected in the model. For each simulation scenario, the desired effective aspect ratio (N_{RL}) was obtained by adjusting the k_z/k_x ratio. Gravity number was adjusted by varying the density of *oil* component to create the desired density difference between oil and solvent. Finally, mobility ratio was adjusted by varying the viscosity of injected solvent (μ_s). Although the input physical dispersion is zero, there is a fixed background dispersion in both orientations as a result of the finite size of the grid blocks. For our simulation studies, this corresponds to dispersivities of 3.125ft and 0.78125ft in horizontal and vertical orientations respectively (Fanchi 1983), which in turn corresponds to longitudinal and transverse Peclet numbers of 512 and 8 (Equations (4.4) and (4.5)).

Table 4.5: Summary of the synthetic model properties. Arrows show how key dimensionless numbers are coupled with synthetic model parameters

Grid	256×1×64
Length	1600ft
Height	100ft
Dip Angle	0
Horizontal Permeability	100mD
k_z/k_x	**0.1**
Porosity	20%
Components	Oil, Solvent, Incompressible and FCM
Injection (pore) velocity	0.5ft/day 3200days to inject 1PV
Injector location	Left-side of the model
Producer location	Right-side of the model
Solvent density	29.15lb/ft^3
Oil Density	**30.15lb/ft^3**
Solvent viscosity	**0.01cP**
Oil viscosity	0.1cP
N_{RL}	**5.06**
N_g	**0.0055**
M	**10.0**

Table 4.5 summarises the synthetic model parameters. Arrows and colours show that the specified properties are coupled, in that by varying either of these model parameters, the desired dimensionless number will be generated.

4.7 Results and Discussion

We illustrate the results based on the same terminology presented in Table 4.4. In each scenario (e.g. *MMM*), we identify the dominant flow patterns by comparing the concentration profiles between cross sectional, areal and areal unit mobility models. All the screenshots depicted in this section have been taken after 0.3PV solvent injection. For each flooding scenario in either onshore or offshore systems, the dominant flow patterns have been identified in all the six stochastic permeability fields described earlier (Section 4.6). Thus each screenshot consists of 12 individual images; the top six for onshore system classes of reservoirs and the bottom six for offshore classes of reservoirs. Note that only cross sectional images have been shown in this study.

4.7.1 Flow Patterns Comparison at the Median Magnitudes of Dimensionless Numbers in each Class of Reservoirs

This flooding scenario may represent flow patterns for the averages of onshore and offshore classes of reservoirs listed in Table 4.1 and Table 4.2, which show the major reservoir properties for these two classes of reservoirs. The majority of the data were obtained from Brock & Bryan (1977) and Awan *et al*. (2008).

The properties of the two systems are fundamentally different as depicted in Table 4.4. The mobility ratio is much higher in the onshore model (20.36 *vs.* 4.47); cross flow is slightly higher (6.42 for the onshore model vs 3.33 for the offshore model). Both gravity and time-defined gravity numbers are significantly larger for the offshore model (0.005 vs. 0.146 for gravity number and 4.52 vs. 7.23 for time-defined gravity number).

Figure 4.15 shows the concentration profiles after injecting 0.3PV solvent in both models. Comparison of profiles at low correlation length stochastic permeability field shows that for both V_{DP}*'s* of 0.5 and 0.8, the flow pattern is clearly gravity dominated in the offshore model, while for the onshore model and at V_{DP}=0.5, it is dominated by fingering and at V_{DP}=0.8 is dispersive.

For the offshore model, gravity is only dominant at the shortest correlation length of 0.025. At larger correlation length of 0.5, the flow pattern is no longer gravity dominated in either of the onshore or offshore models. In fact it is very similar between the two systems and for both magnitudes of heterogeneity (V_{DP}). At very long correlation length of 3.0, the flow pattern is perfectly channelling dominated, while a residual tendency for gravity can be identified in the offshore model. Note that as a result of smaller effective aspect ratio (N_{RL}), cross flow is further limited in the offshore model. These results show that for the majority of the offshore North Sea reservoirs, upon CO_2 flooding, gravity will only be important if the target formation is characterised by a relatively short (horizontal) dimensionless correlation length. The flow patterns in the onshore model is not gravity dominated in either of the permeability fields. Except at very short correlation length where the displacement is either dispersive or fingering, the flow patterns are mostly channelling dominated in the onshore model.

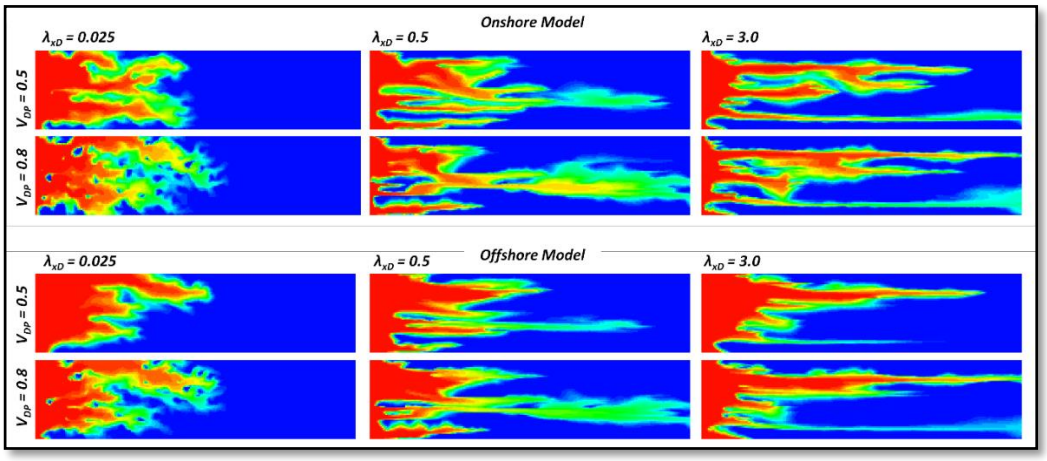

Figure 4.15: Flow pattern comparison for the MMM scenario after 0.3PV solvent injection

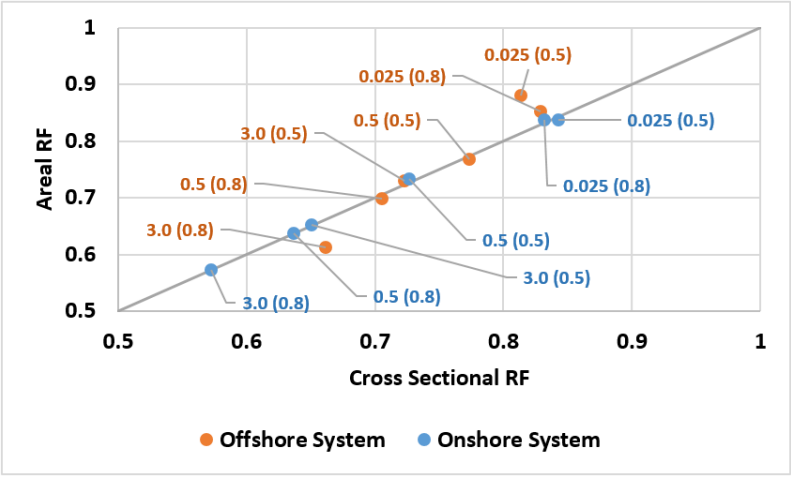

Figure 4.16: Ultimate recovery factor comparison between cross sectional and areal flooding scenarios for the MMM scenario. For each data point, the first and second (inside parenthesis) numbers are respectively λ_{xD} and V_{DP}.

Figure 4.16 compares the ultimate recovery factors after injecting 1.0PV solvent in all the stochastic permeability fields shown in Figure 4.15. Note that, as expected, recovery generally decreases when either the correlation length or the degree of heterogeneity increases. Once again it can be seen that at only very short correlation length, the flow pattern is gravity dominated in the offshore *MMM* model, however, as the correlation length increases, the significance of gravity decreases. At very large correlation length gravity helps the displacement in the offshore model to avoid taking the high permeability streak at the bottom of the model, hence recovery slightly improves in this model.

Comparison of the ultimate recovery factors for the cross sectional models also shows that except at very short correlation length of 0.025, for other comparable stochastic permeability fields, the ultimate recovery factors are always better for the offshore model. This is primarily because of less favourable (higher) mobility ratio in the onshore model. At short correlation length gravity easily dominates in the offshore model, hence its ultimate recovery factor is lower. Comparison of the ultimate recovery factors for the areal model shows that for all the comparable stochastic permeability fields, recovery is better in the offshore model. This is again due to better (lower) mobility ratio in the offshore model.

The conclusion is that at comparable permeability fields and away from gravity dominated conditions, the flow patterns are more stable offshore due to better (lower) mobility ratio. The impact of gravity in the offshore system may make the performance poorer or better depending on the relative placement of the high and low permeability layers.

4.7.2 Flow Pattern Comparison at the Extremes of N_{RL} and N_g in each Class of Reservoirs

In these comparative scenarios, the flow patterns are compared between the two systems at the combinations of minimums and maximums of N_{RL} and N_g numbers for either of the systems, but at the same *median* calculated mobility ratio. These comparisons plus the comparison conducted previously (*MMM* scenario) may provide a broader insight into the likely dominant flow patterns in the onshore and offshore reservoir systems.

LLM Scenarios: In this scenario, the flow patterns are compared for the two systems at the extreme minimums of both gravity and effective aspect ratio numbers depicted in

Table 4.4. This consequently implies flow pattern investigation at the minimum magnitude of N_{gt} in both systems. The flow patterns have been depicted in Figure 4.17. Although the minimum N_g and N_{gt} are two orders of magnitudes larger in the offshore model, in neither of these models are the flow patterns gravity dominated, and in fact they are purely (viscous) unstable. At short (horizontal) correlation length of 0.025, the flow pattern is fingering in both models, though the degree of fingering is slightly more significant in the onshore model due to the higher mobility ratio. For all the larger correlation lengths, the flow patterns are similar and are purely channelling, irrespective of the magnitude of the mobility ratio.

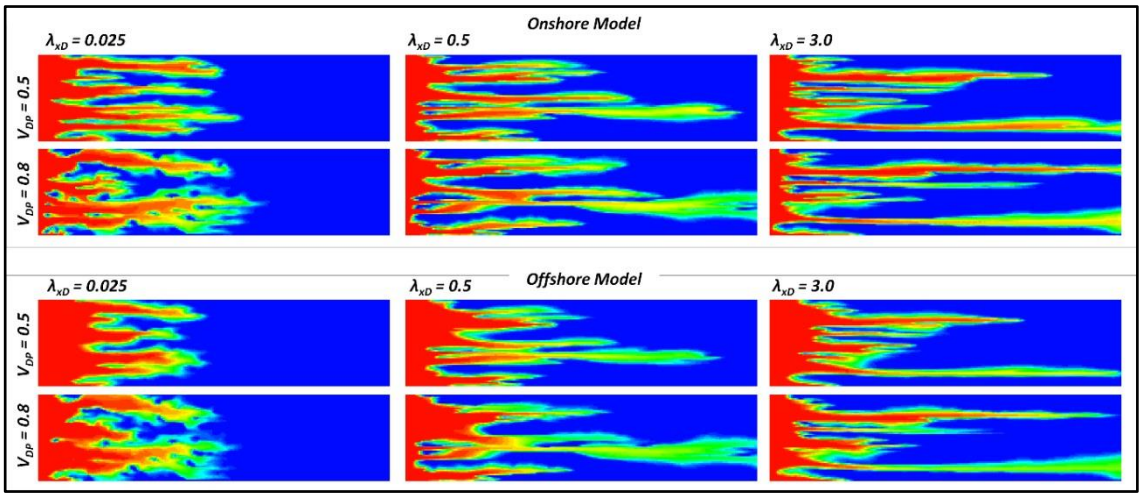

Figure 4.17: Comparison of flow patterns between onshore and offshore systems at N_{RL}^{min} and N_g^{min}

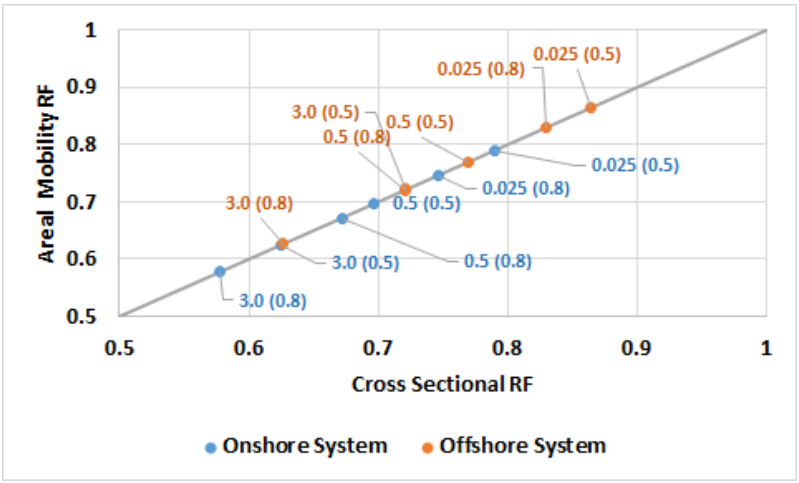

Figure 4.18: Ultimate recovery factor comparison between cross sectional and areal flooding scenarios for the LLM scenario. For each data point, the first and second (inside parenthesis) numbers are respectively λ_{xD} and V_{DP}.

Figure 4.18 compares the ultimate recovery factors between cross sectional and areal flooding configurations for the same stochastic permeability fields shown in Figure 4.17.

Note that, first, gravity is not significant at all for either of the systems at these prevailing conditions; second, for any stochastic permeability field, recovery factor is better in the offshore models.

HHM Scenarios: The flow patterns are now compared for the two systems at the maximums of both gravity and the effective aspect ratio. This accordingly makes the N_{gt} at its maximum for both systems (1045 *vs*, 534). Figure 4.19 shows the flow pattern in each model. Now, the flow patterns are gravity dominated in both systems and in all the permeability fields, with gravitational effects even more significant in the offshore model.

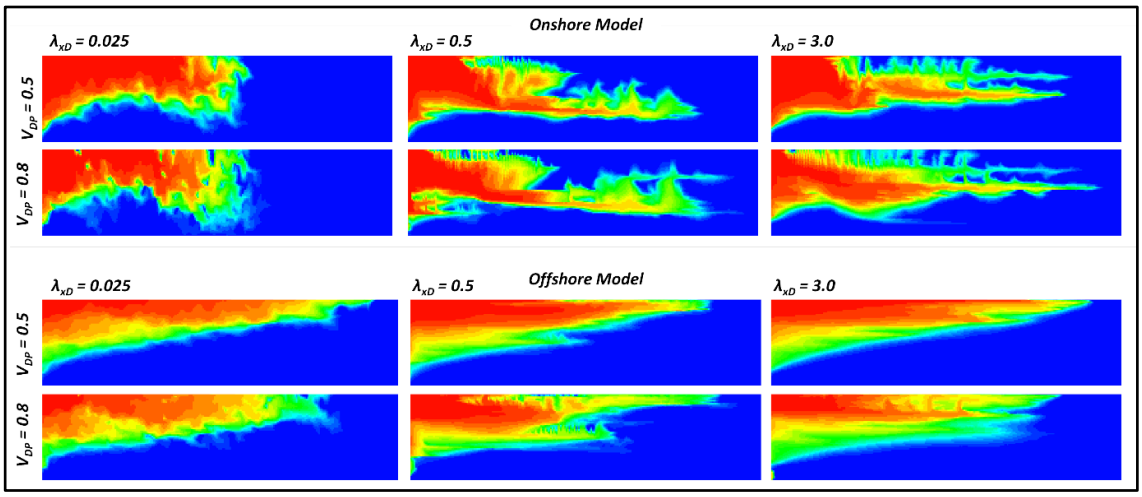

Figure 4.19: Comparison of flow patterns between onshore and offshore systems at N_{RL}^{max} and N_g^{max}

LHM Scenarios: This scenario compares the flow pattern between the two systems at the prevailing condition of minimum effective aspect ratio (N_{RL}^{min}) and maximum gravity number (N_g^{max}) for either of the two systems. The estimated N_{gt} for these scenarios are respectively 10.8 and 1.2 for offshore and onshore system which may describe a more significant gravity dominated flow pattern in the offshore model. Figure 4.20 shows the results. Now the flow pattern is gravity dominated in the offshore system, while it is completely unstable for the onshore system. This shows that gravity could be significant for the offshore systems even at the lowest estimated effective aspect ratio.

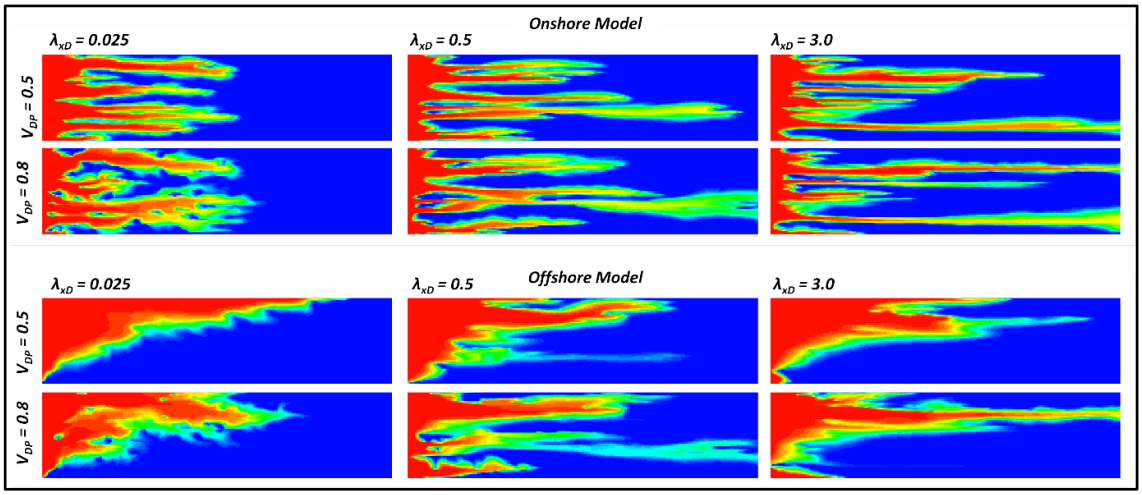

Figure 4.20: Comparison of flow patterns between onshore and offshore systems at N_{RL}^{min} and N_g^{max}

Figure 4.21 compares the cross sectional and areal recovery factors between the two models. It can be seen that the cross sectional recovery factors for the offshore models now vary in a much smaller window, irrespective of the pattern of heterogeneity which indicates a significant gravity dominated flow pattern in all the permeability fields. For the onshore system at these prevailing conditions, flow patterns are not gravity dominated and are similarly unstable in all the stochastic permeability fields.

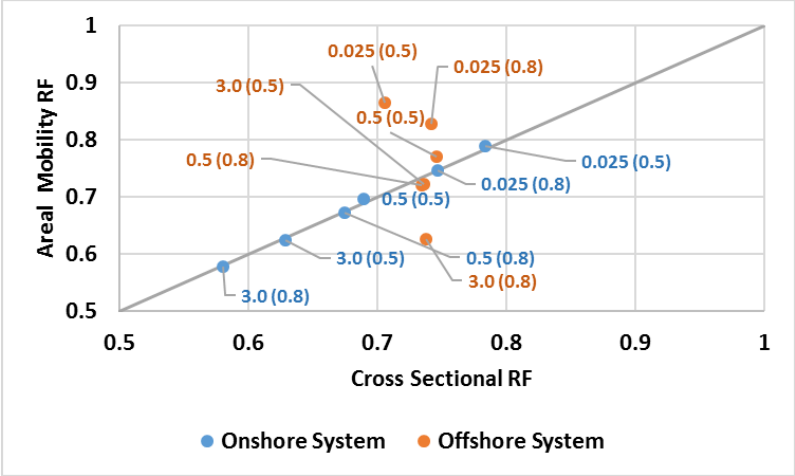

Figure 4.21: Ultimate recovery factor comparison between cross sectional and areal flooding scenarios for the LHM scenario. For each data point, the first and second (inside parenthesis) numbers are respectively λ_{xD} and V_{DP}.

HLM Scenarios: The calculated N_{gt} for this scenario are respectively 6.08 and 1.57 for the offshore and onshore systems. Figure 4.22 illustrates the actual flow patterns at these prevailing flooding conditions. For this scenario, the flow patterns are no longer gravity dominated in either of the systems. Now the flow pattern only varies between viscous stable (dispersive) and viscous unstable flow patterns. The flow pattern is dispersive for

the short correlation length permeability field in both systems and channelling for the other longer correlation lengths permeability fields, though the degree of channelling is much less than the *LLM* case and they are more stable due to higher crossflow within system. As before, Figure 4.23 compares cross sectional and areal recovery factors for the same stochastic permeability fields depicted in Figure 4.22. Recovery factors are always better for the offshore model due to lower mobility ratio; this is relevant for both cross sectional and areal flooding configurations. Note that in Figure 4.23 that gravity is still important for the offshore system at very short correlation length of 0.025.

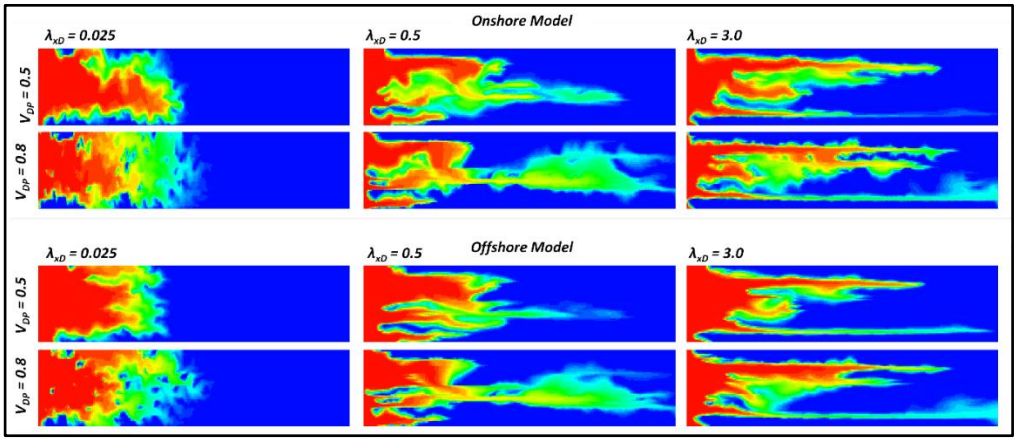

Figure 4.22: Comparison of flow patterns between onshore and offshore systems at N_{RL}^{max} and N_g^{min}

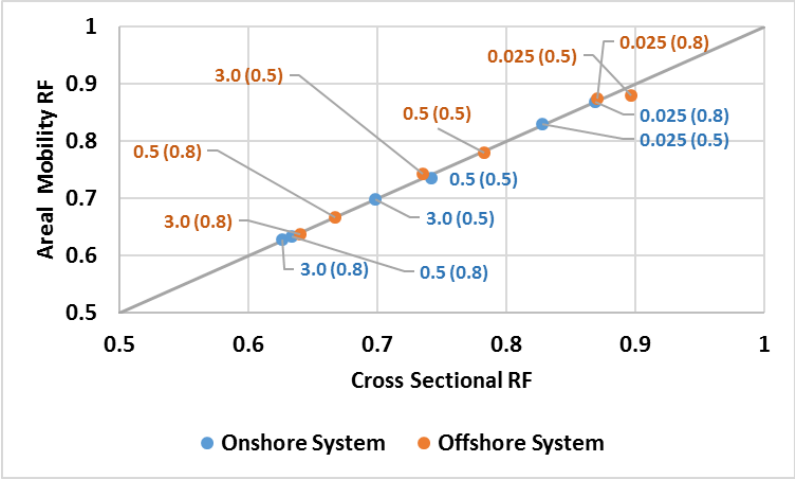

Figure 4.23: Case HLM, comparison of ultimate recovery factors between cross sectional and areal models.

It is important to note that while the magnitude of N_{gt} in the onshore system is comparable between this scenario and the previous scenario (1.57 for *HLM* scenario vs. 1.2 for *LHM* scenario), the flow patterns are very different between these two scenarios (Figure 4.20

and Figure 4.22). This shows that although N_{gt} is an informative number for evaluating the significance of gravity, it is not sufficient at all.

4.7.3 Flow Pattern Comparison at the Extremes of Each Dimensionless Number in Each Class of Reservoirs

This section compares the flow patterns for each class of reservoirs at the extreme high and low of only one dimensionless number, while the other two dimensionless numbers are kept at their median estimated values.

Mobility ratio (Cases MMH and MML): Figure 4.24 and Figure 4.25 compare flow patterns at the extreme maximum and minimum mobility ratios for the two reservoir systems depicted in Table 4.4, while the rest of dimensionless numbers are kept at their original median values. The order and configurations of the screenshots has now been changed to better reflect the comparative nature of this analysis. Note that the ranges of mobility ratio variation is not identical between the two systems. Mobility ratios in the offshore system vary between 2.61 and 16.6 and for the onshore system vary between 4.13 and 98.2.

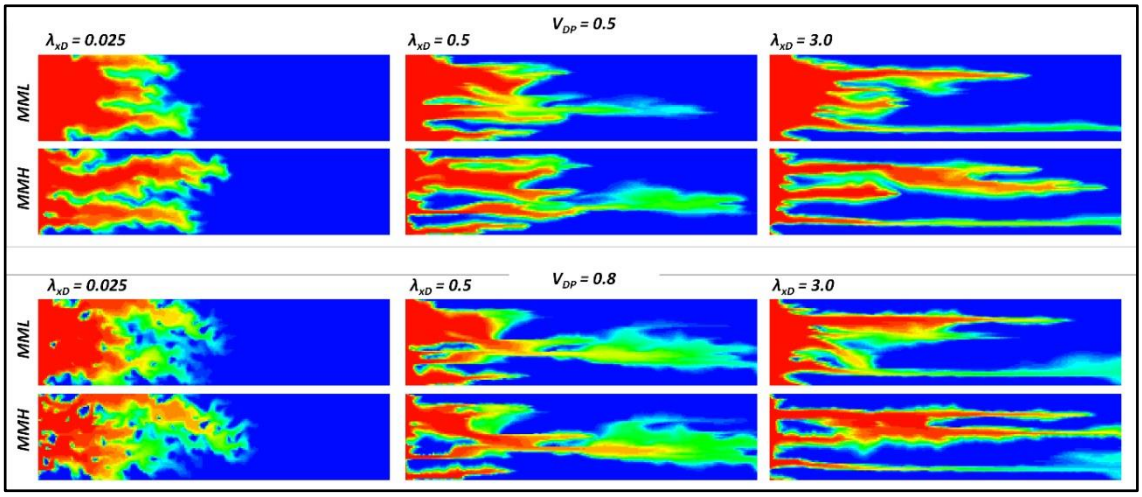

Figure 4.24: Flow patterns comparison for the extreme maximum and minimum of the mobility ratio (onshore system)

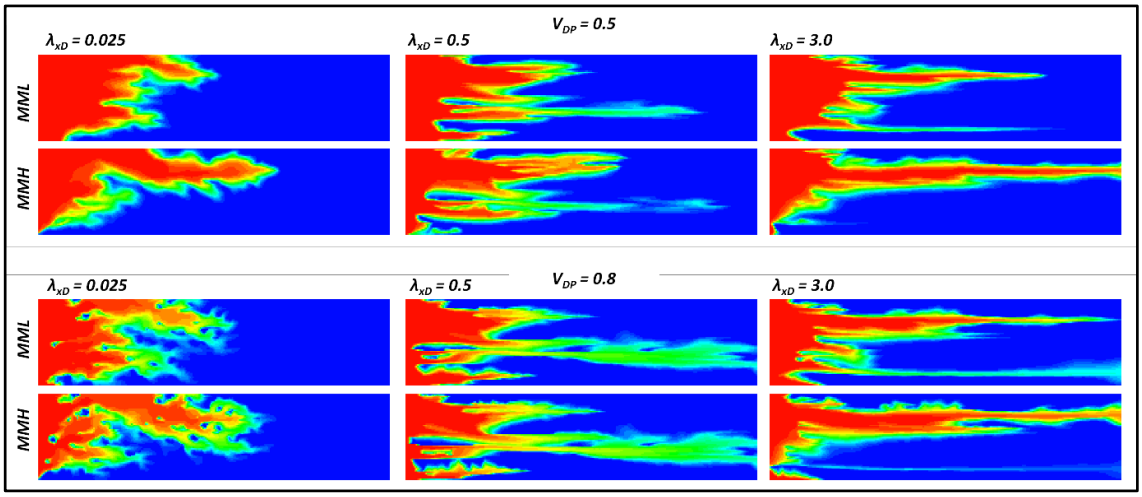

Figure 4.25: Flow patterns comparison for the extreme maximum and minimum of the mobility ratio (offshore system)

For all the stochastic permeability fields in the onshore system, flow patterns vary between relatively more and less unstable flow patterns within the ranges of mobility ratios specified. This is the case for the offshore system, except that at very short horizontal correlation length flow patterns vary between more and less gravity dominated.

Figure 4.26 compares the areal and cross sectional recovery factors for onshore and offshore systems for *MML* and *MMH* scenarios. The same observations inferred from Figure 4.24 and Figure 4.25 can be again observed in this figure. Figure 4.26 shows that for some permeability fields in the offshore model, flow patterns become gravity dominated, only as a result of a change of mobility ratio.

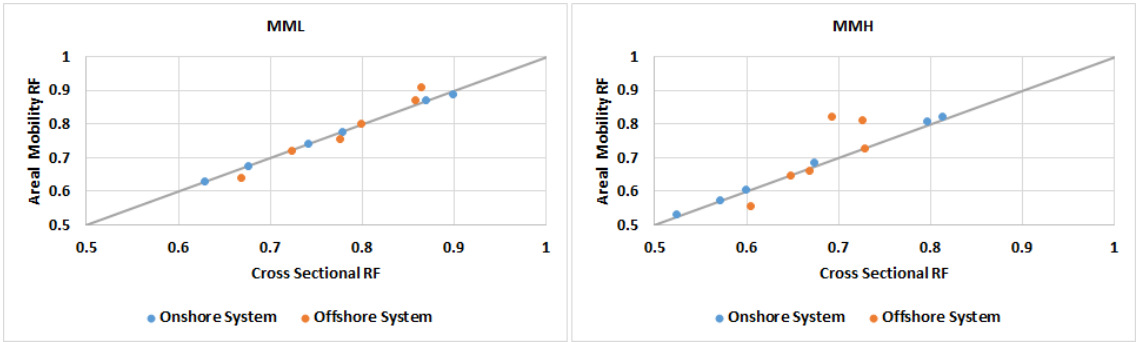

Figure 4.26: Comparison of ultimate recovery factors between cross sectional and areal models for cases MML (left) and MMH (right)

Gravity Number (MLM and MHM scenarios): Figure 4.27 and Figure 4.28 compare flow patterns in each class of reservoir for the extreme maximum and minimum gravity numbers depicted in Table 4.4 for both classes of reservoirs. Comparison of flow patterns for the onshore system shows that for the ranges of gravity numbers investigated in this

analysis (0.0001 to 0.0478), the observed flow patterns are mostly channelling, except at very short horizontal correlation length of 0.025 (Figure 4.27) where they are slightly gravity dominated. For the offshore system, as expected, a more significant change of flow patterns, between the two extremes of gravity numbers, can be observed. The flow patterns become significantly gravity dominated for all the stochastic permeability fields in the offshore model (Figure 4.28).

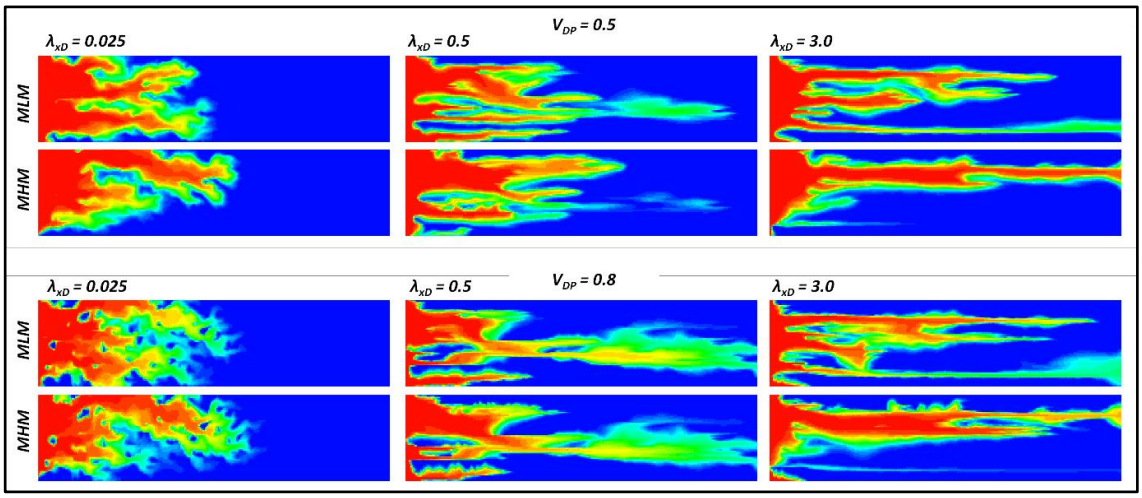

Figure 4.27: Flow patterns comparison for the extreme maximum and minimum of the gravity number (onshore system)

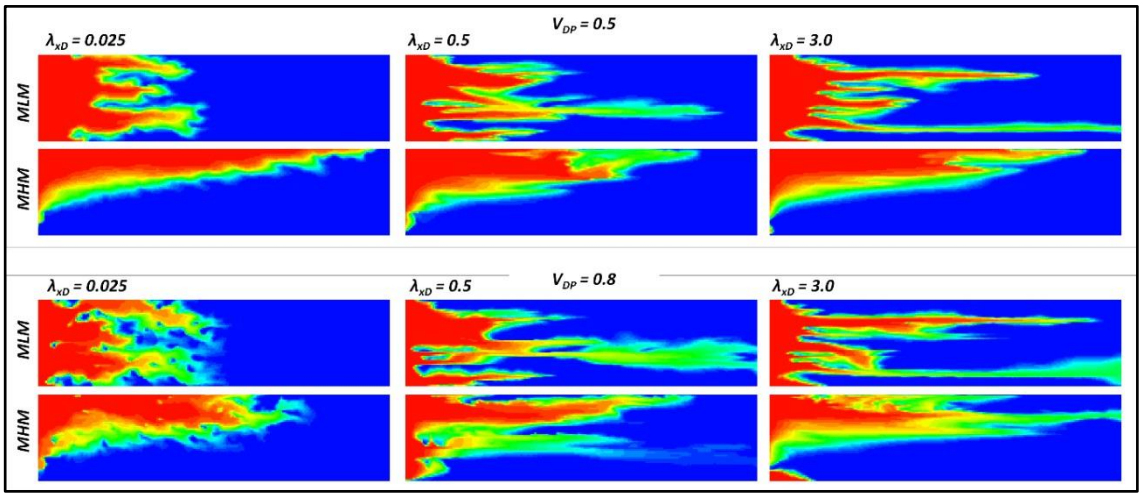

Figure 4.28: Flow patterns comparison for the extreme maximum and minimum of the gravity number (offshore system)

As before, Figure 4.29 compares cross sectional and areal recovery factors for both *MLM* and *MHM* scenarios. The areal recovery factors between *MLM* and *MHM* scenarios are identical since only gravity number changes in this analysis. As with the flow pattern comparison results presented in Figure 4.27 and Figure 4.28, Figure 4.29 shows that the displacement in the offshore model, become significantly more gravity dominated at the

extremes of maximum gravity number than that in the onshore model. Note that the cross sectional recovery factors in all the stochastics permeability fields in the offshore model vary in a much smaller window than that of the onshore model, illustrating the significant gravity dominated flow regime at the maximum of its gravity number.

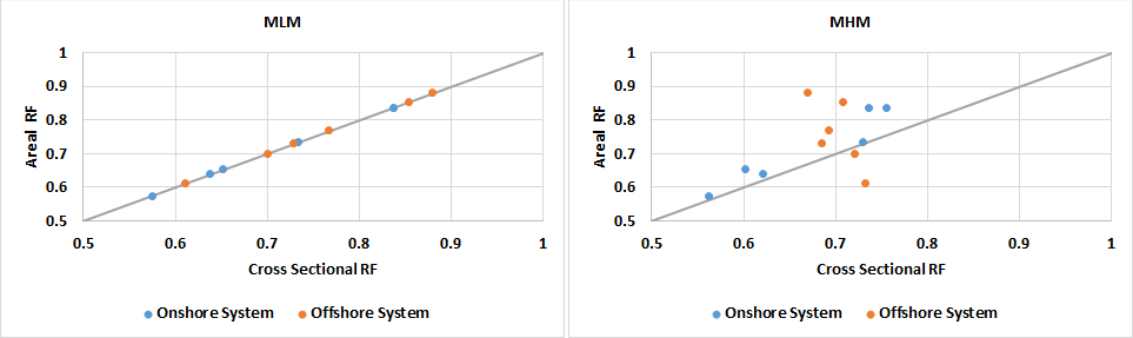

Figure 4.29: Comparison of ultimate recovery factors between cross sectional and areal models for cases MLM (left) and MHM (right)

Effective Aspect Ratio (LMM and HMM scenarios): This final comparative scenario investigates the variation of flow patterns under the extreme ranges of maximums and minimums of the effective aspect ratio (N_{RL}) derived in both systems. For onshore systems, N_{RL} varies from 1.09 to 32.80, while for offshore systems, it varies from 1.66 to only 11.71; a relatively smaller window in the offshore systems. Figure 4.30 and Figure 4.31 compare the actual flow patterns at the respective extremes of the effective aspect ratio.

Figure 4.30 shows that the flow patterns are unstable for the entire ranges of the effective aspect ratio in the onshore system, though the degree of instability varies between the two extremes of the effective aspect ratio. For offshore systems, flow patterns vary between strictly unstable (channelling dominated) and gravity dominated flow patterns (Figure 4.31).

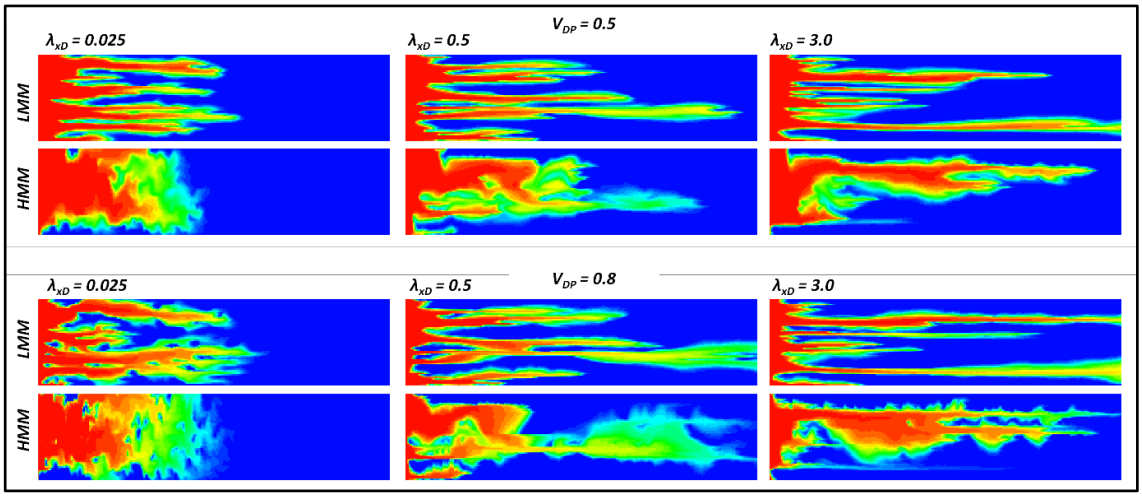

Figure 4.30: Flow patterns comparison for the extreme maximum and minimum of the effective aspect ratio (onshore system)

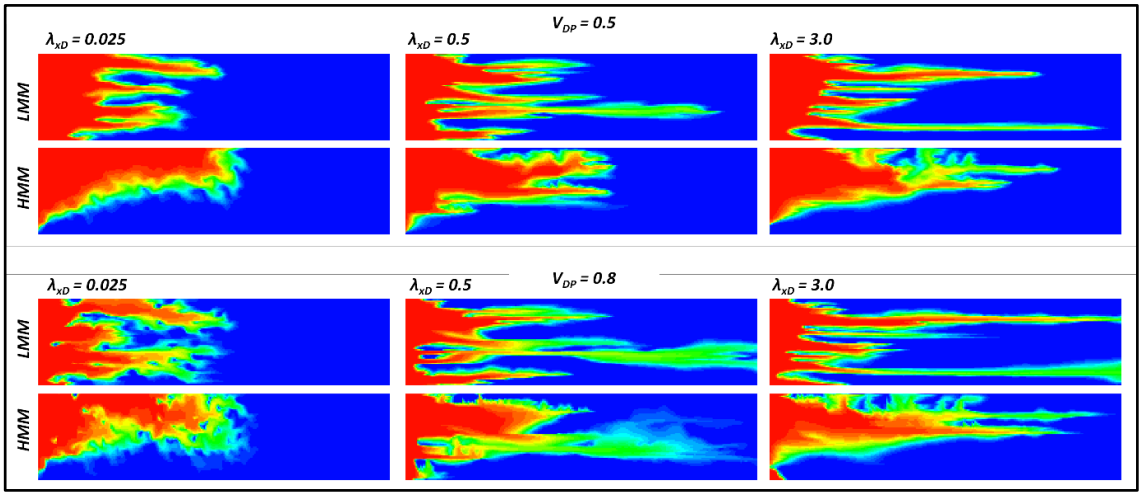

Figure 4.31: Flow patterns comparison for the extreme maximum and minimum of the effective aspect ratio (offshore system)

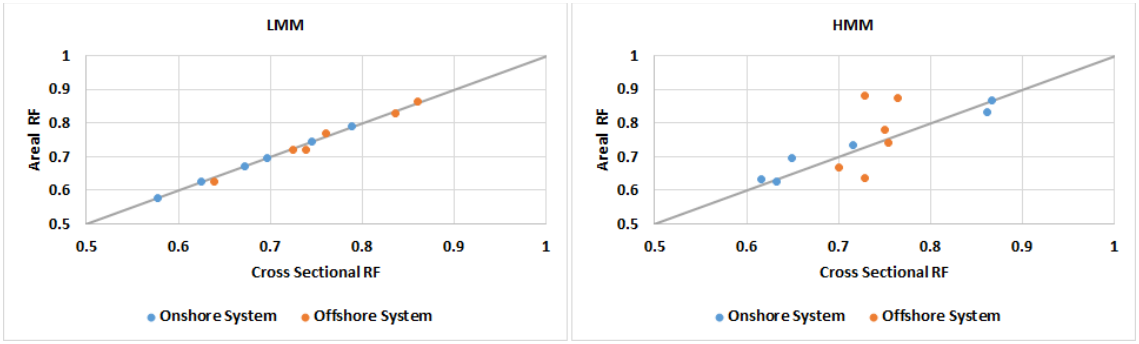

Figure 4.32: Comparison of ultimate recovery factors between cross sectional and areal models for cases LMM (left) and HMM (right)

4.8 Sensitivity of Flow Patterns to Grid Refinement

It is important to investigate to what extent the observed results are sensitive to the degree of grid refinement. To investigate this, the *MMM* scenario was simulated under 2 times grid refinement in either of the orientations. This increases the total number of grid blocks from original 16834 (256×64) to 65536 (512×64) grid blocks. Figure 4.33 compares flow patterns after 0.3PV solvent injection in the onshore model for both original and refined model descriptions in the onshore model and for all the six permeability fields.

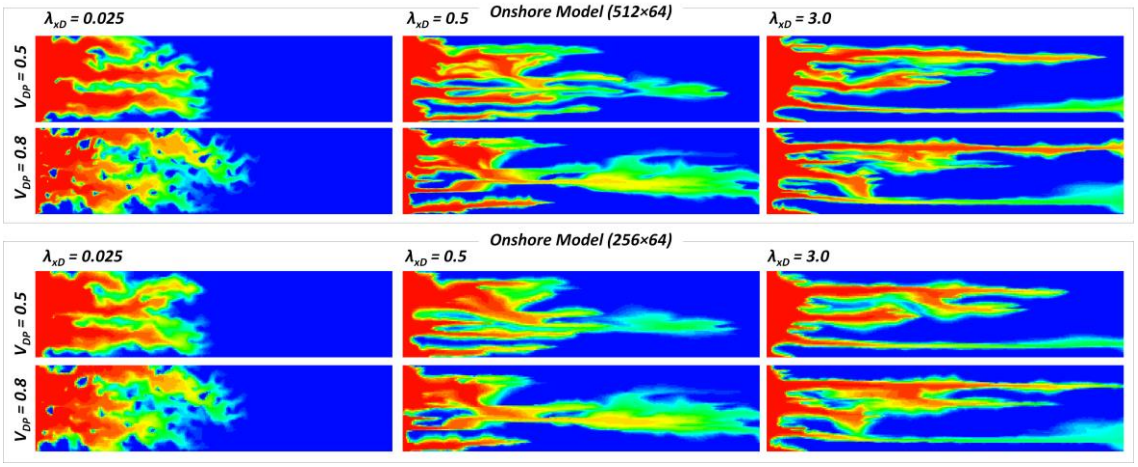

Figure 4.33: Comparison of flow patterns between original and fine models (onshore MMM scenario)

It can be seen that flow patterns broadly follow the same earlier identified profiles. The largest difference is at only very large correlation length of λ_{xD}=3.0 where the degree of channelling is not similar between the two models. The refined model shows more channelling and less cross flow accordingly, particularly at lower degree of heterogeneity (V_{DP}=0.5). For the onshore model, the difference between the ultimate recovery factors of the original and fine versions of all the stochastic permeability fields lie between 2.4% and 7%, where the largest difference belongs to the longest correlation length stochastic permeability field (λ_{xD}=3.0).

For the offshore model, however, the differences in the flow patterns are much less noticeable than the onshore model (Figure 4.34). In fact the differences in the ultimate recovery factors vary only between 0.9% and 2.6% between original and fine versions of all the stochastic permeability fields. This is because of the lower degree of cross flow in the offshore system and a slightly more gravity dominated flow pattern in the offshore model. Evidently, it is not affordable to conduct all the simulations at the very fine degree of refinement of 65536 grid blocks.

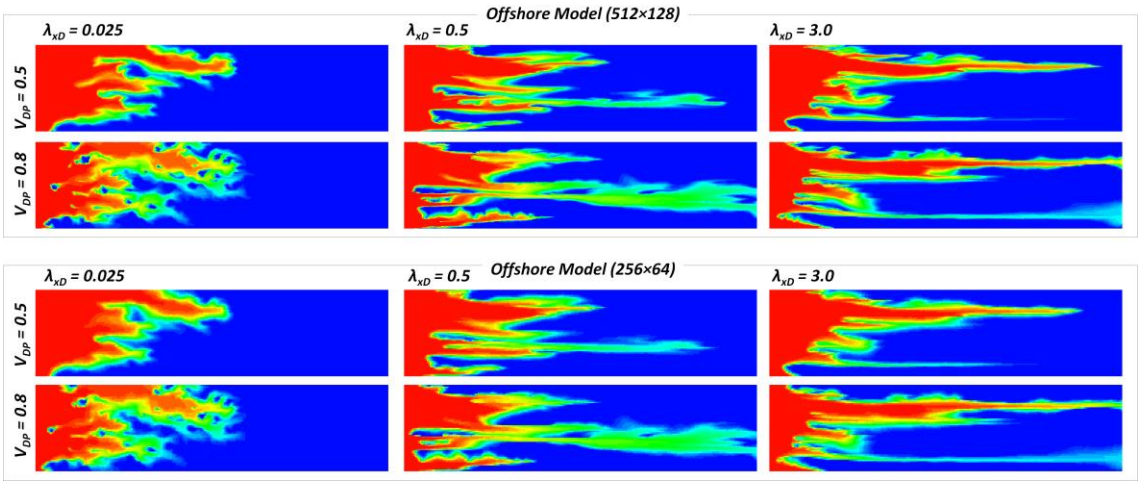

Figure 4.34: Comparison of flow patterns between original and fine models (offshore MMM scenario)

4.9 Discussion

So far we have investigated flow patterns in a broad range of combinations of dimensionless number for each class of reservoirs. The above results show that the flow patterns in both systems of reservoir can vary between the four main flow patterns of stable (dispersive), gravity dominated and unstable (fingering and channelling) depending on the prevailing stochastic permeability field and particular dimensionless numbers. In each system of reservoirs, one or two flow patterns are, however, more dominant than others. The CO_2 flow patterns in the offshore classes of reservoirs show more tendency for gravity domination, while CO_2 flow pattern in the onshore United States classes of reservoirs are mostly viscous unstable. For the majority of North Sea offshore reservoirs, gravity is expected to be important only at very short correlation lengths. At longer correlation lengths, the chandelling flow pattern dominates in both systems. If the gravity flow pattern is neglected from the analysis, then flow patterns are relatively more stable in the North Sea classes of reservoirs due to better (lower) mobility ratio which ensures higher recovery factors. In terms of cross flow, those CO_2 flooded reservoirs located in the United States undergo a higher degree of cross flow, principally due to their particular dimensionality (large *L/H* ratio).

A few considerations may limit the application of our findings to actual CO_2 flooding systems in both classes of reservoirs. First, we have estimated gravity numbers (Equations 4.7 and 4.8) in this study, for a process where CO_2 displaces oil under FCM conditions. In reality, secondary water injection preceded CO_2 injection, particularly in

the offshore North Sea classes of reservoirs. A secondary waterflooding makes gravity effects much more pronounced between CO_2 and water than between CO_2 and oil. This in turn may result in larger gravity numbers than those calculated in this study. Second, the assumption of FCM displacement is not truly accurate for CO_2 flooding systems (Chapter 2) as the compositional effects and the impact of relative permeabilities always dominate the CO_2 flooding and this was not taken into account in this study. Usually the impact is to further stabilise the displacement due to formation of a low mobility transition zone between oil and CO_2 (Chapter 2). Hence, the mobility ratios are expected to be slightly better (lower) than those predicted in this study. This, however, depends on the relative permeability characteristics (i.e. endpoints) in both classes of reservoirs.

The above findings were also obtained based on the background assumptions that fluids are incompressible. However, in reality CO_2 is very compressible, or at least more compressible than typical hydrocarbon gases. A pressure drop from injector to producer may affect CO_2 properties (i.e. density and viscosity) depending on the degree of pressure variation from injector to producer. This can affect the estimated gravity numbers (Equations 4.7 and 4.8). The magnitude of pressure drop within either of the systems can be compared with the aid of the pressure drop correlation developed in Appendix-1. From Appendix-1, the pressure drop within a given system can be approximated by the following correlation;

$$\Delta p = \left(p_{inj} - p_{prod}\right) = 0.515 \frac{r_{frac} \times {L_{ft}}^2 \times \mu_{cP}}{k_{mD}} \tag{4.16}$$

Where r is the rate of depletion (fraction), L is well spacing (ft), μ is the viscosity of the fluid (cP) and finally k is the absolute permeability of the system (mD). As was mentioned in Appendix-1, this correlation can only give a *very rough estimate* of pressure drop within systems, since relative permeability effects and also radial flow pressure drop around wells have not been taken into account. However, we believe the estimated pressure drop by this correlation is enough for our comparative analysis. We can transpose the above correlation into the dimensionless domain by diving it by initial reservoir pressure. This approach is similar to the one undertaken by Wood *et al.* (2008). Hence;

$$\Delta p_D = \frac{\Delta p}{p_i} = 0.515 \frac{r_{frac} \times {L_{ft}}^2 \times \mu_{cP}}{p_i \times k_{mD}} \tag{4.17}$$

Δp_D shows the ratio of pressure variation within a system relative to initial reservoir pressure. The larger the Δp_D, the higher will be the relative variation of pressure within the system. We estimate the Δp_D for all the reservoirs in each class of reservoirs using the data depicted earlier in Table 4.1 and Table 4.2. Figure 4.35 shows the final results.

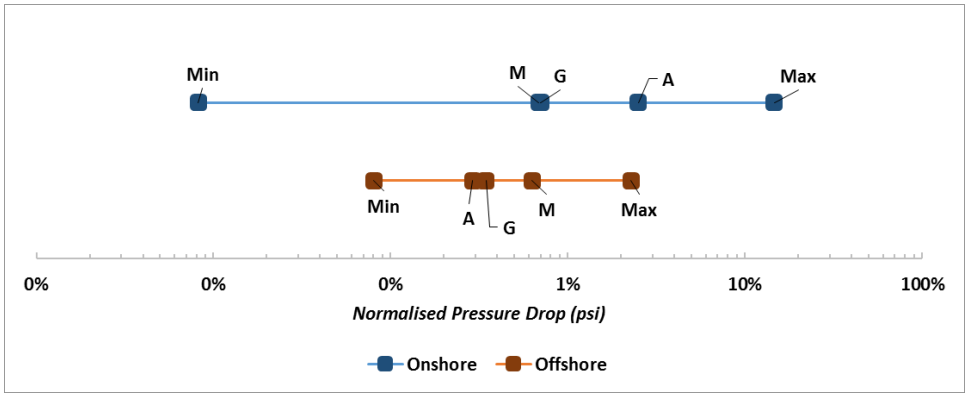

Figure 4.35: Comparison of the ranges of Δp_D variation between offshore and onshore classes of reservoirs

The estimated Δp_D depicted in Figure 4.35 are based on a displacement process where the system is filled with CO_2 with a relatively small viscosity of 0.05-0.07cP, so they may look very small. Nevertheless, the comparison of Δp_D is important in this section, not the absolute values. It can be seen in Figure 4.35 that the range of Δp_D variation is much larger in the onshore system of reservoirs. Second, the average Δp_D is larger in the onshore classes of reservoirs despite their relatively closer well spacing. This is because of both lower formation permeabilities and lower average reservoirs pressures, which makes Δp_D more significant compared to offshore classes of reservoirs. This, accordingly, demonstrates that variation of CO_2 properties within offshore classes of reservoirs are likely smaller than in the onshore classes of reservoirs.

4.10 Conclusions

In this study, we have compared CO_2 flow patterns between two major classes of reservoirs; the United States CO_2 flooded reservoirs located mainly in the Permian Basin and North Sea group of reservoirs. We have characterised the flow patterns in each class of reservoirs based on the magnitude of principal dimensionless numbers using their reported reservoir and fluid properties. This study was interesting in that it extends already developed scaling analysis and flow patterns related knowledge into a real comparative application. Results of this study show that;

- Mobility ratios between CO_2 and oil are generally better (lower) in the North Sea classes of reservoirs. This is because of lower oil viscosities which can be found offshore.
- In terms of the geometry (dimensionality) of the two groups of reservoirs, North Sea reservoir systems are characterised with a relatively smaller *L/H* ratio. This is mainly because of thicker reservoirs pays in these systems, although well spacing is relatively larger in this system of reservoirs.
- Under comparable k_z/k_x conditions, effective aspect ratios are relatively smaller in the North Sea reservoirs which indicates that cross flow is more limited compared to United States CO_2 flooded reservoirs.
- Due to larger spacing between wells and higher rates of depletion, *in-situ* fluid velocities are significantly higher in the North Sea reservoirs.
- Both gravity numbers and time-defined gravity numbers are larger in the North Sea system of reservoirs by almost two orders of magnitude, despite the fact that *in-situ* fluid velocities are higher in the North Sea class of reservoirs. This is mainly because of significantly better formation permeabilities in this class of reservoirs.
- For the majority of the combinations of dimensionless numbers investigated in this study, it was found that CO_2 flow patterns are more gravity dominated in the North Sea class of reservoirs, particularly at very short horizontal correlation lengths. At larger horizontal correlation lengths, the displacement is channelling dominated in both classes of reservoirs.
- If gravity flow pattern is, however, ignored, then flow patterns are more favourable (more stable) in the North Sea class of reservoirs due to better mobility ratios in this system.

Chapter 5 The Driving Force behind CO_2 Flooding and Its Impacts on Offshore CO_2 Flooding Process Design

5.1 Introduction

A significant input parameter affecting the design of a given CO_2 flooding processes in onshore and offshore classes of reservoirs is the driving force behind conducting the CO_2 flood (Chapter 1). In the onshore classes of reservoirs e.g. the Permian Basin of the United States, (valuable) CO_2 traditionally has been sourced from natural sources and the incentive for CO_2 flooding has come purely from EOR (though this has been changed in the past few years as was discussed in Chapter 1). Therefore, project design in this class of reservoirs calls for minimising the CO_2 consumption while maximising the ultimate oil recovery.

For a potential CO_2 flooding offshore, CO_2 may be supplied from anthropogenic CO_2 sources with incentives come from both EOR and (CO_2) storage, which means that unlike past CO_2-EOR projects conducted in the United States, safe and permanent CO_2 storage will be another co-important objective. Thus, the project design philosophy in the offshore classes of reservoirs should allow for efficient use of pore volume for CO_2 storage in addition to maximising the EOR response. This difference between the objectives of CO_2 flooding in both classes of reservoirs can affect elements of CO_2 process design.

Therefore, the aim of the study presented in this chapter is to address how the difference in the driving force behind running a CO_2 flood can affect the design elements of the CO_2 flood. Elements such as the type of the process, optimum CO_2 slug size, optimum operating pressure, choice between CO_2 separation and recycling on CO_2 breakthrough and finally the relative benefits of WAG.

To answer these questions, we first characterise the objectives of CO_2 flooding with two different objective functions, as will be discussed in the next section. Basically, one objective functions aims to maximise EOR and minimise CO_2 consumption (f_{EOR}), while the other objective function aims to maximise both EOR and (CO_2) storage (f_{CCUS}).

In this study we may use terms such as '*optimum CO_2 slug size*' or '*optimum operating pressure*'. However, the reader should note that it is not the aim of this study to present

any optimisation analysis. Instead, we investigate how different evolutions of the above two objective functions may affect the design of a given CO_2 flooding process.

5.2 Development of the Objective Functions

To address the co-importance of storage and EOR for a likely CO_2 flooding project offshore, an objective function is first introduced in this section (Equation 5.1). This objective function is essentially a modified version of the objective function developed by Kovscek *et al*. (2005) for co-optimisation of EOR and CCS.

$$f = w_1 \frac{N_p^*}{N_{OIP}} + w_2 \frac{N_p^* \times U_{CO2}}{V_R} \tag{5.1}$$

This objective function combines the importance of both storage and EOR in a typical CO_2 flood. The first and second terms in the above equation respectively describe the relative importance of EOR and storage and w_1 and w_2 are appropriate weight factors. N_{OIP} in the above equation is not the original oil in place; instead, it is the oil remaining at the beginning of the tertiary CO_2 flood. N_P^* represents the recovered oil after CO_2 flooding and therefore the first ratio demonstrates the fraction of tertiary oil that potentially has been recovered by CO_2 flooding (EOR objective term). U_{CO2} in the second term is the net CO_2 utilisation efficiency, therefore $N_P^* \times U_{CO2}$ in the second term shows the cumulative CO_2 volume at equivalent standard conditions that has been retained at the end of flooding process. V_R represents the total reservoir pore volume available for CO_2 storage. Thus the second term has the units of scf/Rft^3, which evidently could be larger than 1. The larger this ratio, the better will be the storage efficiency.

Kovscek *et al*. (2005) assumed that the sum of w_1 and w_2 is always 1 for a coupled EOR and CCS process; however, we assume that the magnitude of w_1 and w_2 could be independent and depend on the economics and incentives for a likely CO_2 flood; i.e. the driving force behind CO_2 flooding, the relative price of oil and CO_2 and the cost of CO_2 separation against fresh CO_2 purchase. In the United States, w_1 and w_2 are likely to be respectively positive and negative numbers because the CO_2 that will be left behind in the formation after the termination of the process is regarded as a valuable left (lost) commodity which is unrecoverable and the operator has to buy it again for future flooding phases. Meanwhile, under the likely CO_2 flooding scenario in the offshore classes of reservoirs e.g. in the North Sea, both the w_1 and w_2 weight factors are likely to be positive, implying that both EOR and storage are simultaneously important.

In the analysis that follows, we assume that w_1 and w_2 are +0.5 and -0.001 for purely EOR driven scenario and are +0.5 and +0.001 for a combined EOR and storage (CCUS) CO_2 flooding. In other words;

$$f_{EOR} = 0.5\frac{N_p^*}{N_{OIP}} - 0.001\frac{N_p^* \times U_{CO2}}{V_R} \tag{5.2}$$

$$f_{CCUS} = 0.5\frac{N_p^*}{N_{OIP}} + 0.001\frac{N_p^* \times U_{CO2}}{V_R} \tag{5.3}$$

A value of $w_2 = 0$ indicates that the cost of CO_2 processing is the same as the cost of fresh CO_2 purchase. The form of the objective function shown above is simplistic and can never replace a full comprehensive economic analysis. There are other important considerations, e.g. any penalty for CO_2 emissions or accounting for operating and recycling costs which have not been taken into account. However, this objective function is still useful for evaluating the benefit of different CO_2 flooding processes. It can be an important input parameter for any likely more comprehensive economic analysis.

While the above objective function treats the storage and EOR objectives in two separate terms, they are technically dependent. In other words, there is always a correlation (or synergy) between the quantity of stored CO_2 and the oil which have been recovered in any CO_2 flood. A better EOR response usually means that more CO_2 has been stored in place of mobilised oil.

The evolution of the objective function with regard to the variation of a given input parameter can determine the optimum magnitude of that respective parameter. For a given function which is positively sensitive to the variation of the input parameter (e.g. x), the incremental benefit usually decreases as x further increases and finally reaches an asymptotic limit. For example, the incremental recovery of injecting the second 0.1HCPV CO_2 is always less than the first 0.1HCPV and ultimately this incremental improvement disappears as infinite volumes of CO_2 are injected. This implies that the derivative of the objective function with regard to x becomes progressively smaller as x increases. In other words for any x_1 and x_2 where $x_2 > x_1$;

$$\left(\frac{\partial f}{\partial x}\right)_{x_2} < \left(\frac{\partial f}{\partial x}\right)_{x_1}$$

A threshold critical parameter, (c) can be defined to help identifying the critical limit after which increasing the parameter x does not merit any significant improvement for the process under study. In other words, for a given process, x can be increased as long as;

$$\left(\frac{\partial f}{\partial x}\right) \geq c$$

f in the above analysis is the desired objective function (either f_{EOR} or f_{CCUS}) and x refers to any parameters that need a kind of optimisation e.g. the length of the process, the optimum CO_2 slug size or the optimum operating pressure. The critical parameters (c) can be determined by economic analysis and could be different for different parameters under investigation. Note that this analysis, although informative, does not replaces a comprehensive economic analysis.

5.3 The Choice of the Flooding Strategy

Apart from gravity stable CO_2 flooding and CO_2 flooding for secondary recovery, the majority of conventional onshore CO_2-EOR processes, e.g. in the Permian Basin in the United States, start when initial waterflooding reaches the economic limit. Usually, a fixed volume (in terms of HCPV) of CO_2 is injected, either in the form of single slug or alternately with water (WAG) or a combination of both. Once the desired volume of CO_2 has been injected, waterflooding resumes to produce any mobilised but remaining oil plus part of the injected CO_2. Recovered CO_2 is used again for future CO_2 flooding phases in the same field to reduce the net import of CO_2. This flooding strategy reduces the net import (consumption) of CO_2 while allowing a more rapid oil response which improves project economics in terms of *EOR*.

Figure 5.1 compares the evolution two different objective function, "pure EOR" and "combined EOR and storage" described above, for the same CO_2 flooding process in a heterogeneous model. The model parameters are those depicted in Table 5.1. The fluid description and relative permeability parameters are similar to those described in Section 1 of Chapter 2. CO_2 dissolution in water has also been taken into account to consider the significance of trapped CO_2 dissolution by extended final waterflooding and its consequent impact on the evolution of the objective functions. The average flooding pressure is always higher than MMP, thus compositional effects do not affect the results.

Table 5.1: Details of the areal heterogeneous model used in this study

Grid	256 × 64 × 1
Length (L)	25.6ft
Width (W)	6.4ft
Dip angle	0
Average horizontal permeability (k_x)	100mD (log-normally distributed)
V_{DP}	0.8
Dimensionless correlation length (λ_{xD}, λ_{zD})	0.25, 0.1
k_z/k_x	0.1
Porosity	0.2
Initial pressure and temperature	3000psi and 212°F
Minimum miscibility pressure	2400psi
Rate of depletion (r)	4%HCPV/year
Injection interval	Left-side of the model
Production interval	Right-side of the model
Fluid model	Table 2.1
Relative permeability model	Table 2.3

The simulation in this model starts with injecting 1HCPV of water which is followed by injecting 0.4HCPV of CO_2. Once the desired volume of CO_2 has been injected, the final phase of waterflooding resumes and is continued until an additional 2.6HCPV water has been injected. This implies that a total of 4HCPV fluid (either water or CO_2) has been injected in the model (the horizontal axis of Figure 5.1).

Figure 5.1 shows the evolution of the objective functions in terms of the cumulative volume of fluid (either water or CO_2) injected after the initial phase of waterflooding. In other words, the initial phase of waterflooding has not been shown in this figure.

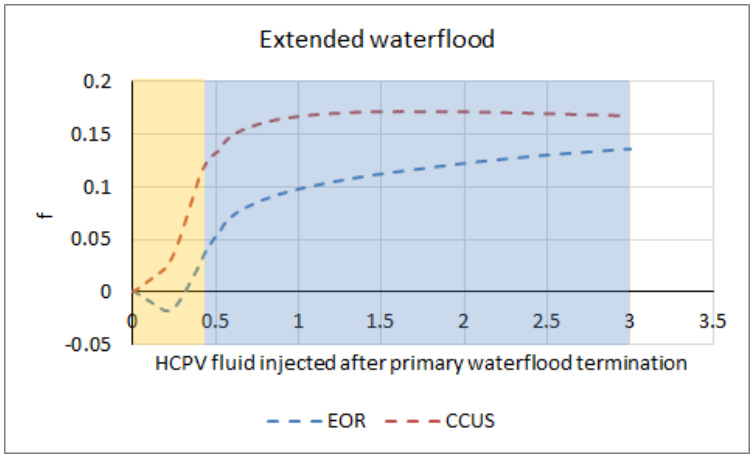

Figure 5.1: Evolution of the objective function (f) for an extended final waterflood (yellow shade represents CO_2 injection, blue shade represents water injection), comparison between EOR driven and combined EOR and storage driven CO_2 flooding scenarios.

It can be seen in Figure 5.1 that the coupled EOR and storage objective function (f_{CCUS}) stabilises fairly quickly, while the EOR driven response function (f_{EOR}) improves continuously by more water injection. The f_{CCUS} evolution shows that by extending the length of the second phase of waterflooding, the EOR response term increases (first term in Equation 5.1) while the storage response term decreases (second term in Equation 5.1), thus the final profile stabilised fairly quickly. Nevertheless, it is expected that the two responses converge if enough water is injected. As per the discussions presented earlier, this suggests that it is likely for a combined EOR and storage CO_2 flooding to terminate earlier because its objective function rapidly increases and stabilizes with further water injection during the second phase of waterflooding

Figure 5.1 shows that while extending final waterflooding in the onshore classes of reservoirs driven purely by EOR may improve project performance as more oil and CO_2 are simultaneously recovered, in the offshore classes of reservoirs driven by combined EOR and storage, this may cause production of a fraction of *in-situ* CO_2 (either free or trapped) which is stored within the formation complex (Section 7 of Chapter 2). Evidently, this is not desirable from the storage point of view. Therefore, the length of final waterflooding should be optimised and possibly become shorter if the target of CO_2 flooding is combined EOR and CO_2 storage.

If abundant sources of CO_2 become available offshore, i.e. cluster scale CO_2 flooding with large capture and transport facilities is deployed in this province, then alternate flooding strategies can be undertaken different from those practiced onshore. One alternate flooding strategy could be avoiding the second phase of water flooding, such that the CO_2 flooding stage is extended allowing greater volumes of CO_2 to be injected. This will increase the pore volume usage efficiency as water will not replace CO_2, while recovering additional hydrocarbon. Figure 5.2 schematically compares these two different flooding strategies.

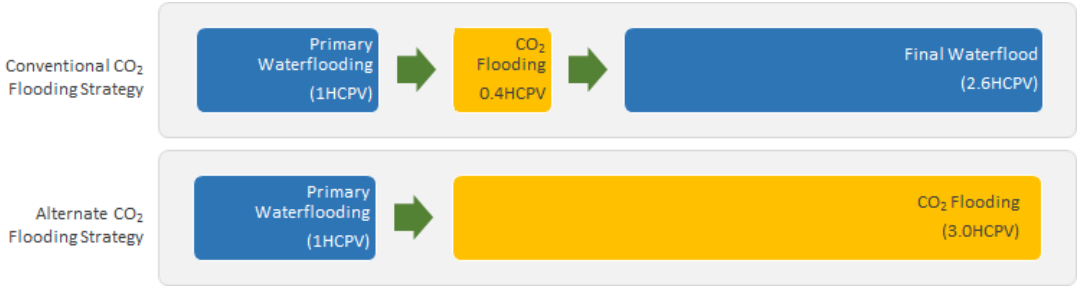

Figure 5.2: Different CO_2 flooding process designs; extended final water flooding (conventional) and extended CO_2 flooding (alternate).

Figure 5.3 compares the evolution of the f_{EOR} and f_{CCUS} objective functions once again to investigate the effectiveness of this alternate flooding strategy. In this alternate flooding strategy, CO_2 injection has been extended until 3.0HCPV CO_2 is injected into the model (instead of 0.4HCPV CO_2 previously) and the second phase of waterflooding has been avoided accordingly.

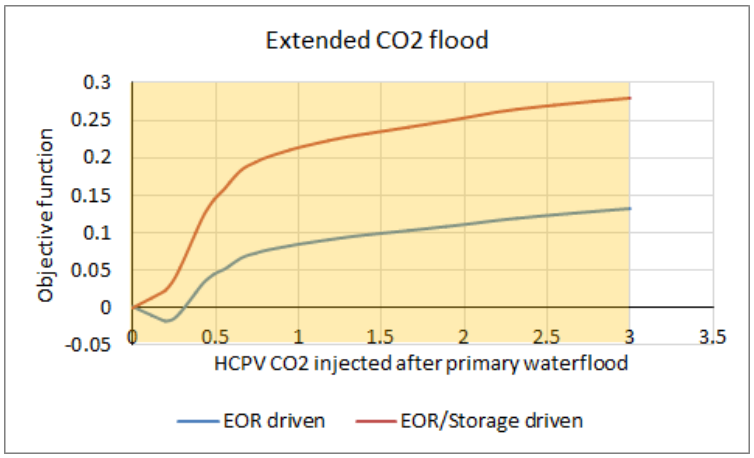

Figure 5.3: Evolution of the objective function for an extended CO_2 flooding (yellow shade represents CO_2 injection). There is no final waterflooding.

Note unlike the profiles observed previously in Figure 5.1, in Figure 5.3 both the f_{EOR} and f_{CCUS} response functions continue to improve as further CO_2 is injected. A greater volume of injected CO_2 implies that more oil has been recovered as well; however, since CO_2 storage is a negative objective for f_{EOR}, its response function evolution is always poorer than the f_{CCUS}.

Figure 5.4 compares the evolution of f_{EOR} and f_{CCUS} for these two different flooding strategies. Note that while there is not a remarkable difference for the f_{EOR} objective function between extended waterflooding and extended CO_2 flooding strategies, continuous CO_2 flooding strategy is superior for the f_{CCUS} objective function.

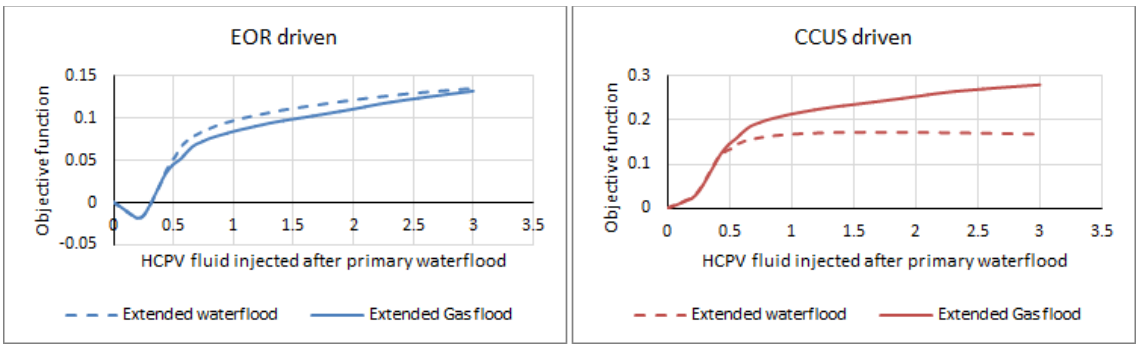

Figure 5.4: Comparison of the objective function between pure EOR and combined EOR/storage scenarios.

Comparing left and right hand figures in Figure 5.4, it can be seen that for both flooding strategies, the f_{CCUS} objective function improves from the beginning of CO_2 flooding since CO_2 injection (storage) can be considered as a source of revenue for the process.

For the "purely EOR" driven scenario (f_{EOR}), there is an initially negative predicted objective function as CO_2 is injected before any oil response appears. Furthermore, under either of the flooding strategies, the f_{CCUS} objective function is always better than its f_{EOR} counterpart.

These are just two examples of different CO_2 flooding strategies that can be practiced in reality. Evidently the choice of the flooding strategies would not be limited to these. Alternatively, CO_2 can be injected as the secondary (and not tertiary) method of recovery for the offshore classes of reservoirs. This avoids a fraction of pore volume being occupied by injected water rather than CO_2.

Gravity stable CO_2 flooding may also become attractive offshore compared to onshore experience. Although gravity stable projects can potentially offer very good macroscopic sweep efficiency, their application has been limited in the onshore classes of reservoirs (e.g. Weeks Island project in the US), mainly because of their relatively slow oil response. A gravity stable CO_2 flood is a negative rate sensitive process in that the ultimate oil recovery decreases as the rate of flooding increases.

This is opposite to horizontal CO_2 flooding where the recovery factor is either neutral or is positively sensitive to rate variations. Note that a higher rate of flooding in horizontal flooding may dampen the severity of the gravity effect. Figure 5.5 compares the recovery factor vs. the rate of depletion for horizontal and gravity stable CO_2 flooding simulations. In all the flooding scenarios a total of 1HCPV CO_2 has been injected. Figure 5.5 shows that while for horizontal CO_2 flooding recovery factor slightly increases as the rate of depletion increases, for gravity stable CO_2 flooding this is evidently negative. This may limit the achievable flood rates to very limiting uneconomic values in gravity stable CO_2 flooding scenarios.

Coupling EOR and storage may allow gravity stable processes to survive in the offshore classes of reservoirs if the added benefit of CO_2 storage from the beginning of the project compensates for the slower oil response in the gravity stable CO_2 flood.

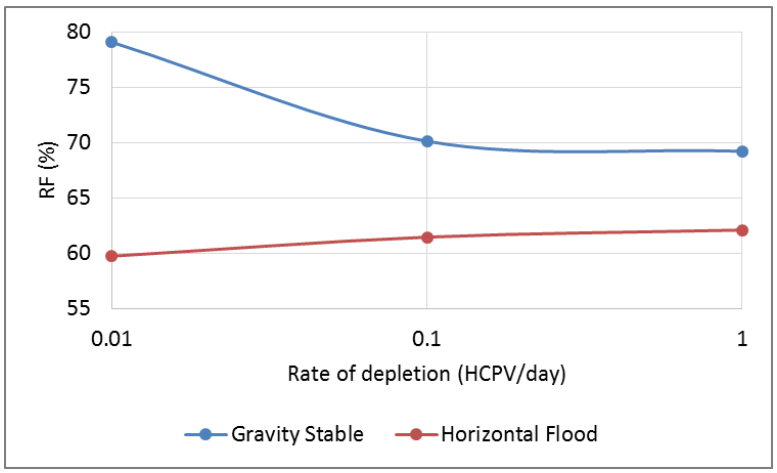

Figure 5.5: Sensitivity to the rate of depletion; gravity stable vs. horizontal CO_2 flooding.

In the North Sea, which is a potential candidate for future CO_2 flooding, gravity stable projects have been favourable because of good structural dip, higher vertical permeabilities and limited gas export infrastructures (Chapter 4).

Although these reservoirs have shown excellent gravity stable performance with hydrocarbon gas injection, the performance of gravity stable CO_2 flooding in them will need to be scrutinised. Equation 5.2 is used to calculate the critical rate of CO_2 injection in a gravity stable process, after which the displacement becomes unstable (Mathews 1989).

$$u_c = k_z \frac{0.0439(\rho_o - \rho_{co2})}{\frac{\mu_o}{k_o} - \frac{\mu_{co2}}{k_{co2}}} sin\alpha \qquad (5.4)$$

In the above equation u_c is the front velocity (ft/day), ρ_o and ρ_{co2} are the density of oil and CO_2 (lb/ft^3) and μ_o/k_o and μ_c/k_c are the inverses of mobilities of oil and CO_2 phases respectively. k_z and α are vertical permeability and the dip angle of the formation, respectively.

Since CO_2 and oil densities are very similar in the North Sea, designing gravity stable CO_2 flooding in this province should be more challenging than gravity stable HC-EOR projects (Bath 1987, Akervoll & Bergmo 2010).

At average ambient North Sea conditions of 5000psi and 212°F (Section 3.7); CO_2, methane and ethane have densities of 43.8, 11.1 and 24.6lb/ft^3 respectively. Assuming an average oil density of 41lb/ft^3 and endpoint relative permeabilities taken from Chapter 2, Table 5.2 calculates the critical rates for a conceptual gravity stable CO_2 flood in the North Sea.

Table 5.2: Critical gravity stable CO_2 flooding rate at typical North Sea reservoir conditions

	Oil-CO_2	**Oil-Methane**	**Oil-Ethane**
Oil density (*lb/ft^3*)	42		
CO_2 density (*lb/ft^3*)	43.75	11.13	24.6
Oil viscosity (*cP*)	0.5		
CO_2 viscosity (*cP*)	0.06	0.02	0.06
k_o	0.57		
k_{co2}	0.28		
k_z	200mD		
u_c (*ft/day*)	**-0.02**	**0.34**	**0.23**

It can be seen that the calculated critical velocity for the CO_2-oil case is negative, which implies that CO_2 density is slightly higher than oil density under these conditions. Comparison of the absolute magnitudes also shows that critical rate for conducting a gravity stable CO_2 flood in the North Sea is prohibitively small. One solution for this negligible density contrast might be to initiate the flood at lower pressures where the CO_2 has lower density or dilute the CO_2 with another lighter hydrocarbon gas (as in the case of Weeks Island project), both of which may reduce the storage efficiency of CO_2.

5.4 The Choice of the Optimum CO_2 Slug Size

The designs of the CO_2 flooding projects in the onshore classes of reservoirs often calls for identifying the minimum quantity of CO_2 that can achieve the job. In these classes of reservoirs, operators do their best to reduce the net injected CO_2 volume, either by injecting it along with water (numerous field examples) or along with another relatively less expensive gas (e.g. Twofred and Slaughter state fields in the Permian Basin) to minimise CO_2 consumption. In the Slaughter State field, the injected gas was composed 72% of CO_2 and 28% of H_2S (Brock & Bryan 1989). In the majority of cases, the optimum injection volume can be determined by simulation (Brinkman *et al*. 1999) though analytical approaches can also assist in this regard (Mungan 1982).

The fact that the incentive for CO_2 flooding is dissimilar between the two flooding processes can also affect the optimum CO_2 slug size. To investigate this, the above model depicted in Table 5.1 was flooded with different injected CO_2 volumes. The same *conventional* flooding strategy described in Figure 5.2 has been applied in all simulation scenarios, in that CO_2 flooding is preceded and followed by two phases of 1HCPV waterflooding. Figure 5.6 (left) compares the evolution of f_{EOR} and f_{CCUS} objective

functions with regard to the volume of injected CO_2. The right figure shows the derivative of the data depicted in the left figure.

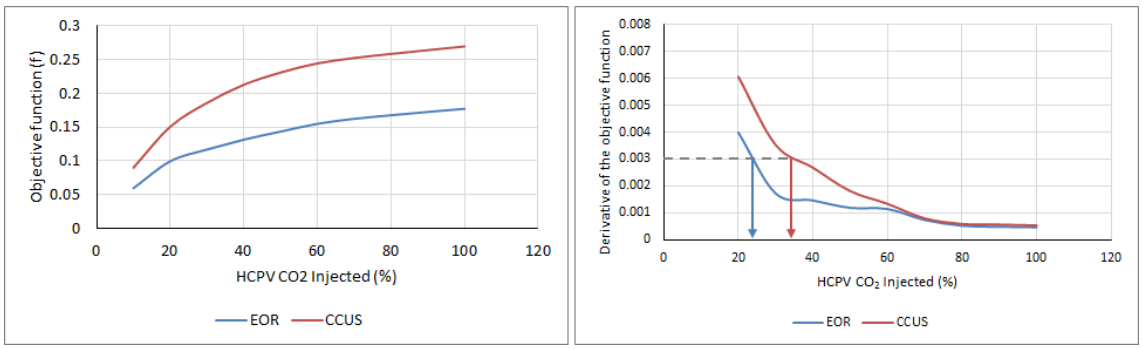

Figure 5.6: Comparison of the objective functions, sensitivity to the injected CO_2 volume. (Left: Evolution of actual objective functions, Right: evolution of the derivative of objective functions)

It can be seen that both of the objective functions constantly improve as further CO_2 is injected, though the incremental improvement gradually decreases. Two observations can be made from this figure. First, as before the f_{CCUS} objective function is always better than the f_{EOR} objective function. Second, for small to medium size CO_2 slug sizes (less than about 60%HCPV), the derivative of the f_{CCUS} objective function is always higher than derivative of the f_{EOR} objective function, which indicates that under other comparable conditions (i.e. comparable compression cost and comparable cost of recycling) more CO_2 can be injected when the purpose of CO_2 flooding is both EOR and storage. Note that an identical limiting threshold may be met later (after injecting more CO_2) for the CCUS driven CO_2 flooding scenarios than for the EOR driven CO_2 flooding. At very high injected CO_2 volumes, the incremental improvement of both response functions becomes similarly very low, due to excessive CO_2 breakthrough.

5.5 The Optimum Operating Pressure

Two important considerations affect the choice of the optimum operating pressure in the CO_2 flooding projects practiced in the United States onshore classes of reservoirs. First, the minimum miscibility pressure and second, the net CO_2 utilisation efficiency. Operation at higher pressures, although improving the flooding efficiency, requires more expensive compression and more importantly, more equivalent CO_2 at surface conditions, which has not been economically attractive in these classes of reservoirs where CO_2 has been a valuable commodity. This means that the operators try to operate as close to MMP

as possible, but not higher. This way, miscibility will be attained while CO_2 utilisation efficiencies and compression requirements are controlled.

Nevertheless, there have been cases which have deviated from this design philosophy i.e. operation has been conducted at pressures either higher or lower than MMP due to other considerations. In some examples, CO_2 flooding has been conducted at higher than MMP to provide enough lift for the producer wells or to allow full associated gas recycling, thus eliminating the need for CO_2 separation and recovery. In some other examples, CO_2 flooding has been conducted at lower than MMP (i.e. immiscibly) because attaining miscibility required pressures higher than formation fracturing pressures. In the Mattoon field, for example, miscible CO_2 flooding was not possible as the CO_2 MMP was higher than fracturing pressure (1780psi and 1800psi, resepctively) (Baroni 1995).

The requirement to optimise both the "EOR and storage" for the CO_2 flooding in the offshore classes of reservoirs may require a different philosophy in terms of the choice of the optimum operating pressure. Figure 5.7 compares the evolution of the f_{EOR} and f_{CCUS} objective functions for a series of CO_2 floods conducted at different operating pressures in the same model whose properties has been described in Table 5.1. The injection strategy is the same for all the injection scenarios as described before (single 40%HCPV CO_2 slug preceded and followed by waterflooding).

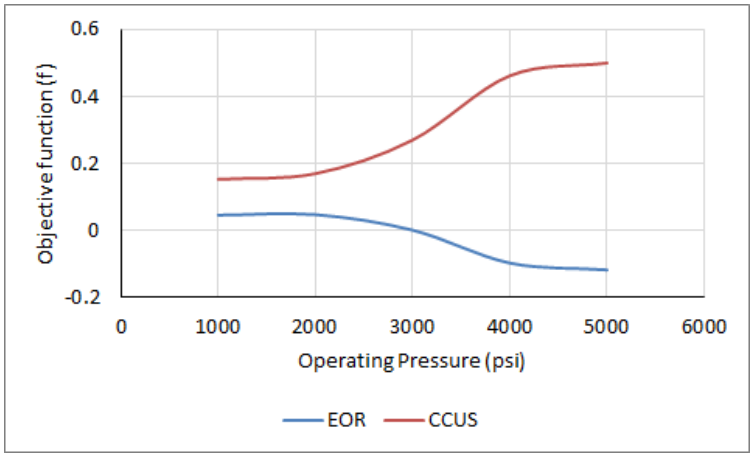

Figure 5.7: Impact of operating pressure on the evolution of the EOR and CCUS objective functions.

It can be seen that the f_{EOR} objective function monotonically becomes poorer as pressure increases, while the f_{CCUS} objective function monotonically improves. Both the objective functions depicted in Figure 5.7 reach some asymptotic limits at higher flooding pressures as CO_2 compressibility progressively becomes smaller.

This implies that unlike onshore classes of reservoirs, offshore, the opportunity for CO_2 flooding at higher pressures could be more significant. There are, however, other considerations, e.g. the security of CO_2 storage and the cost of compression which may affect this conclusion.

The opportunity for flooding at high pressures is significant in the North Sea group of reservoirs. North Sea reservoirs are deep (Chapter 3) which means that they can tolerate higher fracturing pressures and therefore conducting CO_2 flooding at elevated pressures is more feasible in them. The fact that North Sea reservoirs are also deeper implies that they require more lift to bring the reservoir fluids to surface. Apart from artificial lift, one alternate solution is to operate the flood at higher pressures to provide the fluids enough lift to be produced. North Sea reservoirs are often supported by strong aquifers, which may limit the opportunity for pressure management (Bath 1987, Fayers *et al*. 1981). Higher operating pressure required for improving storage efficiency may provide some residual benefits in terms of improving the EOR response of the flood, as was discussed in Chapter 2.

5.6 CO_2 Separation and Recycling

An important consideration in a CO_2 flooding project is how to deal with the produced gas which contains CO_2. The initial choice is often between produced gas *venting* or *recycling*. If it comes to recycling, then the second question is the choice between *whole* produced gas recycling or *separating* CO_2 and then recycling it. Figure 5.8 schematically illustrates the possible alternatives regarding the handling of produced associated gas and CO_2.

In the onshore classes of reservoirs where CO_2 flooding was historically driven by only EOR and the CO_2 was supplied from natural sources, it has been possible to vent the whole produced gas to atmosphere without any penalty, considering only the balance between the costs of fresh CO_2 purchase and recycling.

However, in the offshore classes of reservoirs this philosophy is not practical. Offshore, venting of the produced gas containing CO_2 may face significant penalties, as the source of supplied CO_2 in these classes of reservoirs is from capture plants. Therefore, it does not make sense to release the already captured CO_2 back to atmosphere for whatever

reason. This means that recycling is expected to be an integrated part for any CO_2 flooding activity which will be conducted in the offshore classes of reservoirs.

In those CO_2 floods conducted in the onshore classes of reservoirs e.g. in the Permian Basin, recycling the *whole* produced gas (associated gas and CO_2) is sometimes an attractive option as it reduces fresh CO_2 purchase in addition to CO_2 separation costs. In the offshore classes of reservoirs, recycling the whole produced gas may reduce the operation costs similar to the onshore classes of reservoirs; however, it may lower the CO_2 storage efficiency as part of the pore volume is occupied by less desirable associated gas instead of CO_2.

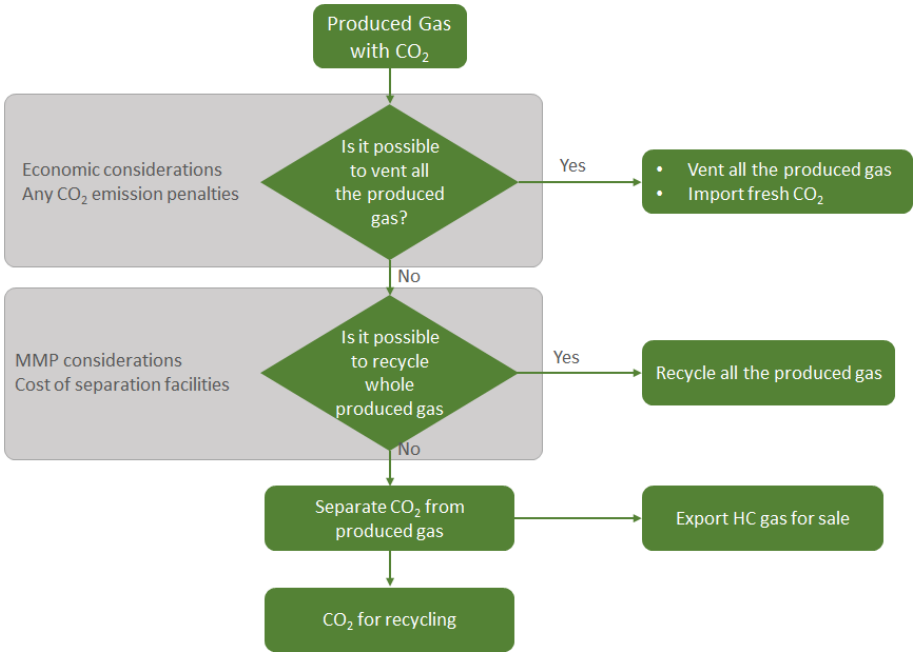

Figure 5.8: Possible alternatives for handling the produced associated gas and CO_2

Figure 5.9 compares the evolution of "pure EOR" and "combined EOR and storage (CCUS)" objective functions under two different recycling strategies; full associated gas recycling and only separated CO_2 recycling for the same model described above in Table 5.1.

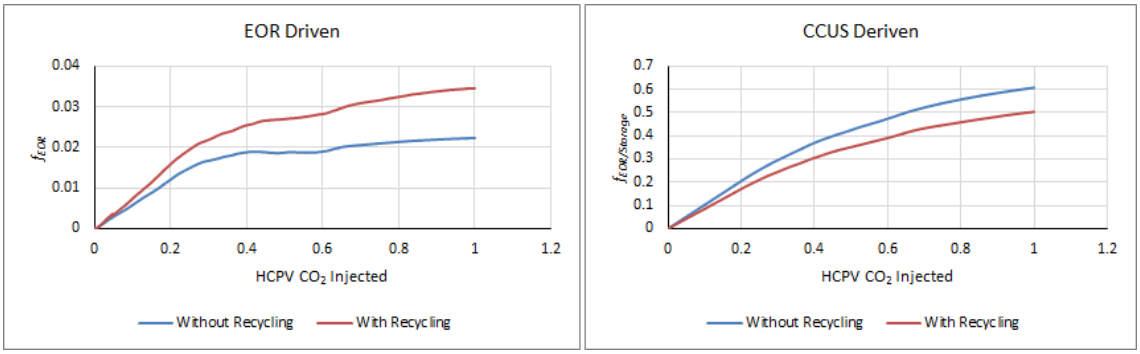

Figure 5.9: Comparison of EOR and combined EOR/CCS objective functions with and without recycling

The flooding strategy is similar to that depicted in Figure 5.2 (*conventional flooding*). Recycling reduces the recovery factor by slightly more than 1%; however, it reduces the net stored CO_2 almost 8%. Therefore, the EOR response improves while on the other hand, recycling reduces the cumulative amount of CO_2 stored within the system and this adversely affects the combined EOR/Storage response as depicted in the right figure.

In some offshore provinces e.g. in the North Sea, the produced gas has a considerable market value which makes separation of CO_2 a necessity from another perspective. Apart from the storage consideration, when it comes to the choice between w*hole produced gas* and *only pure CO_2* recycling, the extent that MMP will be affected by the presence of impurities (associated gas along with CO_2) is important. Gas oil ratio (GOR) could be a significant indicator in this regard. The higher the GOR, the more the MMP will be affected by the produced gas and hence processing becomes more of a necessity. Figure 5.10 compares GORs between two example onshore (the Permian Basin) and offshore (the North Sea) provinces. Although the North Sea fields have slightly higher gas oil ratios, a conclusive difference cannot be determined.

It has been shown in Chapter 2 that due to higher reservoir temperatures in the North Sea, CO_2 MMPs in the North Sea ambient reservoirs conditions are less sensitive to impurities than in the Permian Basin (Figure 2.11). These results show that, apart from a storage consideration, it would be technically possible to reinject all the produced gas containing CO_2 in the North Sea province with only minimal considerations. These results also have been confirmed by Akervoll *et al*. (2010) who suggested that recycling the contaminated CO_2 with hydrocarbon at the North Sea prevailing reservoir conditions has a negligible impact on the CO_2-EOR process efficiency.

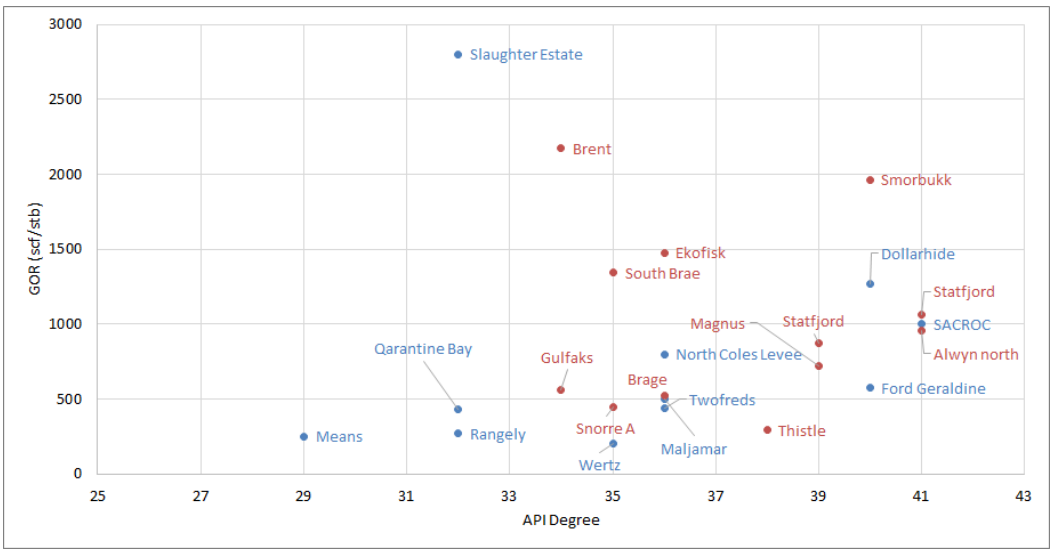

Figure 5.10: GOR comparison between the two provinces (data are from various references)

Review of the field experiences in the relevant onshore and offshore provinces is also worth considering. In the Dollarhide field, CO_2 could be mixed with up to 35%HC produced gas before the MMP is severely affected. Therefore, the produced CO_2 stream could be either recycled or reused for other patterns without full CO_2 recovery (Wang & Robertson 1998). In the Mean San Andres field, all the produced gas was reinjected as the economics of the project did not warrant a full CO_2 separation (Magruder *et al*. 1990). This is also because the field GOR was very low. In the North Cross field, part of the produced gas was reinjected into the designated areas of the field (Mizenko 1992). In the Hanford field, CO_2 should have been stripped from the produced gas, otherwise the MMP would increase significantly (Merritt & Groce 1992).

For the North Sea, the data is far more limited as yet there is no CO_2 flooding in this province, however, a CO_2 flooding study in the Forties field has estimated that up to 15% mole fraction of methane can be tolerated in the recycling stream before MMP is adversely affected (Mathiassen 2003). The successful application of hydrocarbon flooding in the North Sea, however, may create confidence regarding the effective miscibility development between mixtures of CO_2 and associated gas containing hydrocarbon and the reservoir fluid upon recycling. However, given the requirement to maximise the storage efficiency in any North Sea CO_2 floods, as was mentioned previously, it might be necessary to eliminate all the associated hydrocarbon in the produced gas stream before recycling.

5.7 WAG; Is It Useful or Detrimental for Combined EOR and Storage CO_2 Flooding?

WAG increases the ultimate recovery factor while decreasing the net CO_2 utilisation efficiency, both of which are favourable in term of "pure EOR". Applying WAG in a reservoir, however, means that a fraction of reservoir pore volume will be occupied by water rather than CO_2 and this may have a negative impact for the CO_2 flooding in the offshore classes of reservoirs where CO_2 storage is a major consideration.

To investigate this, the evolution of the above described objective functions were compared between single slug and WAG CO_2 flooding strategies. The injection strategies are depicted in Figure 5.11. CO_2-water interaction has also been taken into account. The model parameters are the same as before. In both models, after an initial waterflooding

period (up to 1HCPV), CO_2 is injected either as a single slug or WAG with a 1:1 ratio (up to 40%HCPV). The processes are terminated by final waterflooding where another 1HCPV of water is injected. Figure 5.12 compares the evolution of objective functions in two different injection strategies with and without WAG.

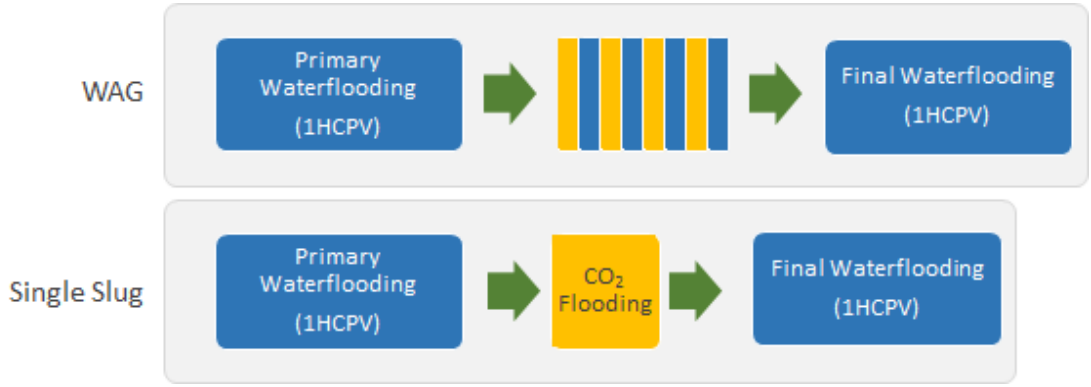

Figure 5.11: Schematic of WAG and single slug CO_2 injection. In both models 40% HCPV CO_2 has been injected.

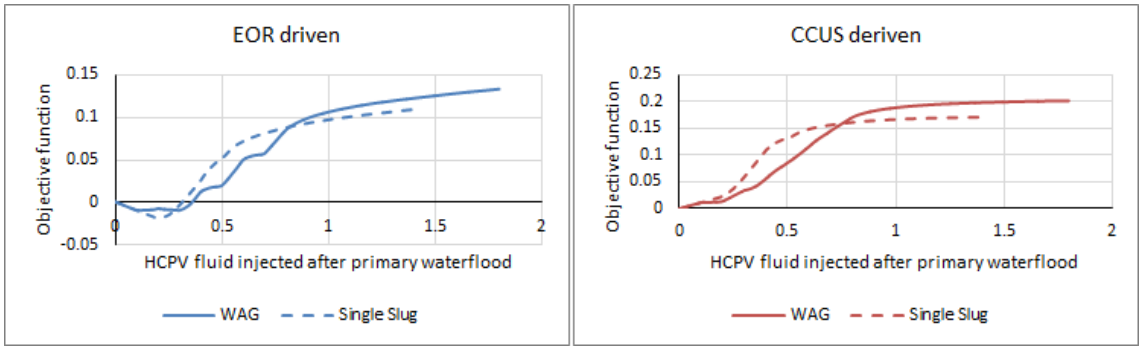

Figure 5.12: Comparison of the "pure EOR" and "combined EOR and Storage" CO_2 flooding between WAG and single slug CO_2 injection strategies

Figure 5.12 shows that applying WAG has a positive impact on the evolution of both "pure EOR" and "coupled EOR and storage" objective functions, though the relative improvement is slightly different. The final relative improvements are respectively 21% and 17% for the "pure EOR" and "combined EOR and storage" driven scenarios. For the "purely EOR" driven CO_2 flooding, this is expected anyway as WAG generally improves the ultimate oil recovery in addition to decreasing the CO_2 utilisation efficiency, both of which are favourable in terms of EOR. However, for the "combined EOR and storage" scenarios, it is interesting to note that similar improvement benefits can still be observed, though part of the pore volume has now been filled with water instead of CO_2. This shows that although part of the pore volume is now occupied by water as a result of applying WAG, WAG has diverted CO_2 to other regions of the system which means that the

macroscopic storage of the system has been improved (while the *microscopic storage* may of have been impaired).

Moreover, alternate cycles of WAG trap a larger fraction of injected CO_2 as an immobile phase, which is advantageous from the storage point of view. Note that in this scenario, WAG has not changed the flow pattern to gravity dominated.

5.8 Conclusions

The followings conclusions are derived for the study conducted in this section:

- Different motivations for CO_2 flooding among different classes of reservoirs may cause certain elements of the conventional CO_2-EOR process design, which have been practiced historically in the onshore classes of reservoirs, to be altered when the same process is taken offshore.
- This means that the conventional practice of CO_2 flooding (i.e. waterflooding after CO_2 flooding) should either be modified or replaced with alternate flooding strategies to satisfy the requirements of both EOR and storage. It was shown that the final waterflooding should, for example, be conducted for a relatively shorter time or it can even be avoided and replaced with extended CO_2 flooding if abundant sources of CO_2 are available as likely alternatives. Gravity stable CO_2 flooding and secondary CO_2 flooding are other potential options.
- Coupling the EOR and storage considerations in the offshore classes of reservoirs makes the CO_2-EOR process potentially more rewarding, since there is an incentive for CO_2 injection from the beginning of CO_2 flooding in addition to enhanced oil recovery, which usually appears later.
- The incremental benefit of flooding with higher CO_2 volumes is always larger for a combined EOR and storage process than for a purely EOR driven process, similar concept is expected to be relevant in the offshore classes of reservoirs.
- If the EOR and storage processes are coupled, then flooding at elevated pressures can become attractive and practical in the offshore classes of reservoirs.
- Recycling is expected to be an integrated part of any CO_2 flooding activity which will be conducted in the offshore classes of reservoir, where emission is not permitted.

- Similar to pure EOR CO_2 flooding, WAG is still useful for the "coupled EOR/CCS" CO_2 flooding, if it does not change the flow pattern to gravity dominated, though the relative improvement might be different. WAG may reduce the microscopic storage, but simultaneously improves the macroscopic storage.

The analysis conducted in this chapter, however, does not replace a comprehensive economic analysis. A full economic analysis may be required to better address the impact of, for example, any reward for CO_2 storage in addition to oil produced from EOR and the net benefit of operating at higher pressures versus the compression cost. This economic analysis may also include the costs of separation and processing facilities and any potential penalty for CO_2 emissions to atmosphere due to operation.

Chapter 6 Dispersivity Measurement in Heterogeneous Media and its Application in Permeability Upscaling

6.1 Introduction

Proper gridding of heterogeneous numerical models is a challenging task in reservoir simulations. This is because simulation at fine scales is not usually feasible and a certain degree of upscaling is always required. Upscaling in heterogeneous permeability fields, however, distorts the fluid flow pattern, which in turn may affect important model predictions. Nevertheless, this problem is more significant for miscible processes as, unlike immiscible displacement where varying the shape of relative permeability curves is an efficient tool in matching the performance of coarse and fine models, in miscible displacement this technique is no longer available.

Heterogeneity usually creates an artificial mixing within the system which, if correctly matched with equivalent numerical mixing, can determine the right number of grid blocks. The heterogeneity induced dispersivity is due to mixing of different streamlines at different locations. Permeability irregularity has an important impact on the magnitude of this dispersivity. Measuring the artificial dispersivity created by heterogeneity is not, however, straightforward.

Gelhar and Axness (1983) derived a correlation for estimating the permeability induced dispersion (D_l) as a function of correlation length and the degree of heterogeneity. They showed that the magnitude of dispersivity due to heterogeneity in the longitudinal direction is proportional to the correlation length in the longitudinal direction and model heterogeneity.

$$D_l = \frac{v\sigma_{lnk}^2 \lambda_x}{\gamma^2} \tag{6.1}$$

Where γ in this equation is;

$$\gamma = 1 + \sigma_{lnk}^2 \left[\frac{1}{2} - \frac{1}{1 + \frac{\lambda_x}{\lambda_z}} \right] \tag{6.2}$$

The above correlation, although very informative, only considers permeability irregularity to estimate the magnitude of D_l. Not only heterogeneity definition, but also other model characteristics of the displacement, e.g. cross flow and mobility ratio, affect

the velocity patterns in a heterogeneous permeability field, and hence they are important in determining the degree of mixing; the combination these factors will determine the correct size of grid blocks. Garmeh *et al*. (2010) showed that dispersivity in a heterogeneous permeability field can be described by seven dimensionless numbers. They measured dispersivity in different heterogeneous permeability fields as a function of these dimensionless numbers and fitted their measurements into surfaces (or proxies) and used these proxies as an efficient tool for determining dispersivity in other heterogeneous models for the purpose of upscaling.

Numerical dispersion is an artificial mixing imposed on a system since it is assumed that due to numerical dispersion all the fluids within a certain distance (grid block) are fully mixed. Upscaling usually increases numerical dispersion. An excessive increase of numerical dispersion may, however, affect important model predictions. For example, a large numerical dispersion in a gas injection EOR process increases the degree of solvent dissolution and transportation and therefore affects the time of breakthrough. Furthermore, a large degree of mixing may also cause an MCM miscible flood to become immiscible, by increasing the size of the transition zone due to a larger degree of mixing (Chapter 2).

Fanchi derived the numerical dispersion tensor for a number of numerical solution schemes. He showed that numerical dispersion is a full tensor, and is mainly proportional to the half of the grid block size in both horizontal and vertical orientations (Fanchi 1983).

There have been previous attempts to replace heterogeneity induced mixing with an equivalent numerical dispersion (Garmeh & Johns 2010; Haajizadeh *et al*. 1999, Fanchi 1983). Haajizdeh *et al*. tried to represent the heterogeneity induced mixing with an equivalent grid block size. However, for their specific heterogeneity definition, they found that very fine grid blocks are still required (Haajizadeh *et al*. 1999). Garmeh showed that for an upscaling to be accurate, the magnitude of dispersion in the longitudinal and transverse directions should be closely matched between fine and coarse models (Garmeh & Johns 2010). They measured dispersivity between fine and coarse models based on the proxies that they have obtained by running a large number of simulations.

In this article, we develop a new method for estimating the heterogeneity induced dispersivity in different orientations and in random correlated permeability fields. These measured dispersivities can later be matched with equivalent numerical mixing

(numerical dispersion) for rapid estimation of the required number of grid blocks in different orientations.

It is important to note that in this study all the model properties are described by dimensionless numbers. The miscibility in this study is also of FCM type. Moreover, we do not consider the impact of gravity.

6.2 Theoretical Background

In a two dimensional miscible displacement, longitudinal and transverse Peclet numbers describe the magnitudes of dispersivities in the relevant orientations. Peclet number defines the ratio of the time of dispersion to the time of convection (Orr 2007). In other words, it shows the relative significance of the component transport by advection mechanism against dispersion/diffusion mechanism. The bigger the Peclet number, the less significant will be impact of dispersion in the total component transport.

In a 2D cross sectional model, longitudinal and transverse Peclet numbers are defined by the following equations (Chang *et al*. 1994, Gharbi *et al*. 1998).

$$Pe_L = \frac{L}{\alpha_L} \tag{6.3}$$

$$Pe_T = \frac{H^2}{L\alpha_T} \tag{6.4}$$

Smaller Peclet numbers in the longitudinal direction causes earlier solvent breakthrough and lower recoveries. Unlike longitudinal Peclet number, a smaller transverse Peclet number means a more efficient recovery, as solvent further diffuses into intra layers and recoveries are hence improved. Equations 6.3 and 6.4 show that Peclet numbers in both orientations are inversely proportional to the dispersivity in that respective orientation. If the magnitude of the Peclet numbers in any orientation is known, then the corresponding dispersivity in that orientation can be simply calculated.

Knowing dispersivity, one can then calculate the equivalent grid block size to simulate the same magnitude of physical dispersion. Fanchi (1983) derived the numerical dispersion for an FCM simulation process in two dimensions described with Equation 6.5.

$$\varphi \frac{\partial c}{\partial t} + u_x \frac{\partial c}{\partial x} + u_z \frac{\partial c}{\partial z} = 0 \tag{6.5}$$

The numerical dispersion (error) for the above equation can be estimated as[12]:

$$\varepsilon = \frac{1}{2}\left(u_x(\Delta x + u_x \Delta t)\frac{\partial^2 c}{\partial x^2} + u_x u_z \Delta t \frac{\partial^2 c}{\partial x \partial z} + u_z u_x \Delta t \frac{\partial^2 c}{\partial z \partial x} + u_z(\Delta z + u_z \Delta t)\frac{\partial^2 c}{\partial z^2} \right) \tag{6.6}$$

Assuming the throughput term is very small (very small Δt), all the terms containing Δt can be neglected. This usually happens if a rigorous controlling criterion is selected for simulation (e.g. maximum concentration variation is set to 5%). Therefore, Equation 6.6 becomes:

$$\varepsilon = \frac{1}{2}\left(u_x \Delta x \frac{\partial^2 c}{\partial x^2} + u_z \Delta z \frac{\partial^2 c}{\partial z^2} \right) \tag{6.7}$$

Equation 6.7 shows the difference between analytical and numerical solution if Δt is very small. In other words, numerical solution of Equation 6.5 gives an analytical solution described by Equation 6.8.

$$\varphi \frac{\partial c}{\partial t} + u_x \frac{\partial c}{\partial x} + u_z \frac{\partial c}{\partial z} - \frac{1}{2}\left(u_x \Delta x \frac{\partial^2 c}{\partial x^2} + u_z \Delta z \frac{\partial^2 c}{\partial z^2} \right) = 0 \tag{6.8}$$

The fundamental transport equation with dispersion coefficient has the following form when expressed in terms of dispersion coefficient (K_L and K_T) (Gharbi *et al*. 1998);

$$\varphi \frac{\partial c}{\partial t} + u_x \frac{\partial c}{\partial x} + u_z \frac{\partial c}{\partial z} - \varphi K_L \frac{\partial^2 c}{\partial x^2} - \varphi K_T \frac{\partial^2 c}{\partial z^2} = 0 \tag{6.9}$$

Equation 6.9, when expressed in terms of dispersivities (α_L and α_T), becomes;

$$\varphi \frac{\partial c}{\partial t} + u_x \frac{\partial c}{\partial x} + u_z \frac{\partial c}{\partial z} - \alpha_L u_x \frac{\partial^2 c}{\partial x^2} - \alpha_T u_z \frac{\partial^2 c}{\partial z^2} = 0 \tag{6.10}$$

Term by term comparison of Equations 6.8 and 6.10 shows that the following conditions should be met for the two equations to generate the same results.

$$\alpha_L = \frac{1}{2}\Delta x \text{ and } \alpha_T = \frac{1}{2}\Delta z \tag{6.11}$$

[12] The above error is based on implicit numerical solution of Equation 6.5 with backward difference in the spatial domain.

Knowing the magnitude of Pe_L and Pe_T, α_L and α_T can be easily calculated (Equations 6.3 and 6.4). Assuming $\Delta x = \frac{L}{N_x}$ and $\Delta z = \frac{H}{N_z}$ the number of grid blocks then can be derived as;

$$\alpha_L = \frac{1}{2}\Delta x \Rightarrow \frac{L}{Pe_L} = \frac{1}{2}\frac{L}{N_x} \Rightarrow N_x = \frac{Pe_L}{2} \tag{6.12}$$

$$\alpha_T = \frac{1}{2}\Delta z \Rightarrow \frac{H^2}{LPe_T} = \frac{1}{2}\frac{H}{N_z} \Rightarrow N_z = \frac{Pe_T}{2}\frac{L}{H} \tag{6.13}$$

Where N_x and N_z are the number of grid blocks in the horizontal and vertical directions. In fact Equations 6.12 and 6.13 measure the range that fluids are considered to be fully mixed due to heterogeneity and transpose an equivalent grid block size over it. The aim of this study is to measure Pe_L and Pe_T in a heterogeneous random correlated permeability field and match it with equivalent number of grid blocks. Therefore, an important assumption in this study is that mixing by heterogeneity can be approximated with the convective-diffusive equation. In other words, mixing generated by heterogeneity behaves as physical or numerical mixing.

In the remainder of this study, we first show an example of how physical dispersion can be replaced by its equivalent numerical dispersion and the procedure for determining the right number of grid blocks in a one dimensional model. Next, a new method to measure the Peclet number (or dispersivity) in a discretised numerical models is developed and discussed. This developed method is then applied to heterogeneous discretised numerical domains to measure Peclet (or dispersivities) in different orientations.

The estimated dispersivities, when appropriately averaged over the entire model, can represent the whole model dispersivity which then can be matched with a proper grid block size to correctly determine the required number of grid blocks. This saves the simulation engineer a lot of time and effort by avoiding running sensitivity analysis to find the required number of grid blocks.

6.2.1 Example Case; Matching Physical Dispersion with Numerical Dispersion

The next example shows how physical dispersion can be replaced with an equivalent amount of numerical dispersion. Model-A (Figure 6.1) has 100 grid blocks with a physical dispersivity of α_{phy}=0.01.

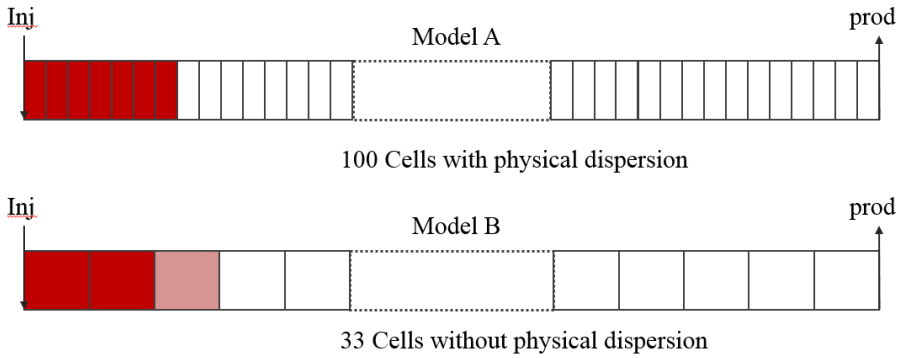

Figure 6.1: Schematic illustration of fine and coarse 1D models.

The solvent is injected from the left side of the model. In a one dimensional FCM displacement, the convective-diffusive equation describes the concentration profiles in time and space domains (Orr 2007);

$$\frac{\partial c}{\partial \tau} + \frac{\partial c}{\partial \xi} - \frac{1}{Pe}\frac{\partial^2 c}{\partial \xi^2} = 0 \qquad (6.14)$$

We want to find the equivalent size of grid blocks where the performance of model-A is simulated. To find the equivalent number of grid blocks, the total magnitude of dispersion of the model-A should be first measured:

$$\alpha_T = \alpha_{phy} + \alpha_{Num}$$

α_{phy} is 0.01 as mentioned above, α_{Num}, however, should be calculated. The numerical dispersion for Model-A, having 100 grid blocks is[13] (Fanchi 1983):

$$[\alpha_{num}]_{model\ A} = \frac{1}{2}\Delta x = \frac{1}{2}\left[\frac{1}{N_x}\right]_{model\ A} = \frac{1}{2}\frac{1}{100} = 0.005$$

Therefore: $\alpha_T = \alpha_{phy} + \alpha_{Num} = 0.01 + 0.005 = 0.015$ (for model-A)

In the second model (model-B), physical dispersivity can be omitted (α_{phy}=0) and the total equivalent magnitude of dispersion observed in model-A can be represented exclusively by numerical dispersion.

$$\alpha_T = 0.015 = [\alpha_{Num}]_{model\ B} = \frac{1}{2}\Delta x = \frac{1}{2}\left[\frac{1}{N_x}\right]_{model\ B}$$

$[N_x]_{model\ B} \approx 33$ Grid blocks

[13] Models are treated in dimensionless domain, therefore L in the Peclet formula can be assumed 1.

It can be concluded that the larger the physical dispersion, the smaller will be the required number of grid blocks. Figure 6.2 shows the concentration profile at 0.5PV solvent injection along both models. It can be seen that they are fairly matched, although dispersion is represented by two different approaches in each of them.

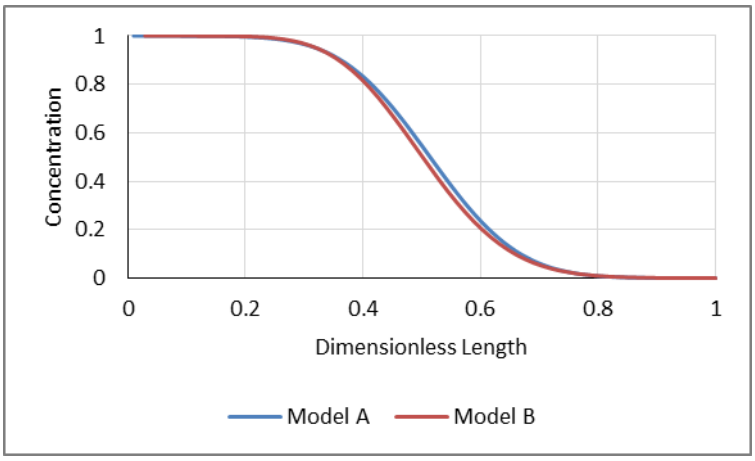

Figure 6.2: Concentration profile at 0.5PV solvent injection along the length of both models. Comparison between fine model with explicit dispersion and coarse model with equivalent numerical dispersion.

6.3 Development of a New Method to Measure Peclet Number in Discretised Numerical Domains

6.3.1 Derivation of Method

Coates and Smith derived the analytical solution of convective-diffusive equation in a one dimensional displacement subject to certain initial and boundary conditions (Coats & Smith 1964). To measure the *in-situ* Peclet number, we use their solution outlined below as the initial starting point;

$$c(\xi,\tau) = \frac{1}{2} erfc\left[\frac{\sqrt{Pe}(\xi-\tau)}{2\sqrt{\tau}}\right] \tag{6.15}$$

To measure the Peclet number, one can measure the effluent concentration, i.e. measure $c(1,\tau)$. Knowing the effluent concertation at $\xi = 1$ at different PV of solvent injection (τ), the magnitude of the Peclet number can be calculated accordingly. This is the preferred method for measuring the Peclet number in the laboratory, since it is easier to measure effluent concentrations rather than *in-situ* ones. However, with modelling (either analytically or numerically), it is possible to determine the exact *in-situ* concentration

anywhere within the model and at any time. Moreover, the observed mixing in the effluent concentration might be due to arrival of components which are transported by different streamlines which are simply mixed at the producer, thus this may not represent true mixing *within the system*.

Therefore, in this study instead of measuring the concentration profile at the outlet of the system, *in-situ* concentrations are measured between a pair of adjacent points in the spatial domain (ξ) at a fixed time (τ) and then are averaged for the entire system. As will be shown later, this approach can accurately measure the magnitude of the Peclet numbers for a given system.

Figure 6.3 schematically shows concentration magnitudes predicted at two adjacent points by the analytical solution of the convective-diffusive equation in a 1D model at a given dimensionless time τ (Equation 6.15).

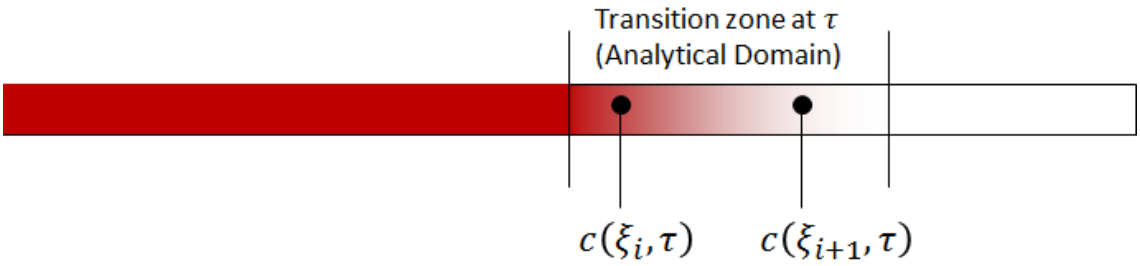

Figure 6.3: A pair of concentration measurement within the transition zone can reveal the magnitude of Peclet number (analytical model). Flow is from left to right.

$c(\xi_{i+1}, \tau)$ and $c(\xi_i, \tau)$ represent the corresponding concentrations at ξ_{i+1} and ξ_i points predicted by Equation 6.15. Therefore, for both of these two points we can write;

$$c(\xi_i, \tau) = \frac{1}{2} erfc\left[\frac{\sqrt{Pe}(\xi_i - \tau)}{2\sqrt{\tau}}\right] \tag{6.16}$$

$$c(\xi_{i+1}, \tau) = \frac{1}{2} erfc\left[\frac{\sqrt{Pe}(\xi_{i+1} - \tau)}{2\sqrt{\tau}}\right] \tag{6.17}$$

We can take the inverse of error function ($erfc^{-1}$) from both sides of the above equations.

$$erfc^{-1}[2c(\xi_{i+1}, \tau)] = \frac{\sqrt{Pe}(\xi_{i+1} - \tau)}{2\sqrt{\tau}} \tag{6.18}$$

$$erfc^{-1}[2c(\xi_i,\tau)] = \frac{\sqrt{Pe}(\xi_i - \tau)}{2\sqrt{\tau}} \tag{6.19}$$

Subtracting Equation 6.19 from Equation 6.18, we then have;

$$erfc^{-1}[2c(\xi_{i+1},\tau)] - erfc^{-1}[2c(\xi_i,\tau)] = \frac{\sqrt{Pe}(\xi_{i+1} - \xi_i)}{2\sqrt{\tau}} \tag{6.20}$$

And hence Peclet number at time τ is which between ξ_{i+1} and ξ_i can be calculated as:

$$[Pe]_\tau = \frac{4\tau\left[erfc^{-1}[2c(\xi_{i+1},\tau)] - erfc^{-1}[2c(\xi_i,\tau)]\right]^2}{(\xi_{i+1} - \xi_i)^2} \tag{6.21}$$

$\xi_{i+1} - \xi_i$ represents the distance in the dimensionless domain (Figure 6.3). Equation 6.21 shows that knowing concentrations at two adjacent points *within the transition zone* at a given dimensionless time (τ), one can measure the respective Peclet number *for that specific time*. It should be mentioned that measurement points must reside within the transition zone i.e. either $c(\xi_{i+1},\tau)$ or $c(\xi_i,\tau)$ concentration should not equal to 0 or 1; otherwise, the measured Peclet number will not be accurate.

6.3.2 Application to Numerical Domains

Although Equation 6.21 has been derived for a continuous system with the analytical solution, we can apply it to numerical domains which are discretised in space and time and measure the Peclet (or dispersion) between pairs of grid blocks. If ξ_{i+1} and ξ_i are two adjacent grid blocks in a numerical domain, we can write:

$$\xi_{i+1} - \xi_i = \frac{x_{i+1}}{L} - \frac{x_i}{L} = \frac{\Delta x}{L} = \frac{1}{N} \tag{6.22}$$

Substituting the above equation in Equation 6.21 we then have:

$$[Pe]_\tau = 4\tau\left[erfc^{-1}[2c(\xi_{i+1},\tau)] - erfc^{-1}[2c(\xi_i,\tau)]\right]^2 N^2 \tag{6.23}$$

Where *N* is the number of grid blocks. Equation 6.23 shows similar to analytical domains, it is also possible to measure Peclet number for a numerical domain. We can also use Equation 6.23 to measure Peclet number in any orientation depending on the position of the pair of grid blocks relative to each other.

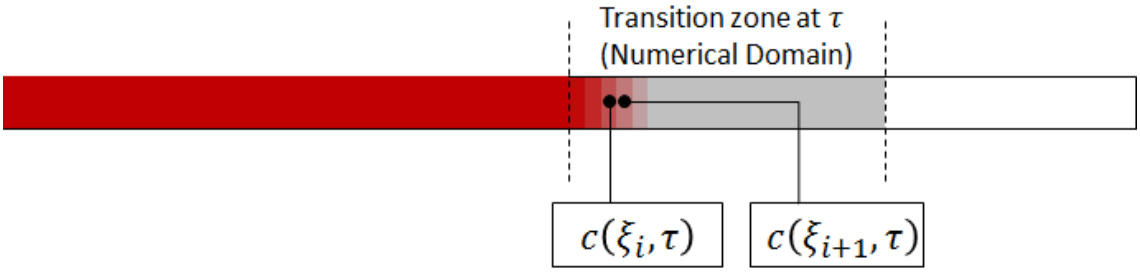

Figure 6.4: Schematic illustration of concentration measurement between pair of grid blocks in a numerical domain.

It should be noted that measurement of Peclet numbers between *N* sampling points (grid blocks) results in *N-1* measured Peclet numbers. Therefore an averaging technique is required to represent the entire model with only one *single* Peclet number.

6.3.3 Validation Test

We apply Equation 6.21 directly to the numerical solution of a convective-diffusive equation (Equation 6.3) and show that it can measure Peclet number accurately. It will be shown that this method is even able to measure the magnitude of the numerical dispersion in addition to conventional physical dispersion. Equation 6.24 shows the convective-diffusive equation in the numerical form when it is solved by backward difference in space and explicitly in time;

$$\frac{c_i^{n+1} - c_i^n}{\Delta\tau} + \frac{c_i^n - c_{i-1}^n}{\Delta\xi} - \frac{1}{Pe}\frac{c_{i-1}^n + c_{i+1}^n - 2c_i^n}{\Delta\xi^2} = 0 \qquad (6.24)$$

Where *i* and *n* refer to discretization in space and time domains, respectively. We assume 100 grid blocks in the horizontal direction and 2000 timesteps to inject 1PV solvent. Hence $\Delta\xi$ and $\Delta\tau$ are 0.01 and 0.0005 accordingly. Timesteps are much smaller than $\Delta\xi$ to allow the explicit numerical solution scheme to remain stable. There is no explicit physical dispersion (α_{phy}=0). Therefore any dispersion observed within the system can be attributed purely due to numerical dispersion. The expected numerical dispersion for the above solution scheme has the form shown below (Fanchi 1983);

$$\alpha_{num} = \frac{1}{2}(\Delta\xi - \Delta\tau) \qquad (6.25)$$

Substituting the relevant magnitudes of $\Delta\xi$ and $\Delta\tau$ in Equation 6.25, the expected numerical dispersion should be;

$$\alpha_{num} = \frac{1}{2}(\Delta\xi - \Delta\tau) = \frac{1}{2}(0.01 - 0.0005) = 0.00475$$

And the expected Peclet number should be around 210.5.

$$Pe = \frac{L}{\alpha} = \frac{1}{0.00475} = 210.5$$

To illustrate this, we solved Equation 6.24 numerically and measured Peclet numbers using Equation 6.23. The measurement was carried out only within the transition zone, i.e. where the concentrations are between 0.1 and 0.9. A geometric average has been used to generate the representative Peclet number for the specific dimensionless time τ. Figure 6.5 illustrates the concentration profile along the calculated Peclet number at $\tau = 0.5$. It can be observed that the measured Peclet numbers are not equal along the transition zone and tend to increase near the tail of the transition zone. However, the average Peclet number is near the predicted value shown above (*Pe*=210.5).

An important observation in Figure 6.5 is that if the transition zone breaks through, the measured Peclet number starts to increase. This is because Peclet numbers are measured over a shorter transition zone and near the tail of the transition zone (e.g. between 0.4 and 0.9 instead of the full range of 0.1-0.9).

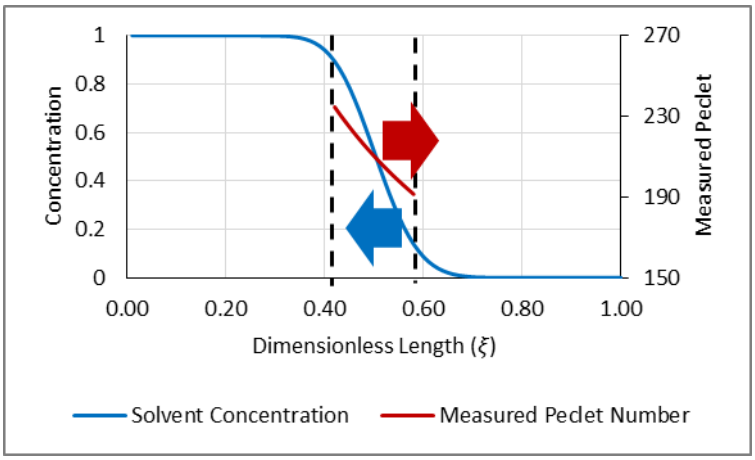

Figure 6.5: Solvent concentration at τ = 0.5 (left axis). The extent of the transition zone is also depicted between dashed lines. Right axis: calculated Peclet numbers; calculated Peclet numbers are not equal and increase near the tail of the transition zone.

We also measured Peclet numbers when there is a fixed amount of physical dispersion within the system. Figure 6.6 shows the evolution of Peclet number in the above system at two different magnitudes of physical dispersivity as a function of PV of solvent injected

(τ). It can be observed that after a few oscillations, the measured Peclet numbers are stabilised at around the expected values. This is the time required for the transition zone to be fully developed. It can also be observed that at around breakthrough time, the measured Peclet number starts to increase as described above in both models.

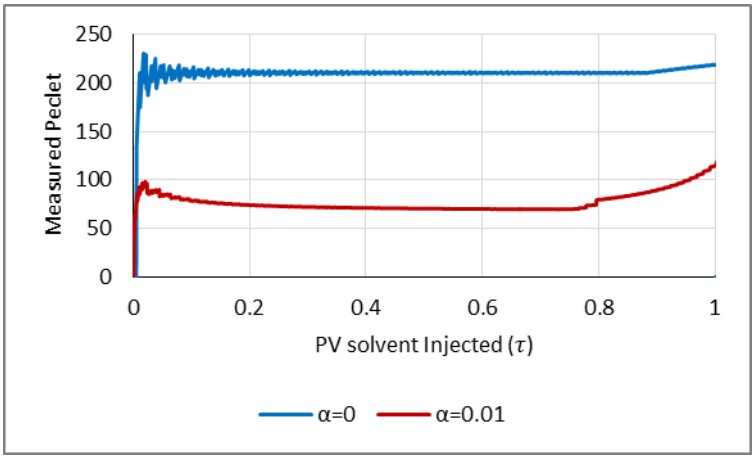

Figure 6.6: Estimated Peclet number for two different scenarios. Blue curve when there is no physical dispersion. Red curve when there is a 0.01 fixed dispersivity. In both cases, the calculated Peclet numbers are corresponding to the expected calculated values.

The red curve in this figure shows the measured Peclet number when a background dispersivity equal to α_{phy}=0.01 has been included in the original analytical and numerical convective-diffusive equations (Equations 6.3 and 6.24). Numerical dispersion is the same as before (α_{num}= 0.00475). The total expected dispersivity therefore is;

$\alpha_{tot} = \alpha_{num} + \alpha_{phy} = 0.00475 + 0.01 = 0.01475$

And hence the expected Peclet number should be around 67.8;

$$Pe = \frac{L}{\alpha} = \frac{1}{0.01475} = 67.8$$

The red data on Figure 6.6 show that the measured Peclet number is again keeping with the expected value. It is interesting to note that although the Peclet number is an average characteristic number defined for the entire system, it can still be traced within the system as well.

Once confident about the accuracy of this approach, the next step is to apply this technique to heterogeneous permeability fields to measure Peclet numbers (or dispersivity) in more complex heterogeneous systems.

6.4 Application to Heterogeneous Permeability Fields

Equation 6.23 can also be applied to heterogeneous permeability fields to measure Peclet numbers in different orientations. Figure 6.7 shows the solvent concentration profile in a fine gridded heterogeneous permeability field after 0.5PV solvent injection.

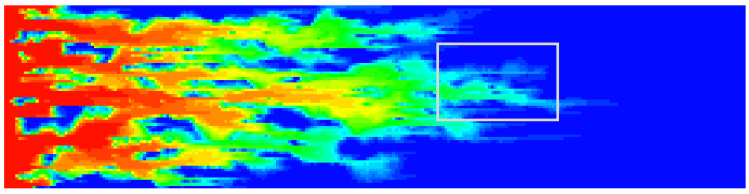

Figure 6.7: Concentration profile after 0.5PV solvent injection. Figure 6.8 is the enlarged version of the rectangle shown in this Figure.

It can be observed that because of heterogeneity, an artificial mixing which is much larger than the mixing anticipated in a homogeneous permeability field has been created in this model. We can apply the same concept as described in Section 6.3 to calculate the Peclet numbers in this more complex heterogeneous permeability field. To calculate longitudinal and transverse Peclet numbers (Pe_L and Pe_T), Equation 6.23 can be applied between all horizontal and vertical pairs of model grid blocks and at any dimensionless time (τ).

$$[Pe_L]_\tau = 4\tau N_x^2 \left(\prod_{j=1}^{N_z} \prod_{i=1}^{N_x} \left[erfc^{-1}\left[2c\left(\xi_{i+1,j},\tau\right)\right] - erfc^{-1}\left[2c\left(\xi_{i,j},\tau\right)\right] \right]^2 \right)^{\frac{1}{N_x N_z}} \quad (6.26)$$

$$[Pe_T]_\tau = 4\tau N_z^2 \left(\prod_{i=1}^{N_x} \prod_{j=1}^{N_z} \left[erfc^{-1}\left[2c\left(\xi_{i,j+1},\tau\right)\right] - erfc^{-1}\left[2c\left(\xi_{i,j},\tau\right)\right] \right]^2 \right)^{\frac{1}{N_x N_z}} \quad (6.27)$$

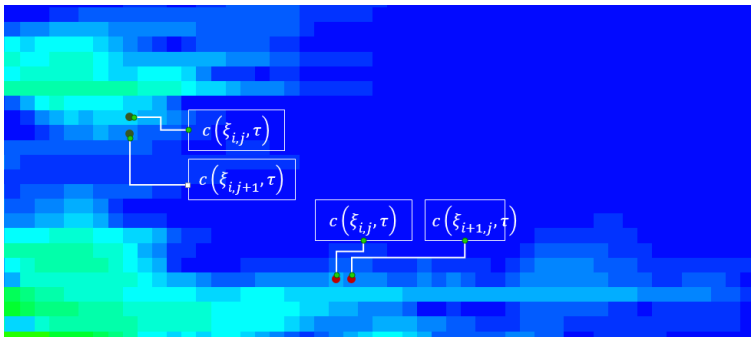

Figure 6.8: Measurement of Peclet numbers between pair of grid blocks in a heterogeneous model. Horizontal measurement for Pe_L and Vertical measurement for Pe_T.

Geometric averaging has been used in Equations 6.26 and 6.27 to calculate the model average Peclet numbers at specific dimensionless times (τ). This is because the measured Peclet numbers have a logarithmic distribution as shown in Figure 6.9. It is also important to mention that, as before, Peclet numbers are measured only within the transition zone. Appendix 4 shows the code to measure the magnitude of Peclet numbers in each orientation at different dimensionless times (τ).

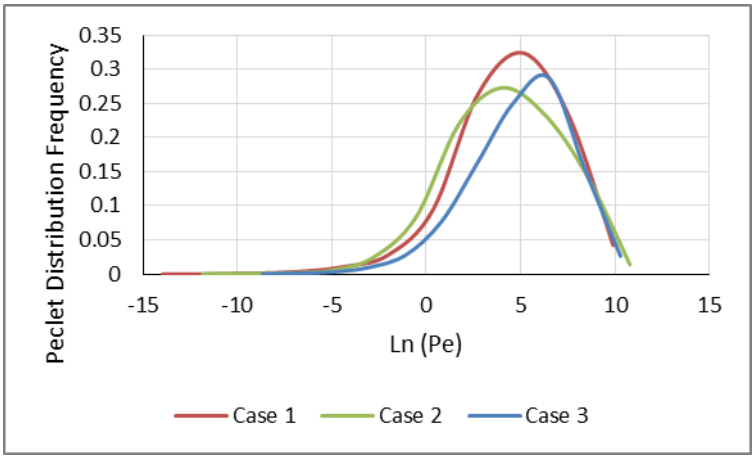

Figure 6.9: Distribution profile of measured Peclet numbers in three different heterogeneous permeability fields. In all cases, the measured Peclet numbers have a logarithmic distribution.

Figure 6.10 shows measured Peclet numbers at different dimensionless times (τ) in a sample heterogeneous permeability field. The right hand side figure shows the effluent concentration profile for this permeability field as well.

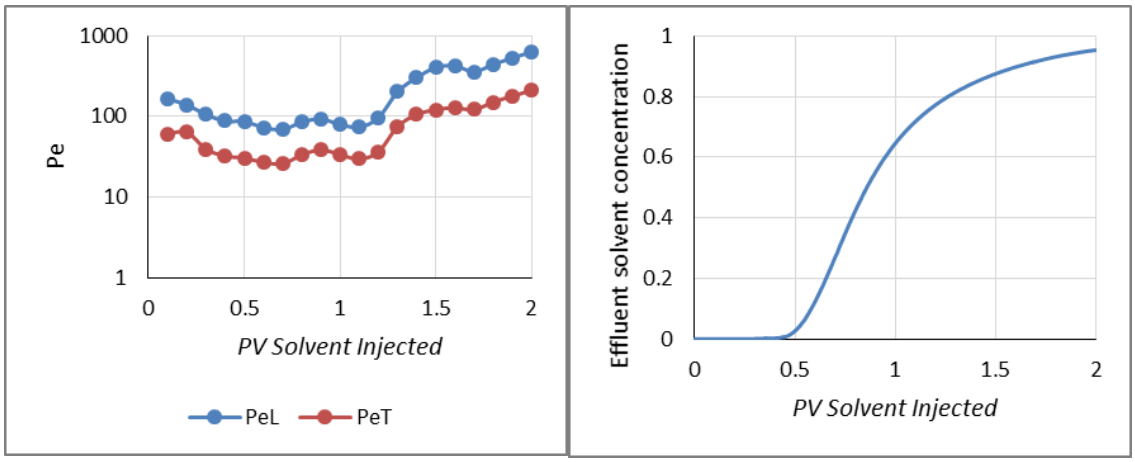

Figure 6.10: Left, Evolution of the measured Peclet number at different dimensionless times (τ). Right, Effluent solvent concentration

Figure 6.10 illustrates that both Pe_L and Pe_T numbers follow almost the same evolution in both orientations, though this is not the case in all permeability fields. Unlike Peclet

numbers measured in a homogeneous one-dimensional model (Figure 6.6), the measured Peclet numbers in a heterogeneous permeability field are not constant during simulation. The evolution of the Pe_L and Pe_T profiles depicted in Figure 6.10 can be regarded as the unique fingerprint of this heterogeneous permeability field which should be preserved across successive levels of upscaling (Section 6.6). It will be shown in Section 6.6 that if the same Peclet pattern is maintained between fine and coarse models, upscaling can be considered accurate.

The evolution of the Peclet profiles observed in Figure 6.10 is a function of the individual fraction of the permeability field that has been contacted by solvent at each time (τ) which is not necessarily identical at different (τ). In other words, the Peclet number which is measured at τ = 0.2 will not necessarily be identical to the Peclet number measured at τ = 0.3 because of the extent to which Peclet numbers are measured are different (Figure 6.11).

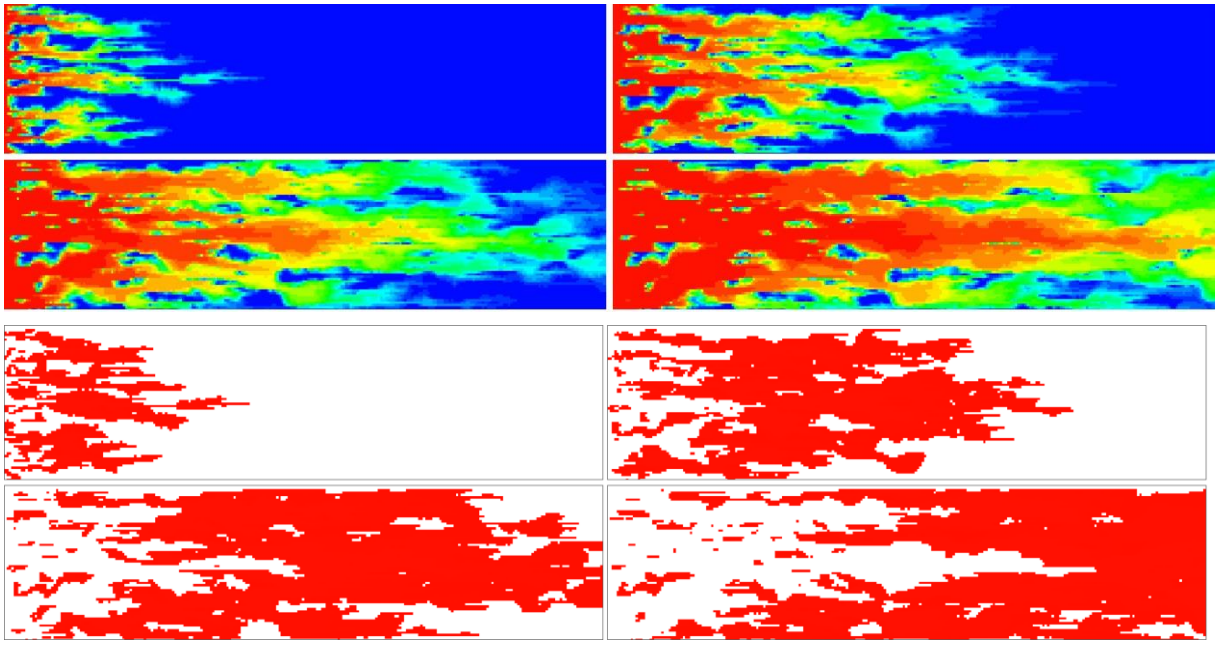

Figure 6.11: Top: Concentration profiles after 0.1, 0.3, 0.5 and 0.8PV of solvent injection. Bottom: Corresponding transition zone in which Peclet numbers have been measured. Peclet numbers are not measured in the same volume of the model at different dimensionless times.

As with the homogeneous model, after solvent breakthrough, the transition zone gradually disappears and measured Peclet numbers start to increase as they are measured near the tail of the transition zone. Figure 6.12 shows the fraction of concentration intervals within the transition zone at different dimensionless times for the above heterogeneous permeability field (Figure 6.11).

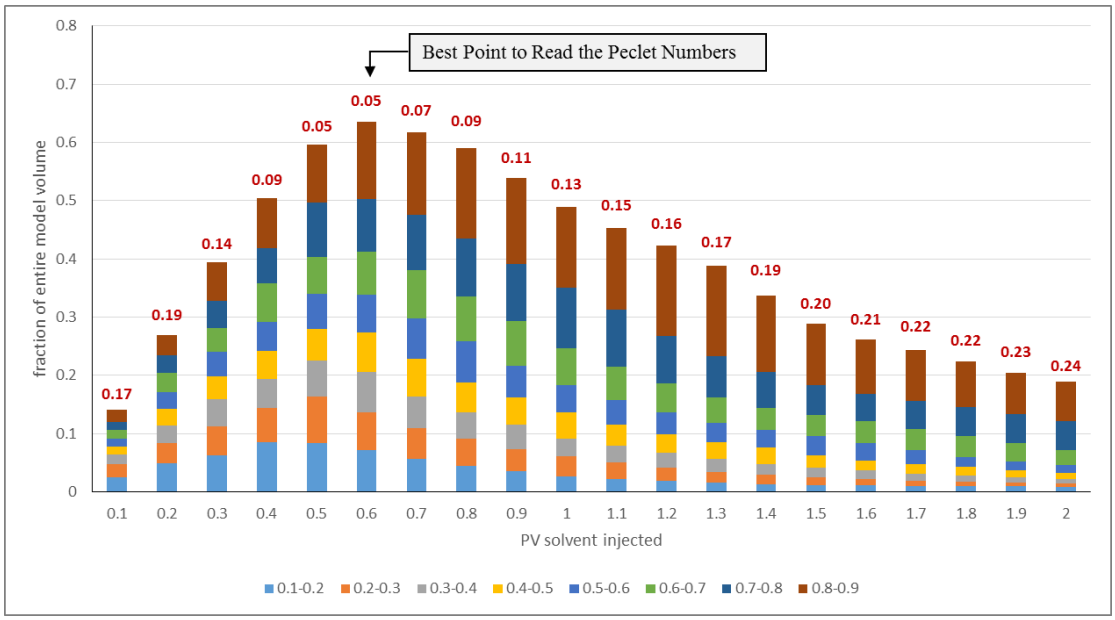

Figure 6.12: Fractions of each concentration interval at different dimensionless times inside a heterogeneous model

It can be observed that for this permeability field, the fractional size of the transition zone varies during simulation and hardly exceeds 60% of the whole model volume, though later this reduces to less than 20% as the transition zone leaves the model. Individual colours in each bar represent the fraction of each concentration interval in the total transition zone. The red numbers above each bar represent the standard deviation of the fractional size of each concertation interval.

Larger numbers mean that concentration intervals are less evenly distributed and hence measured Peclet numbers are less accurate. This usually happens at very early or late times. It can be seen that at late times, the tail of the transition zone (0.7-0.9 interval) occupies a much larger fraction of the whole transition zone compared to mid-times, and Peclet measurements at these times are very inaccurate.

The combination of these factors causes the calculated Peclet number not to remain constant and evolve during simulation. Therefore, the best time to read the Peclet number is when the standard deviation is at its minimum and the transition zone occupies maximum volume accordingly. This usually happens at around mid-times; say 0.4-0.6PV, but could be different depending on model properties. This is an important assumption before analysing the sensitivity results presented in the next section.

6.5 Measured Peclet Numbers; Sensitivity to Model Properties

In this section, the sensitivity of the measured Peclet numbers to model properties including dimensionless correlation length in both orientations (λ_{xD} and λ_{zD}), effective aspect ratio (N_{RL}) and finally mobility ratio (M), are illustrated and discussed. All the model properties in this section are expressed with dimensionless numbers. The range of these numbers is also taken from the work of Garmeh & Johns (2010).

All the heterogeneous permeability fields in this section have a Dykstra-Parsons coefficient of heterogeneity (V_{DP}) of 0.8; moreover, permeability is log-normally distributed having a geometric average of 100mD. All the random correlated permeability fields are generated using Schlumberger Petrel (Schlumberger Petrel, 2014). As described earlier, gravity effects and gravity number is not included in this work. We further assume that both solvent and solute are incompressible and are fully miscible upon their contact (FCM).

There is no background dispersivity in the model and the measured Peclet numbers (or dispersivities) can be exclusively attributed to heterogeneity effects as numerical dispersion is very small. All the models have 256 and 64 grid blocks in the horizontal and vertical orientations, respectively. The Peclet numbers in both orientations are measured at 0.1PV intervals and up to 2.0PV. CMG-GEM is the flow simulator used in this study (CMG-GEM 2014.10).

6.5.1 Impact of Horizontal Correlation Length (λ_{xD})

Figure 6.13 shows the impact of varying λ_{xD} on measured Peclet numbers when N_{RL} is large (N_{RL}=6.0). For this permeability field, it can be seen that as λ_{xD} increases, longitudinal Peclet number (Pe_L) decreases and transverse Peclet number (Pe_T) increases, implying that mixing in the longitudinal and transverse directions increases and decreases, respectively. Note that as mentioned before, Peclet numbers should be compared at mid-times rather than very early or late times.

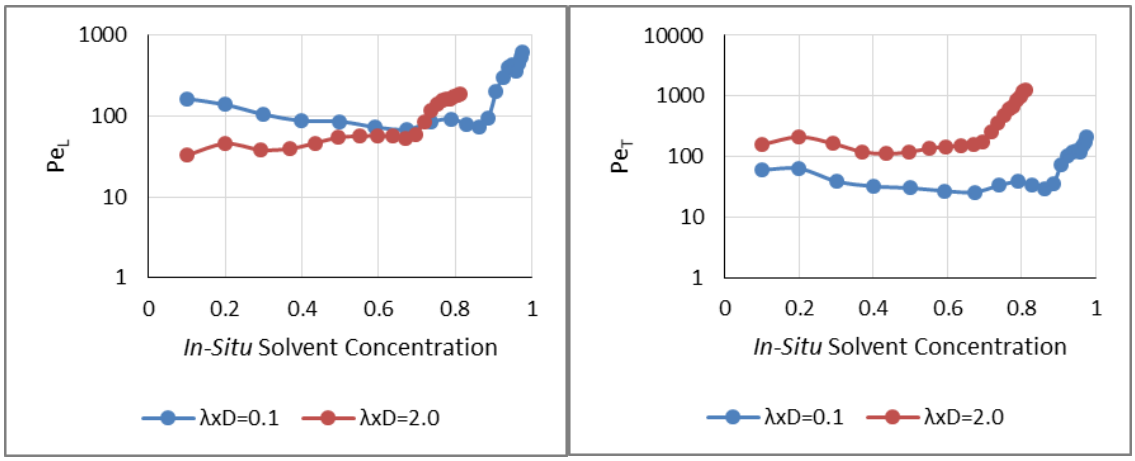

Figure 6.13: Comparison of Pe_L and Pe_T between different horizontal correlation lengths. Other model properties are identical; λ_{zD} = 0.1, N_{RL} = 6.0 and M_o = 1.0

The behaviour observed above is not conclusive and depends on other system properties. Figure 6.14 compares the impact of increasing λ_{xD} when the cross flow is very limited (N_{RL}=0.1). It can be seen that increasing λ_{xD} causes Peclet numbers to increase in both orientations, implying a reduction of mixing in both orientations respectively.

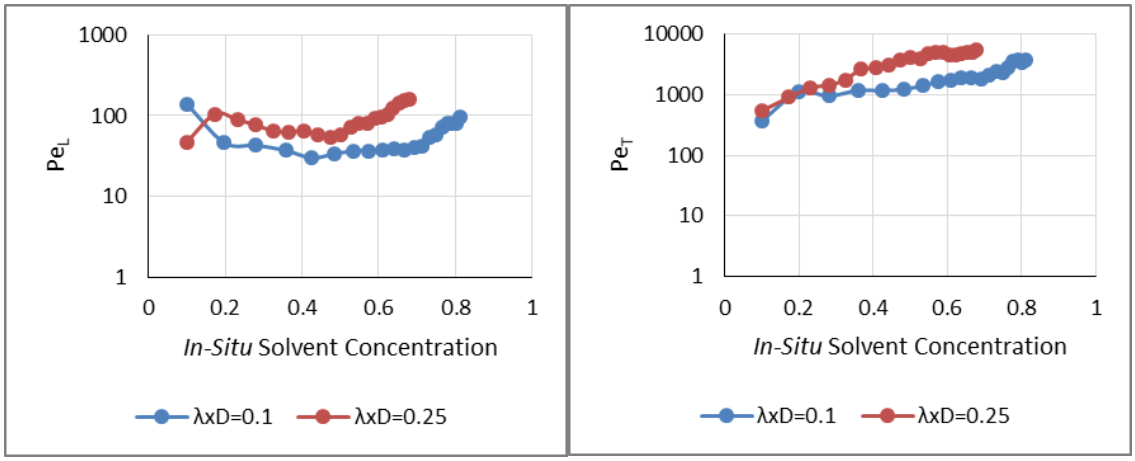

Figure 6.14: Comparison of Pe_L and Pe_T between different horizontal correlation lengths. Other model properties are identical; λ_{zD} = 0.02, N_{RL} = 0.1 and M_o = 5.0

Unlike the behaviour observed in Figure 6.13, at low values of N_{RL} (limited cross flow), increasing λ_{xD} increases Pe_L and decreases mixing in the longitudinal direction. This is because the channelling nature of displacement is promoted as λ_{xD} increases, coupled with limited cross flow makes mixing in the horizontal direction smaller. In other words, as λ_{xD} increases, different streamlines arrive at the production well at different times before they have enough opportunity to mix within the system. Therefore, increasing λ_{xD} may have different impacts on horizontal mixing depending on other model properties.

Nevertheless, under any conditions, increasing λ_{xD}, increases the Pe_T as the channelling nature of the displacement is promoted.

6.5.2 Impact of Vertical Correlation Length (λ_{zD})

As with λ_{xD} shown above, varying λ_{zD} has different impact on the Pe_L depending on the magnitude of N_{RL}. Figure 6.15 compares the impact of varying λ_{zD} on the evolution of Peclet numbers in both orientations when N_{RL}=0.1. It can be seen that as λ_{zD} increases, Pe_T decreases and Pe_L increases implying mixing has been increased and decreased in the transverse and longitudinal orientations, respectively.

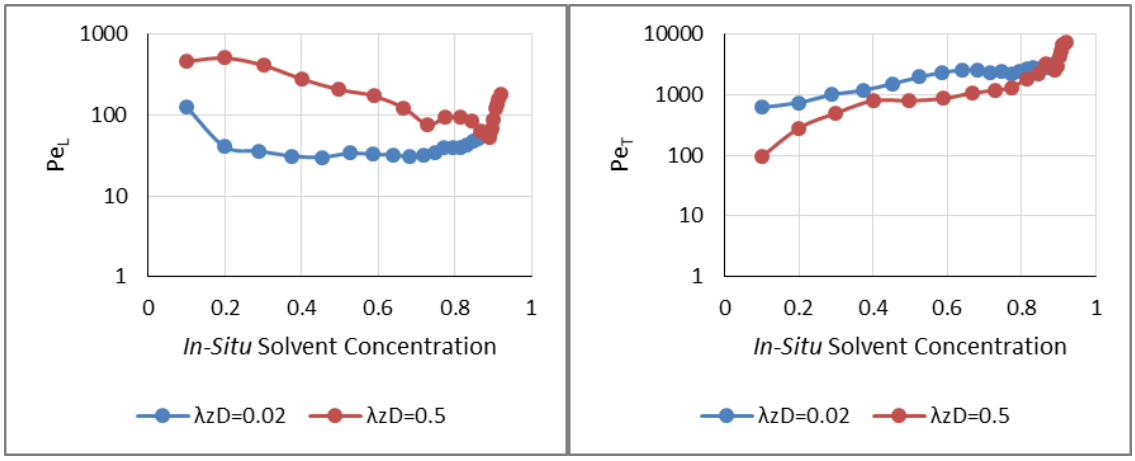

Figure 6.15: Impact of λ_{zD} on Pe_L and Pe_T. Other model properties are identical. λ_{xD} = 0.1, N_{RL} = 0.1 and M_o = 1.0

Figure 6.16 compares the impact of λ_{zD} on the evolution of Pe_L and Pe_T at N_{RL}=6.0. Unlike the behaviour observed in Figure 6.15, now increasing λ_{zD} has almost no impact on the evolution of Pe_L. However, as before, Pe_T has been slightly increased.

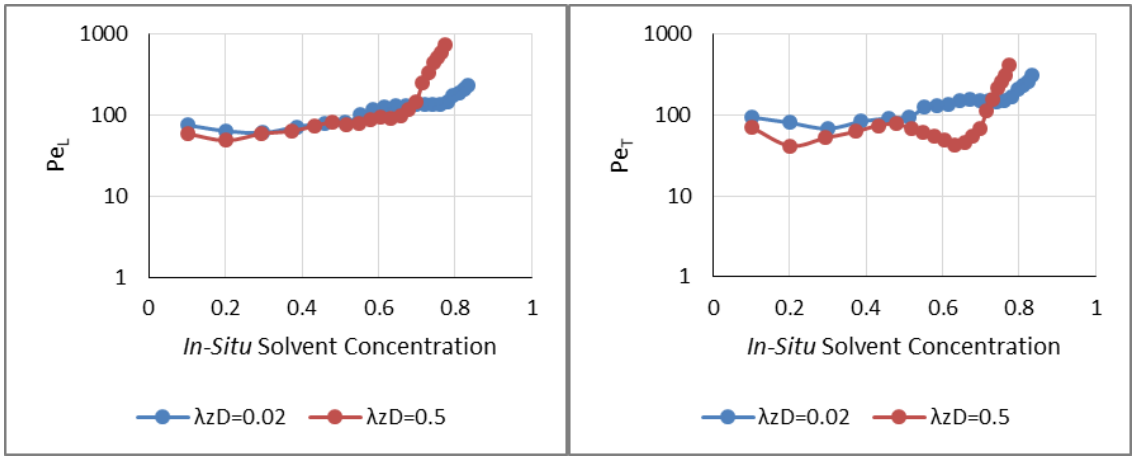

Figure 6.16: Impact of λ_{zD} on Pe_L and Pe_T. Other model properties are identical. λ_{xD} = 0.1, N_{RL} = 6.0 and M_o = 5.0

Under all scenarios, increasing λ_{zD} decreases Pe_T, which implies better mixing in the vertical orientation and less channel dominated displacement as individual layers become thicker. In the horizontal direction, however, mixing is dependent on the magnitude of vertical flow. An increase in the λ_{zD} generally makes vertical flow further limited and thus reduces horizontal mixing. However, this is more significant at lower N_{RL} magnitudes.

6.5.3 Impact of Effective Aspect Ratio (N_{RL})

The magnitude of effective aspect ratio shows the ease with which cross flow can occur within the system. Figure 6.17 compares the magnitude of measured Peclet numbers between two heterogeneous systems with different N_{RL}. Other model properties are identical. It can be seen that as N_{RL} increases, Pe_L and Pe_T increases and decreases, respectively, implying that mixing in the longitudinal and transverse directions have been decreased and increased, respectively. A significant increase of N_{RL} may reduce horizontal mixing as it causes the adjacent streamlines to instantly stabilise. Therefore, mixing in the horizontal direction decreases (or Pe_L to increase).

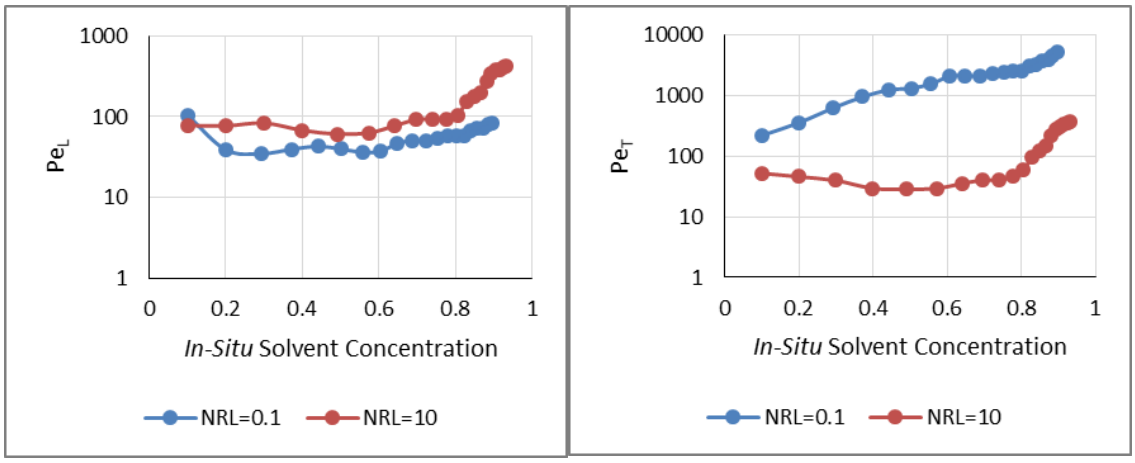

Figure 6.17: Impact of N_{RL} on Pe_L and Pe_T. Other model properties are identical. λ_{xD} = 0.25, λ_{zD} = 0.1 and M_o = 1.0

However, a moderate increase in the N_{RL} may promote larger vertical flow to an extent which may improve the horizontal mixing. It can be seen in Figure 6.18 that an increase in the N_{RL} has decreased the Pe_L, implying that mixing has been increased in the horizontal direction. Now a moderate increase of N_{RL} allows further cross flow within the model, which increases mixing in the horizontal direction. Note that the impact of increasing

N_{RL} on Pe_T is always conclusive in that increasing N_{RL} decreases Pe_T i.e. increases mixing in the vertical direction as depicted in both Figure 6.17 and Figure 6.18.

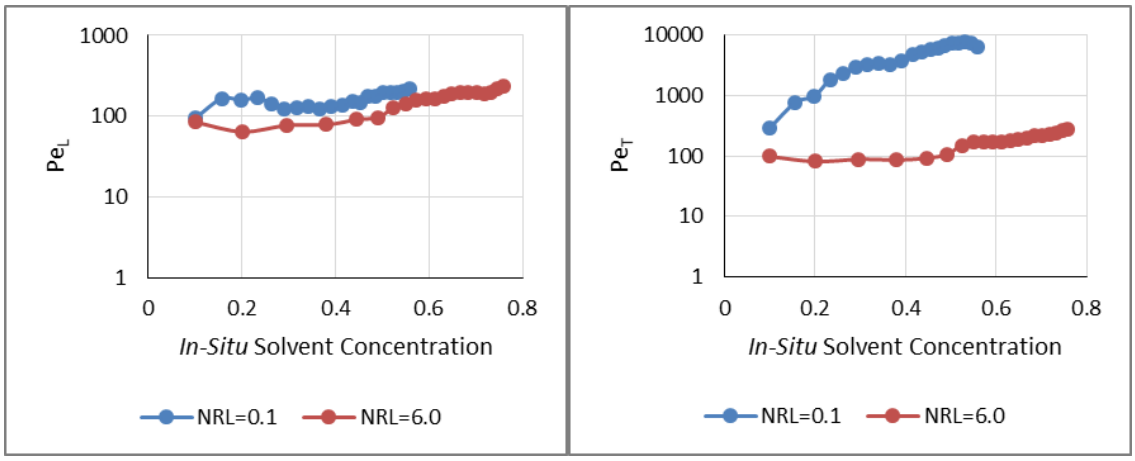

Figure 6.18: Impact of N_{RL} on Pe_L and Pe_T. Other model properties are identical. λ_{xD} = 0.25, λ_{zD} = 0.02 and M_o = 25.0

6.5.4 Impact of Mobility Ratio (*M*)

The impact of varying mobility ratio on the evolution of Pe_L and Pe_T is not unique and depends on other model properties. Figure 6.19 compares the evolution of Peclet numbers in both orientations at different mobility ratios.

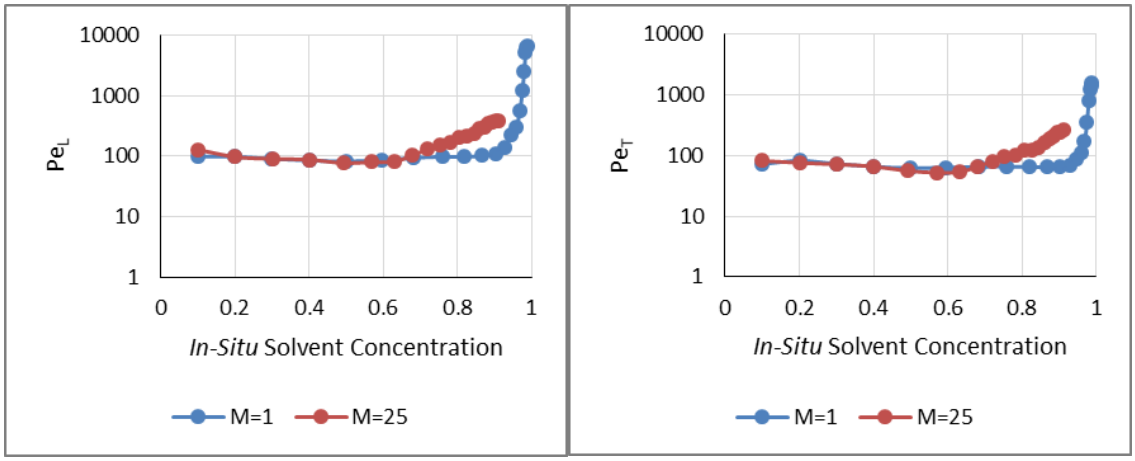

Figure 6.19: Impact of mobility ratio on Pe_L and Pe_T. Other model properties are identical. λ_{xD} = 0.25, λ_{zD} = 0.02 and N_{RL} = 6.0

It can be seen that changing mobility ratio has a negligible impact on the evolutions of Peclet profiles. Figure 6.20 shows the impact of varying mobility ratio on the measured Peclet numbers in another scenario. This figure shows that while the impact of increasing mobility ratio on Pe_T in the vertical direction is minimal, Pe_L has been increased in the

horizontal direction implying mixing has been reduced in the horizontal direction. This usually arises when a significant increase in the mobility ratio does not allow the fluids to remix as they propagate horizontally.

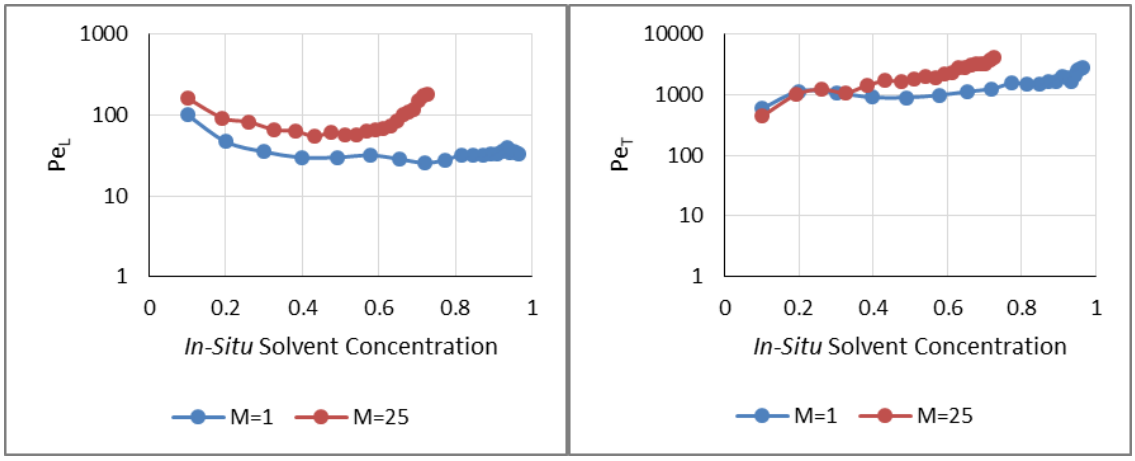

Figure 6.20: Impact of mobility ratio on Pe_L and Pe_T. Other model properties are identical. λ_{xD} = 0.1, λ_{zD} = 0.02 and N_{RL} = 0.1

In another scenario, Figure 6.21 shows that increasing mobility ratio has increased Peclet numbers in both orientations i.e. has decreased mixing in all orientations.

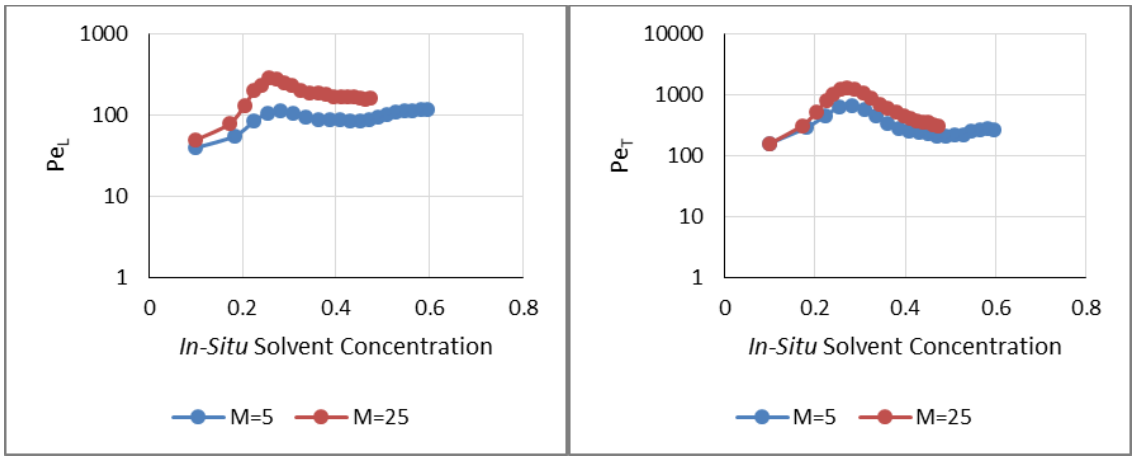

Figure 6.21: Impact of mobility ratio on Pe_L and Pe_T. Other model properties are identical. λ_{xD} = 2.0, λ_{zD} = 0.1 and N_{RL} = 6.0

Figure 6.22 shows another scenario where increasing mobility has decreased Pe_L while the impact is minimal on Pe_T. Inspecting these figures (Figure 6.19 to Figure 6.22) it can be concluded that the impact of increasing mobility ratio on the evolution of Pe_T is rather conclusive. This indicates that Pe_T generally increases as mobility ratio increases. As mobility ratio increases the channelling nature of the displacement is promoted, thus the Peclet number in the vertical orientation increases.

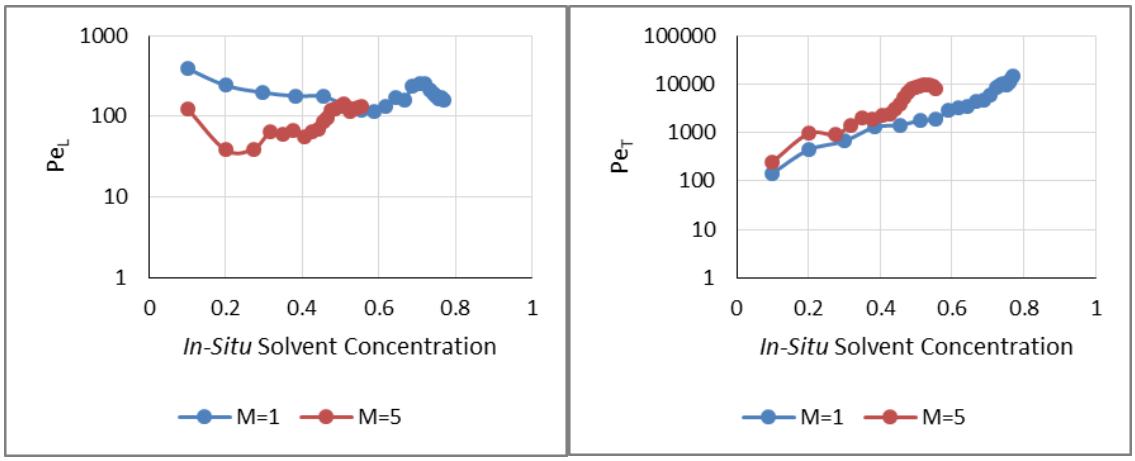

Figure 6.22: Comparison of longitudinal and transverse Peclet numbers between models having different mobility numbers. Other model properties are identical. $\lambda_{xD} = 2.0$, $\lambda_{zD} = 0.5$ and $N_{RL} = 0.1$

However, Pe_L variation is not conclusive. If other model properties allow individual streamlines to better mix horizontally as mobility ratio increases, this may increase mixing (or decrease Pe_L), otherwise, dispersivity may decrease. If, however, the displacement is extremely channel dominated, increasing mobility does not affect mixing and both Peclet numbers remain constant (Figure 6.19).

6.5.5 Discussion

Comparison of our results with Garmeh *et al*. (2010) results is also worth considering. Garmeh and Johns measured *in-situ* dispersivity for a number of heterogeneous models described with dimensionless numbers without implying the orientation. They showed that an increase in the mobility, effective aspect ratio and horizontal dimensionless correlation length increases the *in-situ* dispersivity while increasing vertical dimensionless correlation length decreases it. In this study we first, differentiated the direction of Peclet (dispersivity) measurement and second, we showed that horizontal mixing variation due to varying model parameters does not show a conclusive trend and dependent on other system properties rather than just varying only one single parameter.

The concept of mixing presented in this study by measuring the magnitudes of Peclet numbers is, however, different in the longitudinal and vertical orientations where the primary flow is in the horizontal direction. In the horizontal direction, mixing changes due to the mixing of different streamlines at different locations. In the vertical direction, however, the concept of mixing implies the degree of velocity contrast between different

layers and not actual fluid mixing in the vertical direction. Therefore, measured Pe_L may refer to actual mixing in the system while measured Pe_T refers to the degree of channelling or velocity contrast in the vertical orientation perpendicular to the major flow direction. In other words, an increase in the transverse Peclet number can be fairly correlated with the change of flow pattern toward a channelling dominated displacement, hence any mechanism that promotes lower velocity contrast in the vertical orientation.

From the discussions presented in this section, it can also be concluded that longitudinal and transverse Peclet numbers (or their equivalent dispersivities) do not necessarily have a reciprocal relationship. In fact, their behaviour could be different based on all the model properties.

6.6 Evolution of Peclet Profiles; Comparison between Fine and Coarse Models

In this section, the evolution of measured Peclet numbers is compared between fine and coarse models in both orientations. Since all the permeability fields in this work are random correlated permeability fields which are lognormally distributed, the geometric average has been used for permeability averaging.

6.6.1 Horizontal Coarsening

Figure 6.23 compares the Pe_L and Pe_T evolutions in fine and a few coarsened models in the horizontal orientation. The model properties for this heterogeneous system are λ_{xD}=0.1, λ_{zD}=0.02, N_{RL}=10 and M_o=25. The fine model has 256 grid blocks in the horizontal direction which is successively coarsened to 128, 64, 32 and 16 grid blocks. The vertical number of grid blocks remains 64 for all models.

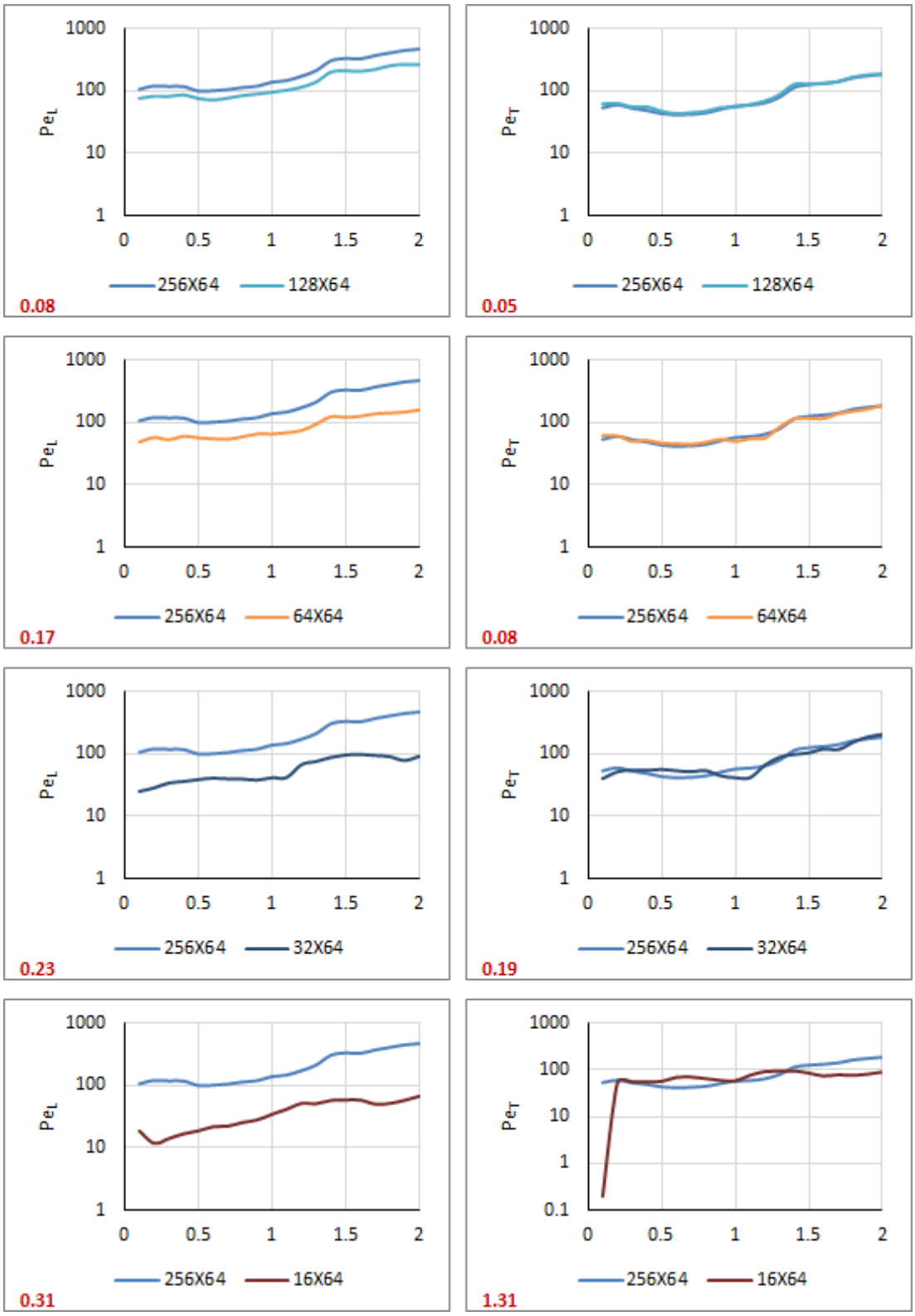

Figure 6.23: Evolution of Pe_L and Pe_T profiles at different levels of horizontal coarsening; Horizontal axis shows the dimensionless time.

It can be seen in Figure 6.23 that any degree of upscaling decreases the longitudinal Peclet number (or increases mixing), in other words, the total system dispersivity *always* increases, irrespective of the accuracy of upscaling. To some extent, however, upscaling

does not distort the profile of the Peclet curves as they are fairly parallel between fine and coarse models, while there is an offset between them. This shows that although the total system dispersivity has been increased, upscaling has not markedly distorted velocity patterns, so the same Peclet profile can be reproduced, albeit, with an offset. In other words, the transition zone resides exactly in the same position in both fine and coarse models and the Peclet numbers are measured over exactly the same range of the transition zone.

The red number on each figure shows the standard deviation of offsets measured at different dimensionless times between fine and coarse models during simulations. A lower standard deviation indicates that offsets are almost equal and the two curves are more parallel. It can be seen that this number increases in both orientations as a result of further upscaling. Figure 6.24 compares the concentration profile after 0.4PV solvent injection in fine and coarse models.

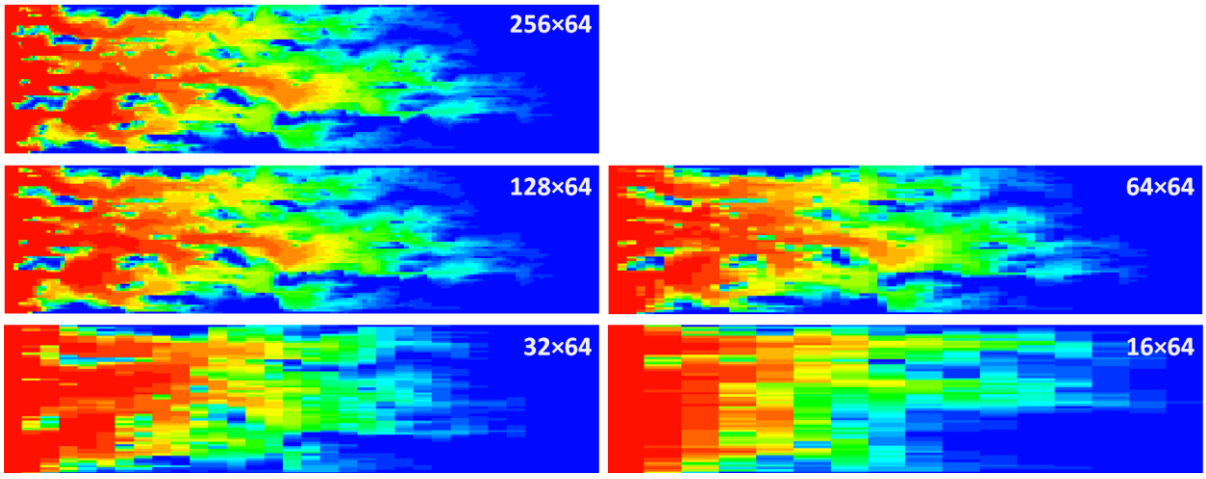

Figure 6.24: Comparison of solvent concentration profiles between fine and horizontally coarsened models at 0.4PV

This concept can be used as a measure of the validity of upscaling; in other words, as long as the Peclet profiles are exactly parallel on a logarithmic scale, upscaling can be regarded as accurate. Nevertheless, after a certain degree of coarsening, the Peclet profiles starts to deviate from the original fine model profile and they are no longer completely parallel with the original fine model. This is the point where the model heterogeneity is affected to such an extent that the velocity patterns have been distorted. In the above example, four times of coarsening in the horizontal direction (64×64) is probably the maximum limit of upscaling that can be tolerated in the horizontal direction, after which the upscaled model's performance deviates markedly from the original fine model.

The evolution of transverse Peclet numbers when the above model is coarsened in the horizontal direction is also worth considering. The same behaviour observed as for Pe_L can be observed again. Two and four times coarsening (i.e. 128 and 64 grid blocks) in the horizontal direction does not distort the transverse Peclet profile in comparison with the fine model. At eight times coarsening (32 grid blocks), there are indications of deviation from original fine scale evolution. At sixteen times horizontal coarsening (16 grid blocks), the transverse Peclet profile is completely distorted and upscaling is no longer accurate.

Since upscaling in the horizontal direction does not affect the velocity profile in the vertical direction, measured transverse Peclet numbers follow exactly the fine model pattern.

6.6.2 Vertical Coarsening

The same observations described in the previous section are still relevant for vertical upscaling. Figure 6.25 shows the impact of coarsening in the vertical direction on the evolution of Peclet numbers in both orientations. The model properties, in this case, are as before (λ_{xD}=0.1, λ_{zD}=0.02, N_{RL}=10 and M_o=25). The fine model has 64 grid blocks in the vertical direction which is successively coarsened to 32, 16 and 8 grid blocks. The horizontal number of grid blocks remains 256 for all models.

As before, upscaling in the vertical direction increases total dispersivity (or reduces Peclet numbers) in *both* orientations. Comparison of Figure 6.23 and Figure 6.25 shows that, while Pe_T is not affected during horizontal coarsening, in vertical coarsening both Pe_L and Pe_T magnitudes decrease. This suggests that horizontal coarsening only affects Pe_L while vertical coarsening affects both Pe_L and Pe_T. This is expected, as vertical coarsening affects fluid flow and mixing in the horizontal direction as described before.

Similar to the discussion presented in Section 6.6.1, if the profiles of Peclet numbers remains exactly parallel between fine and coarse models, upscaling can be considered accurate. Nevertheless, since the displacement is primarily in the horizontal direction, upscaling is usually more sensitive to vertical gridding rather than horizontal gridding. This is depicted in Figure 6.26. It can be seen in this figure that model performance is much more sensitive to vertical coarsening than the horizontal coarsening observed in the previous section.

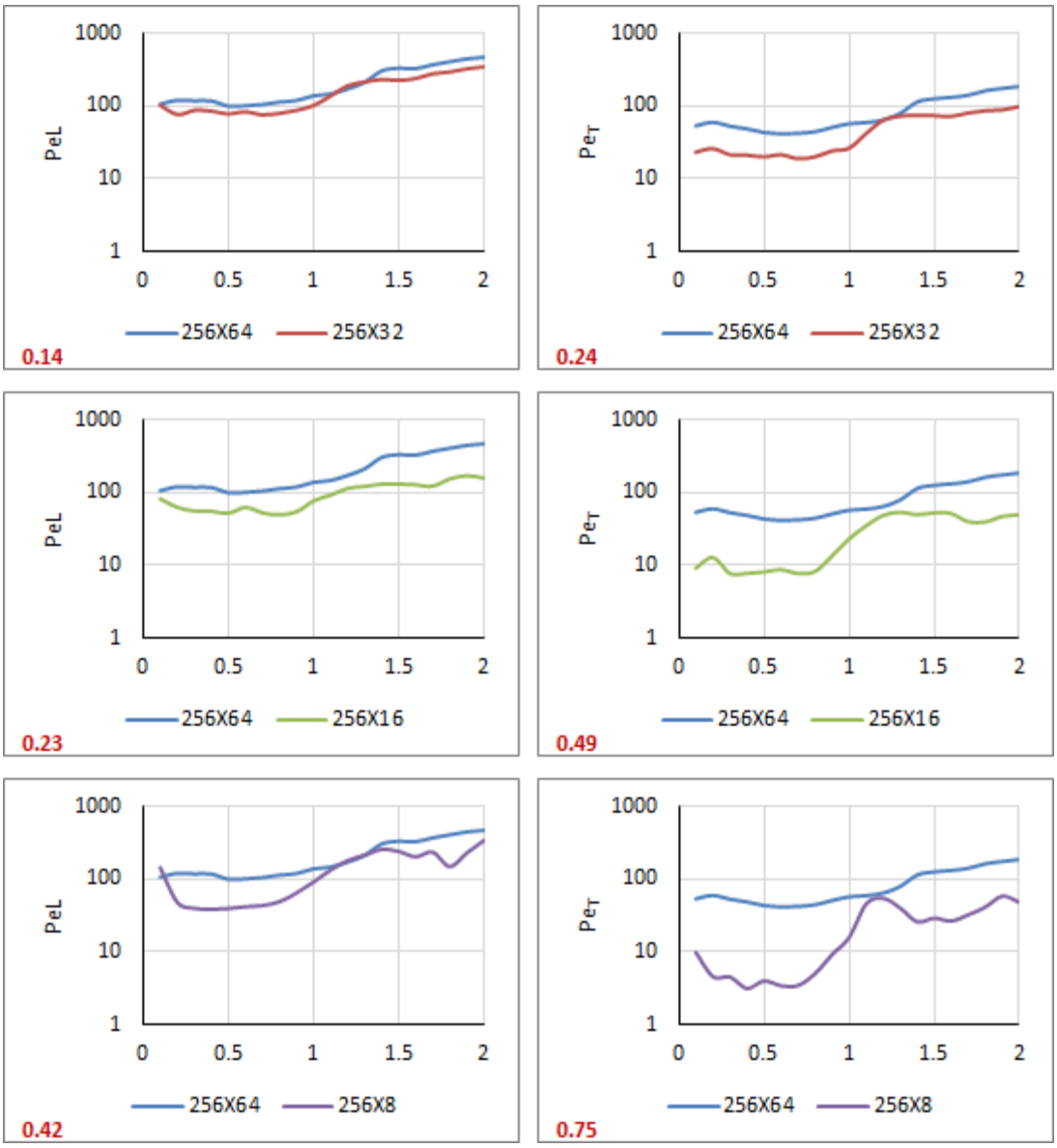

Figure 6.25: Evolution of Pe_L and Pe_T profiles at different levels of vertical coarsening; Horizontal axis shows the dimensionless time.

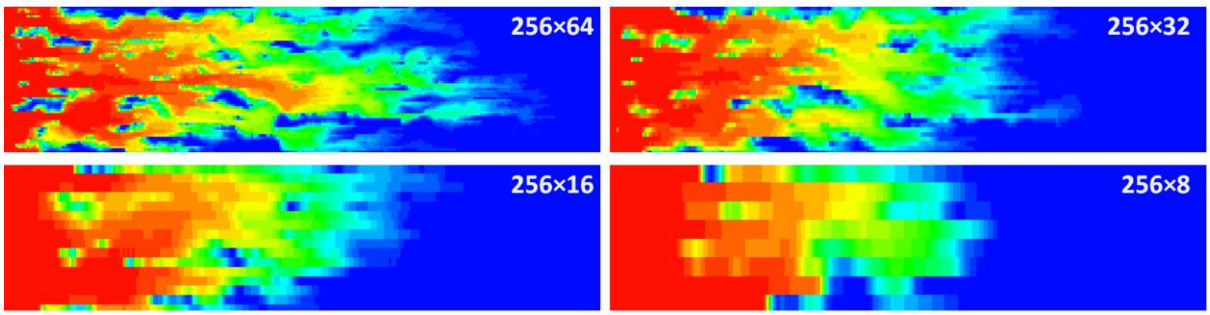

Figure 6.26: Comparison of solvent concentration profiles between fine and vertically coarsened models at 0.4PV

6.6.3 Discussion

It was shown in Section 6.2.1 that physical dispersion can be replaced by an equivalent numerical dispersion in a one dimensional numerical model. This way, both models will have exactly the *same* performance and *identical* Peclet numbers.

Similarly, in a random correlated permeability field, a literature review suggests that heterogeneity induced dispersivity (or mixing) can be replaced by an equivalent numerical dispersion (Haajizadeh *et al*. 1999). However, our results show that although an equivalent grid block size may represent the actual concentration profiles, the total model dispersivity (mixing) *always* increases as a result of progressive upscaling (Figure 6.23 and Figure 6.25). This is because in heterogeneous permeability fields, any degree of upscaling irrespective of the accuracy of model predictions (i.e. *in-situ* solvent concentration profile or the time of solvent breakthrough), *always* modifies the velocity pattern compared to the original fine model. Evidently, for the one-dimensional simulations observed earlier this is not the case, as the velocity pattern never becomes distorted as a result of upscaling.

The evolution of Pe_L and Pe_T profiles in Figure 6.23 and Figure 6.25 can be described by the following equations;

$$Pe_L = f(\tau)\frac{L}{\alpha_L} \tag{6.28}$$

$$Pe_T = g(\tau)\frac{H^2}{L\alpha_T} \tag{6.29}$$

Where $f(\tau)$ and $g(\tau)$ are those functions which represent the evolution of measured Peclet numbers profile at different dimensionless times (τ). The shape of $f(\tau)$ and $g(\tau)$ are functions of those phenomena discussed in Section 6.4 i.e. the extent of the transition zone that can be observed at each dimensionless time which are not necessarily equal during the simulation. It was shown, however, that for an accurate upscaling, the evolution of Peclet profiles must be exactly parallel on the logarithmic scale (Figure 6.23 and Figure 6.25), i.e. $f(\tau)$ and $g(\tau)$ should follow the same profile between fine and coarse models irrespective of the magnitudes of α_L and α_T. α_L and α_T in the above equations are measured dispersivities (or mixing) for each degree of upscaling. These dispersivities are always increasing as a result of further upscaling as was discussed earlier.

The measured dispersivity in the longitudinal direction (α_L in Equation 6.28) can be represented by two components (Equation 6.30);

$$\alpha_L = \alpha_{LH} + \alpha_{LN} \tag{6.30}$$

Where α_{LH} is the dispersivity due to heterogeneity and α_{LN} is the numerical dispersion in the horizontal direction as well. Making the grid block sizes twice as large in the horizontal direction causes numerical dispersion to become twice as large in this direction. This should make the measured Pe_L smaller accordingly. If α_{LH} =0 (a homogeneous model), doubling grid block size should make Pe_L twice as small.

Figure 6.27 compares the measured Pe_L profiles between fine (256×64) and horizontally coarse (128×64) models. The model properties are λ_{xD}=2.0, λ_{zD}=0.02, N_{RL}=6 and M_o=5.

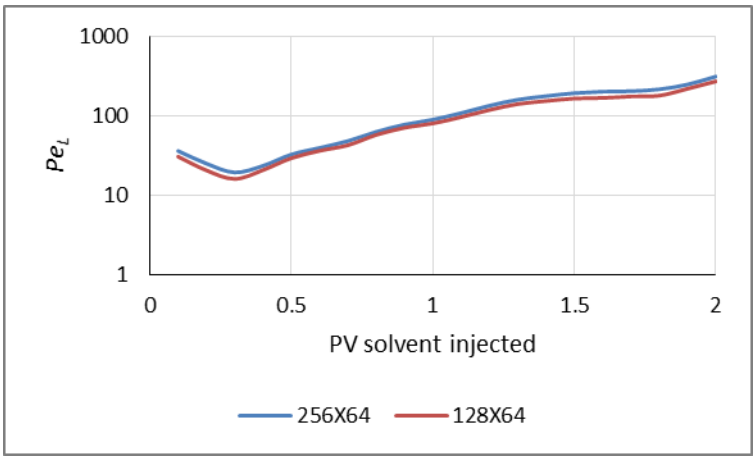

Figure 6.27: Comparison between 256×64 and 128×64 longitudinal Peclet profiles. Although numerical dispersion has been doubled in the horizontal direction, total dispersivity has not been doubled (Pe_L has not become halved).

It can be seen in Figure 6.27 that although numerical dispersion has been doubled in the horizontal direction, Pe_L becomes smaller by a factor less than two[14] (1.14 in this example). This can be attributed to the presence of a background heterogeneity induced dispersivity ($\alpha_H \neq 0$) which has reduced the significance of numerical dispersion for this degree of upscaling. Therefore, the total increase in the horizontal dispersivity between any consequent levels of upscaling in the horizontal direction is less than due to the increase of numerical dispersion. The larger the α_H in the horizontal orientation, the less sensitive will be the model performance to upscaling in the horizontal direction as well.

[14] Recalling that dispersivity and Peclet number have a reciprocal relationship, a decrease in the Peclet number in Figure 6.27 as a result of coarsening means that the magnitude of dispersion has been increased accordingly.

The relative impact of the magnitude of heterogeneity induced dispersivity on the accuracy of upscaling can be compared between different heterogeneous models. Figure 6.28 compares the measured Pe_L in the horizontal orientation between two models of different horizontal correlation lengths (λ_{xD}) and for a number of successive upscaling. Other model properties are identical.

In fact, the model whose performance is depicted on the left has a higher α_H than the model on the right, thus it should be less sensitive to upscaling in the horizontal direction. Red numbers on each plot represent the standard deviation of the offsets measured between fine and coarse model Peclet profiles. It can be observed that the relative variation of Pe_L profiles in the model with longer horizontal correlation length (left figure) is smaller compared to the model with shorter horizontal correlation length (right figure). Moreover, the Peclet profiles are more parallel as the offset between Pe_L curves is smaller.

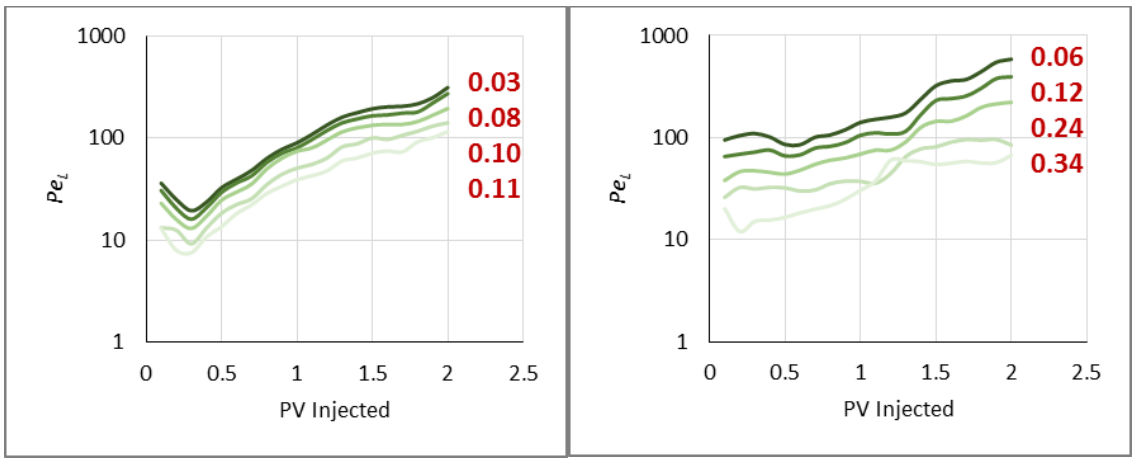

Figure 6.28: Sensitivity of Pe_L profiles to coarsening in the horizontal direction. Left model with longer horizontal correlation length is less sensitive to coarsening in the horizontal direction.

This means that models which have larger heterogeneity induced dispersivity are less sensitive to upscaling and can tolerate a higher degree of coarsening. The same discussion could be relevant in the vertical orientation. In other words, models which have larger dispersivity in the vertical orientation can tolerate a larger degree of numerical dispersion (or upscaling) in the vertical direction before their performance is severely affected by vertical upscaling.

6.7 Measured Peclet Numbers; a Quick Guide for Upscaling

The final aim of this study is to determine the approximate number of grid blocks in a random correlated permeability field based on the measured magnitudes of Pe_L and Pe_T. A common practice in upscaling is to start from a fine model description and vary the number of grid blocks in the two respective orientations until the performance is matched between fine and coarse models. However, if the magnitude of heterogeneity mixing in the fine scale model is known beforehand, sensitivity analysis can be avoided and the equivalent grid block size which represents the same magnitude of mixing can be directly determined. Knowing the magnitude of Pe_L and Pe_T, the required number of grid blocks can be directly determined using Equations 6.12 and 6.13.

It is, however, important to measure Pe_L and Pe_T in as fine as possible gridded model, since as was shown before, Pe_L and Pe_T always decrease during upscaling, even though upscaling may look accurate. Although Peclet numbers are varying throughout the simulation, the discussion presented in Section 6.4 can assist in determining the representative Pe_L and Pe_T for the entire model.

Figure 6.29 summarises the flowchart for calculating the required number of grid blocks in both orientations for a random correlated permeability field.

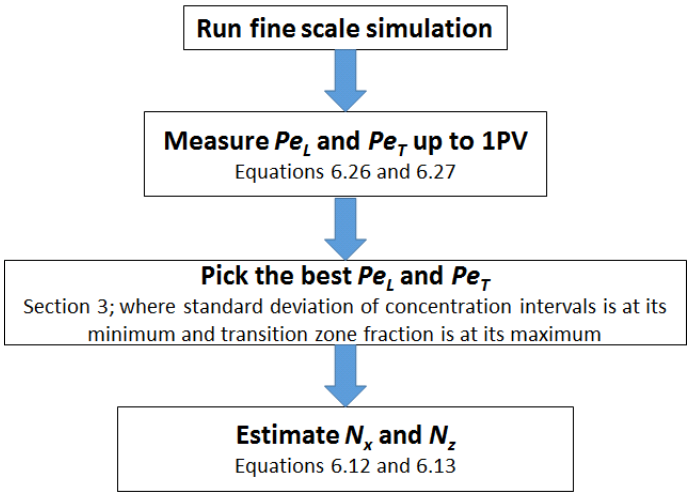

Figure 6.29: Flowchart to estimate the right number of grid blocks in horizontal and vertical orientations

The next section illustrates a few examples of the applicability of this approach.

6.7.1 Example Cases

Table 6.1 shows four heterogeneous models with different model properties depicted in this table. Table 6.2 shows the respective calculated Peclet numbers along the estimated number of grid blocks in both orientations, calculated with Equations 6.12 and 6.13.

Table 6.1: Four different model definitions

	λ_{xD}	λ_{zD}	N_{RL}	M
Model 1	0.25	0.1	6.0	5
Model 2	0.25	0.1	0.1	5
Model 3	2.0	0.02	6.0	5
Model 4	0.1	0.02	10.0	25

Table 6.2: Estimated Peclet numbers and the required number of grid blocks

	Pe_L	Pe_T	N_x	N_z
Model 1	75	50	38	100
Model 2	36	1263	18	2526
Model 3	40	97	20	194
Model 4	80	45	40	90

The ratio *L/H* is 4 in this study (Equation 6.13). The fine model has 256×64 grid blocks. Evidently, it is not possible to discretise models based on the exactly predicted number of grid blocks; instead, the model performance is compared at one level above and one level below the predicted grid requirements in both orientations to see if the predicted number of grid blocks is accurate enough. For example, if the predicted number of grid blocks are 20 by 20 in horizontal and vertical directions, the performances will be compared among 16×16, 16×32, 32×16 and 32×32 discretisations to fully cover the predicted range.

Figure 6.30 compares the effluent solvent concentration between fine and those coarse models predicted in Table 6.2. Although there are slight deviations, it can be seen that the performance is fairly matched between fine and coarse models by gridding the model by the calculated number of grid blocks. One level of coarsening in the vertical direction is also depicted for comparison to show that the required number of grid blocks (64) in the vertical direction is accurate.

A grid requirement larger than 64 in the vertical direction indicates an aggressive channel dominated flow which cannot be further coarsened in the vertical direction. In other words, it means that the original 64 grid block resolution should be maintained in the vertical direction. The advantage of this method is that it is not dependant on any former

dispersivity measurement or derived proxies and can directly measure the dispersivity of the model in different orientations.

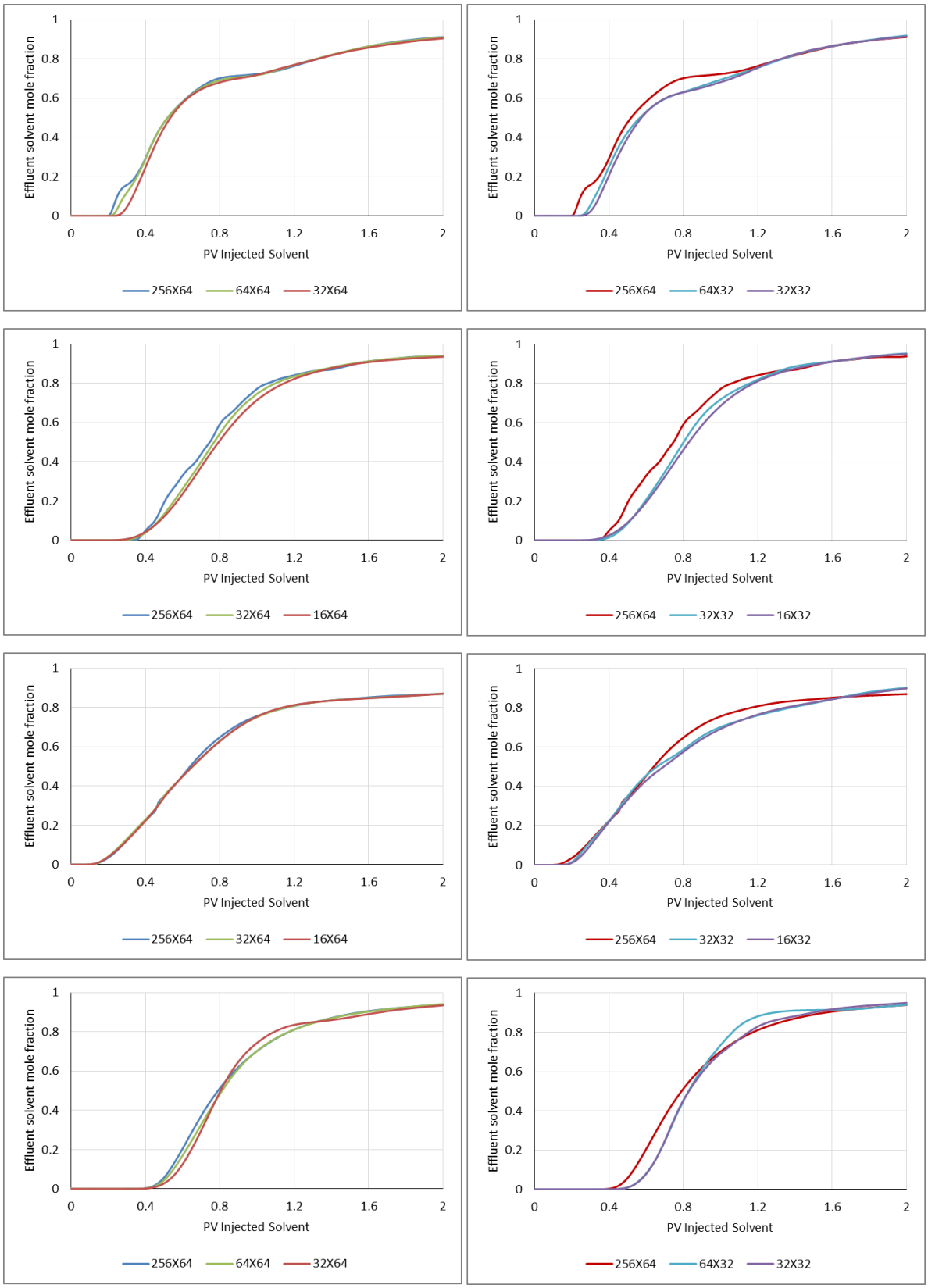

Figure 6.30: Comparison of the effluent solvent concentration profile between fine and coarse models. From top to bottom are models 1 to 4, depicted in Table 6.2

6.8 Closing Remarks, Conclusions and Next Steps

- In this study, we developed a rapid technique to measure dispersivity in heterogeneous permeability fields based on measuring Peclet number between adjacent pairs of grid blocks. Peclet numbers can be measured in different orientations based on the positioning of the adjacent cells. Matching the derived dispersion with equivalent numerical dispersion can determine the approximate number of grid blocks in any orientation.
- The measured Peclet numbers in different orientations have different meanings. The average measured *Pe* in the longitudinal orientations (Pe_L) refers primarily to the magnitude of mixing in the horizontal orientation, while transverse Peclet refers to channelling characteristics of the displacement. Therefore any mechanism which makes flow pattern more channelling dominated, may increase Pe_T.
- An increase in the effective aspect ratio or vertical correlation length which impairs the channelling flow pattern decreases the Pe_T or increases vertical dispersivity. Similarly, an increase in the mobility ratio or increase in the horizontal correlation length may increase Pe_T as well. Pe_L variation with model properties is not, however, straightforward and is a function of the entire model properties rather than the variation of a single property.
- The results obtained in this study is in contrast with other researcher's findings, which had implied that dispersivity remains constant as long as upscaling is accurate. Instead, it was observed that upscaling always increases dispersivity even though upscaling is accurate. Therefore it is important to measure Peclet numbers in a very fine gridded model to eliminate the impact of numerical dispersion in estimating the right number of grid blocks.
- There is a strong correlation between the degree of upscaling in a given orientation and the measured dispersivity in that orientation. It has been shown that models which have higher dispersivity are less sensitive to numerical dispersion and can tolerate a larger degree of upscaling.
- This method can be developed and applied to immiscible displacements as well, though the concept of dispersion in immiscible displacement is not well understood. In immiscible flow, capillary pressure acts as primary dispersive mechanism. Moreover, as with miscible flow, mixing of different streamlines may create a dispersive impact in immiscible flow. However, since mobility ratios are generally better in an immiscible displacement, different gridding might be required

to simulate the process compared to the miscible case. In immiscible displacement, capillary number becomes progressively smaller as the flood velocity increases, which implies that smaller grid blocks will be required as flood velocity increases. This is opposite to miscible displacement where the dispersivity is not affected by flood velocity.

- Although this method tries to capture the required number of grid blocks based on some fundamental principles, its drawbacks should not be overlooked. The fact that the solvent-oil transition zone is not able to contact the entire model at any time coupled with different Peclet readings along the transition zone creates challenges and makes choosing the representative Peclet number for the model challenging. Therefore a better method to estimate Peclet number for the entire model should be developed in future. Moreover, we applied a Peclet measurement approach which is essentially developed and derived in one dimensional FCM flow, to two dimensional displacement models. In fact, obtaining Peclet numbers in two dimensional orientation requires the two dimensional convective-diffusive equation to be solved and then applied to heterogeneous mediums. This is not, however, very straightforward.

Chapter 7 Conclusions and Recommendations

7.1 Summary and Conclusions

The aim of this work was to compare and correlate the characteristics of CO_2 flooding between onshore and offshore classes of reservoirs. The findings of the comparison can be categorised as follows:

How the characteristics of CO_2 flooding can be correlated between the Permian Basin and the North Sea provinces: The elements of CO_2 flooding were compared between two important provinces, i.e. The Permian basin in the United States, which is considered as the benchmark for CO_2 flooding in other provinces, and the North Sea, which is a potential CO_2 flooding candidate in the future. North Sea reservoirs are typically deeper, thicker and hotter compared to the Permian Basin group of reservoirs. It has been shown that, although the two provinces are characterised by a fundamentally different ambient reservoirs conditions, many aspects of the CO_2 flooding process are similar between them. The miscibility development, which is an important requirement for a successful CO_2 flooding, is effectively achievable in the North Sea similar to the Permian basin province. Oils are of similar qualities in both provinces; additionally, CO_2 has almost the same density and viscosity in these two provinces which indicates that required volume of CO_2 to sweep a certain rock volume should be similar in both. Finally, the solubility of CO_2 in water is very similar and small in both provinces. The combination of these will make the microscopic sweep aspect of the displacement very similar between these two provinces.

We believe that CO_2 displacement in the North Sea could be potentially gravity dominated, not because of gravity effects between CO_2 and oil, but because of the gravity effects between CO_2 and water which has been injected for secondary waterflooding. A lot of reservoirs in the North Sea and elsewhere are flooded with water which means that gravity forces naturally becomes more significant compared to the scenario where no water has been injected. Simulation study also confirms the fundamental higher severity of the gravity effects in a typical North Sea reservoir upon CO_2 flooding.

Comparing flow patterns between the North Sea and the Permian Basin classes of reservoirs: We initially derived the key dimensionless numbers which characterise CO_2 flooding in the North Sea and the Permian Basin classes of reservoirs. It has been shown

that CO_2 flooding in the North Sea classes of reservoirs is characterised with larger gravity numbers and smaller mobility and effective aspect ratios. Then flow patterns were investigated in six different random correlated (RCF) permeability fields. It was shown that the CO_2 flow pattern is more gravity dominated in the North Sea classes of reservoirs, particularly at very short correlation lengths, due to a two orders of magnitude larger gravity number that characterises the CO_2 flooding in this province. However, in the absence of gravity, CO_2 flow patterns are relatively more stable (better) in the offshore North Sea classes of reservoirs due to the better mobility ratios that characterise the displacement in this offshore province.

How the motivation behind CO_2 flooding may affect the process designs offshore: The fact that CO_2 flooding in the offshore classes of reservoirs may be equally driven by storage in addition to EOR may imply that new CO_2 flooding strategies different from those undertaken previously in the onshore (Permian Basin) classes of reservoirs may become attractive offshore. Onshore Permian Basin, the most practiced CO_2 flooding strategy is horizontal CO_2 flooding, once waterflooding approaches its economic limits. The CO_2 flooding phase is, however, followed by a period of waterflooding principally to recover part of the injected CO_2 in addition to any remaining recoverable oil. This flooding strategy has the benefit of rapid oil response and relatively lower CO_2 utilisation efficiency. For CO_2 flooding in the offshore classes of reservoirs, which are the likely candidates for combined EOR and CO_2 storage, both responses should be maximised. This may imply that new or modified alternatives to current flooding strategies should be practiced offshore. Alternatives such as limiting the length of final waterflooding to avoid the reproduction of otherwise trapped CO_2 or replacing the final phase waterflooding with extended CO_2 flooding if abundant CO_2 sources are available, flooding at higher pressures, changing the philosophy of recycling or practicing gravity stable CO_2 flooding where it has been less attractive in onshore CO_2 floods are other practical flooding strategies offshore.

Grid size investigation in miscible displacement simulations: The last section of this study showed that dispersivity in different orientations can be effectively measured for miscible displacement simulations. Matching these dispersivities with equivalent size of grid block which mimics the same magnitude of mixing is the key in sizing the cells in a given miscible displacement simulation.

7.2 Recommendations for Future Work

A full economic analysis: The analysis presented in Chapter 5 can be extended by a full economic analysis taking into account the actual cost figures difference between the two provinces. Considerations such as any emission penalties, compression cost, processing and recycling costs and finally relevant oil and CO_2 prices are other potential important inputs into this comprehensive economic analysis. The objective function, developed in Chapter 5 could, however, be an important starting point for this larger economic analysis.

Developing CO_2 flooding screening criteria for offshore classes of reservoirs: Many screening criteria have been suggested in the literature considering only the technical aspects of CO_2 flooding. New screening criteria for CO_2 flooding in those offshore classes of reservoirs might be required considering the co-importance of storage in addition to EOR. The proposed screening criteria would rely on techno-economic considerations rather than purely on technical criteria.

Further research on various aspects of CO_2 flooding in the North Sea: It is recommended that this work is exclusively conducted for a specific province e.g. the North Sea offshore province rather than for all the offshore classes of reservoirs. Nevertheless, the results and methodology can be of value for correlating to other offshore provinces. A review of the CO_2 flooding research conducted in the United States shows that several research areas have been very active for CO_2 flooding in the United States, ranging from fluid characterization (for 3 and 4 phases hydrocarbon systems), relative permeability measurements under typical Permian Basin reservoir conditions, investigating the likely displacement flow pattern, injectivity considerations, production problems e.g. hydrate formation, scale depositions and asphaltenes deposition. All of these aspects can be potential research areas for further investigations. Experimental work will be a major part of these works as well.

Investigating flow patterns in more realistic permeability fields: The conclusions presented in Chapter 4 are based on flow comparison in *comparable* stochastic permeability fields. Although these conclusions are informative, the next step would be better characterising the permeability fields in each class of reservoirs. This, however, requires a more detailed literature review of the different depositional environments in each class of reservoirs and, consequently, identifying the right degree of heterogeneity and correlation lengths that characterise the permeability fields in each class of reservoirs.

Flow pattern comparison under MCM displacement conditions: The CO_2 flow patterns have been investigated having the background assumption that FCM govern the displacement in both classes of reservoirs. The next step, which may better fulfil the potential of this work, is to take into account compositional effects and investigate flow patterns under MCM displacement scenarios for each class of reservoirs.

Combined compositional and thermal simulation for North Sea CO_2 flooding: An important extension of the work conducted in Chapter 3 for comparing CO_2 flooding between the North Sea and the Permian basin provinces could be carrying out a combined thermal and compositional simulation to evaluate the impact of reservoir cooling in those North Sea reservoirs due to prolonged cold sea water injection and its impact on the likely CO_2 flooding characteristics in the North Sea.

Improving the simulation tools: Relative permeability allocation to gas and oil phases is primarily a function of correct characterisation and labelling of the gas and oil phases in the simulator. This may create some problems where at high pressures and low temperatures the CO_2 rich phase may have liquid like properties. CO_2 flooding in the North Sea may also require four phase simulators (3 hydrocarbon phases and 1 water phase) as reservoir temperatures might be low and pressures are high, thus formation of a third hydrocarbon phase and its impact on the displacement characteristics might be significant.

Certain features in the Permian Basin CO_2 flooding simulations which were conducted in 1980-90, were considered important and were always as an integral part of all the CO_2 flooding simulations. The effect of *water blocking* on the CO_2-EOR performance is an important consideration in a large number of these simulations. Whether or not the current approach of representing the three phase relative permeabilities e.g. Stone1 and 2 and other models can replicate this feature in the current compositional simulation is not yet certain. *Incomplete mixing* is also another important characteristic of CO_2 flooding simulations in the United States, conducted with the Todd & Longstaff modelling approach. Although compositional reservoir simulators have been developed significantly since then and use of finer grid blocks is more achievable nowadays, this does not warrant that the concept of incomplete mixing should be discarded. An interesting research topic could be how to incorporate the concept of incomplete mixing in the current compositional simulation formulations. One solution could be DLGR (or Dynamic Local Grid Refinement), but DLGR has its own limitations in terms of permeability fining and coarsening when and where needed.

Grid requirement for miscible/immiscible simulations: A few extensions for this work can be assumed.

First, better Peclet characterisation algorithms for the entire system are needed. As was observed in this chapter, the Peclet estimation algorithm in both fundamental orientations depends very much on the distribution of solvent within the system which is different at each dimensionless time. This will cause the Peclet number to vary and not remain constant during simulations and creates challenge in terms of what is the best point to read the system Peclet numbers.

Second, this work can be extended to immiscible displacements as well, though the concept of dispersion is slightly awkward in the immiscible system. However, we know that capillary effects have almost the same impact as the dispersive effects in miscible displacements. Therefore, two new questions may emerge. What is the grid requirement for an immiscible displacement? And then what is the proper grid requirement for coupled miscible/immiscible displacement simulations?

Finally, for any system, there is a certain magnitude of dispersion where the grid block sizes can be used for matching. Going beyond this limit may increase numerical dispersion larger than that of physical dispersion, leading to an early solvent breakthrough. However, it might be possible to add a negative dispersion terms to the displacement equation and then increase the grid block sizes. This way the added numerical dispersion can be effectively compensated for by the introduced negative numerical dispersion term. The concept should be very similar to the pseudo-relative permeability concept in the context of immiscible displacement simulations. It is certainly an interesting research opportunity.

Appendix 1 Velocity Estimation in Quarter 5-Spot Patterns

To estimate velocity dependent dimensionless numbers (e.g. gravity number), an estimate of the *in-situ* velocity is required. While in linear floods, average velocity at any given distance between injector and producer can be considered constant for a given average injection velocity, since the flow area is not changing, in radial floods, velocity is constantly changing as the front propagates from injector to producer and thus allocating a representative velocity for the whole displacement during radial flow is challenging.

Parsons (1974) measured velocity distribution across twelve individual streamlines in a quarter 5-spot pattern from injector to producer (Figure A1.1, left). He showed that in a 5-spot well placement, the *normalised median frontal velocity* ($\frac{v_f \varphi \sqrt{A}}{q/h}$) *of* 0.016, is the velocity value at which half of the 5-spot pattern has higher velocities and half has lower velocities (Figure A1.1, Right).

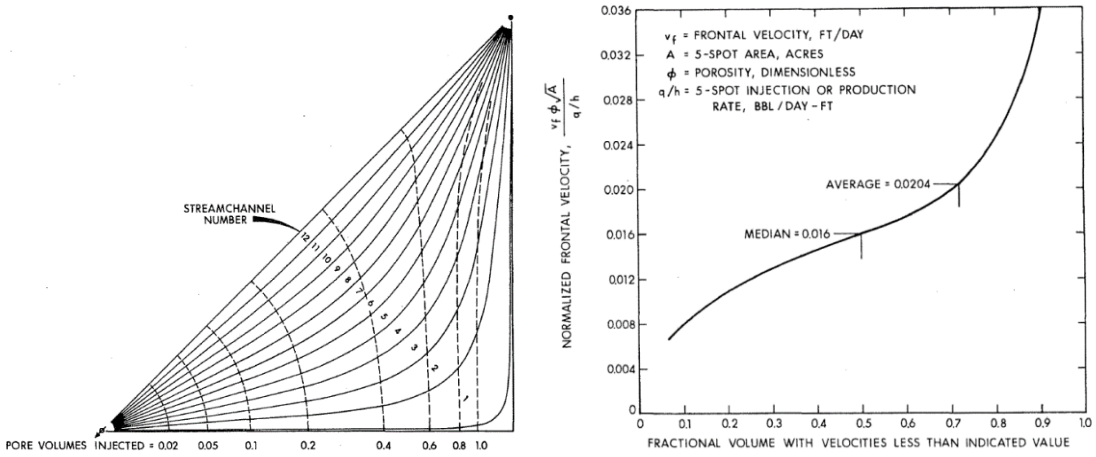

Figure A1.1: Left: Streamlines for a developed 5-spot model, Right: Developed 5-spot velocity distribution (Parsons 1974)

In other words, for any 5-spot well placement we may have:

$$\frac{v_f \varphi \sqrt{A}}{q/h} = 0.016 \qquad \text{(A1.1)}$$

Where v_f is the pore velocity, A is the pattern area (acre), q is the injection rate (bbl/day) and h is the thickness of the formation. The above equation can be rearranged as follows:

$$v_f = 0.016 \frac{q/h}{\varphi\sqrt{A}} \tag{A1.2}$$

We need to establish a relationship between the rate of injection/production (q) and the rate of reservoir depletion (r). Rate of (reservoir) depletion is the fraction of the reservoir hydrocarbon pore volume depleted or injected on an annual basis. To accomplish this for a 5-spot pattern, we first need to identify the no-flow boundary where injection/production rates into this no-flow boundary are identical. Figure A1.2 shows a combination of 9 producers and 4 injectors in a typical 5-spot well placement pattern. Note that q in Equation (A1.2) refers to injection/production at reservoir conditions.

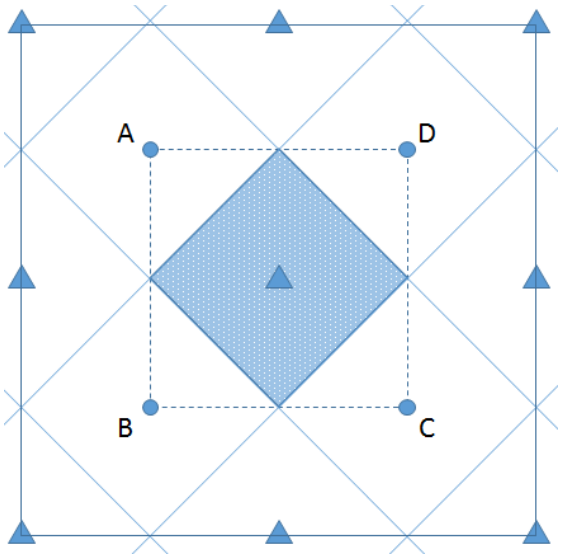

Figure A1.2: 5-spot pattern development with 9 injectors (rectangles) and 4 producers (circles).

Each injector or producer targets a pattern area denoted as *A*. For our analysis, the area depicted by points *ABCD* may represent a no-flow boundary where injection and production volumes are equivalent. The area of this no-flow boundary (*ABCD*) is twice the area of the pattern area (*A*) itself. Thus, the volume of this no-flow boundary is:

$$HCPV_{ABCD}(bbl) = \frac{2\left(A_{(acre)} \times 43560\right) \times h_{(ft)}\varphi}{5.615} \tag{A1.3}$$

The coefficient of 43560 in the above equation is required to convert the pattern size from acre unit to ft^2. Similarly, the coefficient of 5.615 is required to convert the calculated volume from ft^3 to bbl. The injection or production rate into this no-flow boundary can also be expressed in terms of the fraction of this *HCPV* that is injected or produced annually. Thus;

$$r_{(fraction)} = \frac{q_{(bbl/day)} \times 365_{(days)}}{HCPV_{(bbl)}} \tag{A1.4}$$

Thus;

$$q = \frac{r \times HCPV}{365} = \frac{r \times \frac{2(A \times 43560) \times h\varphi}{5.615}}{365} = 42.51\left(rh_{(ft)}\varphi A_{(acre)}\right) \tag{A1.5}$$

Substituting Equation (A1.5) into Equation (A1.2), we then have;

$$v_f = 0.016\frac{q/h}{\varphi\sqrt{A}} = 0.016\frac{42.51(rh\varphi A)/h}{\varphi\sqrt{A}} = 0.68\left(r\sqrt{A_{(acre)}}\right) \tag{A1.6}$$

A in the above equation is the pattern area in terms of acres which can be expressed in terms of well spacing (*L*). Thus;

$$v_f = 0.68\left(r\sqrt{A_{(acre)}}\right) = 0.68\left(r\sqrt{\frac{L^2_{(ft)}}{43560}}\right) \tag{A1.7}$$

Or;

$$v_f\,(\text{ft/day}) = 0.003259 \times r\,(\text{fraction}) \times L\,(\text{ft}) \tag{A1.8}$$

This equation shows that as well spacing increases, the *in-situ* fluid velocities should increase accordingly, if the *same* injection/production rate is to be maintained.

We may check the validity of the above formulation using the example presented by Parsons (1974). Parson estimated that for a 10acre, 5-spot pattern with a porosity value of 0.2, where injection into the pattern is 5bbl/day/ft, the *in-situ* velocity should be around 0.13ft/day. For this specific problem, assuming *h*=1ft, we may have:

$$HCPV_{(no\ flow\ boundary)} = \frac{2\left(A_{(acre)} \times 43560\right) \times h_{(ft)}\varphi}{5.615} = \frac{2(10 \times 43560) \times 1 \times 0.2}{5.615}$$
$$= 31031bbl$$

And the rate of depletion is;

$$r = \frac{q \times 365}{HCPV_{(no\ flow\ boundary)}} = \frac{5 \times 365}{31031} = 0.0588$$

For 10-acre pattern, well spacing is 660ft.

$$L = \sqrt{43560A_{(acre)}} = \sqrt{43560 \times 10} = 660ft$$

Thus, the estimated *in-situ* velocity is;

$$v_f = 0.003259 \times r \times L = 0.003259 \times 0.0588 \times 660 = \mathbf{0.13ft/day}$$

We use the above equation to estimate the *in-situ* fluid velocity for onshore and offshore classes of reservoirs in Chapter 4 to calculate gravity (N_g) and also time-defined gravity (N_{gt}) numbers, knowing the magnitudes of the rate of depletion and the spacing between wells. We acknowledge that the estimated average *in-situ* velocity might be different for other flow configurations (e.g. for linear flow the coefficient may decrease from 0.003259 to 0.002740, an almost 16% reduction, but not an order of magnitude). Nevertheless, the above equation can give a first good estimate of the magnitude of the *in-situ* velocity.

The above correlation may be used to estimate pressure drop within a given system. According to Darcy's law (in field units):

$$q_{(bbl/day)} = \frac{0.001127k_{(mD)}A_{(ft^2)}\Delta p_{(psi)}}{\mu_{(cP)}L_{(ft)}} \tag{A1.9}$$

In terms of the actual *in-situ* velocity; the Darcy's law can be rearranged as:

$$v_{(ft/day)} = \frac{0.006328k_{(mD)}\Delta p_{(psi)}}{\mu_{(cP)}L_{(ft)}} \tag{A1.10}$$

Hence the pressure drop (Δp) is:

$$\Delta p_{(psi)} = \frac{v_{(ft/day)}\mu_{(cP)}L_{(ft)}}{0.006328k_{(mD)}} \tag{A1.11}$$

The velocity term can be replaced from Equation A1.8, hence;

$$\Delta p_{(psi)} = \frac{0.003259 \times r \times L^2 \times \mu}{0.006328k} = 0.515\frac{r_{frac} \times {L_{ft}}^2 \times \mu_{cP}}{k_{mD}} \tag{A1.12}$$

Equation A1.12 shows that pressure drop within a system is simultaneously proportional to the rate of depletion and square root of well spacing. For example, under comparable Δps, a reduction of well spacing by a factor of 2 may increase the rate of depletion by a factor of 4 and simultaneously increase the *in-situ* velocity by a factor of 2 (Equation A1.10,). Both of which are in accordance with the basic definition of Darcy's law (Equation A1.11).

Note that the actual pressure drop in a given system is expected to be higher than that predicted by Equation A1.12, as this equation does not take into account the pressure drop due to radial flow around injection or production wells. Additionally, this equation does not take into account the relative permeability effects. However, even with these limitations, we believe this correlation is an effective tool in comparing pressure drop between different flooding scenarios.

Appendix 2 Derivation of the Time-Defined Gravity Number

Introduction

The main objective of this appendix is to derive the unique scaling group, which describes the severity of gravity in a miscible or an immiscible displacement. For a miscible displacement in a homogeneous permeability field, five dimensionless numbers describe the flow characteristics (Gharbi *et al*. 1998) (Table A2.1). Similarly, for an immiscible displacement, four dimensionless numbers may describe displacement. In addition to these numbers, at least three dimensionless numbers describe the heterogeneity of the system (V_{DP}, λ_{xD} and λ_{zD}) (Garmeh & Johns 2010).

Table A2.1: Dimensionless numbers describing the flow characteristics in miscible and immiscible displacements

		Immiscible	**Miscible**
Gravity number (N_g)		$N_g = \frac{k_{ro}}{\mu_o}\frac{k_x \Delta\rho g}{u_t}\frac{H}{L}$	$N_g = \frac{1}{\mu_o}\frac{k_x \Delta\rho g}{u_t}\frac{H}{L}$
Mobility ratio (M)		$M_{ow} = \frac{k_{rw}}{\mu_w}\frac{\mu_o}{k_{ro}}$	$M_{os} = \frac{\mu_o}{\mu_s}$
Dispersive Numbers	**Capillary number (N_C)**	$N_c = \frac{k_{ro}}{\mu_o}\frac{\sigma}{Lu_t}\sqrt{\varphi k_x}$	-
	Longitudinal Peclet Number (Pe_L)	-	$\frac{u_t L}{\varphi K_L} = \frac{L}{\alpha_L}$
	Transverse Peclet Number (Pe_T)	-	$\frac{u_t H^2}{\varphi L K_T} = \frac{H^2}{L\alpha_T}$
Effective aspect ratio (N_{RL})		$N_{RL} = \frac{L}{H}\sqrt{\frac{k_z}{k_x}}$	

The derivation of these dimensionless numbers will not be shown here, as it is already described by various authors (Garmeh & Johns 2010, Gharbi *et al*. 1998). Instead, the fundamental transport equations in miscible and immiscible displacements are derived and transposed into the dimensionless domain to derive the gravity scaling group.

Derivation of the Fundamental Material Balance Equation

We first derive the fundamental material balance formulation for a miscible flow. The immiscible formulation is essentially similar to the miscible one, which will be illustrated later. Assuming a cross sectional plane in the *X*-*Z* orientation (Figure A2.1), having the length and height of *L* and *H* respectively, an FCM miscible flood can be assumed in this system, where the injected fluid is injected from left and displaces resident fluid miscibly towards the producer. It is also assumed that all the fluids are incompressible, therefore the average flood velocity is constant across the entire system and should be equal to the injection velocity (u_t). The injector and producer, which are located on the opposite sides of the cross sectional plane, have been perforated across the entire height of the model. Permeabilities in the horizontal and vertical directions are k_x and k_z respectively.

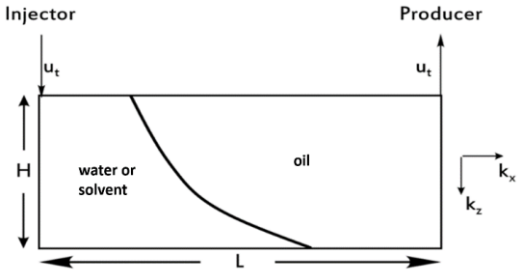

Figure A2.1: Flow displacement in a two dimensional cross sectional model

For any imaginary control volume within the system, a material balance equation can be written as has been described in Figure A2.2. Assuming a miscible displacement, the change of *concentration* (*c*) at any point is equal to the net balance of concentration transportation into/from this imaginary control volume, due to different mechanisms i.e. viscous, gravity and dispersive effects (Figure A2.2).

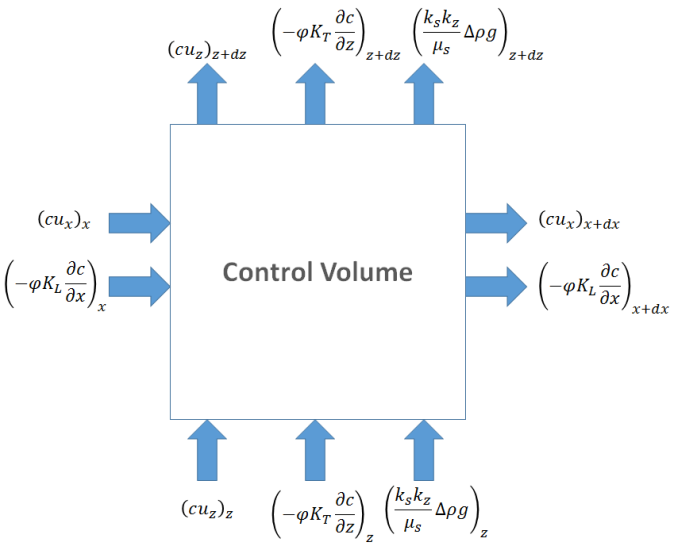

Figure A2.2: Schematics of the material balance elements around the control volume

All the terms have been described in the nomenclature. According to the schematics shown in Figure A2.2, the material balance equation should have the formulation which is shown below (Equation A2.1);

$$\varphi\frac{\partial c}{\partial t}+u_x\frac{\partial c}{\partial x}+u_z\frac{\partial c}{\partial z}-\varphi K_L\frac{\partial^2 c}{\partial x^2}-\varphi K_T\frac{\partial^2 c}{\partial z^2}+\frac{\partial}{\partial z}\left(\frac{k_z k_s}{\mu_s}\Delta\rho g\right)=0 \qquad \text{(A2.1)}$$

The first term in the above equation represents accumulation; second and third terms are component transport by viscous displacement; fourth and fifth terms are component transport by diffusive phenomena and finally the last term is the component transport by gravity effects.

Transposing Into Dimensionless Domain

Equation A2.1 can be easily transposed into the dimensionless domain by the following substitutions (Gharbi *et al*. 1998).

Table A2.2: Parameter substitutions to transpose into dimensionless domain

$u_{xD}=\frac{u_x}{u_t}$	$t_D=\frac{u_t t}{\varphi L}$	$x_D=\frac{x}{L}$	$\frac{1}{Pe_L}=\frac{\varphi K_L}{Lu_t}$
$u_{zD}=\frac{u_z}{u_t\left(\frac{H}{L}\right)}$	$c_D=c$	$z_D=\frac{z}{H}$	$\frac{1}{Pe_T}=\frac{\varphi K_T}{Lu_t H^2}$

After substituting the above into Equation A2.1, we may have:

$$\frac{u_t}{L}\frac{\partial c_D}{\partial t_D}+u_{xD}\frac{u_t}{L}\frac{\partial c_D}{\partial x_D}+u_{zD}\frac{u_t}{L}\frac{\partial c_D}{\partial z_D}-\frac{\varphi K_L}{L^2}\frac{\partial^2 c_D}{\partial {x_D}^2}-\frac{\varphi K_T}{H^2}\frac{\partial^2 c_D}{\partial {z_D}^2}+\frac{1}{H}\frac{\partial}{\partial z_D}\left(\frac{k_z k_s}{\mu_s}\Delta\rho g\right)=0$$

Multiplying all terms by $\frac{L}{u_t}$:

$$\frac{\partial c_D}{\partial t_D}+u_{xD}\frac{\partial c_D}{\partial x_D}+u_{zD}\frac{\partial c_D}{\partial z_D}-\frac{\varphi K_L}{u_t L}\frac{\partial^2 c_D}{\partial {x_D}^2}-\frac{\varphi L K_T}{u_t H^2}\frac{\partial^2 c_D}{\partial {z_D}^2}+\frac{L}{u_t H}\frac{\partial}{\partial z_D}\left(\frac{k_z k_s}{\mu_s}\Delta\rho g\right)=0$$

$$\frac{\partial c_D}{\partial t_D}+u_{xD}\frac{\partial c_D}{\partial x_D}+u_{zD}\frac{\partial c_D}{\partial z_D}-\frac{1}{Pe_L}\frac{\partial^2 c_D}{\partial {x_D}^2}-\frac{1}{Pe_T}\frac{\partial^2 c_D}{\partial {z_D}^2}+\frac{L}{u_t H}\frac{\partial}{\partial z_D}\left(\frac{k_z k_s}{\mu_s}\Delta\rho g\right)=0$$

The last term describes the significance of gravity and is what we are looking for. Since the displacement is miscible, it can be assumed that k_s=*c*. Therefore , this term may be rearranged as follows;

$$\frac{L}{Hu_t}\frac{\partial}{\partial z_D}\left(\frac{k_z k_s}{\mu_s}\Delta\rho g\right)=\frac{\partial}{\partial z_D}\left(\frac{k_z c}{\mu_s}\frac{L}{Hu_t}\Delta\rho g\right)=\left(\frac{k_z}{\mu_s}\frac{L}{Hu_t}\Delta\rho g\right)\left(\frac{\partial c_D}{\partial z_D}\right)$$

$$=\left(\frac{\mu_o}{\mu_s}\right)\left(\frac{1}{\mu_o}\frac{k_x\Delta\rho g}{u_t}\frac{H}{L}\right)\left(\frac{k_z}{k_x}\left(\frac{L}{H}\right)^2\right)\frac{\partial c_D}{\partial z_D}=\left(\boldsymbol{M_{os}\times N_g\times N_{RL}^2}\right)\frac{\partial c_D}{\partial z_D}$$

Therefore Equation A2.1 in dimensionless domain should have the following form:

$$\boldsymbol{\frac{\partial c_D}{\partial t_D}+u_{xD}\frac{\partial c_D}{\partial x_D}+u_{zD}\frac{\partial c_D}{\partial z_D}-\frac{1}{Pe_L}\frac{\partial^2 c_D}{\partial x_D^2}-\frac{1}{Pe_T}\frac{\partial^2 c_D}{\partial z_D^2}+\left(M_{os}N_{RL}^2N_g\right)\frac{\partial c_D}{\partial z_D}=0} \qquad \text{(A2.2)}$$

Equation A2.2 shows that the importance of gravity is determined by a combination of the mobility, gravity and effective aspect ratio dimensionless numbers. The larger the above group, the more significant will be the impact of gravity. Equation A2.2 also demonstrates that the magnitude of the gravity number (N_g) does not solely determine the severity of gravity, and all of the gravity, effective aspect ratio and mobility numbers are important in this regard. While the gravity number illustrates the potential for gravity domination, the effective aspect ratio allows this potential to have an impact.

Similar to the miscible formulation derived above, the same formulation can be derived for an immiscible displacement. Equation A2.3 shows the final form of the material balance equation in an immiscible displacement in the dimensionless domain.

$$\boldsymbol{\frac{\partial s_{wD}}{\partial t_D}+u_{xD}f'_w\frac{\partial s_{wD}}{\partial x_D}+u_{zD}f'_w\frac{\partial s_{wD}}{\partial z_D}+\frac{\partial}{\partial x_D}\left(M_wN_c\frac{\partial s_{wD}}{\partial x_D}\right)}$$
$$\boldsymbol{+\frac{\partial}{\partial z_D}\left(M_wN_{RL}^2N_c\frac{\partial s_{wD}}{\partial z_D}\right)+\frac{\partial}{\partial z_D}\left(M_{ow}N_{RL}^2N_g\right)=0} \qquad \text{(A2.3)}$$

In the above equation, f_w and f'_w represent the water fractional flow and its derivative with respect to water saturation. Comparing Equations A2.2 and A2.3 it can be seen that there is similarity in the gravity scaling group in that both of them are a combination of effective aspect ratio, gravity and mobility ratio numbers. Additionally, in both of them, there are dispersive terms (second order derivative terms), in that capillary forces in an immiscible displacement have the same effect as dispersion in miscible displacement. Finally, capillary effects in the transverse direction in an immiscible displacement are proportional to the magnitude of effective aspect ratio. Table A2.3 summarises the magnitude of the gravity scaling group (or from now on the N_{gt}[15]) in miscible and immiscible displacements.

[15] Time defined gravity number

Table A2.3: The magnitude of time defined gravity number (N_{gt}) in miscible and immiscible displacements scenario

	Miscible Displacement	**Immiscible Displacement**
Gravity Scaling Group (N_{gt})	$\frac{L}{H}\frac{k_z}{u_t\mu_s}\Delta\rho g$	$\frac{L}{H}\frac{k_w}{\mu_w}\frac{k_z}{u_t}\Delta\rho g$[16]

It is important within the context of this discussion that, under the same rate of depletion, as the spacing between injector and producer increases ($L\uparrow$), the magnitude of N_{gt} does not change as the *in-situ* fluid velocity increases accordingly ($u_t\uparrow$), hence gravity effects remain fairly comparable.

We call this group N_{gt} in this study, because it takes into account both the significance of the motivation for the gravity and the time required for this driving force to be applied in reality. This number could be another criterion for comparing the significance of gravity between different flooding scenarios rather than conventional gravity number depicted earlier in Table A2.1. For both miscible and miscible the above scaling group can be written as;

$$N_{gt(miscible)} = \frac{L}{H}\frac{k_z}{u_x\mu_s}\Delta\rho g = \frac{L/u_x}{H\Big/\left(\frac{k_z}{\mu_s}\Delta\rho g\right)} = \frac{L/u_x}{H/u_z} = \frac{t_v}{t_g} \tag{A2.4}$$

The immiscible formulation is similar to the above and has not been shown here. In the above equation t_v is the time that is required for viscous transport in the horizontal direction and t_g is the time required for gravity transport in the vertical direction. The larger this ratio, the larger will be the N_{gt} which implies that gravity is more significant for the given displacement.

[16] Where water displaces oil.

Appendix 3 The First Contact Miscible Model

This appendix shows the first contact miscible model which was used in Chapters 3 and 6 to investigate flow patterns and also to measure Peclet numbers. The model is basically a modified version of the model that was used by Garmeh *et al*. (2011). The model represents an incompressible 2-component first contact miscible model in a single (oil) phase. The properties of the components, i.e. densities and viscosities can be varied to generate models with desired dimensionless numbers. The model can be run in CMG-GEM (CMG-GEM 2014.10). The red underlined bold numbers in this model represent those model parameters that may be varied to generate desired magnitudes of dimensionless numbers.

```
INUNIT FIELD
*OUTSRF *RES
*OUTSRF *GRID PRES VISO ZALL DENO VELOCRC
*OUTSRF *SPECIAL *SIMPERF
**WPRN GRID 0
OUTPRN GRID NONE
OUTPRN RES
WSRF GRID TIME
WSRF WELL 1


GRID CART 256 1 64
KDIR DOWN
DI CON 6.25
DJ CON 6.25
DK CON 1.5625
DTOP 256*100
**DIP 30 0

NULL CON   1
POR CON 0.2

Include '../Inc256X64/Perms/Perm2.dat' **6 different permeability descriptions
PERMJ *EQUALSI * 1.0
PERMK *EQUALSI * 1.0  ** Varied to adjust the effective aspect ratio

PINCHOUTARRAY CON     1
PRPOR 3000.01
CPOR 0
*MODEL *PR
*NC 2 2
*COMPNAME 'SOL' 'OIL'

*PCRIT 220.0 220.0 **atm
*TCRIT 650.0 650.0 **k
*VCRIT 0.055 0.055 **m3/kmole
*MW 10 18 ** Varied to adjust the Density Difference and gravity number
**MW SOL OIL

*AC 0.04 0.04
*HCFLAG 0 0
*OMEGA 0.45 0.45
*OMEGB 0.077 0.077
*PHASEID *OIL
```

```
*TRES 60.0 **deg F
*PSAT -1

*VISCOSITY 0.01 0.1 ** Varied to adjust the mobility ratio

ROCKFLUID
KROIL STONE1 SWSG
RPT 1

*SWT **SNORM KRW NKRWO NPCWOD
0 0 1 0
1 1 0 0

*SGT **SL KRG KROG PCGOD
0 0 1 0
1 1 0 0

**Dispersion
**DISPERARRAY-LNG *CON   2.0
**DISPERARRAY-TRN *CON   5
**Initial Conditions -------------------------

INITIAL
*VERTICAL *off
*PRES *CON 4000
*SW *CON 0
*ZGLOBAL *CON
0 1
**SOL OIL

NUMERICAL
*DTMIN 1E-10
*NORM *PRESS 10
*NORM *GMOLAR 0.01
*PRECC 1E-6
*MAXCHANGE *GMOLAR 0.05

**RUN-----------------------------------------------
RUN
DATE 2000 1 1
**AIMSET *CON 3
DTWELL 1e-8

*GROUP 'GROUPP' ATTACHTO 'FIELD'

WELL   1      'PROD' ATTACHTO 'GROUPP'
WELL   2      'INJ'  ATTACHTO 'GROUPP'

PRODUCER 1
GEOMETRY K 0.01 0.37 1.0 0.0

INJECTOR 2
INCOMP SOLVENT 1 0
GEOMETRY K 0.01 0.37 1.0 0.0

PERF GEO      'PROD'
256:256 1:1 1:64    1.0    OPEN


PERF GEO      'INJ'
1:1    1:1    1:64                1.0    OPEN


PRODUCER 1
OPERATE MAX BHF     11.1308             CONT REPEAT
**OPERATE MIN BHP   4000                CONT REPEAT

INJECTOR 2
OPERATE MAX   BHF    11.1308            CONT REPEAT
OPERATE MAX   BHP    20000.0            CONT REPEAT
```

```
*TIME  320
*TIME  640
*TIME  960
*TIME  1280
*TIME  1600
*TIME  1920
*TIME  2240
*TIME  2560
*TIME  2880
*TIME  3200

*STOP
```

Appendix 4 Excel Macro to Evaluate Peclet Numbers

The code below, developed in Excel, takes the raw concertation values (c) at each dimensionless time and measures the average Peclet number in the longitudinal and transverse orientations for those cells whose concentrations reside between 0.1 and 0.9 (within transition zone). Note that there is no direct function to evaluate the inverse of complementary error function ($erfc^{-1}$) in Excel, However, it can be calculated by the following alternative function;

$erfc^{-1}(p)=-Norm.S.Inv(p/2)/Sqrt(2)$

```
Sub ProcessFiles()
    Dim Filename, Pathname As String
    Dim wb As Workbook

    Pathname = "C:\Users\saeed ghanbari\Desktop\Dispersivity\"
    Filename = Dir(Pathname & "*.xlsx")
    Do While Filename <> ""
        Set wb = Workbooks.Open(Pathname & Filename)
        DoWork_H wb
       wb.Close SaveChanges:=True
       Filename = Dir()
   Loop

    Pathname = "C:\Users\saeed ghanbari\Desktop\Dispersivity\"
    Filename = Dir(Pathname & "*.xlsx")
    Do While Filename <> ""
        Set wb = Workbooks.Open(Pathname & Filename)
        DoWork_V wb
       wb.Close SaveChanges:=True
       Filename = Dir()
   Loop


End Sub

'-------------------------------------Longitudinal Peclet Measurement
Sub DoWork_H(wb As Workbook)

On Error Resume Next
Application.DisplayAlerts = False

       With wb
       Worksheets(1).Select
       Range("A1").SpecialCells(xlLastCell).Select
       m = ActiveCell.Row '64
       n = ActiveCell.Column '256

           For i = 1 To 21
           wb.Worksheets(i).Copy After:=Worksheets(Sheets.Count)
           Next i

           For i = 1 To 21
           wb.Worksheets(i + 21).Name = CStr(i - 1)
           Next i

           For i = 1 To 21
           wb.Worksheets(i).Name = "D" & CStr(i - 1)
```

```
          Next i

             For k = 0 To 20
                    wb.Worksheets(k + 22).Activate
                    wb.Worksheets(k + 22).Range("a1:iv64").Clear

                           For i = 1 To m
                           For j = 2 To n
                           PageNum = "D" + CStr(k)


'***********Evaluate Peclet Numbers
wb.Worksheets(k + 22).Cells(i, j).FormulaR1C1 = "=IF(AND(" & Chr(39) & PageNum
& Chr(39) & "!R[0]C[-1]>=0.1, " & Chr(39) & PageNum & Chr(39) &
"!R[0]C[0]>=0.1," & Chr(39) & PageNum & Chr(39) & "!R[0]C[-1]<=0.9, " &
Chr(39) & PageNum & Chr(39) & "!R[0]C[0]<=0.9),IFERROR(4*" & CStr(k / 10) &
"*" & CStr(n) & "*" & CStr(n) & "*(ABS(NORM.S.INV(" & Chr(39) & PageNum &
Chr(39) & "!R[0]C[-1])-NORM.S.INV(" & Chr(39) & PageNum & Chr(39) &
"!R[0]C[0]))/SQRT(2))^2,0),0)"
t = wb.Worksheets(k + 22).Cells(i, j)
wb.Worksheets(k + 22).Cells(i, j).Interior.Color = RGB(255 * (1 - t), 255, 255
* (1 - t))

                           Next j
                           Next i

                    '***********Geometric Average
                    For i = 1 To m
                    For j = 1 To n
                    If Cells(i, j) = 0 Then
                    Cells(i, j).Clear
                    End If

                    Next j
                    Next i

                    For i = 1 To m
                    For j = 1 To n

                    If IsEmpty(Cells(i, j).Value) = False Then
                    Cells(i, j) = Log(Cells(i, j))
                    End If

                    Next j
                    Next i
                    wb.Worksheets(k+22).Range("A65").Formula =
"=exp(average(a1:iv64))"
                    '***********

             Next k

          For i = 1 To 21
          wb.Worksheets(1).Delete
          Next i

      End With
End Sub

'-------------------------------------Transverse Peclet Measurement
Sub DoWork_V(wb As Workbook)

On Error Resume Next
Application.DisplayAlerts = False

      With wb
      Worksheets(1).Select
      Range("A1").SpecialCells(xlLastCell).Select
      m = ActiveCell.Row '64
      n = ActiveCell.Column '256

          For i = 1 To 21
```

```
          wb.Worksheets(i).Copy After:=Worksheets(Sheets.Count)
          Next i

          For i = 1 To 21
          wb.Worksheets(i + 21).Name = CStr(i - 1)
          Next i

          For i = 1 To 21
          wb.Worksheets(i).Name = "D" & CStr(i - 1)
          Next i

             For k = 0 To 20
                   wb.Worksheets(k + 22).Activate
                   wb.Worksheets(k + 22).Range("a1:iv64").Clear

                         For i = 1 To m
                         For j = 2 To n
                         PageNum = "D" + CStr(k)


'***********Evaluate Peclet Numbers
wb.Worksheets(k + 22).Cells(i, j).FormulaR1C1 = "=IF(AND(" & Chr(39) & PageNum
& Chr(39) & "!R[-1]C[0]>=0.1, " & Chr(39) & PageNum & Chr(39) &
"!R[0]C[0]>=0.1," & Chr(39) & PageNum & Chr(39) & "!R[-1]C[0]<=0.9, " &
Chr(39) & PageNum & Chr(39) & "!R[0]C[0]<=0.9),IFERROR(4*" & CStr(k / 10) &
"*" & CStr(m) & "*" & CStr(m) & "*(ABS(NORM.S.INV(" & Chr(39) & PageNum &
Chr(39) & "!R[-1]C[0])-NORM.S.INV(" & Chr(39) & PageNum & Chr(39) &
"!R[0]C[0]))/SQRT(2))^2,0),0)"
t = wb.Worksheets(k + 22).Cells(i, j)
wb.Worksheets(k + 22).Cells(i, j).Interior.Color = RGB(255 * (1 - t), 255, 255
* (1 - t))

                         Next j
                         Next i

                   '***********Geometric Average
                   For i = 1 To m
                   For j = 1 To n
                   If Cells(i, j) = 0 Then
                   Cells(i, j).Clear
                   End If

                   Next j
                   Next i

                   For i = 1 To m
                   For j = 1 To n

                   If IsEmpty(Cells(i, j).Value) = False Then
                   Cells(i, j) = Log(Cells(i, j))
                   End If

                   Next j
                   Next i
                   wb.Worksheets(k + 22).Range("A65").Formula =
"=exp(average(a1:iv64))"
                   '***********

             Next k

          For i = 1 To 21
          wb.Worksheets(1).Delete
          Next i

       End With
End Sub
```

References

Articles

Abu Bakar, M., Yeap, Y. C., Nasir, E., Din, A., Fui C. C., Adamson, G. Agarwal B., Valdez, R. (2011). EOR Evaluation for Baram Delta Operations Fields, Malaysia. SPE Enhannced Oil Recovery Conference, Kuala Lumpur. doi:10.2118/144533-MS.

Ader, J. C., & Stein, M. H. (1984). Slaughter Estate Unit Tertiary Miscible Gas Pilot Reservoir Description. *Journal of Petroleum Technology*, Vol 36, No 5, pp837-845.

Agustsson, H., & Grinestaff, G. H. (2004). A Study of IOR by CO_2 Injection in the Gullfaks Field, Offshore Norway. SPE/DOE 14th Symposium on Improved Oil Recovery, Oklahama. doi:10.2118/89338-MS.

Ahmadi, K., & Johns, R.T. (2011). Multiple Mixing-Cell Method for MMP Calculations. *SPE Journal*, doi:10.2118/116823-MS, pp733-742.

Akervoll, I., & Bergmo, P. (2010). CO_2 EOR from Representative North Sea Oil Reservoirs. SPE conference on CO_2 Capture, Storage and Utilisation, New Orleans, doi:10.2118/139765-MS.

Algharaib, M., Gharbi, R., & Malallah, A. (2006). Scaling immiscible displacements in porous media with horizontal wells. *Transport in porous media*, *65*(1), 89-105.

Alkemade, P. J. C. (1995). CO_2 Miscible Displacement Enhanced Oil Recovery In Dutch North Sea. Proceedings of the Fifth International Offshore and Polar Engineering Conference. Hauge. International Society of Offshore and Polar Engineers, pp231-243.

Araktingi, U. G., & Orr, F. M. (1990). Viscous Fingering, Gravity Segregation, and Reservoir Heterogeneity in Miscible Displacements in Vertical Cross Sections. SPE/DOE 17th Symposium on Enhanced Oil Recovery, Tulsa, Oklahoma. doi:10.2118/20176-MS.

Aryana, S., Barclay, C., & Liu, S. (2014). North Cross Devonian Unit - A Mature Continuous CO_2 Flood Beyond 200% HCPV Injection. SPE Annual Technical Conference, Amsterdam. doi:10.2118/170653-MS.

Awan, A., Teigland, R., & Kleppe, J. (2008). A survey of North Sea Enhanced-Oil-Recovery Projects Initiated During the Years 1975 to 2005. *SPE Reservoir Evaluation and Engineering*, pp497-512.

Bargas, C., Montgomery, H., Sharp, D., & Vosika, J. (1992). Immiscible CO_2 Process for the Salt Creek Field. *SPE Reservoir Engineering*, doi:10.2118/21577-PA, pp397-402.

Baroni, M. (1995). Applications of advanced petroleum production technology and water alternating gas injection for enhanced oil recovery-Mattoon Oil Field, Illinois. Final report (No. DOE/BC/14955--8). American Oil Recovery, Inc., Decatur, IL (United States).

Bath, P.G.H. (1987). Enhanced Oil Recovery in the North Sea. In *North Sea Oil and Gas Reservoirs*: Vol 1, ed. J. Kleppe et al., pp217–230. Norwegian Institute of Technology: Kluwer Academic Publishers.

Beecroft, W., Mani, V., Wood, A., & Rusinek, I. (1999). Evaluation of Depressurisation, Miller Field, North Sea. SPE Annual Technical Conference and Exhibition, Houston, doi:10.2118/56692-MS.

Belhaj, H., Aljarwan, A., Haroun, M., & Ghedan, S. (2012). Increasing Oil Recovery with CO_2 Miscible Injection: Thamama-IV Reservoir, Zakum Field Case Study. SPE Internation petroleum conference and Exhibition, Kuwait, doi:10.2118/163319-MS.

Bellavance, J. (1996). Dollarhide Devonian CO_2 Flood: Project Performance Review 10 years Later. SPE Permian Oil and Gas Recovery Conference. Midland, TX. doi:10.2118/35190-MS.

Blunt, M., & Christie, M. (1994). Theory of Viscous Fingering in Two Phase, Three Component Flow. *SPE Advanced Technology Series*, Vol 2, No 2, pp52-60.

Brinkman, F., Kane, T., McCullough, R., & Miertschin, J. (1999). Use of Full-Field Simulation to Design a Miscible CO_2 Flood. *SPE Reservoir Evaluation and Engineering*, Vol 2, No 3, pp230-237.

Brock, W. R., & Bryan, L. A. (1989). Summary results of CO_2 EOR field tests, 1972-1987. SPE Joint Rocky mountain/low permeability reservoirs symposium. Denver, doi:10.2118/18977-MS.

Brodie, J., Zhang, P., Mellemstrand , H., Moulds, T., & Jhaveri, B. (2012). BP North Sea Gas Injection Projects: Sustaining Offshore Production. SPE International petroleum exhibition & conference, Abu Dhabi. doi:10.2118/161189-MS.

Brownlee, M. H., & Sugg, L. A. (1987). East Vacuum Grayburg-San Andres Unit CO_2 Injection Project: Development and Results to Date. SPE 62nd Annual Technical Conference and Exhibition, Dallas, doi:10.2118/16721-MS.

Burns, L., Richardson, G., & Kimber, R. (2002). Tertiary Miscible Gas Injection in the Alwyn North Brent Reservoirs. SPE 13th European Petroleum Conference, Aberdeen. doi:10.2118/78349-MS.

Cardenas, R. L., Alston, R. B., Nute, A. J., & Kokolis, G. P. (1984). Laboratory design of a gravity-stable miscible CO_2 process. *Journal of Petroleum Technology*, Vol 36, No 1, pp111-118.

Caudle, B., & Dyes, A. (1958). Improving miscible displacement by Gas-Water Injection. *Petroleum Transactions*, AIME, Vol 213, pp281-284.

Cebrucean D., Cebrucean V. & Ionel I. (2014). CO_2 Capture and Storage from Fossil Fuel Power Plants, *Energy Procedia*, Volume 63, pp18-26.

Chang, Y.-B., Lim, M., Pope, G., & Sepehrnoori, K. (1994). CO_2 Flow Patterns under Multiphase Flow, Heterogeneous Field-Scale Conditions. *SPE Reservoir Engineering*, Vol 9, No 3, pp208-216.

Christensen, J., Stenby, E., & Skauge, A. (2001). Review of WAG Field Experience. *SPE Reservoir Evaluation and Engineering*, Vol 4, No 2, pp97-106.

Schenk C.J., Approaches to characterising fluid-flow heterogeneity in carbonate reservoirs. (1992). In *US Geological Survey Bulletin* by Margo *et al*, Denver, pp40-43.

Clyne, P., Bajsarowicz, C., Jones, K., Milne, D., & Richardson, S. (1993). Saving Thistle's Bacon: The Role of Reservoir Management in Optimising a High Watercut Field. SPE Offshore European Conference, Aberdeen. doi:10.2118/26787-MS.

CMG-GEM. Software Manual (2014.10). Computer Modelling Group.

CMG-GEM Technical Manual. (2014.10). Computer Modelling Group.

CMG-WinProp. (2014.10). Computer Modelling Group.

Coats, K., & Smith, B. (1964). Dean-End Pore Volume and Dispersion in Porous Media. *Society of Petroleum Engineers Journal*, Vol 4, No 1, pp73-84.

Coats, K. H., Dempsey, J. R., & Henderson, J. H. (1971). The Use of Vertical Equilibrium in Two-Dimensional Simulation of Three-Dimensional Reservoir Performance. *Society of Petroleum Engineers Journal*. Vol 11, No 1, pp 63-71.

Crameik, T., & Plassey, J. (1972). Carbon Dioxide Injection Project SACROC Unit, Scurry County, Texas. In *Annual Meeting Papers*, Division of Production. American Petroleum Institute.

Crogh, N., Eide, K., & Morterud, S. (2002). WAG Injection at the Statfjord Field, A Success Story. SPE 13th European Petroleum Conference, Aberdeen, doi:10.2118/78348-MS.

Dauben L. D. (1988), A Review of the West Sussex Unit CO_2 Flood Project, DOE Report, DOE/BC/10830-7.

Davis, D., Scott, M., Roberson, K., & Robinson, A. (2011). Large Scale CO_2 Flood Begins Along Texas Gulf Coast. SPE Enhanced Oil Recovery Conference, Kuala Lumpur. doi:10.2118/144961-MS.

Dicharry, R. M., Perryman, T. L., & Ronquille, J. D. (1973). Evaluation and Design of a CO_2 Miscible Flood Project-SACROC Unit, Kelly-Snyder Field. *Journal of Petroleum Technology*, Vol 25, No 11, pp1309-1318.

Deutsch, C. (2002). Geostatistical reservoir modelling: Oxford Univ. *Press, New York, New York*.

Dooley, J. J., Dahowski, R. T., & Davidson, C. L. (2010). CO_2-driven Enhanced Oil Recovery as a Stepping Stone to What? (No. PNNL-19557). Pacific Northwest National Laboratory (PNNL), Richland, WA (US).

Dria, D. E., Pope, G. A., & Sepehrnoori, K. (1993). Three-phase gas/oil/brine relative permeabilities measured under CO2 flooding conditions. *SPE Reservoir Engineering*, Vol 8, No 2, pp143-150.

El-Feghi F. A. (1992). Miscible flooding in correlated random fields (PhD thesis). Institute of Petroleum Engineering, Heriot-Watt University, UK.

Erbas, D., Dunning, M., Nash, T., Cox, D., Stripe, J., & Duncan, E. (2014). Magnus WAG Pattern Optimization through Data Integration. SPE Improved Oil Recovery Symposium, Tulsa, doi:10.2118/169167-MS.

Fanchi, J. R. (1983). Multidimensional numerical dispersion. *Society of Petroleum Engineers Journal*, Vol 23, No 1, pp143-151.

Fanchi J. R. (2000), Integrated Flow modelling, Vol 49, Elsevier publications.

Fatemi, S., & Sohrabi, M. (2012). Cyclic hysteresis in Three-Phase Relative Permeability Application to WAG Injection: Water-wet and Mixed Wet Systems under Low Gas-Oil IFT. SPE Annual Technical Conference and Exhibition, Texas, doi:10.2118/159816-MS.

Fayers, F. J., Hawes, R. I., & Mathews, J. D. (1981). Some aspects of the potential application of surfactants or CO_2 as EOR processes in North Sea reservoirs. *Journal of Petroleum Technology*, Vol 33, No 9, pp1617-1627.

Flanders, W. A., & DePauw, R. M. (1993). Update Case History: Performance of the Twofreds Tertiary CO_2 Project. SPE Annual Technical conference and Exhibition, Houston. doi:10.2118/26614-MS.

Flanders, W. A., Stanberry, W. A., & Martinez, M. (1990). CO_2 injection increases Hansford Marmaton production. *Journal of Petroleum Technology*, Vol 42, No 1, pp68-73.

Gardner, J. W., Orr, F. M., & Patel, P. D. (1981). The effect of phase behaviour on CO_2-flood displacement efficiency. *Journal of Petroleum technology*, Vol 33, No 11, pp2067-2081.

Garlick, T. DECC/Pilot EOR Workstream Update. Presentation delivered 23rd May 2012.

Garlick T., (2014) Maximising Enhanced Oil Recovery – Time to Commit Presentation.

Garmeh, G. (2010). *Investigation of scale-dependent dispersivity and its impact on upscaling miscible displacements* (PhD dissertation). University of Texas.

Johns, R. T., & Garmeh, G. (2010). Upscaling of miscible floods in heterogeneous reservoirs considering reservoir mixing. *SPE Reservoir Evaluation & Engineering*, Vol 13, No 5, pp747-763.

Gelhar, L. W., & Axness, C. L. (1983). Three-dimensional stochastic analysis of macrodispersion in aquifers. *Water Resources Research*, Vol 19, No 1, pp161-180.

Ghanbari, S., Al-Zaabi, Y., Pickup, G. E., Mackay, E., Gozalpour, F., & Todd, A. C. (2006). Simulation of CO_2 storage in saline aquifers. *Chemical Engineering Research and Design*, Vol 84, No 9, pp764-775.

Gharbi, R. B. (2002). Dimensionally Scaled Miscible Displacements in Heterogeneous Permeable Media. *Transport in porous media*, Vol 48, No 3, pp271-290.

Gharbi, R., Peters, E., & Elkamel, A. (1998). Scaling Miscible Fluid Displacements in Porous Media. *Energy & fuels*, Vol 12, No 4, pp801-811.

Ghomian, Y., Pope, G. A., & Sepehrnoori, K. (2008). Hysteresis and Field-Scale Optimization of WAG Injection for Coupled CO_2-EOR and Sequestration. SPE/DOE Improved Oil recovery Symposium, Tulsa. doi:10.2118/110639-MS.

Glennie, K. (1998). Petroleum Geology of the North Sea: Basic Concepts and Recent Advances. John Wiley & Sons; 4th edition.

Gluyas, J., & Mathias, S. (Eds.). (2013). *Geological storage of carbon dioxide (CO_2): geoscience, technologies, environmental aspects and legal frameworks*. Elsevier.

Gluyas, J. (2009). Carbon Geo-storage & CO_2-EOR; A UK Perspective, presentation delivered at the 7th Annual EOR Carbon Management Workshop, Houston.

Goodrich, J. (1980). Review and Analysis of Past and Ongoing Carbon Dioxide Injection Field Tests. SPE/DOE 6th Symposium on Improved Oil Recovery, Tulsa. doi:10.2118/8832-MS.

Goodyear, S. G., Hawkyard, I. R., Masters, J. H. K., Woods, C. L., Jayasekera, A. J., & Balbinski, E. (2003). Subsurface issues for CO_2 flooding of UKCS reservoirs. *Chemical Engineering Research and Design*, Vol 81, No 3, pp315-325.

Goodyear, S., Koster, M., Marriott, K., Paterson, A., Sipkema, A., & Young, I. (2011). Moving CO_2 EOR Offshore. SPE Enhanced Oil Recvoery Conference, Kuala Lumpur. doi:10.2118/144939-MS.

Grigg, R., & Schechter, D. (1997). State of the Industry in CO_2 Floods. Society of Petroleum Engineers. SPE Annual Technical Conference and Exhibition, San Antonio. doi:10.2118/38849-MS.

Guan, L. L., Du, Y., & Wang, Z. (2005). Water injectivity; what we have learned in the past 30 years. In *Canadian International Petroleum Conference*. Petroleum Society of Canada. pp9-13.

Ha, G., Tran, N., Vu, H., Takagi, S., Mitsuishi, H., Hatakeyama, A., & Dinh, Q. (2012). Design & Implementation of CO_2 Huff-n-Puff Operation in a Vietnam Offshore Field. International Petroleum Conference, Abu Dhabi, doi:10.2118/161835-MS.

Haajizadeh, M., Fayers, F. J., Cockin, A. P., Roffey, M., & Bond, D. J. (1999). On the Importance of Dispersion and Heterogeneity in the Compositional Simulation of Miscible Gas Processes. SPE Asia Pacific Improved Oil Recovery Conference, doi:10.2118/57264-MS.

Haajizadeh, M., Narayanan, R., & Waldren, D. (2001). Modelling Miscible WAG Injection EOR in the Magnus Field. SPE Reservoir Simulation Symposium, Houston. doi:10.2118/66378-MS.

Hadlow, R. (1992). Update of Industry Experience with CO_2 Injection. SPE 67th Annual Technical Conference and Exhibition, Washington. doi:10.2118/24928-MS.

Halil, T., Skinner, R., Brand, P., MacDonald, C., Grinestaff, G., & Trythall, R. (2002). Forties CO_2 IOR Evaluation Integrating Finite Difference and Streamline Simulation Techniques. SPE 13th European Petroleum Conference, Aberdeen. doi:10.2118/78298-MS.

Hardy, J., Barthorpe, R., & Rhudy, J. (1994). Scale Control in the South Brae Field. *SPE Production & Facilities*, Vol 9, No 2, pp127-131.

Hawkins, J., Benvegnu, A., Wingate, T., McKamie, J., Pickard, C., & Altum, J. (1996). SACROC Unit CO_2 Flood: Multidisciplinary Team Improves Reservoir Management and Decreases Operating Costs. *SPE Reservoir Engineering*, Vol 11, No 3, pp141-148.

Hansen, P. W. (1977). A CO_2 Tertiary Recovery Pilot Little Creek Field, Mississippi. SPE 52nd Annual Technical Conference and Exhibition, Denver, doi:10.2118/6747-MS.

Henderson, L. E. (1974). The Use of Numerical Simulation to Design a Carbon Dioxide Miscible Displacement Project. *Journal of Petroleum Technology*, Vol 26, No 12, pp1327-1334.

Hervey, J. R., & Iakovakis, A. C. (1991). Performance Review of a Miscible CO_2 Tertiary Project: Rangely Weber Sand Unit, Colorado. *SPE Reservoir Engineering*, Vol 6, No 2, pp163-168.

Hill, W. J., Tinney, T. J., Young, L. C., & Stark, K. L. (1994). CO_2 Operating Plan, South Welch Unit, Dawson County, Texas. SPE Permian Basin Oil and Gas Recovery Conference, Midland, Texas, doi:10.2118/27676-MS.

Hillier, G., Cobb, R., & Dimmock, P. (1978). Reservoir Development Planning For the Forties Field. European Offshore Petroleum Conference and Exhibition, London, doi:10.2118/8123-MS.

Holm, L., & Josendal, V. (1974). Mechanism of Oil Displacement by Carbon Dioxide. *Journal of Petroleum Technology*, Vol 26, No 12, pp1427-1438.

Holt, T., Lindeberg, E., & Wessel-Berg, D. (2009). EOR and CO_2 disposal – economic and capacity potential in the North Sea. *Energy Procedia*, Vol 1, No 1, pp4159-4166.

Holtz, M. H. (2002). Residual Gas Saturation to Aquifer Influx: A Calculation Method for 3-D Computer Reservoir Model Construction. SPE Gas Technology Symposium, Calgary, doi:10.2118/75502-MS.

Hsie, J. C., & Moore, J. S. (1988). The Quarantine Bay 4RC CO_2 WAG Pilot Project: A Postflood Evaluation. *SPE Reservoir Engineering*, Vol 3, No 3, pp809-814.

Instefjord, R., & Todnem, A. C. (2002). 10 Years of WAG Injection in Lower Brent at the Gullfaks Field. SPE 13th European petroleum conference, Aberdeen, doi:10.2118/78344-MS.

Jayasekera, A., & Goodyear, S. (2002). Improved Hydrocarbon Recovery in the United Kingdom Continental Shelf: Past, Present and Future. SPE/DOE Improved Oil Recovery Symposium, Tulsa. doi:10.2118/75171-MS.

Jennings Jr, J. W., Ruppel S.C., Ward, W. B. (2000). Geostatistical analysis of permeability data and modelling of fluid-flow effects in carbonate outcrops. *SPE Reservoir Evaluation & Engineering*, Vol 3, No 4, pp292-303.

Jensen, T., Harpole, K., & Østhus, A. (2000). EOR Screening for Ekofisk. SPE European Petroleum Conference, Paris, doi:10.2118/65124-MS.

Jethwa, D., Rothkopf, B., & Paulson, C. (2000). Successful Miscible Gas Injection in a Mature U.K. North Sea Field. SPE Annual Technical Conference and Exhibition, Dallas. doi:10.2118/62990-MS.

Jikich, S., & Ammer, J. (2012). Update on CO_2-EOR Research at the Office of Fossil Energy. CO_2 Conference Week. NETL, US Department of Energy.

Jonas, T. M., Chou, S. I., & Vasicek, S. L. (1990). Evaluation of a CO_2 Foam Field Trial: Rangely Weber Sand Unit. SPE 65th Annual Technical Conference and Exhibition, New Orleans, doi:10.2118/20468-MS.

Keeling, R. J. (1984). CO_2 Miscible Flooding Evaluation of the South Welch Unit, Welch San Andres Field. SPE 4th Symposium on Enhanced Oil Recovery, Tulsa, doi:10.2118/12664-MS.

Kemp, A. G., & Kasim, S. (2013). The Economics of CO_2-EOR Cluster Developments in the UK Central North Sea. *Energy policy*, Vol 62, pp1344-1355.

Khan, S. A., Pope, G. A., & Sepehrnoori, K. (1992). Fluid Characterization of Three-Phase CO_2/Oil Mixtures. SPE/DOE 8th Symposium on Enhanced Oil Recovery, Tulsa, doi:10.2118/24130-MS.

Kirkpatrick, R., Flanders, W., & DePauw, R. (1985). Performance of the Twofreds CO_2 Injection Project. SPE 60th Annual Technical Conference and Exhibition, Las Vegas, doi:10.2118/14439-MS.

Kleinstelber, S. W. (1990). The Wertz Tensleep CO2 Flood: Design and Initial Performance. *Journal of Petroleum Technology*, Vol 42, No 5, pp630-636.

Kohl, A. L., & Nielsen, R. (1997). *Gas purification*. Gulf Professional Publishing.

Kovscek, A. R., & Cakici, M. D. (2005). Geologic storage of carbon dioxide and enhanced oil recovery. II. Cooptimization of storage and recovery. *Energy Conversion and Management*, Vol 46, No 11, pp1941-1956.

Kuo, M. C. T., Dulaney, J. P., Deer, M. W., Evans, B. S., & Granquist, M. R. (1990). Optimization of Waterflood Performance and CO_2-Flood Design Using a Modelling Approach, Mallet Unit, Slaughter Field. SPE 65th Annual Technical Conference and Exhibition, New Orleans, doi:10.2118/20377-MS.

Lake L. W. (1989). Enhanced Oil Recovery. *Prentice Hall, Englewood Cliffs, New Jersey, 7632*, pp195-197.

Land, C. S. (1990). Calculation of the Water-Blocking Effect in Tertiary Miscible Displacement, SPE 26126.

Lin, E., & Poole, E. (1991). Numerical Evaluation of Single-Slug, WAG and Hybrid CO_2 injection Processes, Dollarhide Devonian Unit, Andrew County, Texas. *SPE Reservoir Engineering*, Vol 6, No 4, pp415-420.

MacAllister, D. J. (1989). Evaluation of CO_2 Flood Performance: North Coles Levee CO_2 Pilot, Kern County, California. *Journal of Petroleum Technology*, Vol 41, No 2, pp185-194.

McCain Jr, W. D. (1991). Reservoir-Fluid Property Correlations-State of the Art (includes associated papers 23583 and 23594). *SPE Reservoir Engineering*, Vol 6, No 2, pp266-272.

MacGregor, A. G., Trussell, P., Lauver, S., Bedrock, M., Bryce, J., & Moulds, T. (2005). The Magnus Field: extending field life through good reservoir management and enhanced oil recovery. In *Geological Society, London, Petroleum Geology Conference series*, Vol 6, No 1, pp. 469-475). Geological Society of London.

Magruder, J., Stiles, L., & Yelverton, T. (1990). Review of the Means San Andres Unit CO_2 Tertiary Project. *SPE Journal of Petroleum Technology*, Vol 42, No 5, pp638-644.

Malone, T., Kuuskraa, V., & DiPietro, P. (2014). CO_2-EOR Offshore Resource Assessment. US DOE/NETL.

Matthews, C. S. (1989). Carbon dioxide flooding. *Developments in Petroleum Science*, Vol 17, pp129-156.

Mathiassen, O. (2003). CO_2 as injection gas for Enhanced Oil Recovery and Estimation of the Potential on the Norwegian Continental Shelf. Norwegian University of Science and Technology, Trondheim, Norway.

Merritt, M., & Groce, J. (1992). A Case History of the Hanford San Andres Miscible CO_2 Project. *SPE Journal of Petroleum Technology*, Vol 44, No 8, pp924-929.

Meyer, J. (2006). Summary of Carbon Dioxide Enhanced Oil Recovery (CO_2-EOR) Injection Well Technology. American Petroleum Institute.

Meyers, B. D., & Hagler, J. A. (1977). Field Study - Ford Geraldine (Delaware Sand) Unit. SPE Permian Basin Oil and Gas Recovery Conference, Midland, Texas, doi:10.2118/6383-MS.

Mizenko, G. (1992). North Cross (Devonian) Unit CO_2 Flood: Status Report. SPE/DOE 8th Symposium on Enhanced Oil Recovery, Tulsa, doi:10.2118/24210-MS.

Moffitt, P., Pecore, D., Trees, M., & Salts, G. (2015). East Vacuum Grayburg San Andres Unit, 30 Years of CO_2 Flooding: Accomplishments, Challenges and Opportunities. SPE Annual Technical Conference and Exhibition, Texas, doi:10.2118/175000-MS.

Moore, J. S., & Clark, G. C. (1988). History Match of the Maljamar CO_2 Pilot Performance. SPE/DOE Enhanced Oil Recovery Symposium, Tulsa, doi:10.2118/17323-MS.

Morgenthaler, L., Lawson, J., Faircloth, R., & Berkshire, D. (1993). Scale Prediction and Control in the Denver Unit CO_2 Flood. SPE 68th Annual Technical Conference and Exhibition, Houston, doi:10.2118/26603-MS.

Moulds, T., Trussell, P., Erbas, D., David, C., Laws, E., Davies, C., & Strachan, N. (2010). Post-Plateau Reservoir Management in the Magnus Field. SPE Annual Technical Conference and Exhibition, Florence, doi:10.2118/134953-MS.

Muller, T., & Lake, L. (1991). Theoretical Study of Water Blocking in Miscible Flooding. *SPE Reservoir Engineering*, Vol 6, No 4, pp445-451.

Mungan, N. (1981). Carbon dioxide Flooding Fundamentals. *Journal of Canadian Petroleum Technology*, Vol 20, No 1, pp87-92.

Mungan, N. (1982). Carbon Dioxide Flooding - Applications. *Journal of Canadian Petroleum Technology*, pp112-117.

Nadeson, G., Anua, N., Singhal, A., & Ibrahim, R. (2004). Water-Alternating-Gas (WAG) Pilot Implementation, A First EOR Development Project in Dulang Field, Offshore Peninsular Malaysia. SPE Asia Pacific Oil and Gas Conference and Exhibition, Perth, doi:10.2118/88499-MS.

Novakovic, D. (2002). Numerical Reservoir Characterization Using Dimensionless Scale Numbers with Application in Upscaling (PhD dissertation), Louisiana State University).

Olden, P., Mackay, E., Pickup, G., Stewart, J., & Johnson, G. (2015). CO_2-EOR: Security of Storage. Scottish Carbon Capture & Storage.

Olden, P., Mackay, E., Pickup, G., Stewart, J., & Johnson, G. (2015). Techno-Economic Reservoir Modelling Final Report.

Orr, F. M. (2007). Theory of Gas Injection Processes. Tie-Line Publications.

Orr Jr, F. M., & Taber, J. J. (1981). Displacement of oil by Carbon Dioxide. Final report (No. DOE/ET/12082-9). New Mexico Inst. of Mining and Technology, Socorro (USA).

Parisi, D. M., Vahedifard, F., & Mazzola, M. S. (2015). Further Advances of CO_2-EOR by Promoting a "Triple-E" Approach: Energy Security, Environmental Quality and Economic Viability. Carbon Management Technology Conference, Sugarland doi:10.7122/439549-MS.

Parsons, R. (1974). Velocities in Developed 5-Spot Patterns, Journal of Petroleum Technology, Vol 26, pp550.

Perry G. E. & Johnston J. R. (1989) Weeks Island gravity stable CO_2 pilot: Final report, AC05-77ET12004

Peters, E., Afzal, N., & Gharbi, R. (1993). On Scaling Immiscible Displacements in Permeable Media. *Journal of Petroleum Science and Engineering*, pp183-205.

Peterson, C., Pearson, E., Chodur, V., & Pereira, C. (2012). Beaver Creek Madison CO_2 Enhanced Recovery Project Case History; Riverton, Wyoming. SPE 18th Improved Oil Recovery Symposium, Tulsa, doi:10.2118/152862-MS.

Petterson, O., Storli, A., Ljosland, E., & Massie, I. (1990). The Gullfaks field: Geology and Reservoir Development. *In North Sea Oil and Gas Reservoirs—II* (pp. 67-90). Springer Netherlands.

Pham, V., & Halland, E. (2017). Perspective of CO_2 for Storage and Enhanced Oil Recovery (EOR) in Norwegian North Sea. 13th International Conference on Greenhouse Gas Control Technology, Lausanne.

Phillips, L. A., McPherson, J. L., & Leibrecht, R. J. (1983). CO_2 Flood: Design and Initial Operations, Ford Geraldine (Delaware Sand) Unit. SPE 58th Annual Technical Conference and Exhibition, San Francisco, doi:10.2118/12197-MS.

Pittaway, K., Albright, J., Hoover, J., & Moore, J. (1987). The Maljamar CO_2 Pilot: Review and Results. *Journal of Petroleum Technology*, Vol 39, No 10, pp1256-1260.

Pittaway, K. R., & Rosato, R. J. (1991). The Ford Geraldine Unit CO_2 Flood-Update 1990. *SPE Reservoir Engineering*, Vol 6, No 4, pp410-414.

Pizarro, J., & Branco, C. (2012). Challenges in Implementing an EOR Project in the Pre-Salt Province in Deep Offshore Brazil. SPE EOR Conference at Oil and Gas West Asia, Muscat, doi:10.2118/155665-MS.

Pontious, S. B., & Tham, M. J. (1978). North Cross (Devonian) Unit CO_2 Flood - Review of Flood Performance and Numerical Simulation Model. *Journal of Petroleum Technology*, Vol 30, No 12, pp1706-1714.

Poole, E. (1988). Evaluation and Implementation of CO_2 Injection at the Dollarhide Devonian Unit. SPE Permian Basin Oil and Gas Recovery Conference. Midland Texas. doi:10.2118/17277-MS.

Reid, T. B., & Robinson, H. J. (1981). Lick Creek Meakin Sand Unit Immiscible CO_2 Waterflood Project. *Journal of Petroleum Technology*, Vol 33, No 9, pp1723-1729.

Rogers, J., & Grigg, R. (2001). A Literature Analysis of the WAG Injectivity Abnormalities in the CO_2 Process. *SPE Reservoir Evaluation and Engineering*, Vol 4, No 5, pp375-386.

Roper, M., Pope, G., & Sepehrnoori, K. (1992). Analysis of Tertiary Injectivity of Carbon Dioxide, SPE 23974. SPE Permian Basin Oil and Gas Recovery Conference. Midland Texas. doi:10.2118/23974-MS.

Rosman, A., Riyadi, S., & Kifli, A. (2011). Oil Recovery Optimization by Immiscible WAG in Offshore Mature Field: Dulang Case Study. SPE Enhanced Oil Recovery Conference, Kuala Lumpur, doi:10.2118/144531-MS.

UK-DTI Sustainable Hydrocarbon Additional Recovery Programme (SHARP) Reports (2001). CO_2-EOR issues: Phase 1 - Literature Review. ECL technology.

Schlumberger Petrel Manual (2014).

Schlumberger PVTi. Manual (2014).

Shook, M., Li, D., & Lake, L. W. (1992). Scaling immiscible flow through permeable media by inspectional analysis. *IN SITU-NEW YORK*-, Vol 16, pp311-311.

Sim, S., Udegbuanam, E., Haggerty, D., Baroni, J., & Baroni, M. (1994). Laboratory Experiments And Reservoir Simulation Studies In Support of CO Injection Project In Mattoon Field, Illinois, USA. *Journal of Canadian Petroleum Technology*, Vol 35, No 2, pp25-32.

Simlote, V., & Withjack, E. M. (1981). Estimation of Tertiary Recovery by CO_2 Injection-Springer A Sand, Northeast Purdy Unit. *Journal of Petroleum Technology*, Vol 33, No 5, pp808-818.

Skauge, A., & Sorbie, K. (2014). Status of Fluid Flow Mechanisms for Miscible and Immiscible WAG. SPE EOR Conference at Oil and Gas West Asia. Muscat, doi:10.2118/169747-MS.

Sorbie, K. S., Feghi, F., Pickup, G. E., Ringrose, P. S., & Jensen, J. L. (1994). Flow regimes in miscible displacements in heterogeneous correlated random fields. *SPE Advanced Technology Series*, Vol 2, No 2, pp78-87.

Spence, B., Horan, D., & Tucker, O. (2014). The Peterhead-Goldeneye gas post-combustion CCS project. *Energy Procedia*, Vol 63, pp6258-6266.

Spiteri, E., & Juanes, R. (2006). Impact of Relative Permeability Hysteresis on the Numerical Simulation of WAG Injection. *Journal of Petroleum Science and Engineering*, Vol 50, No 2, pp115-139.

Stalkup, F. I. (1978). Carbon Dioxide Miscible Flooding: Past, Present and Outlook for the Future. *Journal of Petroleum Technology*, Vol 30, No 8, pp1102-1112.

Stalkup, F. I. (1983). Miscible Displacement, Monograph Volume 8, Henry L. *Doherty Series, SPE, Richardson*, Texas.

Stewart, G. (1977). Enhanced Oil Recovery: A Review of Technological Achievement in the United States and Potential Application in the North Sea, Heriot-Watt University. Department of Petroleum Engineering.

Stewart, G. (2011). Well Test Design & Analysis. Penn-Well Corporation.

Stiles, L., & Magruder, J. (1992). Reservoir Management in the Means San Andres Unit. *SPE Journal of Petroleum Technology*, Vol 44, No 4, pp469-475.

Suffridge F. E., Duaben L. D., Pezzullo, J. A. (1986), Evaluation of the Little Knife CO_2 Minitest, DOE Report, DOE/BC/10830-3.

Taber, J., Martin, F., & Seright, R. (1997). EOR Screening Criteria Revisited - Part 1: Introduction to Screening Criteria and Enhanced Recovery Field Projects. *SPE Reservoir Engineering*, Vol 12, No 3, pp189-198.

Tanner, C., Baxley, P., Crump, J., & Miller, W. (1992). Production Performance of the Wasson Denver Unit CO_2 Flood. SPE/DOE 8th Symposium on Enhanced Oil Recovery, Tulsa, doi:10.2118/24156-MS.

Tchelepi H. A., & Orr, F. M. (1994). Interaction of Viscous Fingering, Permeability Heterogeneity, and Gravity Segregation in Three Dimensions. *SPE Reservoir Engineering*. Vol 9, No 4, pp266-271.

Thomas, S., Duncan, J., Haajizadeh, M., & Williams, J. (2008). Ula Field-Life after the Flood: Core & Log Experience from behind a Mature WAG Front. In *49th Annual Logging Symposium*, Society of Petrophysicists and Well-Log Analysts.

Thrash, J. (1979). Twofreds Field A Tertiary Oil Recovery Project. SPE Annual Technical Conference and Exhibition, Las Vegas, doi:10.2118/8382-MS.

Todd, M. (1979). Modelling Requirement for Numerical Simulation of CO_2 Recovery Processes, SPE California Regional Meeting, Ventura, doi:10.2118/7998-MS.

Tollefsen, S., Graue, E., & Svinddal, S. (1992). The Gullfaks Field Development: Challenges and Perspectives. European Petroleum Conference, Cannes, doi:10.2118/25054-MS.

Uchiyama, T., Fujita, Y., Ueda, Y., Nishizaki, A., Okabe, H., Takagi, S., & Nguyen Ngoc, H. (2012). Evaluation of a Vietnam Offshore CO_2 Huff & Puff Test. SPE 18th Improved Oil Recovery Symposium, Tulsa, doi:10.2118/154128-MS.

Waggoner, J., Castillo, J., & Lake, L. (1992). Simulation of EOR Processes in Stochastically Generated Permeable Media. *SPE Formation Evaluation*, Vol 7, No 2, pp173-180.

Wallace, M., Goudarzi, L., Callahan, K., & Wallace, R. (2015). A Review of the CO_2 Pipeline Infrastructure in the U.S. US DOE/NETL-2014/1681 Report.

Wang, S., & Robertson, S. (1998). Find Grid CO_2 Injection Process Simulation for Dollarhide Devonian Reservoir. SPE Permian Basin Oil and Gas Recovery Conference, Texas. doi:10.2118/39787-MS.

Warner, H. R. (1977). An evaluation of miscible CO_2 flooding in waterflooded sandstone reservoirs, *Journal of Petroleum Technology*, Vol 22, No 10, pp1339-1347.

Warren, E., & Smalley, P. (1994). North Sea Formation Waters Atlas, Issue 15. Geological Society.

William, C., & Plisga, G. (2011). Standard Handbook of Petroleum and Natural Gas Engineering. Gulf Professional Publishing.

Williams, J. D. O., Jin, M., Bentham, M., Pickup, G. E., Hannis, S. D., & Mackay, E. J. (2013). Modelling carbon dioxide storage within closed structures in the UK Bunter Sandstone Formation. *International Journal of Greenhouse Gas Control*, Vol 18, pp38-50.

Winzinger, R., Brink, J., Patel, K., Davenport, C., Patel, Y., & Thakur, G. (1991). Design of a Major CO_2 Flood, North Ward Estes Field, Ward County, Texas. *SPE Reservoir Engineering*, Vol 6, No 1, pp11-16.

Worldwide EOR survey (2012), *Oil and Gas Journal*.

Yellig, W., & Metcalfe, R. (1980). Determination and Prediction of CO_2 Minimum Miscibility Pressures. *SPE Journal of Petroleum Technology*, pp160-168.

Yortsos, Y. (1992). Analytical studies for processes at vertical equilibrium. In *ECMOR III-3rd European Conference on the Mathematics of Oil Recovery*.

Yuan, M., Mosley, J., & Hyer, N. (2001). Mineral Scale Control in a CO_2 Flooded Oilfield. SPE International Symposium on Oilfield Chemistry, Houston, doi:10.2118/65029-MS.

Zain, Z., Kechut, N., Nadeson, G., Ahmad, N., & Raja, D. (2001). Evaluation of CO_2 Gas Injection for Major Oil Production Fields in Malaysia - Experimental Approach Case Study: Dulang Field. SPE Asia Pacific Improved Oil Recovery Conference, Kuala Lumpur, doi:10.2118/72106-MS.

Zhang, P., Brodie, J., Daae, V., Erbas, D., & Duncan, E. (2013). BP North Sea Miscible Gas Injection Projects Review. SPE offshore Europe oil and Gas Conference and Exhibition, Aberdeen, doi:10.2118/166597-MS.

Zhou, D., Yan, M., & Calvin, W. (2012). Optimization of a Mature CO_2 Flood - from Continuous Injection to WAG. SPE 18th Improved Oil Recovery Symposium, Tulsa, doi:10.2118/154181-MS.

Webpages

2b1stconsulting.com. (2016). 2b1stconsulting.com. Retrieved from https://www.2b1stconsulting.com/petrobras-to-consider-new-set-of-fpsos-for-jupiter-pre-salt-projects/. Accessed at 10 Dec, 2016.

Bellona.no (2017). Bellona.no. Retrieved, from http://bellona.no/publication/bellonamelding-norges-fremtidige-co2-okonomi. Accessed at 10 May, 2017.

BP (2011). Miller Decommissioning Program. Retrieved from: http://www.bp.com/content/dam/bp-country/en_gb/uk/documents/Miller_Decomm_Programme.pdf; Accessed at 9 Dec 2016.

BP. (2016). Bp.com. Retrieved from http://www.bp.com/en_gb/united-kingdom/where-we-operate/north-sea/north-sea-decommissioning/miller.html. Accessed at 9 Dec, 2016.

Crystolenergy (2016). Crystolenergy.com Retrieved from: http://www.crystolenergy.com/assessing-future-north-sea-oil-gas/. Accessed at 9 Dec, 2016.

Duncan, E. (2014). BP North Sea EOR lessons learned presentation retrieved from: https://www.spe-uk.org/aberdeen/wp-content/uploads/2014/04/BP-N-Sea-EOR-Experience-SPE.pdf; Accessed at 10 Dec 2016.

Durusut, E., Pershad, H., Crerar, A., & Kemp, A. (2014). CO_2-EOR in the UK: Analysis of fiscal incentives. Scottish Carbon Capture and Storage. Retrieved from: http://www.element-energy.co.uk/wordpress/wp-content/uploads/2014/06/SCCS_CO2-EOR_JIP-TaxStudyNon-technicalReport.pdf, Accessed at 10 Dec 2016.

Energypedia (2016). Energy-pedia.com. Retrieved from http://www.energy-pedia.com/news/general/bp-to-abandon-miller-field-production. Accessed at 9 Dec, 2016.

Global CCS Institute (2016). Globalccsinstitute.com. Retrieved from https://www.globalccsinstitute.com/projects/sleipner CO2-storage-project. Accessed at 8 Dec, 2016.

Global CCS Institute (2017). Globalccsinstitute.com. Retrieved from https://www.globalccsinstitute.com/projects/petra-nova-carbon-capture-project. Accessed at 25 April, 2017.

Goldeneye project factsheet (2015). Shell website, retrieved from http://www.shell.co.uk/content/dam/royaldutchshell/documents/lubricants/goldeneye-021799-asset-fact-sheets-marketing.pdf; Accessed at 9 Dec 2016.

IEA Carbon Capture and Storage Technology Roadmap (2009), International Energy Agency; Retrieved from: https://www.iea.org/publications/freepublications/publication/CCSRoadmap2009.pdf Accessed at 10 Dec 2016.

IPCC. (2014). Summary for Policymakers. Retrieved from https://www.ipcc.ch/pdf/assessment-report/ar5/wg3/ipcc_wg3_ar5_summary-for-policymakers.pdf; Accessed at 9 Dec 2016.

MIT University. (2016). Mit.edu. Retrieved from https://sequestration.mit.edu/tools/projects/peterhead.html. Accessed at 10 Dec, 2016.

Norwegian Government. (2017). Regjeringen.no. Retrieved from https://www.regjeringen.no/en/aktuelt/development-of-a-full-scale-ccs-project/id2514804/. Accessed at 14 May, 2017.

Norwegian Petroleum Directorate. (2014). Www.npd.no. Retrieved from http://www.npd.no/en/Publications/Reports/Compiled-CO2-atlas/2-Petroleum-activity-on-the-Norwegian-Continental-Shelf/. Accessed at 10 May, 2017.

NPD, Norskpetroleumno. (2017). Norwegianpetroleum.no. Retrieved from http://www.norskpetroleum.no/en/environment-and-technology/carbon-capture-and-storage/. Accessed at 10 May, 2017.

NRG Company website. (2017). Nrg.com. Retrieved, from http://www.nrg.com/generation/projects/petra-nova/. Accessed at 25 April, 2017

OGAuthority (2016). www.ogauthority.co.uk. Retrieved from https://www.ogauthority.co.uk/data-centre/interactive-maps-and-tools/. Accessed at 8 Dec 2016.

Pennenergycom. (2016). Pennenergy.com. Retrieved from http://www.pennenergy.com/articles/pennenergy/2010/04/adco-starts-co2-injection.html. Accessed at 9 Dec, 2016.

Pershad, H., & Stewart, A. (2010). One North Sea Report. Element Energy. Retrieved from: http://www.ccsassociation.org/docs/2010/OneNorthSea.pdf; Accessed at 10 Dec 2016.

Pershad, H., Durusut, E., Crerar, A., Black, D., Mackay, E., & Olden, P. (2012). Economic impacts of CO_2-enhanced oil recovery for Scotland. Element Energy. Retrieved from: http://www.ccsassociation.org/index.php/download_file/view/538/98/. Accessed at 10 Dec 2016.

Peterhead CCS project (2015). Well Technical Specification. Retrieved from: https://www.gov.uk/government/uploads/system/uploads/attachment_data/file/530920/11.099_-_Well_Technical_Specification.pdf; Access at 10 Dec 2016.

Shell response to the Energy and Climate Change Committee Inquiry into the Future of CCS in the UK (2016) retrieved from https://www.parliament.uk/documents/commons-committees/energy-and-climate-change/Shell-submission-on-Future-of-CCS.pdf Accessed at 10 Dec 2016.

USEIA (2011), "United Kingdom natural gas production and consumption" retrieved from https://www.eia.gov/todayinenergy/detail.php?id=3170. Accessed at 10 May 2017.

USEIA (2013), “Residential Sector Monthly energy-related carbon dioxide emission, 2007-2012” retrieved from https://www.eia.gov/totalenergy/data/monthly/archive/00351309.pdf. Accessed at 9 Dec 2016.

USEIA (2016), “Federal offshore Gulf of Mexico Field production of crude oil” retrieved from https://www.eia.gov/dnav/pet/hist/LeafHandler.ashx?n=pet&s=mcrfp3fm2&f=m Accessed at 9 Dec 2016.

USEIA (2016), “Offshore production nearly 30% of global crude oil output in 2015” retrieved from http://www.eia.gov/todayinenergy/detail.php?id=28492 Accessed at 9 Dec 2016.